Centre for Acoustics, Dynamics and Vibration
School of Mechanical Engineering
The University of Western Australia

Vibration of finite coupled structures, with applications to ship structures

Tian Ran Lin
B.Eng., M.Eng.Sc.

This thesis is presented for the degree of Doctor of Philosophy of Engineering Science of the University of Western Australia

November 2005

Abstract

Shipbuilding is fast becoming a priority industry in Australia. With increasing demands to build fast vessels of lighter weight, shipbuilders are more concerned with noise and vibration problems in ships than ever. The objective of this thesis is to study the vibration response of coupled structures, in the hope that the study may shed some light in understanding the general features of ship vibration.

An important feature characterizing the vibration in complex structures is the input mobility, as it describes the capacity of structures in accepting vibration energy from sources. The input mobilities of finite ribbed plate and plate/plate coupled structures are investigated analytically and experimentally in this study. It is shown that the input mobility of a finite ribbed plate is bounded by the input mobilities of the uncoupled plate and beam(s) that form the ribbed plate and is dependent upon the distance between the source location and the stiffened beam(s).

Off-neutral axis loading on the beam (point force applied on the beam but away from the beam's neutral axis) affects the input power, kinetic energy distribution in the component plates of the ribbed plate and energy flow into the plates from the beam under direct excitation. Its effect on the ribbed plate response is most significant at low frequencies. It was also illustrated that the beam torsional vibration could be ignored in the ribbed plate formulation when the excitation is not a torsional moment, and is applied on the beam's neutral axis or on the plate at more than a quarter of plate bending wavelength away from the beam.

Another important feature of vibration in complex structures is the effect of periodic structural components and their irregularity on the propagation of vibration energy. Physical interpretations were given to the bounding frequencies and the response peaks in each pass band of a finite periodic ribbed plate. The study on vibration of periodic ribbed plates shown that vibration reduction in the pass bands could be achieved by simply imposing a single disorder to the periodic ribbed plate. Imposing beam spacing

disorder to a periodic ribbed plate could only localize the group of modes associated with the shear force couplings at beam/plate interfaces. Torsional stiffness irregularities of the stiffened beams are required to localize the group of modes associated with the moment couplings at the interfaces. Similar phenomena were observed for a coupled system consisting of two finite periodic or irregular ribbed plates coupled at right angles.

Some effort has been made to develop a simple and effective model for predicting vibration response in complex structures. Closed form solutions were obtained for predicting the vibration response of an L-shaped plate to point force and moment excitations. The solutions were then used to examine the validity of statistical energy analysis (SEA) in the prediction of vibration response of an L-shaped plate due to deterministic force excitations. It was found that SEA can be utilized to predict the frequency averaged vibration response and energy flow of L-shaped plates under deterministic force (moment) excitations providing that the source location is more than a quarter of wavelength away from the plate edges.

Furthermore, a simple experimental method was developed in this study to evaluate the frequency dependent stiffness and damping of rubber mounts by impact test.

Finally, analytical methods developed in this study were applied in the prediction of vibration response of a ship structure. It was found that input mobilities of ship hull structures due to machinery excitations are governed by the stiffness of the supporting structure to which the engine is mounted. Their frequency averaged values can be estimated from those of the mounting structure of finite or infinite extents. It was also shown that wave propagation in ship hull structures at low frequencies could be attenuated by irregularities imposed to the periodic locations of the ship frames. The vibration at higher frequencies could be controlled by modifications of the supporting structure.

Contents

Statement of originality

No materials contained in this thesis are presented for the award of any other degree or diploma in any other university. To the best of the author's knowledge, this thesis contains no material previously published or written by another person, except where reference is made in the text.

Tian Ran (Terry) Lin

20 November 2005

Acknowledgements

First and utmost, I would like to thank my supervisor, Professor Jie Pan for his continuing guidance and support during this research, particularly during the preparation of this dissertation. Without this guidance and support, this work would not be accomplished.

I am also indebted to Dr Nabil H. Farag for showing me some of the experimental techniques at the early stage of this research. His contribution to Chapter 8 of this thesis is acknowledged here.

Financial supports from the Australian Research Council, Strategic Marine Pty. Ltd. and Australian Defense Science and Technology Organization for this work is gratefully acknowledged.

I also want to express my gratitude to Dr K. Sum, Dr S. Peng, Ms H. Sun, Dr K. Cheng, A. Prof. H. Chua, Mr Z. Taylor, Mr B. Treeby and Mr A. Guzzomi and many other fellow PhD students and staff in this school for their advice, friendship and support during this PhD candidature.

Thanks to chief technician I. Hamilton, technician M. Reid of the mechanical workshop for preparing the test-rigs used in this project. I also want to thank Dr K. Haq of Graduate Research School for advice on correct use of English in this thesis.

Finally, I want to thank my wife, Miao Ling Wang for the sacrifices she made to support my personal endeavor in pursuing the knowledge and wisdom of mankind during this research.

To my ***Mum*** and ***Dad***

Shu Xia, **Ding** and You Zhu, **Lin**

Nomenclature

A_b , A_{bi}	Beam cross sectional area
$A_{1n} \sim A_{20n}$	Wave coefficients
$A_{i,j}$	Matrix element
B_b , B_{bi} , B_{bj}	Beam flexural stiffness
$B_{i,j}$	Matrix element
$C_{i,j}$	Matrix element
D , D_1 , D_2	Plate bending stiffness
E_0 , E_p , E_b	Young's modulus
F_d	Damping force
F_i , F_n	Modal force component
F_p	External point force acting on plates
F_b , F_{bi}	External point force acting on beams
$G_{m,n}$, G_{ni} , G_{Tni}	Modal stiffness terms of plates and beams
H , $H_1 \sim H_4$	Wave number ratio
H^{ss} , H^{sc} , H^{cs} , H^{cc}	Modal coupling terms
I	Second moment of inertia
IL	Insertion Loss
I_P	Polar moment of inertia
I_w	Warping constant
J	Torsional constant
K	Frequency dependent stiffness of rubber mounts
L_x , L_y	Plate edge lengths, beam length

M_0, M_T	External moment excitation
M_c, M_i, M_j, M_{Ln}, M_{Rn},	Modal coupling moment on beam/plate interfaces
M_n^x, M_n^y	Modal moment component
N	Number of beams on the plate
$\langle P \rangle$	Energy flow, input power
Q, Q_p, Q_b	General external forcing terms
Q_{Ln}, Q_{Rn}	Modal coupling force on beam/plate interfaces
R	Warping to torsional stiffness ratio
$\overline{R}$	Receptance
S, S_1, S_2	Plate surface areas
T, T_i, T_j	Torsional stiffness of beams
$\langle T \rangle_P$, $\langle T \rangle_B$	Kinetic energy of plates and beams
U	Flexural displacements
V	Flexural displacements
W	Flexural displacements
Y	Mobility
a	The dipole distance between the forces that form a dipole moment
$a_1 \sim a_4$	Constants
b, b_i, b_1, b_2	Beam depth, constants
$c_1 \sim c_{10}$, c_{21}, c_{22}	Constants
d_2	Constant
f	Frequency
h	Plate thickness
i	Numerical index unless specified otherwise (i.e. imaginary)
j	Numerical index unless specified otherwise (i.e. imaginary)

k_p, k_{p1}, k_{p2}	Plate bending wave number
k_b, k_{bi}, k_{bj}	Beam flexural wave number
$k_{n1} \sim k_{n4}$	Trace wave number
k_l, k_m, k_n	Modal wave number
$k_{l,m}$, $k_{m,n}$	Plate modal wave number
k_t, k_{ti}, k_{tj}	Beam torsional wave number
l	Modal index
m	Modal index, mass
m_c, m_i, m_j	Coupling moments at beam/plate and plate/plate interfaces
n	Modal index
q_c, q_L, q_R, q_i, q_j	Coupling forces at beam/plate interfaces
r	Stiffness ratio, frequency ratio, or the number of beams on a plate
$r_1 \sim r_4$	Constants
s	The number of beams on a plate, wave number ratio
t	Beam width
u_n	Modal coefficient
v_n	Modal coefficient
w_n	Modal coefficient
$\tilde{x}$	Displacement
x	Coordinate
x_b, x_i, x_1, x_2	Beam location
x_I, x_{II}, x_{III}	Local coordinates
y	Coordinate
z	Coordinate
Δx, Δz	Span of the plate sections of a ribbed plates
Δ_0	Off-neutral axis distance

Δ_1 , Δ_2	Constants
Λ_m , Λ_n , Λ_n^* , $\Lambda_{m,n}$	Modal constants
$\Theta_1 \sim \Theta_4$	Constants
α , $\alpha_1 \sim \alpha_7$	Constants
β	Constants
β_n	Modal constants
ϕ_l , ϕ_m , ϕ_n	Mode shape functions
φ	Moment angles of the external moment acting on the plate
η , η_p , η_b	Structural loss factor of plates or beams
λ_p , λ_x , λ_b , λ_t	Wavelengths
ν	Poisson's ratio
θ	Angular displacement
θ_n	Modal coefficients of beam torsional vibration
ϑ	Angular displacement
ϑ_n	Modal coefficients of beam torsional vibration
ρ , ρ_p , ρ_b	Material densities of the plate or beams
ρ_s	Plate surface mass
ρ_L	Beam mass per unit length
σ_0	Point force location
σ_1 , σ_2	Constants
τ_1 , τ_2	Moment components
$\gamma_1 \sim \gamma_4$	Constants
$\Delta\omega$	Half power bandwidth
ω	Angular frequency
ω_n	Natural frequency

Chapter 1
General introduction

1.1 Introduction

Vibration in complex structures, such as ship hull structures, has been a research topic for decades. The continuous effort for building a lighter and faster ship has resulted in the extensive usage of beam stiffened plates and higher power engines in ship constructions. At the same time, noise and vibration problems are often encountered, which often pose a challenge for shipbuilders and for structural and vibro-acoustic engineers. The understanding of wave motions in such complex structures is vital for the effective control of those noise and vibration problems.

Unlike the vibration in simple continuous structures, such as beams and plates [1-7], a detailed analysis of wave motions in complex structures is often difficult to implement because of the complexity of structural configurations and the uncertainty of boundary conditions. There is a tendency in the engineering community to seek either numerical solutions, such as finite element analysis (FEA) or statistical solutions, such as statistical energy analysis [8]. However, both approaches provide limited fundamental understanding of wave propagation in such structural systems, which is critical for many passive and active vibration control techniques. There is thus a need for analytical solutions to provide a direct physical interpretation of wave motions in coupled structures.

The wave motions in continuous systems can be well described by partial differential equations. One common approach of analyzing the wave motions in a continuous

structure is to treat the structure as an infinite system when the effect of boundary wave reflections on the structure response is insignificant. The partial differential equations of the system can then be solved by wave approaches or by Fourier transformation. However, because engineering structures including ship hull plates are finite in size and are often lightly damped, many of them can not be regarded as infinite systems where the boundary wave reflections increase the complexity of the analysis. Therefore, central to the vibration problems in engineering applications is the vibration of finite coupled structures, particularly when the structures are lightly damped.

Finite coupled structures usually consist of finite beams and plates coupled in forms of beam/beam, beam/plate and plate/plate couplings. These couplings can co-exist in a large complex coupled system. Exact solutions for the vibrations of finite coupled systems are obtainable when the boundary conditions of the system can be precisely described. Fourier transformation can be employed to provide solutions to the partial differential equations of a finite coupled structure at discrete frequencies. The partial differential equations of a finite coupled system can also be solved by wave guide approaches or by modal expansion solutions. In the modal expansion solution, the system response is determined by the sum of an infinite series, which includes all the modal responses of the system. Truncation of the series is normally embraced in the calculation where contributions from higher order structural modes are often ignored. The wave guide method, which is the combination of semi-modal decomposition and travelling wave solutions can be employed when the structure components of a coupled system share the same boundary conditions in the direction of wave propagation. The wave guide method and modal expansion solution are utilized in this study to provide analytical solutions for the finite coupled structures under investigation.

Finite coupled structures typical for ship structures i.e. beam stiffened plates, periodic and irregular ribbed plates, L-shaped plates and a coupled system consisting of two finite periodic or irregular ribbed plates coupled at right angles are considered in this study. Wave propagation in these coupled structures is controlled by the coupling mechanisms at the structural interfaces. For beam stiffened plates, wave propagation in the structure is governed by the coincidence conditions between the plate bending waves and the flexural/torsional waves of the beam(s). For two plates coupled at right angles, the vibration transmission is mainly controlled by the moment coupling at the plate/plate junction. Periodic ribbed plates are a special class of beam stiffened plates where plates are regularly reinforced by uniform beams at equal intervals. One of the typical characteristics of a periodic system is the 'pass band' and 'stop band' where some waves can propagate freely in the system while others can't. The 'pass band' of a periodic ribbed plate can be classified further into two groups. One is governed by the shear force couplings at the beam/plate interfaces (the coupling between beam flexural waves and plate bending waves), another is governed by the moment couplings at the interfaces (the coupling between beam torsional waves and plate bending waves). Irregularities in a disordered periodic system result in a vibration localization phenomenon, which is well known in solid state physics as Anderson localization [9]. The principle of vibration localization phenomenon of disordered periodic systems can also be employed in the passive vibration control of ship hull structures.

Only flexural wave motions in plates are considered in this study, while both the flexural and torsional vibrations of beam(s) are included. The excitations to the structures can be either force or moment sources and, can be applied either on the beam(s) or on the plate. The analytical results obtained from the wave guide and

modal expansion methods are validated by results obtained from FEA analysis and experimental measurements.

Because of the increasing importance of rubber mounts in the isolation of vibration transmission from machinery to the supporting structures, a chapter of this thesis is devoted to the development of a simple experimental method to estimate the frequency dependent stiffness and damping of rubber mounts.

Finally, the results obtained for coupled finite structures are compared with those from finite element analysis of vibration in a ship structure. Useful links between idealized coupled structures and complex ship structures are discussed.

1.2 Objective of this work

The aim of this thesis is to achieve some understanding of wave motions in complex structures by studying several finite coupled structures and by using analytical, numerical and experimental methods. Another aim is to develop simple and useful analytical solutions for the vibration in beam/plate coupled structures. Also included in this thesis is the development of an experimental method to evaluate the frequency dependent stiffness and damping coefficient of rubber mounts, since rubber mounts are of growing importance in the control of energy transmission from vibrating machinery to supporting structures.

The main objectives of the research in this thesis are:

1. To obtain analytical and closed form solutions to predict the vibration response of finite beam stiffened plates to point force and moment excitations.
2. To study effects of off-neutral axis loading on the ribbed plate response.

3. To investigate the characteristics of energy flow between the beam and the component plates of finite ribbed plates.
4. To study the dependency of ribbed plate responses on the distance between the stiffened beam and the excitation locations and the relation between the ribbed plate response with that of the corresponding un-ribbed plate and beam of finite and infinite extents.
5. To explore the 'pass band' and 'stop band' properties of a finite periodic ribbed plate.
6. To provide physical interpretations to the bounding frequencies and the peak responses in each pass band of a finite periodic ribbed plate.
7. To study the vibration confinement of a finite irregular ribbed plate.
8. To study the vibration response of an L-shaped plate to point force and moment excitations, and to examine the validity of SEA in the prediction of vibration response of coupled plate systems due to deterministic force (moment) excitations.
9. To study the vibration energy propagation and attenuation of a coupled system consisting of two finite periodic or irregular ribbed plates coupled at right angles.
10. To investigate the vibration localization of the coupled system by imposing structural irregularities to the system.
11. To study the vibration characteristics of a completely clamped-clamped ribbed plate analytically and experimentally.
12. To develop a simple experimental method to evaluate the frequency dependent stiffness and damping coefficient of a rubber mount (*in situ*).
13. To explore the possibility of implementing the analytical and numerical methods for the prediction and vibration controls in ship structures.

1.3 Introduction to thesis

To be directly relevant, the literature reviews of ribbed plates relating to work in Chapters 2, 3 and 7 are incorporated into Chapter 2. The literature reviews for both periodic and periodic disorder systems closely related to work in Chapters 4 and 6 are included into Chapter 4. The part of literature reviews for plate/plate coupled structures is integrated into Chapter 5 while the part of literature reviews relating to the measurement of the frequency dependent rubber dynamic stiffness and damping is integrated into Chapter 8. The literature relating to the analysis of ship structure vibrations are incorporated into Chapter 9.

The first three objectives are covered in Chapter 2 where wave guide approaches are employed to obtain analytical solutions for predicting the vibration response of a finite ribbed plate to point force (moment) excitations applied either on the beam or on the plate. Effects of off-neutral axis loading on the ribbed plate response are investigated. The characteristics of energy flow between the beam and the two component plates on each side of the beam to point force and moment excitations applied on the beam are investigated.

Chapter 3 focuses on the derivation of closed form solutions for the vibration response of finite ribbed plates to point force and moment excitations applied either on the plate or on the beam. The relationship between the input mobility functions of ribbed plates with respect to the asymptotic mobilities of the corresponding infinite beam and infinite plate and the dependency of the input mobility functions on the distance between the source location and the beam are studied. The general properties of the input mobility functions of a finite ribbed plate are summarized.

In Chapter 4, analytical solutions are presented to predict the vibration response of finite periodic and irregular ribbed plates by employing the modal expansion solution. The excitation to the system can be either point force or moment and can be applied either on the plate or on the beams. The solutions are utilized to study the band pass/stop properties of a finite periodic ribbed plate and the vibration confinement phenomenon when structural irregularities are introduced. The characteristics of modal vibration in pass bands are studied. The mechanism of vibration confinement of disordered periodic ribbed plates is studied by the effect of structural irregularities on the nature of beam/plate couplings.

Closed form solutions are obtained in Chapter 5 to predict the vibration response of an L-shaped plate to point force and moment excitations by utilizing the wave guide approach. Explicit expressions are given for input mobilities, energy flow between the plates and wave coefficients of the travelling wave solution. The validity of SEA for predicting the frequency averaged vibration response of coupled plate structures due to deterministic force excitations is examined.

Chapter 6 presents an analytical solution for the vibration response of a coupled system consisting of two finite periodic or irregular ribbed plates coupled at right angles. Vibration confinement phenomenon is also examined by imposing structural irregularities to the source ribbed plate.

The vibration response of a completely clamped-clamped ribbed plate is investigated both analytically and experimentally in Chapter 7. Explanations are given to the discrepancies found between the analytical predictions and the measured responses.

A simple experimental method for evaluating the frequency dependent stiffness and damping of rubber mounts is presented in Chapter 8 by utilizing the measured complex frequency response function obtained from impact test in conjunction with the least-squares polynomial curve fitting of the data obtained from the test.

Analytical and numerical approaches are applied for the prediction and vibration controls of a ship hull structure in Chapter 9. Two passive vibration control methods are proposed. One aims to control the vibration transmission at the source location and the other aims to control the wave propagation in the ship hull structure.

Finally, general conclusions of this research work and some recommendations for the future work are given in Chapter 10.

Chapter 2

The effect of off-neutral axis loading on the vibration response of finite ribbed plates

2.1 Introduction

Beam stiffened plates (ribbed plates) are often found in ship hull structures where plates are reinforced by beams to give lighter and stronger composite structures. Machinery excitations to beam stiffened plates are usually via the machine mounts attached to the beam(s). Such excitations are often idealized as point force (moment) excitations applied on the beam. For some cases, the machine mounts are not concentric with the neutral axis of the supporting beam(s) (e.g. the centre of each mount is not coincided with the beam's neutral axis due to installation errors). Effects of such off-neutral axis loading to the response of the supporting structure are not well known, and are investigated in this chapter. The study also considers external excitations applying on the plate of a beam stiffened plate since such excitations can also be found in some engineering applications. One typical example is the hydrodynamic pressure excitation on the ship hull plate due to propellers. Another example is the practical requirement of estimating input power into the hull structure of a ship due to excitations of propeller shafts through mechanical joints between the shaft and hull.

2.2 Literature review

The vibration response of beam stiffened plates has been an interesting research topic for decades due to the growing importance of beam stiffened plates in engineering applications. The three landmark papers published in early 60s by Maidanik [10],

Lamb [11] and Ungar [12] constructively highlighted the relevance of the vibration of ribbed plates to important vibro-acoustical problems. Maidanik focused on the vibration response of ribbed panels to diffuse sound fields. He found that the ribbing increases the radiation resistance of the panel and therefore encourages the energy exchange between the panel and sound field. His work also significantly contributed to the development of a technique, called Statistical Energy Analysis, which has become a common tool used in the vibro-acoustical area. The work by Lamb concentrated on the point force input impedance of an infinite elastic beam attached to a thin elastic plate. The property of the impedance was related to the vibration radiation characteristics from the beam to the plate in terms of the ratio of flexural wave speed on the plate to that on the beam. Strong radiation into plate was found possible when the ratio is less than one, while plate excitation by the beam becomes localized when the ratio is larger than one. His work reveals a strong coupling between the beam and plate at the low frequencies. At very high frequencies, the impedance approaches that of a free beam. Ungar, on the other hand, looked at plate flexural wave transmission through reinforcing beams with specific interests on the dynamic stress concentration induced by wave interference near the beam/plate interfaces. The phenomenon of coincidence transmission of flexural wave in the plate corresponding to its trace matching with flexural and torsional waves in the beam was discovered.

Since the publication of these three important papers [10-12], many papers on ribbed plate vibration and its interaction with surrounding fluid were published. The effort has been mainly in the areas of developing techniques to solve the coupled beam/plate partial differential equations and using ribbed plates as a model to gain a better understanding of the vibro-acoustical properties in complex structures. A ribbed plate structure is often modeled as an infinite system when the boundary wave

reflection to the structure response is insignificant. Kovinskaya and Nikiforov [13] investigated the flexural response of infinite plates reinforced by one, two and three parallel beams under symmetrical point force excitations. The integral resulting from Fourier transformation for the plate response in the far field was approximated by using the method of steepest descent in the polar coordinate system. They found that the directivity of the plate's far field flexural wave motion to symmetrical force excitation was not affected by increasing the number of equal spaced beams on the plate. Rumerman [14] presented a closed form solution for an infinite periodic ribbed plate to general force excitations by utilizing the spectral impedance of the plate and the spectral flexural and torsional impedance of the ribs obtained from the Fourier transformation. Nevertheless, no discussions were given for the analytical expressions in his study.

Mace [15] studied the vibration response of infinite periodic stiffened fluid loaded plates to line and point force excitations by employing the Fourier transformation where the Fourier integrals were evaluated either by contour integration or by numerical integration. He observed that the infinite ribbed plate behaves as an orthotropic plate at low frequencies when the span between two consecutive beams is less than one third of the plate bending wavelength. He also found that the response of the stiffened plate approaches that of the corresponding orthotropic plate at low frequencies when the excitation is applied on the plate and when the fluid loading effect is ignored. The response of the ribbed plate approaches that of the rib at high frequencies when the excitation is applied on the rib. He further illustrated that the infinite periodic ribbed plates also have peak responses at frequencies associated with the coherent influence of the reflections from the ribs.

Goyder [7] extended the work of Lamb [11] by studying the response of infinite ribbed plates to point force and moment excitations applied on the beam where the integrals of Fourier transformation was approximated by the method of steepest descent as described by Kovinskaya and Nikiforov [13]. He found that in point force and bending moment excitation cases, the beam flexural stiffness initially controls the transmitted power flow into the plate. At distance away from the source location, the power flow in the beam is negligible when compared with the power in the plate. The radiated vibration field from the beam has certain directionality and the maximum vibration response occurs at the coincidence angles $\pm \sin^{-1}(k_b / k_p)$ where k_b and k_p are respectively the flexural wavenumber of the beam and the plate. This result agrees well with those obtained by Cremer et al [1] and Unger [12] using propagation wave approaches. In torsional moment excitation case, it was found that a ribbed plate behaves like a plate at low frequencies or when the beam torsional stiffness and inertia are relatively small. At high frequencies or when the plate bending stiffness is relatively small, the ribbed plate response approaches to the response of a corresponding beam. It was also found that the beam could radiate energy freely to the plate from the driving point at low frequencies.

Cremer et al [1] and Ungar [12] obtained the wave transmission and reflection coefficients of infinite beam stiffened plates by wave approaches where the 'trace-matching' conditions between the incident plate bending wave and the beam flexural and torsional waves were discussed. Kessissoglou and Pan [16] also discussed the 'trace-matching' conditions at the beam/plate interface of an infinite ribbed plate and showed that wave transmission across the reinforced beam could be attenuated by applying an active control force on the beam. They [17] illustrated that a similar control technique could be employed to control the sound radiation from an infinite ribbed plate by applying an array of control point forces on the beam. Additionally,

Kessissoglou [18] studied the active control of flexural wave transmission across the reinforced beam of a semi-infinite ribbed plate by employing the wave guide approach. Experimental results were also presented in her study, which shown good agreement with the analytical prediction.

Besides the two common analytical approaches, other methods have also been developed. Mead [19] considered the free response of an infinite fluid loaded periodic plate reinforced by ribs in one and two orthogonal directions to distributed harmonic pressure fields by using the space harmonics method and phased array receptance functions. Finite element method was employed for finding the wave propagation constants of the ribbed plates. Maidanik and Dickey [20] obtained the impulse response function of a singly ribbed plate and extended the analysis to derive the impulse response function of a regular ribbed plate. The ribs were modeled by line force and line moment impedance in the formulation. Ji et al [21] studied the vibration response of an infinite plate reinforced by a finite beam to point force excitation applied on the beam by the hybrid method of modal expansion (for the beam) and Fourier transformation (for the infinite plate). Only shear force coupling at the beam/plate interface was considered in their analysis. Moreover, the vibration response and sound radiation of infinite ribbed plates by including the fluid loading effect were also investigated by many other researchers [22-26].

The investigations of vibration response and sound radiation of infinite ribbed plates provided the fundamental understanding of wave motions in a ribbed plate and their effectiveness when coupled with driving forces and the acoustic medium. However, when the structures become finite, the interference between incident and reflecting waves increases the complexity of analysis, which requires further efforts from the researchers.

Several analytical methods, such as Rayleigh-Ritz energy method [27-30], finite difference [31], transfer matrix [32], semi-modal decomposition [33] and differential quadrature [34] methods have been developed to predict the free vibration of finite ribbed plates. Moreover, Mahalingham [35] studied the free vibration of a rectangular plate having a central stiffener parallel to a pair of plate edges by using approximately characteristic beam functions. Langley [36] studied the free and forced vibration response of finite and infinite aircraft panels (ribbed plates) by finite element method where a dynamic stiffness matrix formulation and a particular integral were used. Through studying the vibration of finite ribbed plates, Mead and Yaman [37] provided an analytical solution for the vibration response of a finite sandwich beam stiffened rectangular plate to line force excitations by wave approaches. Experimental work was also presented in the study, which shown good agreement with the analytical prediction. Grice and Pinnington [38] obtained the input impedance of an infinite beam attached to a plate with finite or infinite extent to point force excitation applied on the beam where only shear force coupling at the interface was considered. They found that the plate behaved as locally reacting impedance to the beam when the plate flexural wavenumber was more than twice the beam flexural wavenumber. It was recognized that when a beam is attached to a finite plate, the transmission along the beam was attenuated significantly in the narrow frequency bands in which the plate was anti-resonant. Nevertheless, the beam used in their analysis could not carry complex waves and the result was inaccurate at low frequencies due to the neglecting of near field effects at the driving location.

In contrast to the analytical methods, the rapid advance of computer technologies has made it possible to use numerical methods, such as finite element analysis (FEA) for the vibration analysis of complex coupled structures, such as ribbed plates. Mead et al [39] used the hierarchical finite element model and calculated the natural modes of

a flat plate reinforced by grids of beam stiffeners in both plate directions. Effects of boundary conditions on the natural frequencies of stiffened plates and the coincident effect of the plate response on the pressure field were discussed. Panali et al [40] used direct finite element formulations for both static and vibration analysis of beam stiffened plates with different boundary conditions. Transverse shear deformations of plates were included in the formulation. Orrenius and Finnveden [41] applied the FEA analysis to study wave propagation of ribbed plate structures in a wave guide model. Grice and Pinnington [42] used the locally reacting plate impedance to solve the vibration response of a finite plate stiffened beam by finite element analysis. In general, FEA is an effective numerical tool in predicting the vibration characteristics of ribbed plate structures with complex configurations, such as ship structures at low frequencies. However, simple and closed form analytical solutions for the response and input mobility of complex structures (even though they may be approximated solutions) are always sought for a quick and qualitative engineering estimate.

In summary, a ribbed plate system is often considered as an infinite system (e.g. references [11], [13] and [12], etc) where force excitations on the systems are either applied on the beam (e.g. references [7], [13], [21] and [24], etc) or applied on the plate between two beams (e.g. references [13], [22] and [23], etc). For analysis where the point force excitation is on the beam, a common implicit assumption is that the point force acts on the neutral axis of the beam. However, in practical applications, force excitations could be applied at locations away from the beam's neutral axis, e.g. the off-neutral axis loading of engine excitations on the supporting ribbed plate structures because of installation errors of the mounts on the beam(s). The importance of engine feet positions on energy transmission from an engine to the supporting structure was studied experimentally by Coja and Nilsson [43]. Effects of off-neutral axis loading on the vibration response of a finite ribbed plate are

investigated in this chapter in terms of input power, energy flow between the beam and the plates and kinetic energy distribution in the component plates by utilizing the analytical solution obtained from the wave guide approach.

2.3 General formulations

A ribbed plate model and the associated coordinate system are shown in Figure 2.1. The stiffened beam is assumed firmly attached on one side of the plate so that no slippery motion occurs between the beam and the plate during vibration. This type of coupled structures is typical for ship hull structure and has been reported in many literatures [44, 45]. It is assumed that the plate thickness is small when compared to the other plate dimensions so that both shear deformation and rotational inertia can be ignored. The plate is assumed to have simply supported boundary conditions on the pair of plate edges perpendicular the beam's neutral axis. It is further assumed that the beam is also simply supported and is symmetrical so that the flexural and torsional vibrations of the beam are uncoupled.

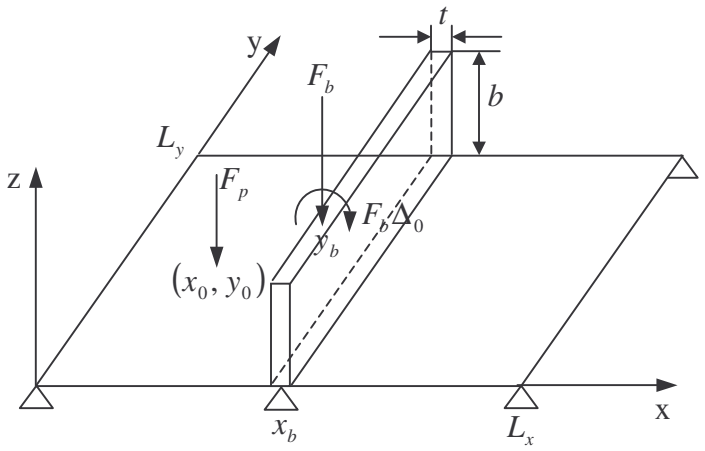

Figure 2.1. Model description and the coordinate system of the ribbed plate.

The ribbed plate is divided into three structural components in this analysis as shown in Figures 2.2(a) – 2.2(c), the component plate on the left of the beam is termed as Plate 1 and the component plate on the right as Plate 2.

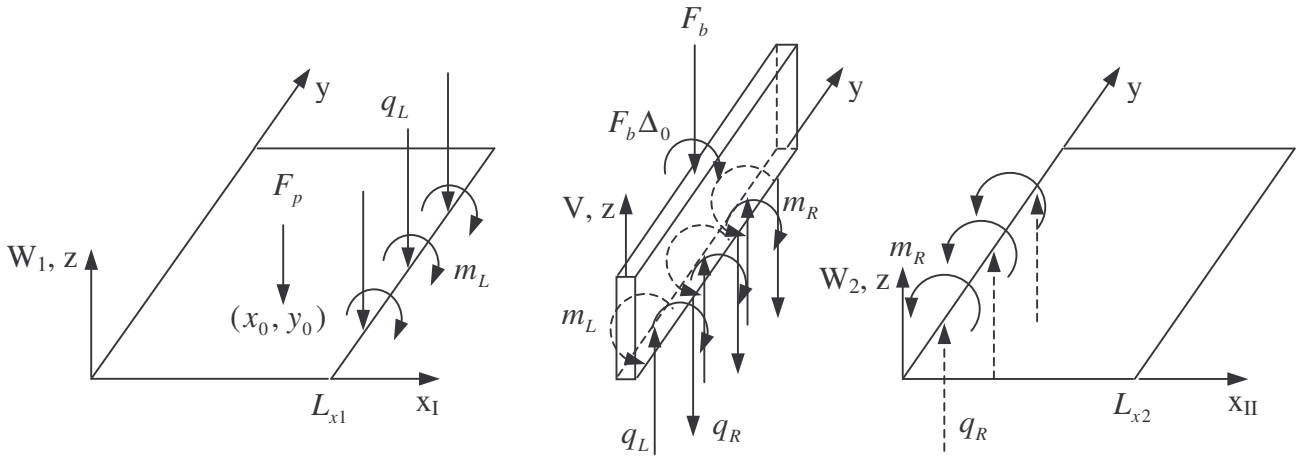

Figure 2.2. The three structural components and the associated local coordinate systems of the ribbed plate.

The governing equation of the plate bending displacement (W_1) for Plate 1 to point force excitation (F_p) applied at plate location (x_0, y_0) is:

$$\nabla^4 W_1 - k_p^4 W_1 = \frac{F_p}{D}\delta(x_I - x_0)\delta(y - y_0) \ , \tag{2.1}$$

where $k_p = (\frac{\rho_s \omega^2}{D})^{1/4}$ and $D = \frac{E_p h^3}{12(1-\nu^2)}$ are the wave number and plate bending rigidity, h, E_p, ν, ρ_s are respectively the thickness, Young's modulus, Poisson's ratio and surface mass of the plate. x_I and y are the local coordinates of Plate 1.

The governing equations of the uncoupled beam flexural and torsional displacements (V and θ) are written as [44, 45]:

$$\frac{\partial^4 V}{\partial y^4} - k_b^4 V = \frac{F_b}{B_b}\delta(y - y_b) + \frac{q_L - q_R}{B_b}, \tag{2.2}$$

and

$$\frac{\partial^2 \theta}{\partial y^2} + k_t^2 \theta - R\frac{\partial^4 \theta}{\partial y^4} = \frac{F_b \Delta_0}{T}\delta(y - y_b) + \frac{m_R - m_L}{T} + \frac{q_R + q_L}{T}\frac{t}{2}, \tag{2.3}$$

where $k_b = (\frac{\rho_L \omega^2}{B_b})^{1/4}$ and $k_t = (\frac{\rho_b I_p \omega^2}{T})^{1/2}$ are the beam flexural and torsional wave numbers, ρ_L is the beam mass per unit length and $\rho_b I_p$ is the mass moment of inertia per unit length of the beam. $B_b = E_b I$ and $T = GJ$ are respectively the bending and torsional stiffness of the beam, G is the shear modulus, $R = \frac{E_b I_w}{T}$ is the warping to torsional stiffness ratio of the beam, I and I_p are respectively the second moment and polar moment of inertia, while I_w and J are the warping and torsional constants of the beam, F_b is the external point force applied on the beam at location $y = y_b$ (see Figure 2.2(b)), Δ_0 is the off-neutral axis distance of the point force to the beam's neutral axis and t is the beam width. m_L and q_L are the coupling moment and shear force on the left hand side of the beam/plate interface while m_R and q_R are the coupling moment and shear force on the right hand side of the interface. The value of I_w and J for some commonly used beam cross section areas can be found in reference [4].

Similarly, the governing equation of the plate bending displacement (W_2) for Plate 2 is given by:

$$\nabla^4 W_2 - k_p^4 W_2 = 0. \tag{2.4}$$

Equations (2.1) – (2.4) can be solved by semi-modal decomposition of W_1, V, θ and W_2 as:

$$W_1 = \sum_n w_{1n}\phi_n(y), \tag{2.5a}$$

$$V = \sum_n v_n\phi_n(y), \tag{2.5b}$$

$$\theta = \sum_n \theta_n\phi_n(y), \tag{2.5c}$$

and

$$W_2 = \sum_n w_{2n}\phi_n(y), \tag{2.5d}$$

where $\phi_n(y) = \sin(k_n y)$, $k_n = \dfrac{n\pi}{L_y}$ is the n[th] simply supported vibration mode shape and modal wave number of the plate in the y-direction.

Equations (2.5a) – (2.5d) are substituted into Equations (2.1) – (2.4) to have:

$$\frac{\partial^4 w_{1n}}{\partial x_I^4} - 2k_n^2\frac{\partial^2 w_{1n}}{\partial x_I^2} + (k_n^4 - k_p^4)w_{1n} = \frac{F_p\phi_n(y_0)\delta(x_I - x_0)}{D\Lambda_n}, \tag{2.6}$$

$$v_n = \frac{1}{G_n}[F_b\phi_n(y_b) + Q_{Ln} - Q_{Rn}], \tag{2.7}$$

$$\theta_n = -\frac{1}{G_{Tn}}[F_b\Delta_0\phi_n(y_b) - M_{Ln} + M_{Rn} + \frac{t}{2}(Q_{Ln} + Q_{Rn})], \tag{2.8}$$

and

$$\frac{\partial^4 w_{2n}}{\partial x_{II}^4} - 2k_n^2\frac{\partial^2 w_{2n}}{\partial x_{II}^2} + (k_n^4 - k_p^4)w_{2n} = 0, \tag{2.9}$$

where x_{II} is the local coordinate of Plate 2. $Q_{Ln} = \int_0^{Ly} q_L\phi_n(y)dy$, $Q_{Rn} = \int_0^{Ly} q_R\phi_n(y)dy$, $M_{Ln} = \int_0^{Ly} m_L\phi_n(y)dy$ and $M_{Rn} = \int_0^{Ly} m_R\phi_n(y)dy$ are the modal coupling forces and moments at the beam/plate interface, $G_n = B_b\Lambda_n(k_n^4 - k_b^4)$, $G_{Tn} = T\Lambda_n(Rk_n^4 + k_n^2 - k_t^2)$ and $\Lambda_n = \dfrac{L_y}{2}$.

2.4 Ribbed plate response to point force excitation on the beam

For this case, $F_P = 0$, the modal displacements of Plate 1 and Plate 2 (Equations (2.6) and (2.9)) can be represented by the travelling wave solutions as:

$$w_{1n} = A_{1n}e^{-k_{n1}(L_{x1}-x_I)} + A_{2n}e^{-k_{n1}x_I} + A_{3n}e^{-k_{n2}(L_{x1}-x_I)} + A_{4n}e^{-k_{n2}x_I}, \tag{2.10}$$

and

$$w_{2n} = A_{5n}e^{-k_{n1}(L_{x2}-x_{II})} + A_{6n}e^{-k_{n1}x_{II}} + A_{7n}e^{-k_{n2}(L_{x2}-x_{II})} + A_{8n}e^{-k_{n2}x_{II}}, \tag{2.11}$$

where $k_{n1} = \sqrt{k_n^2 + k_p^2}$ and $k_{n2} = \sqrt{k_n^2 - k_p^2}$.

In Equations (2.10) and (2.11), the wave components are exponential decay waves when $k_p < k_n$. The last two wave components in Equations (2.10) and (2.11) become propagation waves when $k_p > k_n$.

The unknown wave coefficients and the modal coupling forces and moments at the beam/plate interface can be determined from the compatibility and continuity conditions at the interface together with the boundary conditions of the plate edges at $x_I = 0$ and $x_{II} = L_{x2}$.

The boundary conditions for the plate edges at $x_I = 0$ and $x_{II} = L_{x2}$ are given here for the three classical boundary conditions as:

a) Clamped-clamped boundary conditions

$$W_1\big|_{x_I=0} = W_2\big|_{x_{II}=L_{x2}} = \left.\frac{\partial W_1}{\partial x_I}\right|_{x_I=0} = \left.\frac{\partial W_2}{\partial x_{II}}\right|_{x_{II}=L_{x2}} = 0. \tag{2.12}$$

b) Free-free boundary conditions

$$D(\frac{\partial^2 W_1}{\partial x_I^2}+\nu\frac{\partial^2 W_1}{\partial y^2})\Big|_{x_I=0} = D(\frac{\partial^2 W_2}{\partial x_{II}^2}+\nu\frac{\partial^2 W_2}{\partial y^2})\Big|_{x_{II}=L_{x2}} = 0,$$

$$D(\frac{\partial^3 W_1}{\partial x_I^3}+(2-\nu)\frac{\partial^3 W_1}{\partial x_I \partial y^2})\Big|_{x_I=0} = D(\frac{\partial^3 W_2}{\partial x_{II}^3}+(2-\nu)\frac{\partial^3 W_2}{\partial x_{II} \partial y^2})\Big|_{x_{II}=L_{x2}} = 0. \quad (2.13)$$

c) Simply supported boundary conditions

$$W_1\big|_{x_I=0} = W_2\big|_{x_{II}=L_{x2}} = D(\frac{\partial^2 W_1}{\partial x_I^2}+\nu\frac{\partial^2 W_1}{\partial y^2})\Big|_{x_I=0} = D(\frac{\partial^2 W_2}{\partial x_{II}^2}+\nu\frac{\partial^2 W_2}{\partial y^2})\Big|_{x_{II}=L_{x2}} = 0. \quad (2.14)$$

Nevertheless, for simplicity, only simply supported boundary conditions are considered in the subsequent analysis.

The compatibility and continuity conditions on the left hand side of the beam/plate interface are:

$$w_{1n}(L_{x1}) = v_n,\ w'_{1n}(L_{x1}) = -\theta_n,$$

$$D(\frac{\partial^2 W_1}{\partial x_1^2}+\nu\frac{\partial^2 W_1}{\partial y^2})\Big|_{x_1=L_{x1}} = m_L,\ D(\frac{\partial^3 W_1}{\partial x_1^3}+(2-\nu)\frac{\partial^3 W_1}{\partial x_1 \partial y^2})\Big|_{x_1=L_{x1}} = q_L. \quad (2.15)$$

Correspondingly, the compatibility and continuity conditions on the right hand side of the beam/plate interface are given by:

$$w_{2n}(0) = v_n,\ w'_{2n}(0) = -\theta_n,$$

$$D(\frac{\partial^2 W_2}{\partial x_2^2}+\nu\frac{\partial^2 W_2}{\partial y^2})\Big|_{x_{II}=0} = m_R,\ D(\frac{\partial^3 W_2}{\partial x_2^3}+(2-\nu)\frac{\partial^3 W_2}{\partial x_2 \partial y^2})\Big|_{x_{II}=0} = q_R. \quad (2.16)$$

For each wave number index n, combining Equations (2.14) – (2.16) gives rise to:

$$\begin{Bmatrix}\{A\}_n\\ \{Q\}_n\end{Bmatrix} = [C]_n^{-1}\{F\}_n, \quad (2.17)$$

where

$$\{A\}_n = \lfloor A_{1n} \quad A_{2n} \quad A_{3n} \quad A_{4n} \quad A_{5n} \quad A_{6n} \quad A_{7n} \quad A_{8n} \rfloor^T, \quad (2.18)$$

is the wave coefficient vector, and

$$\{Q\}_n = \lfloor M_{Ln} \quad Q_{Ln} \quad M_{Rn} \quad Q_{Rn} \rfloor^T \,, \tag{2.19}$$

is the modal coupling force vector, and the external force vector is given by:

$$\{F\} = \left[0 \quad 0 \quad 0 \quad 0 \quad 0 \quad 0 \quad 0 \quad 0 \quad 0 \quad 0 \quad \frac{F_b \phi_n(y_b)}{G_n} \quad \frac{F_b \Delta_0 \phi_n(y_b)}{G_{Tn} k_{n1}} \right]^T . \tag{2.20}$$

The square matrix $[C]_n$ in Equation (2.17) is given in *Appendix B* for the boundary conditions where all plate edges are simply supported. A similar matrix can be obtained by replacing the corresponding terms in $[C]_n$ if the two plate edges parallel the beam's neutral axis have the boundary conditions other than simply supported.

The matrix $[C]_n$ is a complex matrix if system damping is included. It is usually an ill-conditioned matrix (e.g. the matrix condition number of the chosen ribbed plate is up to 10^{11} in the simulation). The accuracy of inverting the ill-conditioned matrix $[C]_n$ is sensitive to the rounding error of digital computers [46], particularly when difference between the values of real and imaginary parts of each complex element in the matrix is large (about 2 orders of magnitude scale in our case). To overcome this numerical difficulty, the matrix $[C]_n$ is first expanded to a real matrix [47, 48] prior to matrix inversion. After the matrix expansion, each element in $[C]_n$ becomes:

$$C_{ij} = \begin{bmatrix} \mathrm{Re}(C_{ij}) & -\mathrm{Im}(C_{ij}) \\ \mathrm{Im}(C_{ij}) & \mathrm{Re}(C_{ij}) \end{bmatrix}, \quad i, j = 1,2,...,12 \,. \tag{2.21}$$

The elements in Equations (2.18) – (2.20) are also expanded correspondingly. For example, the first element in Equation (2.18) is expanded as:

$$A_{1n} = \left[\mathrm{Re}(A_{1n}) \quad \mathrm{Im}(A_{1n}) \right]^T . \tag{2.22}$$

2.5 Ribbed plate response to point force excitation on the plate

For this excitation case ($F_b = 0$), the modal displacement of Plate 1 (Equation (2.6)) can be solved by travelling wave solutions as:

$$w_{1n1} = A_{1n}e^{-k_{n1}(L_{x1}-x_I)} + A_{2n}e^{-k_{n1}x_I} + A_{3n}e^{-k_{n2}(L_{x1}-x_I)} + A_{4n}e^{-k_{n2}x_I}, \qquad 0 \le x_I \le x_0, \tag{2.23}$$

and

$$w_{1n2} = A_{5n}e^{-k_{n1}(L_{x1}-x_I)} + A_{6n}e^{-k_{n1}x_I} + A_{7n}e^{-k_{n2}(L_{x1}-x_I)} + A_{8n}e^{-k_{n1}x_I}, \qquad x_0 \le x_I \le L_{x1}. \tag{2.24}$$

Four additional boundary conditions can be obtained at the source location as:

$$w_{1n1}(x_0) = w_{1n2}(x_0),\ w'_{1n1}(x_0) = w'_{1n2}(x_0),$$

$$w''_{1n1}(x_0) = w''_{1n2}(x_0),\ w'''_{1n1}(x_0) = w'''_{1n2}(x_0) + \frac{F_p\phi_n(y_0)}{D\Lambda_n}. \tag{2.25}$$

The travelling wave solution for Plate 2 is still the same as in the previous excitation case. However, the indices of the wave coefficients in Equation (2.11) need to be replaced by:

$$w_{2n} = A_{9n}e^{-k_{n1}(L_{x2}-x_{II})} + A_{10n}e^{-k_{n1}x_{II}} + A_{11n}e^{-k_{n2}(L_{x2}-x_{II})} + A_{12n}e^{-k_{n2}x_{II}}. \tag{2.26}$$

Combining Equation (2.25) together with Equations (2.14) – (2.16), a matrix equation in the form of Equation (2.17) can also be obtained, where the unknown wave coefficient vector $\{A\}_n$ now becomes:

$$\{A\}_n = \lfloor A_{1n} \quad A_{2n} \quad A_{3n} \quad A_{4n} \quad A_{5n} \quad A_{6n} \quad A_{7n} \quad A_{8n} \quad A_{9n} \quad A_{10n} \quad A_{11n} \quad A_{12n} \rfloor^T. \tag{2.27}$$

The modal coupling force vector at the interface is the same as in the previous section, while the excitation force vector is now given by:

$$\{F\}_n = \left\lfloor 0 \quad 0 \quad 0 \quad 0 \quad 0 \quad \frac{F_p\phi_n(y_0)}{D\Lambda_n k_{n1}^3} \quad 0 \quad 0 \quad 0 \quad 0 \quad 0 \quad 0 \quad 0 \quad 0 \quad 0 \quad 0 \right\rfloor^T. \tag{2.28}$$

The square matrix $[C]_n$ for this excitation case is also given in *Appendix B* for the boundary conditions where all plate edges are simply supported. It should be noted

that the matrix $[C]_n$ should also be expanded to a real matrix before matrix inversion for better prediction accuracy. More discussions for effects of matrix expansion on the prediction accuracy are given in the latter analysis.

2.6 Vibration energy and energy flow

2.6.1 Kinetic energy in the plates due to point force excitation applied on the beam

For this excitation case, the time and spatial averaged kinetic energy in Plate 1 is given by:

$$\begin{aligned}\left\langle \overline{T} \right\rangle_{p1} &= \frac{1}{2}\iint_{S_1} \rho_s \dot{W}_1 \dot{W}_1^{*} dS = \frac{\rho_s \omega^2 \Lambda_n}{2} \int_0^{Lx1} \sum_n \left| w_{1n} \right|^2 dx \\ &= \frac{\rho_s \omega^2 \Lambda_n}{2} \sum_n \{ \frac{\left|A_{1n}\right|^2 + \left|A_{2n}\right|^2}{2\,\mathrm{Re}(k_{n1})}(1-\left|c_1\right|^2) + \frac{\left|A_{3n}\right|^2 + \left|A_{4n}\right|^2}{2\,\mathrm{Re}(k_{n2})}(1-\left|c_2\right|^2) - \frac{2\,\mathrm{Re}(A_{1n}^{*}A_{2n})\,\mathrm{Im}(c_1)}{\mathrm{Im}(k_{n1})} - \\ &\quad \frac{2\,\mathrm{Re}(A_{3n}^{*}A_{4n})\,\mathrm{Im}(c_2)}{\mathrm{Im}(k_{n2})} + 2\,\mathrm{Re}[\frac{A_{1n}^{*}A_{4n} + A_{2n}^{*}A_{3n}}{k_{n1}^{*} - k_{n2}}(c_2 - c_1^{*}) + \frac{A_{1n}^{*}A_{3n} + A_{2n}^{*}A_{4n}}{k_{n1}^{*} + k_{n2}}(1 - c_1^{*}c_2)]\}\end{aligned} \quad , \tag{2.29}$$

where S_1 is the surface area of Plate 1, $dS = dxdy$ and the asterisk (*) indicates a complex conjugate. $c_1 = e^{-k_{n1}Lx_1}$ and $c_2 = e^{-k_{n2}Lx_1}$ are the exponential constants for each given wave number k_{n1} and k_{n2}.

Similarly, the time and spatial averaged kinetic energy in Plate 2 is given by:

$$\begin{aligned}\left\langle \overline{T} \right\rangle_{p2} &= \frac{\rho_s \Lambda_n \omega^2}{2} \sum_n \{ \frac{\left|A_{5n}\right|^2 + \left|A_{6n}\right|^2}{2\,\mathrm{Re}(k_{n1})}(1-\left|c_3\right|^2) + \frac{\left|A_{7n}\right|^2 + \left|A_{8n}\right|^2}{2\,\mathrm{Re}(k_{n2})}(1-\left|c_4\right|^2) - \frac{2\,\mathrm{Re}(A_{5n}^{*}A_{6n})\,\mathrm{Im}(c_3)}{\mathrm{Im}(k_{n1})} - \\ &\quad \frac{2\,\mathrm{Re}(A_{7n}^{*}A_{8n})\,\mathrm{Im}(c_4)}{\mathrm{Im}(k_{n2})} + 2\,\mathrm{Re}[\frac{A_{5n}^{*}A_{8n} + A_{6n}^{*}A_{7n}}{k_{n1}^{*} - k_{n2}}(c_4 - c_3^{*}) + \frac{A_{5n}^{*}A_{7n} + A_{6n}^{*}A_{8n}}{k_{n1}^{*} + k_{n2}}(1 - c_3^{*}c_4)]\}\end{aligned} \quad , \tag{2.30}$$

where $c_3 = e^{-k_{n1}L_{x2}}$ and $c_4 = e^{-k_{n2}L_{x2}}$.

2.6.2 Kinetic energy in the plates due to point force excitation applied on the plate

For this excitation case, the time and spatial averaged kinetic energy in Plate 1 is calculated by:

$$\left\langle \overline{T} \right\rangle_{p1} = \frac{1}{2}\iint_{S_1} \rho_s \dot{W}_1 \dot{W}_1^{*} dS = \frac{\rho_s \omega^2 \Lambda_n}{2}\left(\int_0^{x_0} \sum_n \left|w_{1n1}\right|^2 dx + \int_{x_0}^{L_{x1}} \sum_n \left|w_{1n2}\right|^2 dx\right), \tag{2.31}$$

where the two integration terms in the bracket are given in terms of the wave coefficients as:

$$\begin{aligned}\int_0^{x_0} \sum_n \left|w_{1n1}\right|^2 dx = \sum_n \{ & \frac{\left|A_{1n}\right|^2\left(\left|c_5\right|^2 - \left|c_1\right|^2\right) + \left|A_{2n}\right|^2\left(1 - \left|c_6\right|^2\right)}{2\,\mathrm{Re}(k_{n1})} + \frac{\left|A_{3n}\right|^2\left(\left|c_7\right|^2 - \left|c_2\right|^2\right) + \left|A_{4n}\right|^2\left(1 - \left|c_8\right|^2\right)}{2\,\mathrm{Re}(k_{n2})} - \\ & \frac{\mathrm{Im}[A_{1n}^{*}A_{2n}(c_1 e^{-2j\arg(c_5)} - c_1^{*})]}{\mathrm{Im}(k_{n1})} - \frac{\mathrm{Im}[A_{3n}^{*}A_{4n}(c_2 e^{-2j\arg(c_7)} - c_2^{*})]}{\mathrm{Im}(k_{n2})} + \\ & 2\,\mathrm{Re}[\frac{A_{1n}^{*}A_{4n}(c_5^{*}c_8 - c_1^{*}) + A_{2n}^{*}A_{3n}(c_2 - c_7 c_6^{*})}{k_{n1}^{*} - k_{n2}} + \frac{A_{1n}^{*}A_{3n}(c_5^{*}c_7 - c_1^{*}c_2) + A_{2n}^{*}A_{4n}(1 - c_6^{*}c_8)}{k_{n1}^{*} + k_{n2}}]\}\end{aligned}$$

, (2.32)

and

$$\begin{aligned}\int_{x_0}^{Lx1} \sum_n \left|w_{1n2}\right|^2 dx = \sum_n \{ & \frac{\left|A_{5n}\right|^2\left(1 - \left|c_5\right|^2\right) + \left|A_{6n}\right|^2\left(\left|c_6\right|^2 - \left|c_1\right|^2\right)}{2\,\mathrm{Re}(k_{n1})} + \frac{\left|A_{7n}\right|^2\left(1 - \left|c_7\right|^2\right) + \left|A_{8n}\right|^2\left(\left|c_8\right|^2 - \left|c_2\right|^2\right)}{2\,\mathrm{Re}(k_{n2})} - \\ & \frac{\mathrm{Im}[A_{5n}^{*}A_{6n}c_1(1 - e^{-2j\arg(c_5)})]}{\mathrm{Im}(k_{n1})} - \frac{\mathrm{Im}[A_{7n}^{*}A_{8n}c_2(1 - e^{-2j\arg(c_7)})]}{\mathrm{Im}(k_{n2})} + \\ & 2\,\mathrm{Re}[\frac{A_{5n}^{*}A_{8n}(c_2 - c_5^{*}c_8) + A_{6n}^{*}A_{7n}(c_7 c_6^{*} - c_1^{*})}{k_{n1}^{*} - k_{n2}} + \frac{A_{5n}^{*}A_{7n}(1 - c_5^{*}c_7) + A_{6n}^{*}A_{8n}(c_6^{*}c_8 - c_1^{*}c_2)}{k_{n1}^{*} + k_{n2}}]\}\end{aligned}$$

, (2.33)

where $c_5 = e^{-k_{n1}(L_{x1} - x_0)}$, $c_6 = e^{-k_{n1}x_0}$, $c_7 = e^{-k_{n2}(L_{x1} - x_0)}$ and $c_8 = e^{-k_{n2}x_0}$.

Correspondingly, the kinetic energy in Plate 2 is given by:

$$\left\langle \overline{T} \right\rangle_{p2} = \frac{\rho_s \Lambda_n \omega^2}{2} \sum_n \{ \frac{\left|A_{9n}\right|^2 + \left|A_{10n}\right|^2}{2\,\mathrm{Re}(k_{n1})}(1-\left|c_3\right|^2) + \frac{\left|A_{11n}\right|^2 + \left|A_{12n}\right|^2}{2\,\mathrm{Re}(k_{n2})}(1-\left|c_4\right|^2) - \frac{2\,\mathrm{Re}(A_{9n}^* A_{10n})\,\mathrm{Im}(c_3)}{\mathrm{Im}(k_{n1})} - \frac{2\,\mathrm{Re}(A_{11n}^* A_{12n})\,\mathrm{Im}(c_4)}{\mathrm{Im}(k_{n2})} + 2\,\mathrm{Re}[\frac{A_{9n}^* A_{12n} + A_{10n}^* A_{11n}}{k_{n1}^* - k_{n2}}(c_4 - c_3^*) + \frac{A_{9n}^* A_{11n} + A_{10n}^* A_{12n}}{k_{n1}^* + k_{n2}}(1 - c_3^* c_4)]\} \tag{2.34}$$

2.6.3 Beam vibration energy

For both excitation cases, the time averaged kinetic energy of the beam flexural and torsional vibrations are calculated by utilizing the compatibility conditions at the interface as:

$$\left\langle \overline{T} \right\rangle_b = \frac{1}{2}\rho_L \int_0^{Ly} \dot{V}\dot{V}^* dy = \frac{\rho_L \Lambda_n \omega^2}{2} \sum_n \left| w_{1n(x_I = L_{x1})} \right|^2, \tag{2.35}$$

and

$$\left\langle \overline{T} \right\rangle_t = \frac{1}{2}\rho_b I_p \Lambda_n \int_0^{Ly} \dot{\theta}\dot{\theta}^* dy = \frac{\rho_b I_p \Lambda_n \omega^2}{2} \sum_n \left| \frac{\partial w_{1n(x_I = L_{x1})}}{\partial x_I} \right|^2. \tag{2.36}$$

2.6.4 Vibration energy flow

The energy flow on each side of the beam/plate interface has two components, one is governed by the shear force coupling, which is termed as the shear force component, and the other is controlled by the moment coupling, which is termed as the moment component. By summing the two components, the time averaged, steady state net energy flow between the beam and Plate 1 is:

$$\left\langle \overline{P} \right\rangle_L = -\frac{1}{2}\,\mathrm{Re} \int_0^{Ly} (q_L \dot{V}^* - m_L \dot{\theta}^*) dy\,. \tag{2.37}$$

While the net energy flow between the beam and Plate 2 is:

$$\left\langle \overline{P} \right\rangle_R = -\frac{1}{2}\,\mathrm{Re} \int_0^{Ly} (q_R \dot{V}^* - m_R \dot{\theta}^*) dy\,. \tag{2.38}$$

2.7 Results and discussion

In the numerical simulations, it is assumed that both plate and beam are made of aluminum with material properties $E_0 = 7.1\times10^{10} N/m^2$, $\rho = 2660 kg/m^3$, $\nu = 0.3$. These material properties are also used in the simulations of other chapters in this thesis unless specified otherwise. The plate has a surface area of $S = 3.6\times1 m^2$ and is $8mm$ thick. The beam is $1m$ long with cross sectional area of $A = 150\times10 mm^2$. The size and the material properties of the plate and the beam are chosen based on one of the ship hull plates of a $30m$ crew vessel currently under investigation. The ship hull plate is bounded by two parallel frames ($1m$ apart), the keel and a perpendicular ship hull plate so that simply supported boundary conditions can be assumed for all four plate edges. The plate and the beam are assumed to have constant internal loss factors of $\eta_p = 0.03$ and $\eta_b = 0.01$ respectively. The loss factors for the plate and the beam are incorporated into the formulation by using complex Young's modulus such that $E_p = E(1+j\eta_p)$, $E_b = E(1+j\eta_b)$ [1]. For all excitation cases, the source is fixed at location $(x_0, y_0) = (1.4m, 0.32m)$ in the global coordinate system. Point force excitation applied on the beam is accomplished by moving the beam to the source location in the simulation. Effects of off-neutral axis loading are studied by applying a point force on the beam but away from the beam's neutral axis ($\Delta_0 \neq 0$).

2.7.1 Input mobilities

The real part of the point force input mobility of the ribbed plate when the force is applied on the neutral axis of the beam is calculated and shown in Figure 2.3 together with that obtained from finite element analysis (FEA) for cross check. The input mobility of the ribbed plate to point force excitation applied on the plate is also calculated for two sizes of the source plate, one for $L_{x1} = 1.44m$ and another for

$L_{x1} = 1.6m$. The results are shown in Figure 2.4 together with the FEA predictions. The commercial software – MSC/NASTRAN [49] is used in the FEA analysis where 2250 CQUAD4 shell elements and 25 CBAR elements are utilized for the ribbed plate. Shear deformations are removed for both shell and bar elements in the finite element formulation. Good agreement is found between the analytical and FEA results in the whole frequency range of interest when the complex matrix $[C]_n$ is expanded to a real matrix before the matrix inversion. In contrast, directly inverting the complex matrix $[C]_n$ in the solution leads to a large discrepancy in the prediction at low and medium frequencies and also results to negative value of input mobility at some discrete frequencies (note: the negative of input mobility is suppressed in the figure for clear illustration of the results).

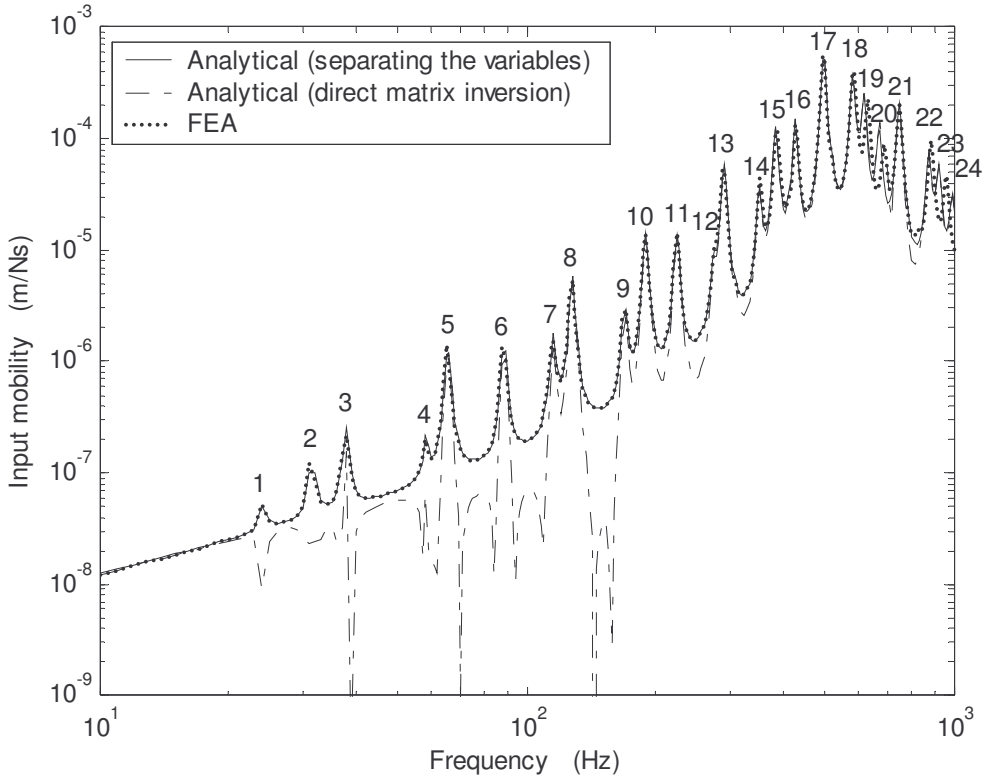

Figure 2.3. The real part of input mobility of the ribbed plate to point force excitation on the beam.

It is also shown in Figure 2.4 that if the point force is applied on the plate at more than a quarter of wavelength away from the beam, i.e. at frequencies above 120Hz when the source location is 200m away from the beam, good accurate results could be predicted by the current approach without the matrix expansion.

The formulation presented in Section 2.3 can also be employed to predict the vibration response of finite ribbed plates to torsional moment excitation applied on the beam. Such excitation is not studied here as an independent excitation case. Instead, it is combined with point force excitations in the study for effects of off-neutral axis loading on the ribbed plate response.

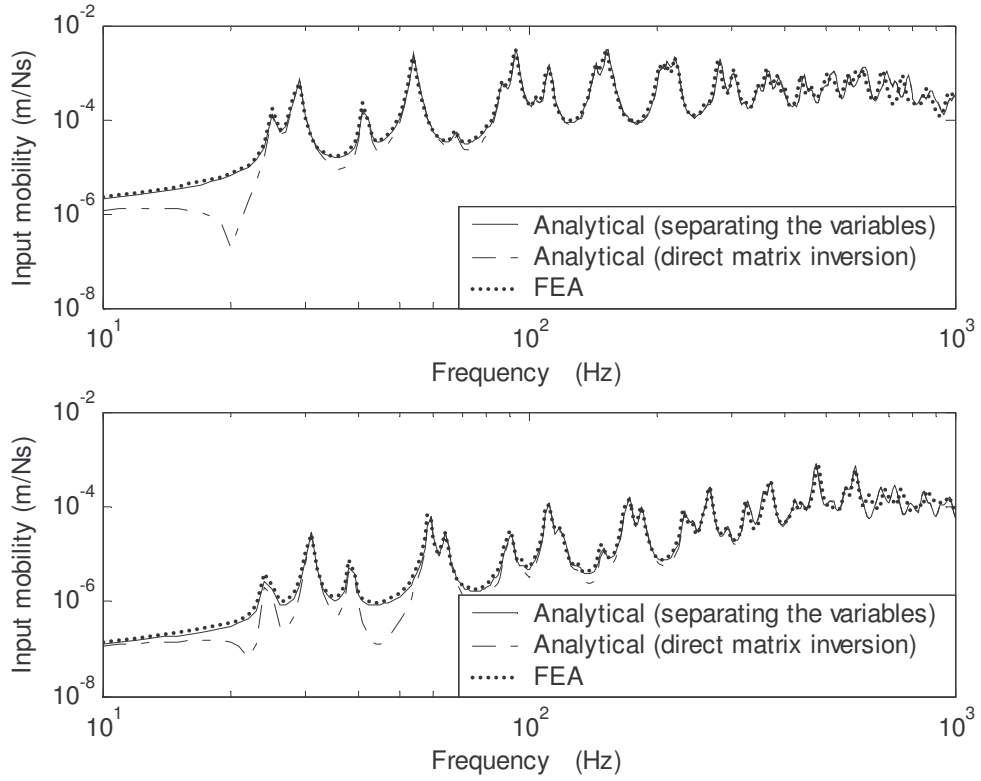

Figure 2.4. Input mobilities of the ribbed plate to point force excitation on the plate. Top: beam is 0.2m away from the source; Bottom: beam is 0.04m away from the source.

2.7.2 Effects of off-neutral axis loading

Traditionally, effects of off-neutral axis loading on the vibration response of ribbed plates are ignored where the point force excitation is implicitly assumed to be applied on the beam's neutral axis [7, 13, 24]. This is because the effect of off-neutral axis loading to the response of infinite ribbed plates is usually small, particularly at frequencies below the coincidence between the beam torsional wave and the plate bending wave. For example, the input power ratio between a torsional moment excitation (amplitude $M_T = F_b\Delta_0$, $\Delta_0 = 5mm$) and a point force excitation (F_b) of a corresponding infinite ribbed plate is less than 10% for frequencies up to 3000Hz. Nevertheless, when the ribbed plate becomes finite, vibration characteristics of the ribbed plate would be affected by off-neutral axis loading because of the interference between the individual induced modal response by the point force and the moment excitations. Effects of off-neutral axis loading to the ribbed plate response are investigated by studying the input power and the kinetic energy distribution in the two component plates of the finite ribbed plate for the two off-neutral axis distances, $\Delta_0 = 0$ and $\Delta_0 = 5mm$.

To understand the behaviours of input power and energy flow between the structural components of the finite ribbed plate, the modal characteristics of the ribbed plate is studied where the response peaks are marked by serial numbers as shown in Figure 2.3. The peak frequencies and the corresponding mode shapes are listed in Table 2.1.

The modal vibration of the finite ribbed plate can be generally classified into two groups according to the effect of the stiffened beam on the modal response of the plate. When the beam is located at or near the nodal location of a plate mode, the beam flexural stiffness has little effect on the modal vibration of the plate. The modal response in terms of resonance frequencies and mode shapes for this group is only

slightly difference to that of the un-ribbed plate. For the second group, the beam behaves as an elastic boundary, which divides the plate into two parts. The energy flow between the beam and the two component plates or between the two component plates is accomplished by the coupling mechanism at the beam/plate interface. According to the modal vibration distribution in the component plates, the group of modes can be further classified into two subgroups, one is dominated by the resonant response of Plate 1, which is marked by P1 and another is dominated by the resonant response of Plate 2, which is marked by P2 in Table 2.1. The modal index number enclosed by the bracket following P1 or P2 in Table 2.1 indicates the modal wave number of the resonant component plate.

Table 2.1 Modal classification of the finite ribbed plate

	Ribbed plate			Un-ribbed plate	
Peak number	$f_{m,n}$ (Hz)	Plate 1 (m,n)th	Plate 2 (m,n)th	$f_{m,n}$ (Hz)	(m,n)th
1	24	(1*,1)	P2(1,1)		
2	31	P1(1,1)	(2*,1)		
3	38	(1,1)	P2(2,1)		
4^	58	(2,1)	P2(3,1)	57.6	(5,1)
5	65	P1(2,1)	(3,1)		
6	89	(3*,1)	P2(4,1)		
7^	116	P1(3,1)	(5,1)	116.7	(8,1)
8	128	(3,1)	P2(5,1)		
9^	170	(4,1)	P2(6,1)	171.2	(10,1)
10	190	P1(4,1)	(6,1)		
11	225	(4,1)	P2(7,1)		
12^	275	P1(5,1)	(8,1)	275.8	(13,1)
13	290	(5,1)	P2(8,1)		
14	351	(5,1)	P2(9,1)		
15	384	P1(6,1)	(9,1)		
16	425	(6,1)	P2(10,1)		
17	497	P1(7,1)&	(10,1)		
18	579	(7,1)	P2(12,1)&		
19	616	P1(8,1)	(12,1)		
20	670	(9,1)	P2(12,1)		
21^	747	(91)	P2(13,1)	753.4	(22,1)
22	871	P1(9,1)	(15,1)		
23	920	(10,1)	P2(15,1)		
24	988	P1(10,1)	(15,1)		

Note: * indicates that the mode shape is incomplete;
& indicates that the largest modal amplitude occurs at the beam location;
^ indicates that the corresponding mode belongs to the group where the contribution of the beam flexural stiffness is relatively unimportant.

As expected, the coupling between the beam and the plate is dominated by the $n=1$ beam bending mode at frequencies below and near the first resonance frequency of the uncoupled beam bending vibration, which is the lowest resonance frequency of the beam. As the frequency increase further, the modal coupling is dominated by higher order beam bending modes. Because the torsional stiffness of the beam is much less than the plate bending stiffness, the torsional vibration modes of the beam could not be excited alone and the involvement of the attached plate bending modes becomes evident in the response of the ribbed plate. Similarly, such involvement with the beam bending modes is also significant. Therefore, the resonance peaks in the input mobility at the beam is always associated with the plate vibration regardless whether the beam vibration is in resonance or not.

a) Effects on the input power

The input power to the ribbed plate due to a point force (F_b) applied at the neutral axis of the beam, an equivalent torsional moment excitations ($M_T = F_b\Delta_0$, $\Delta_0 = 5mm$) and their combination (representing the off-neutral axis loading) are shown in Figure 2.5. It is found that the effect of off-neutral axis loading on the input power is most significant at low frequencies ($< 200Hz$ as in Figure 2.5). To understand this effect, the velocity and angular velocity responses (shown in Figure 2.6) at the source location due to the point force and the moment excitations are examined. It is found that the velocity response due to the moment excitation is only comparable to that due to the point force excitation at a few lower resonance frequencies (see those for modes 5, 6, 7 and 9 shown in Figure 2.6(a)). In this frequency range, the point force induced velocity is in the stiffness controlled region of beam bending vibration and has small amplitude. While the moment induced velocity may have a few peaks due to the torsional resonances. As a result, the total

input power due to the point force can be significantly affected by the off-neutral axis loading even though the magnitude of moment is much smaller than the force.

Although the angular velocity due to the moment excitation is also comparable to that due to the point force as shown in Figure 2.6(b) and has significantly larger peak amplitudes than those in the velocity response, the input power due to the moment excitation (limited by the small off-neutral axis distance which generates the moment) is only comparable to the input power due to the force component at a few lower resonance frequencies (i.e. modes 1-7, 9 as shown in Figure 2.5). Therefore, the total input power to the ribbed plate for the off-neutral axis loading case is still dominated by the point force input power except at a few low resonance frequencies. Furthermore, because the moment also excites the higher order plate modes ($n > 1$) through the moment coupling (not excited by the point force in this frequency range), the off-neutral axis loading increases the number of peaks (such as the peaks marked by T in Figure 2.5) in the ribbed plate response although the amplitude of these peaks is usually small.

The off-neutral axis loading includes a combined force and moment excitation, the velocity and the angular velocity at the source location are the superposition of the two individual responses, which can be either constructive or destructive depending upon the relative phase between the two responses (see Figure 2.6). Therefore, negative input power (such as modes 2 and 5, which are also indicated by the arrows in Figure 2.5) is possible at low frequencies in off-neutral axis loading cases when only one component of the input power (either by the point force or by the torsional moment) is considered.

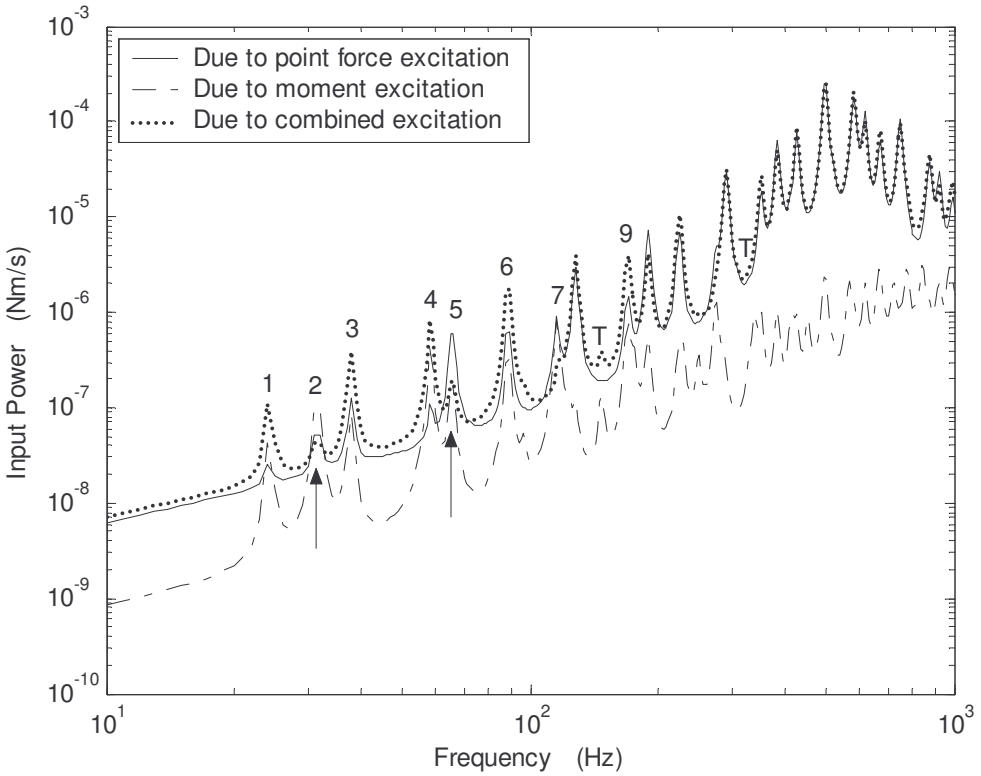

Figure 2.5. Input power of the ribbed plate due to point force and torsional moment excitations.

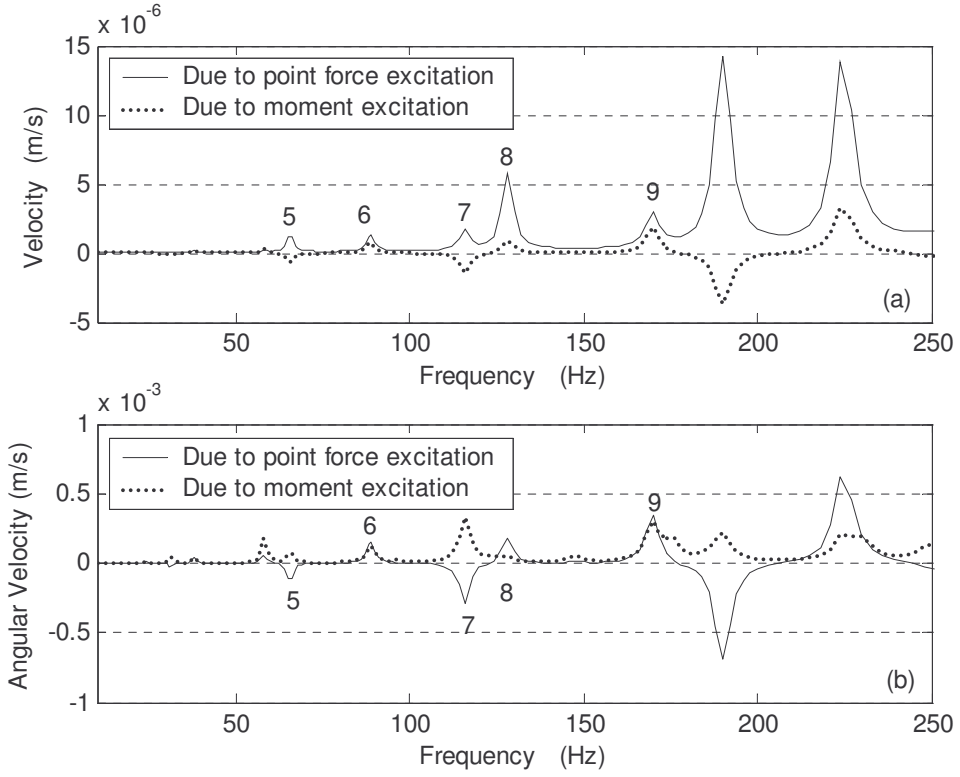

Figure 2.6. The velocity and angular velocity responses at the source location of the ribbed plate due to point force and moment excitations

b) Effects on the vibration energy flow

To understand the mechanism of energy flow at the beam/plate interfaces, the shear force and moment components of the energy flow between the beam and the two component plates are investigated.

For point force excitation applied on the neutral axis of the beam, energy flow between the beam and the component plates is dominated by the shear force coupling (P_s^f) at the interface as shown in Figures 2.7(a1) and 2.7(a2). The energy flows (P_m^f) due to the moment coupling on both sides of the interface have the same phase and same amplitude. For this case, the beam serves purely as medium for the energy exchange between the two component plates. The energy flow from the non-resonant component plate to the resonant component plate or from the component plate with higher modal energy to the component plate with lower modal energy is accomplished by the moment coupling at the interface. Therefore, for this type of excitation, the contribution of the beam torsional vibration to the overall response of the ribbed plate is negligible as there is no net energy flow from the beam to the plates via the moment coupling.

On the contrary, the energy flow between the beam and the two component plates of the ribbed plate due to a pure torsional moment excitation on the beam is dominated by the moment coupling (P_m^m) at the beam/plate interface. While the energy flow between the two component plates of the ribbed plate is accomplished by the shear force coupling (P_s^m) at the interface as shown in Figures 2.7(b1) and 2.7(b2).

For off-neutral axis loading on the beam, although the energy flows due to the moment coupling on the two interfaces are still in phase with each other, they have different amplitude as illustrated in Figure 2.8. This is due to the non-negligible

contribution of beam torsional vibration to the net energy flow into the plates. In addition to the changes and interference in velocity responses at the interfaces, the energy flow between the beam and the plate is also affected by the changes of the coupling forces and moments at the interfaces. As illustrated in Figure 2.9, at most of the frequencies, attributed to the off-neutral axis loading, the shear force coupling on the left of the interface decreases while that on the right of the interface increases attributed to the fact that the off-neutral axis loading force is located at the right. This is also the case for the moment couplings at the interface. According to the velocity compatibility conditions given by Equations (2.15) and (2.16), those increases in coupling force and moment at the left interface may explain the increase of the net energy flow from the beam to the component plate on the force side (where the interface is closed to the force location) at the frequencies.

c) Effects on the kinetic energy distribution

Based on the discussion on the energy flows at the beam/plate interfaces and the relationships between the input energy flow, energy and loss factor of the component plates, the behaviour of the kinetic energy distributed in the two component plates can be readily explained. The kinetic energy in the two component plates due to a point force, an equivalent torsional moment ($M_T = F_b \Delta_0$, $\Delta_0 = 5mm$) and their combined excitations on the beam are shown in Figures 2.10 and 2.11. As expected, the kinetic energy in the two component plates is largely affected by the off-neutral axis loading for a few resonance peaks at low frequencies attributed to the interference between the individual induced modal responses by the force and the moment (Figure 2.6). Furthermore, the kinetic energy in Plate 1 decreases from that due to the point force excitation alone in general because of the decreased energy flow from the beam to this component plate. On the contrary, the off-neutral axis loading results to decrease kinetic energy in Plate 2

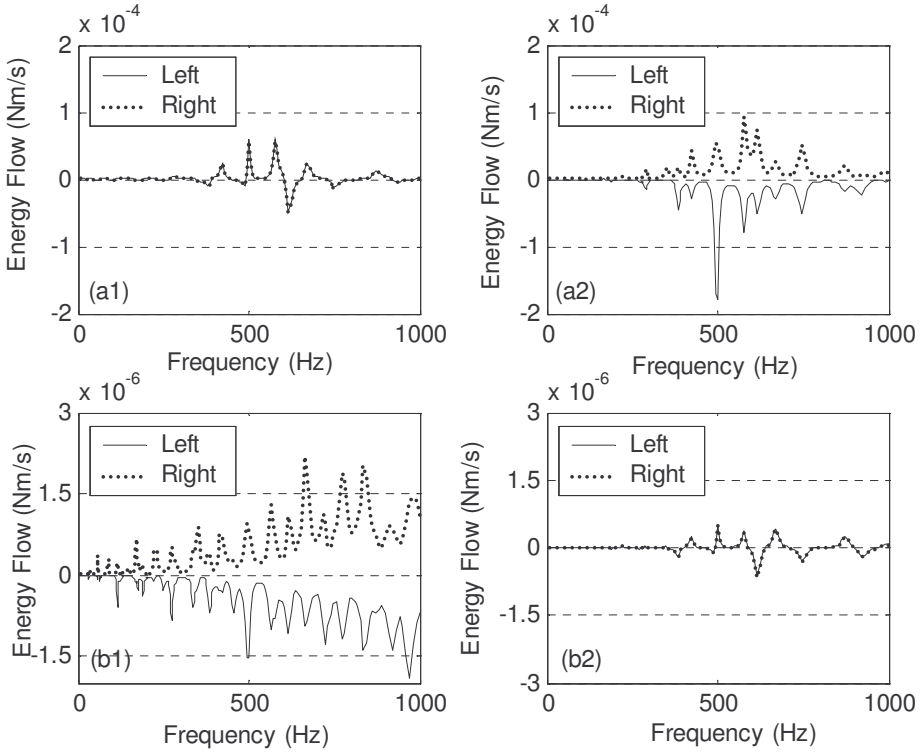

Figure 2.7. The moment and shear force components of energy flow between the beam and the two component plates due to point force excitation and moment excitations on the beam; (a1) P_m^f, energy flow component due to moment couplings at the interface and point force excitation at the beam; (a2) P_s^f due to shear force coupling and point force excitation; (b1) P_m^m due to moment coupling and moment excitation; (b2) P_s^m due to shear force coupling and moment excitation;

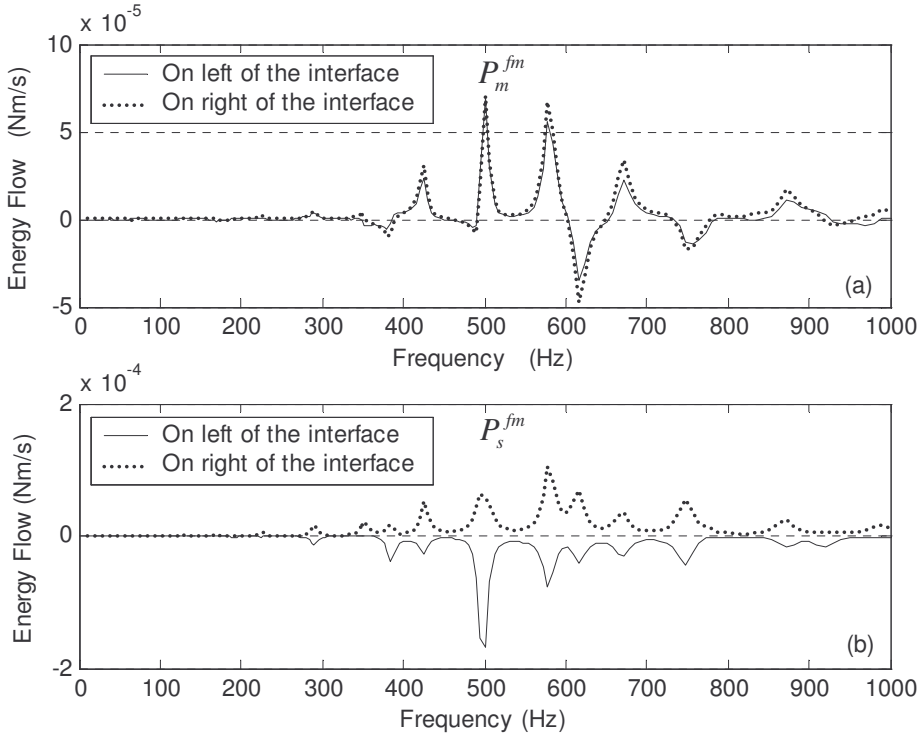

Figure 2.8. The moment and shear components of energy flow between the beam and the two component plates due to the combined force and moment excitations; (a) energy flow due to moment coupling (P_m^{fm}); (b) energy flow due to shear force coupling (P_s^{fm}).

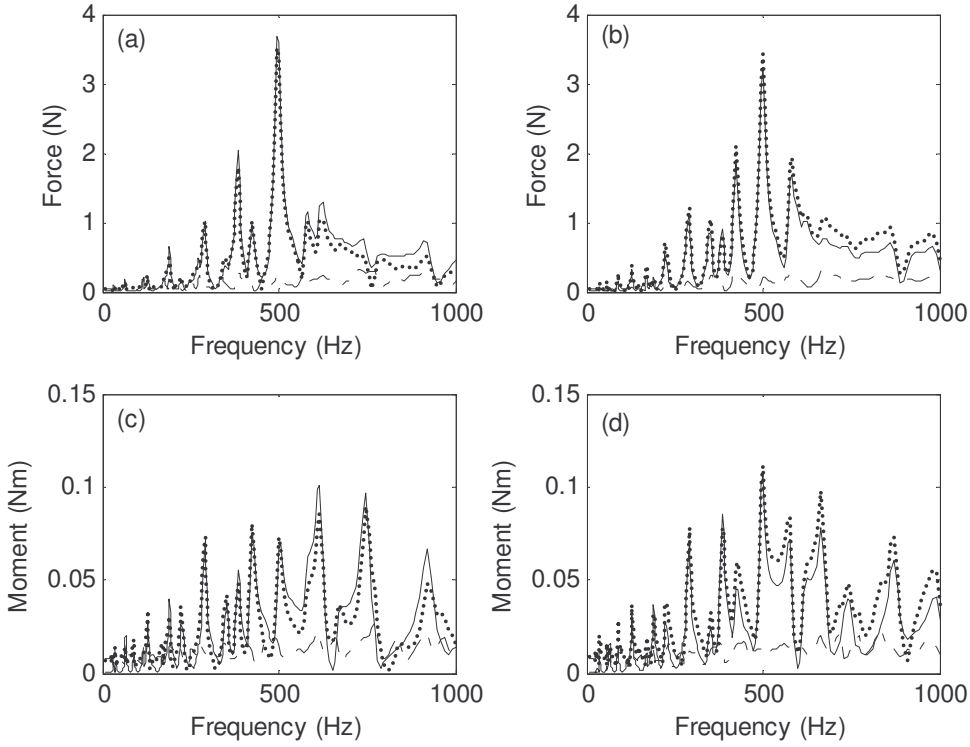

Figure 2.9. The moment and shear force evaluated at $y = y_b$ on both sides of the interface due to point force, moment and their combined excitations. (a) force on the left; (b) force on the right; (c) moment on the left; (d) moment on the right. Solid line – force excitation only; dash dotted line – moment excitation only; dotted line – combined excitation.

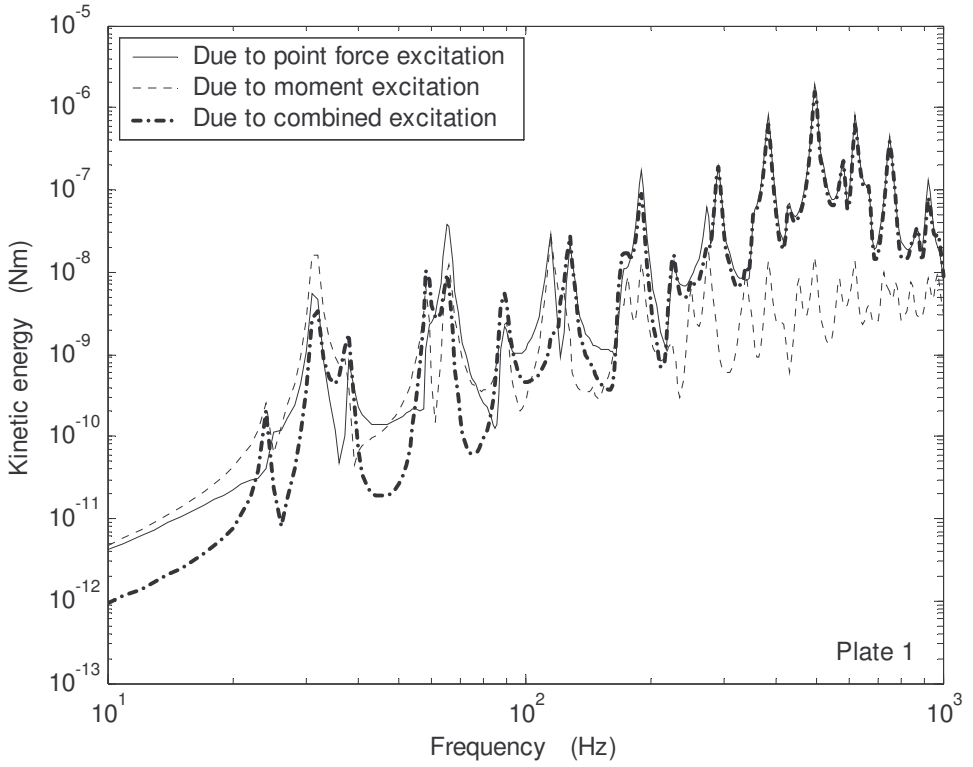

Figure 2.10. Kinetic energy distribution of the left component plate due to point force, torsional moment and combined excitations.

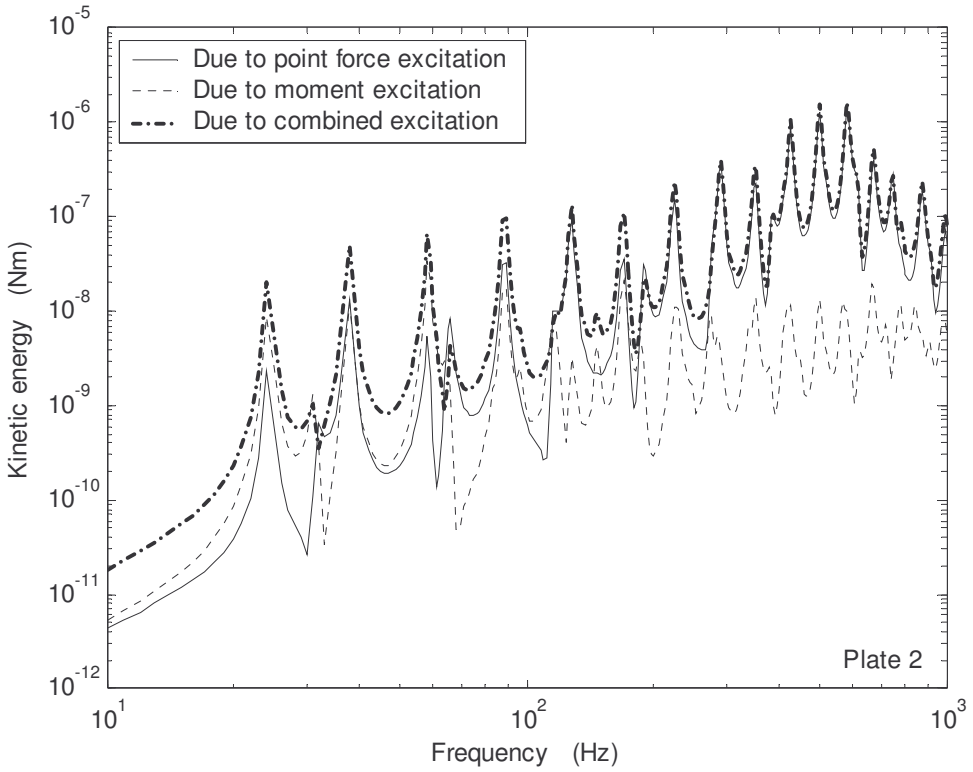

Figure 2.11. Kinetic energy distribution of the right component plate due to point force, torsional moment and combined excitations.

2.8 Conclusion

When a point force is applied at the off-neutral axis of the beam of a ribbed plate, it yields correlated excitations of a force (F_b) and a torsional moment ($F_b\Delta_0$). The velocity and angular velocity at the driving location are resulted by the force and the moment. As shown in this study, the moment can significantly affect these peak velocity responses at low frequencies and thus the input power. At certain frequencies, the moment effect on the velocity can be such that the input power due to the force become negative, which was the observation often regarded as error in the field measurement.

The underline mechanism for the significant contribution of the moment effect on input power due to off neutral loading is as followed:

The energy flows between the beam and the component plates are carried out by the shear force and bending moment distributed along the beam/plate interfaces. The torsional moment due to the off-neutral axis loading affects these energy flows by generating its own shear force and bending moment components and corresponding velocity and angular velocity at the interfaces. As a result, the total shear force ($s_T = s_F + s_M$), bending moment ($m_T = m_F + m_M$), velocity ($v_T = v_F + v_M$) and angular velocity ($\dot{\theta}_T = \dot{\theta}_F + \dot{\theta}_M$) at an interface are the combinations of the contributions of the point force and the torsional moment excitations at the beam (where s_F , m_F , v_F and $\dot{\theta}_F$ are respectively the functions of shear force and bending moment per unit length, velocity and angular velocity due to the point force F_b , and s_M , m_M , v_M and $\dot{\theta}_M$ are those due to the torsional moment $F_b\Delta_0$). As the point force and the torsional moment are correlated, constructive and destructive interference occurs in all the force, moment, velocity and angular velocity terms at the interface. Therefore the total energy flow at the interface is sum of the individual energy flows due to the point force and torsional moment alone and that due to the interferences.

In this chapter, we have showed that effect of off-neutral axis loading on the vibration response of the finite ribbed plate is only significant at low frequencies. Besides changing the amplitude of some peak values of the input power at low frequencies, the off-neutral axis loading also redistributes energy flow at the beam/plate interface and the kinetic energy distribution in the component plates. It is found that negative input power is possible at low frequencies if only one component of the input power (either point force or moment) is considered in off-neutral axis

loading cases. It is also found that beam torsional vibration could be ignored in the ribbed plate formulation if the point force is applied on the neutral axis of the beam.

Furthermore, one has to be awared that effects of off-neutral axis loading on ribbed plate response also depend on beam/plate geometry configurations. For example, if the rib is a T-beam, effects of off-neutral axis loading on the ribbed plate response could propagate to the peak responses at higher frequencies due to the increasing moment excitation amplitude.

A major advantage of the method is that the analytical approach is valid for both narrow (light) and wide (heavy) beam cases and can handle both damped and un-damped ribbed plate structures since the ribbed plate is finite in size and the couplings at each side of the interface are considered separately. However, the matrix $[C]_n$ in Equation (2.17) becomes excessive unwieldy when large number of beams are included in the ribbed plate formulation since matrix $[C]_n$ expands significantly for each additional beam on the plate.

Chapter 3

A closed form solution for the dynamic response of finite ribbed plates

3.1 Introduction

In Chapter 2, analytical solutions were obtained for predicting the vibration response of finite ribbed plates to point force (moment) excitations by utilizing the wave guide approach. Effects of off-neutral axis loading to the ribbed plate response were discussed. Characteristics of energy flow of the ribbed plate to various excitation conditions were investigated. Nevertheless, the wave guide method is most suitable for dealing with a small number of stiffened beams but not for plates reinforced by a large number of beams. To overcome this limitation, an alternative method is proposed in this chapter for ribbed plate structures with narrow stiffened beam(s) (smaller beam width (t) when compared to the plate thickness (h)) where the couplings at each beam/plate interface(s) of a ribbed plate are simplified by a pair of coupling line distributing force and moment acting at the interface. This made it possible for simple close form solutions to the ribbed plate response. The solutions are then utilized to study some of the vibration characteristics of finite ribbed plates. The general properties of the input mobility functions of the finite ribbed plate are summarized.

Given an excitation on the plate, the effect of a stiffened beam on the kinetic energy in the plate is described by the "beam insertion loss" [50]. The dependence of the insertion loss on the distance between the beam location and the excitation source, and on the frequency is investigated.

3.2 General formulations

For narrow stiffened beam ($t \le h$), the ribbed plate model used in Chapter 2 (see Figure 2.1) can be simplified by the model shown in Figure 3.1 where the stiffened beam is idealized by a single line connection. Simply supported boundary conditions are assumed for all of the plate edges and the beam in this analysis.

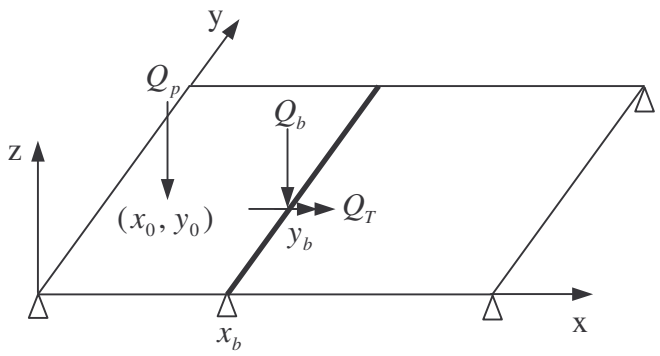

Figure 3.1. Model description and the coordinate system.

Replacing the beam by a pair of line distributing coupling force q_c and moment m_c, the governing equation of the plate bending displacement (W) to the force excitation (Q_p) can be written as:

$$\nabla^4 W - k_p^4 W = \frac{Q_p}{D} - \frac{q_c}{D}\delta(x - x_b) - \frac{m_c}{D}\delta'(x - x_b) \tag{3.1}$$

where Q_p can be either a point force or a moment applied at location (x_0, y_0) on the plate, x_b is the beam location on the plate and the prime (') indicates spatial differential.

For uncoupled beam flexural and torsional motions, the governing equations of the beam flexural and torsional displacements (U , θ) to external force (moment) excitations are written as:

$$\frac{\partial^4 U}{\partial y^4} - k_b^4 U = \frac{Q_b}{B_b} + \frac{q_c}{B_b}, \tag{3.2}$$

and

$$\frac{\partial^2 \theta}{\partial y^2} + k_t^2 \theta - R\frac{\partial^4 \theta}{\partial y^4} = \frac{Q_T}{T} + \frac{m_c}{T}, \tag{3.3}$$

where Q_b and Q_T are the external forcing applied on the beam.

Equations (3.1) – (3.3) can be solved by modal expansions of W, U and θ as:

$$W = \sum_m \sum_n w_{m,n} \phi_m(x) \phi_n(y), \tag{3.4}$$

$$U = \sum_n u_n \phi_n(y), \tag{3.5}$$

and

$$\theta = \sum_n \theta_n \phi_n(y), \tag{3.6}$$

where $\phi_m(x) = \sin(k_m x)$, $\phi_n(y) = \sin(k_n y)$, $k_m = \frac{m\pi}{L_x}$ and $k_n = \frac{n\pi}{L_y}$ are the simply supported mode shape functions and modal wave numbers of the rectangular plate.

Substituting Equation (3.4) into Equation (3.1) and integrating over the plate surface, one has:

$$w_{m,n} = \frac{1}{G_{m,n}} \int_S Q_p \phi_m(x) \phi_n(y) dS - \frac{\phi_m(x_b)}{G_{m,n}} \int_0^{Ly} q_c \phi_n(y) dy - \frac{\phi_m'(x_b)}{G_{m,n}} \int_0^{Ly} m_c \phi_n(y) dy, \tag{3.7}$$

where S is the total plate surface area, $G_{m,n} = D\Lambda_{m,n}(k_{m,n}^4 - k_p^4)$, $\Lambda_{m,n} = \frac{L_x L_y}{4}$ and $k_{m,n} = \sqrt{(k_m^2 + k_n^2)}$ is the wave number of the $(m,n)^{th}$ plate bending mode.

Similarly, substituting Equations (3.5) and (3.6) into Equations (3.2) and (3.3) and integrating over the beam length, one has:

$$u_n = \frac{1}{G_n}\left(\int_0^{Ly} Q_b \phi_n(y)dy + \int_0^{Ly} q_c \phi_n(y)\,dy\right), \tag{3.8}$$

and

$$\theta_n = -\frac{1}{G_{Tn}}\left(\int_0^{Ly} Q_T \phi_n(y)dy + \int_0^{Ly} m_c \phi_n(y)dy\right). \tag{3.9}$$

Using the compatibility conditions at the beam/plate interface ($U(y) = W(x_b, y)$ and $\theta(y) = \frac{\partial W}{\partial x}(x_b, y)$), the modal coupling force and moment at the interface can be determined by:

$$\begin{aligned}\int_0^{Ly} q_c \phi_n(y)\,dy = &\frac{\alpha_3}{\alpha_1\alpha_3 - \alpha_2^2}\left(\sum_m \frac{\phi_m(x_b)\int_S Q_p \phi_m(x)\phi_n(y)dS}{G_{m,n}} - \frac{\int_0^{Ly} Q_b \phi_n(y)dy}{G_n}\right) - \\ &\frac{\alpha_2}{\alpha_1\alpha_3 - \alpha_2^2}\left(\sum_m \frac{\phi_m'(x_b)\int_S Q_p \phi_m(x)\phi_n(y)dS}{G_{m,n}} + \frac{\int_0^{Ly} Q_T \phi_n(y)dy}{G_{Tn}}\right)\end{aligned}, \tag{3.10}$$

and

$$\begin{aligned}\int_0^{Ly} m_c \phi_n(y)\,dy = &-\frac{\alpha_2}{\alpha_1\alpha_3 - \alpha_2^2}\left(\sum_m \frac{\phi_m(x_b)\int_S Q_p \phi_m(x)\phi_n(y)dS}{G_{m,n}} - \frac{\int_0^{Ly} Q_b \phi_n(y)dy}{G_n}\right) + \\ &\frac{\alpha_1}{\alpha_1\alpha_3 - \alpha_2^2}\left(\sum_m \frac{\phi_m'(x_b)\int_S Q_p \phi_m(x)\phi_n(y)dS}{G_{m,n}} + \frac{\int_0^{Ly} Q_T \phi_n(y)dy}{G_{Tn}}\right)\end{aligned}, \tag{3.11}$$

where $\alpha_1 = \frac{1}{G_n} + \sum_m \frac{\phi_m^2(x_b)}{G_{m,n}}$, $\alpha_2 = \sum_m \frac{\phi_m(x_b)\phi_m'(x_b)}{G_{m,n}}$ and $\alpha_3 = -\frac{1}{G_{Tn}} + \sum_m \frac{\phi_m'^2(x_b)}{G_{m,n}}$.

The modal coefficients for the plate bending, the beam flexural and torsional vibrations can now be obtained from Equations (3.7) – (3.9). For better illustration, the modal coefficients and plate response to each individual force or moment

excitation are given by closed form solutions and discussed in the subsequent analysis.

3.3 Closed form solutions

3.3.1 Ribbed plate response to point force excitation on the beam

For this excitation case, $Q_p = Q_T = 0$, $Q_b = F_b\delta(y - y_b)$ where F_b is the external point force applied on the beam at location $y = y_b$. From Equations (3.10) and (3.11), the coupling force and moment at the interface are found to be:

$$\int_0^{Ly} q_c\phi_n(y)\,dy = -\frac{\alpha_3}{G_n(\alpha_1\alpha_3 - \alpha_2^2)} F_b\phi_n(y_b), \tag{3.12}$$

and

$$\int_0^{Ly} m_c\phi_n(y)\,dy = \frac{\alpha_2}{G_n(\alpha_1\alpha_3 - \alpha_2^2)} F_b\phi_n(y_b). \tag{3.13}$$

Substituting Equations (3.12) and (3.13) into Equation (3.7) gives the modal coefficient as:

$$w_{m,n} = F_b \frac{\phi_n(y_b)[\alpha_3\phi_m(x_b) - \alpha_2\phi_m'(x_b)]}{G_{m,n}G_n(\alpha_1\alpha_3 - \alpha_2^2)}. \tag{3.14}$$

The plate response can now be calculated from Equation (3.4).

On the other hand, by applying one of the compatibility conditions at the interface ($U(y) = W(x_b, y)$), the input mobility of the point force can be obtained from Equations (3.4) and (3.14), and is given by:

$$Y_{in}^{F_b} = \frac{\dot{W}(x_b, y_b)}{F_b} = \frac{j\omega}{F_b}\sum_m\sum_n w_{m,n}\phi_m(x_b)\phi_n(y_b), \tag{3.15}$$

where the overhead dot (**.**) indicates temporal differential.

3.3.2 Ribbed plate response to bending moment excitation on the beam

For this excitation case, $Q_p = Q_T = 0$, $Q_b = M_b \delta'(y - y_b)$ where M_b is the bending moment (whose moment axis is perpendicular to the beam's neutral axis) applied on the beam. The modal coupling force and moment at the interface are similar to that given by Equations (3.12) and (3.13) except that the force term $F_b \phi_n(y_b)$ is replaced by $M_b \phi_n'(y_b)$. The modal coefficient of the plate vibration response for this excitation case is then:

$$w_{m,n} = M_b \frac{\phi_n'(y_b)[\alpha_3 \phi_m(x_b) - \alpha_2 \phi_m'(x_b)]}{G_{m,n} G_n (\alpha_1 \alpha_3 - \alpha_2^2)}. \tag{3.16}$$

As a result, the bending moment input mobility of the ribbed plate is:

$$Y_x^{M_b} = \frac{\frac{\partial \dot{W}}{\partial y}(x_b, y_b)}{M_b} = \frac{j\omega}{M_b} \sum_m \sum_n w_{m,n} \phi_m(x_b) \phi_n'(y_b). \tag{3.17}$$

3.3.3 Ribbed plate response to torsional moment excitation on the beam

For this excitation case, $Q_p = Q_b = 0$, $Q_T = M_t \delta(y - y_b)$ where M_t is the torsional moment (whose moment axis is parallel to the beam's neutral axis) applied on the beam. The modal coefficient of the plate response is found to be:

$$w_{m,n} = M_t \frac{\phi_n(y_b)[\alpha_2 \phi_m(x_b) - \alpha_1 \phi_m'(x_b)]}{G_{m,n} G_{Tn} (\alpha_1 \alpha_3 - \alpha_2^2)}. \tag{3.18}$$

Applying the other compatibility condition at the interface ($\theta(y) = \frac{\partial W}{\partial x}(x_b, y)$), the input mobility of the torsional moment is obtained as:

$$Y_{in}^{M_t} = \frac{\frac{\partial \dot{W}}{\partial x}(x_b, y_b)}{M_t} = \frac{j\omega}{M_t} \sum_m \sum_n w_{m,n} \phi_m'(x_b) \phi_n(y_b). \tag{3.19}$$

3.3.4 Ribbed plate response to point force excitation on the plate

For this excitation case, $Q_b = Q_T = 0$, $Q_p = F_p \delta(x - x_0)\delta(y - y_0)$ where F_p is the external point force applied on the plate. The modal coefficient of the ribbed plate response is found to be:

$$w_{m,n} = F_p \frac{\phi_n(y_0)}{G_{m,n}}[\phi_m(x_0) - \frac{\alpha_3\alpha_4 - \alpha_2\alpha_5}{\alpha_1\alpha_3 - \alpha_2^2}\phi_m(x_b) - \frac{\alpha_1\alpha_5 - \alpha_2\alpha_4}{\alpha_1\alpha_3 - \alpha_2^2}\phi_m'(x_b)], \tag{3.20}$$

where $\alpha_4 = \sum_m \frac{\phi_m(x_0)\phi_m(x_b)}{G_{m,n}}$ and $\alpha_5 = \sum_m \frac{\phi_m(x_0)\phi_m'(x_b)}{G_{m,n}}$.

The first term in the square bracket of Equation (3.20) is the modal coefficient of the corresponding uncoupled plate response to the same excitation and the last two terms are the contributions from the force and moment couplings of the stiffened beam. It should be noted that Equation (3.20) becomes Equation (3.14) when $x_0 = x_b$, $y_0 = y_b$. Therefore, the excitation case presented in Section 3.3.1 is simply a special case for this excitation.

The input mobility of the ribbed plate for this excitation case is given by:

$$Y_{in}^{F_p} = \frac{j\omega}{F_p}\sum_m\sum_n w_{m,n}\phi_m(x_0)\phi_n(y_0). \tag{3.21}$$

3.3.5 Ribbed plate response to moment excitation on the plate

For this excitation, $Q_p = M_0 \sin\varphi\delta'(x - x_0)\delta(y - y_0) - M_0 \cos\varphi\delta(x - x_0)\delta'(y - y_0)$ where M_0 is the amplitude of the external moment and φ is the angle of the moment axis with respect to the x-axis of the coordinate system [51], $Q_T = Q_b = 0$. Applying the compatibility conditions at the interface, the modal coefficients of the plate response is given by:

$$w_{m,n} = -\frac{M_0}{G_{m,n}}\{\cos\varphi\ \phi_n'(y_0)[\phi_m(x_0) - \frac{\alpha_3\alpha_4 - \alpha_2\alpha_5}{\alpha_1\alpha_3 - \alpha_2^2}\phi_m(x_b) - \frac{\alpha_1\alpha_5 - \alpha_2\alpha_4}{\alpha_1\alpha_3 - \alpha_2^2}\phi_m'(x_b)] - \sin\varphi\phi_n(y_0)[\phi_m'(x_0) - \frac{\alpha_3\alpha_6 - \alpha_2\alpha_7}{\alpha_1\alpha_3 - \alpha_2^2}\phi_m(x_b) - \frac{\alpha_1\alpha_7 - \alpha_2\alpha_6}{\alpha_1\alpha_3 - \alpha_2^2}\phi_m'(x_b)]\}$$

(3.22)

where $\alpha_6 = \sum_m \frac{\phi_m'(x_0)\phi_m(x_b)}{G_{m,n}}$, $\alpha_7 = \sum_m \frac{\phi_m'(x_0)\phi_m'(x_b)}{G_{m,n}}$.

There are two input mobility components for this excitation case each in association with one of the two angular velocity components at the source location ($\frac{\partial \dot{W}}{\partial x}(x_0, y_0)$ and $\frac{\partial \dot{W}}{\partial y}(x_0, y_0)$). These mobility components are given respectively by:

$$Y_x^{M_0} = \frac{\frac{\partial \dot{W}}{\partial y}(x_0, y_0)}{M_0} = \frac{j\omega}{M_0}\sum_m\sum_n w_{m,n}\phi_m(x_0)\phi_n'(y_0), \tag{3.23}$$

and

$$Y_y^{M_0} = \frac{\frac{\partial \dot{W}}{\partial x}(x_0, y_0)}{M_0} = \frac{j\omega}{M_0}\sum_m\sum_n w_{m,n}\phi_m'(x_0)\phi_n(y_0). \tag{3.24}$$

3.3.6 Vibration energy distributions

For all excitation cases, the time averaged, steady state flexural vibration energy distribution of the plate is calculated by:

$$\langle \overline{T} \rangle_P = \frac{1}{2}\int_S \rho_s \dot{W}\dot{W}^* dS = \frac{\rho_s \Lambda_{m,n}\omega^2}{2}\sum_m\sum_n \left|w_{m,n}\right|^2. \tag{3.25}$$

Similarly, by utilizing the plate bending and angular displacements at the interface, the time averaged, steady state beam flexural vibration energy is given by:

$$\left\langle \overline{T} \right\rangle_b = \frac{1}{2}\int_0^{Ly} \rho_L \dot{U}\dot{U}^* dy = \frac{\rho_L \Lambda_n \omega^2}{2} \sum_n \left| \sum_m w_{m,n}\phi_m(x_b) \right|^2 , \tag{3.26}$$

and the beam torsional vibration energy is:

$$\left\langle \overline{T} \right\rangle_t = \frac{1}{2}\int_0^{Ly} \rho_b I_P \dot{\theta}\dot{\theta}^* dy = \frac{\rho_b I_P \Lambda_n \omega^2}{2} \sum_n \left| \sum_m w_{m,n}\phi'_m(x_b) \right|^2 . \tag{3.27}$$

3.4 Results and discussion

In this simulation, a smaller beam with cross sectional area of $A_b = 50mm \times 5mm$ is used. The source location is still at $(x_0, y_0) = (1.4m, 0.32m)$ in the analysis. The vibration response of the ribbed plate is calculated by including 1000 uncoupled plate modes and 20 uncoupled beam modes in the modal summation.

3.4.1 Prediction accuracy

The accuracy of the proposed method is examined by comparing the predicted input mobilities to that obtained from FEA analysis for the three excitation cases: (a) point force excitation applied on the beam; (b) torsional moment excitation applied on the beam; and (c) point force excitation applied on the plate. The results are shown in Figures 2 – 4 respectively. The beam is located at plate location $x_b = 1.4m$ for the first two excitations and is located at $x_b = 1.6m$ for the third excitation. Good agreements are found in the whole frequency range of investigation for all three excitations.

Nonetheless, it has to be noted that the method developed here is limited by the narrow beam assumption where the beam/plate interface is regarded as a single line

connection. For plates reinforced by wide (heavy) beams ($t > h$), the current method underestimates the plate impedance to the beam torsional vibration, which leads to an over prediction of the ribbed plate response. The wave guide method described in Chapter 2 would be a more appropriate approach for such case. However, an approximate solution for such ribbed plates can still be obtained by the modal expansion solution if the source is not a torsional moment and is applied on the beam or on the plate at more than a quarter of plate bending wavelength away from the beam. For such excitations, according to the discussions given in Chapter 2 and Lin and Pan [52], the contribution of beam torsional vibration to the ribbed plate response is negligible, and can be ignored in the analysis. Therefore, only shear force coupling at the interface needs to be considered. The ribbed plate response can then be solved by the modal expansion solution using an Euler-Bernoulli beam formulation for the beam.

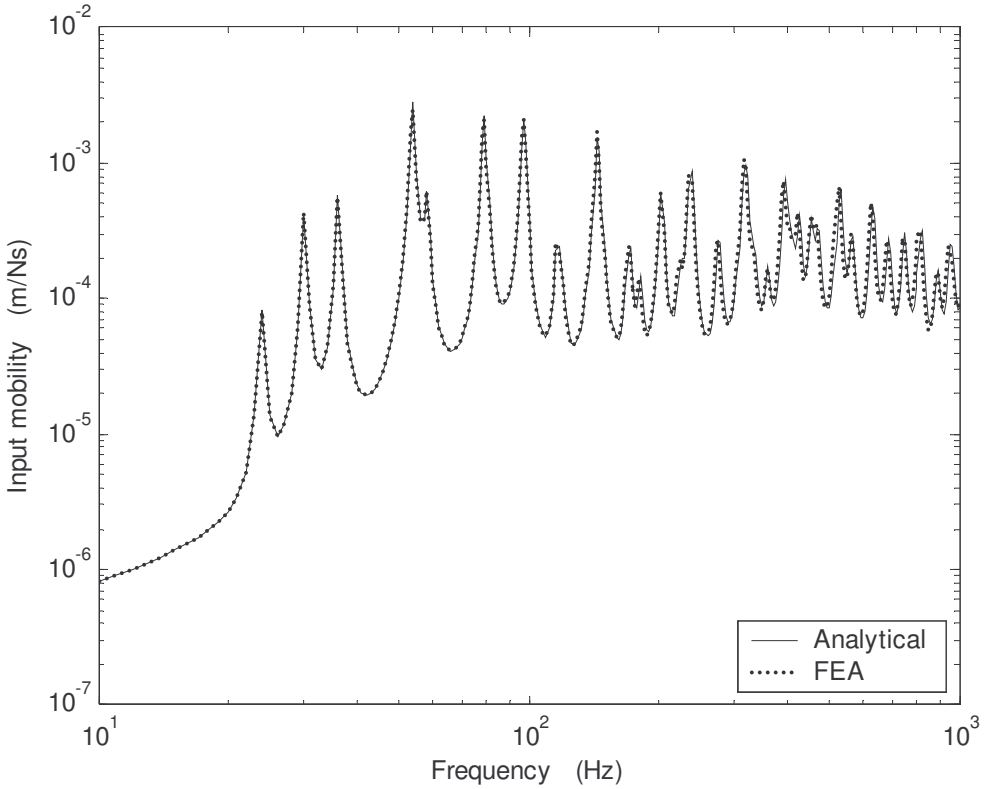

Figure 3.2. Input mobility of the ribbed plate to point force excitation applied on the beam.

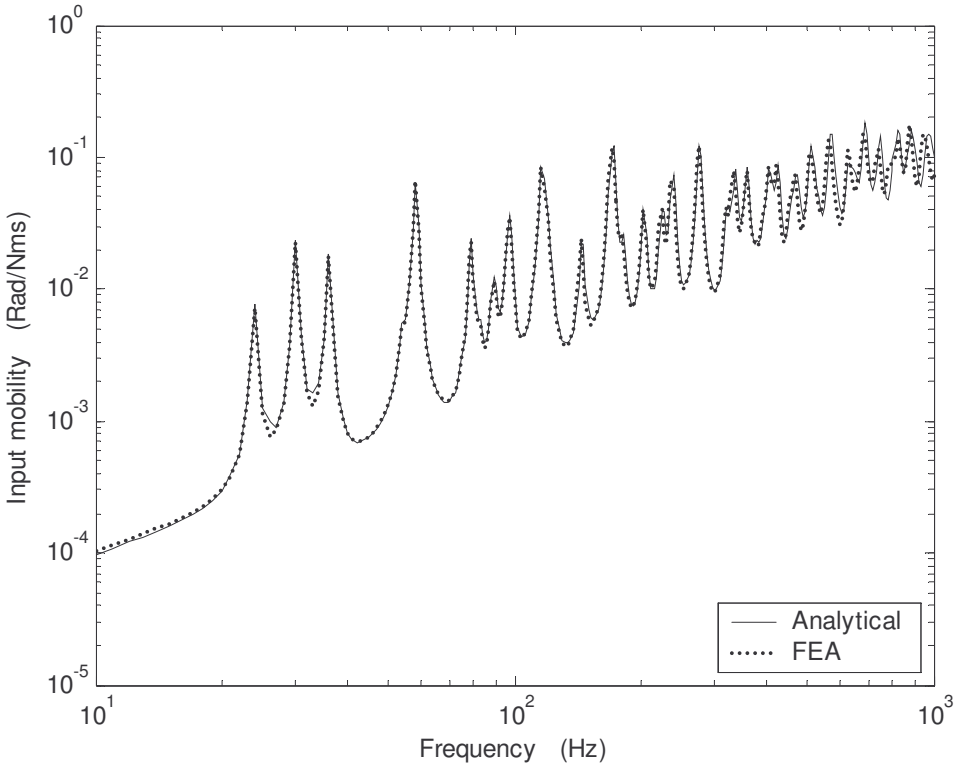

Figure 3.3. Input mobility of the ribbed plate to torsional moment excitation applied on the beam.

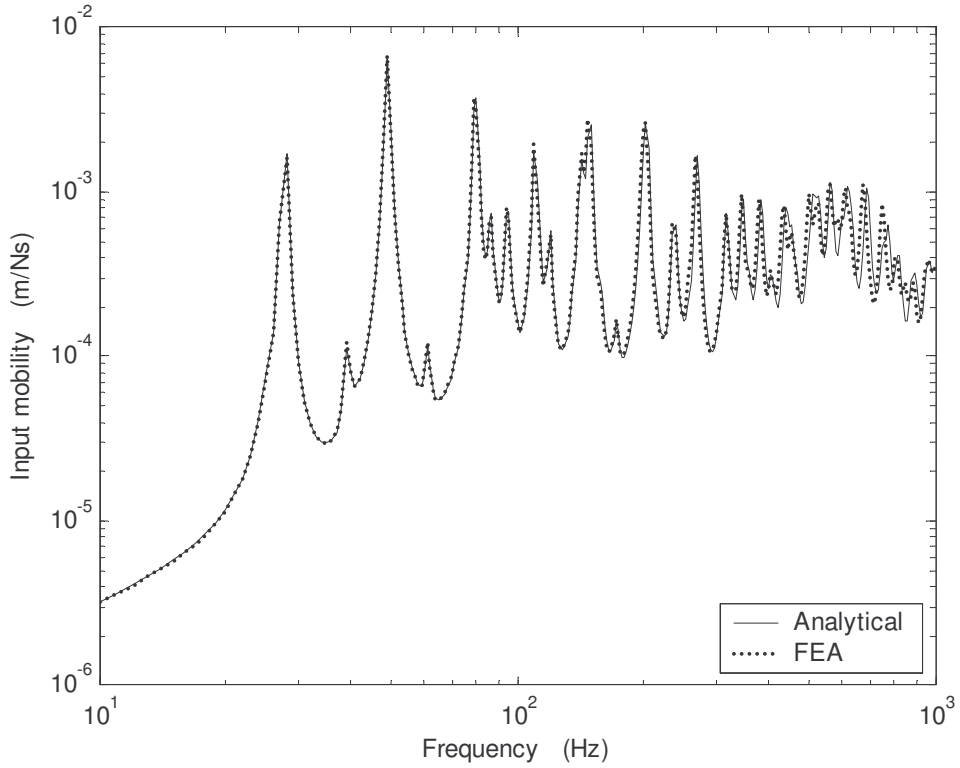

Figure 3.4. Input mobility of the ribbed plate to point force excitation applied on the plate.

3.4.2 Characteristics of the ribbed plate input mobility

Characteristics of input mobilities of the ribbed plate are studied here by moving the stiffened beam from the initial location at $x_b = 1.4m$ to the plate locations at $x_b = 1.45m$ and $x_b = 1.6m$ for the two excitations – point force and moment excitations.

a) Point force input mobility

Figure 3.5 shows the point force input mobilities of the ribbed plate together with those of the corresponding uncoupled plate and beam of finite and infinite sizes. It is shown that the input mobilities of the ribbed plate are bounded by those of the corresponding uncoupled plate and beam in general. The plate bending stiffness controls the input mobility when the beam is more than a quarter wavelength away from the point force location where the input mobility of the ribbed plate is similar to that of the corresponding uncoupled plate. The input mobility of the corresponding

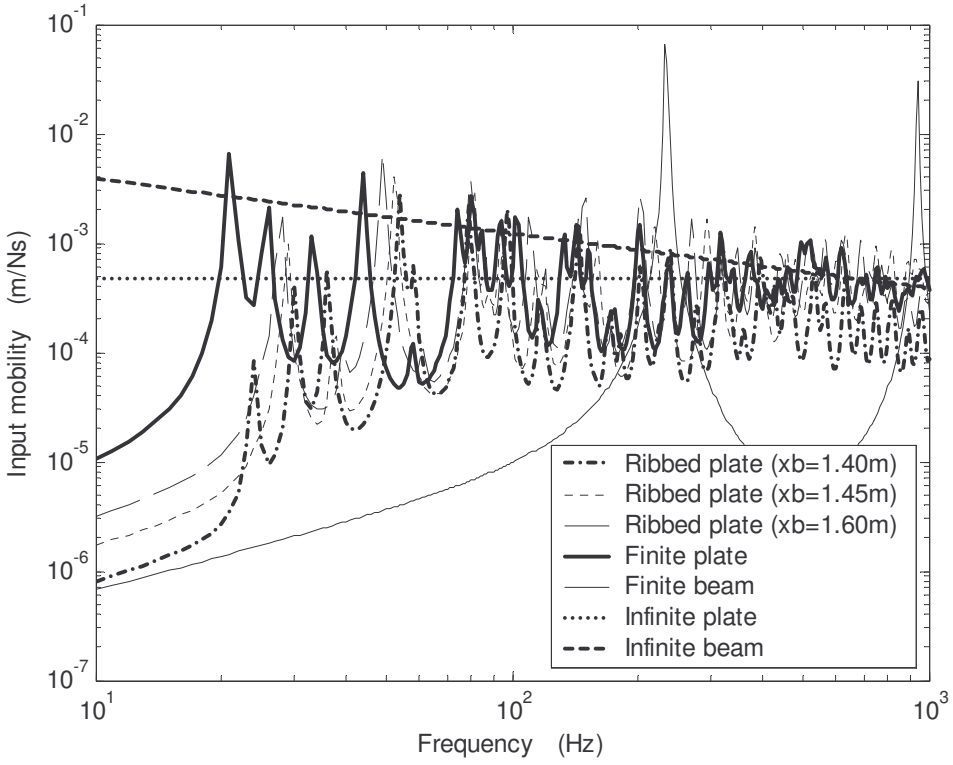

Figure 3.5. Input mobility of the ribbed plate to point force excitations.

infinite plate represents the upper bound of the frequency averaged input mobility of the ribbed plate. In contrast to that reported by Lin and Pan [50], due to the relatively smaller beam/plate flexural stiffness ratio ($\frac{B_b}{D} \approx 5$) of the ribbed plate, the stiffness term of the input mobility is not only controlled by the beam flexural stiffness but also greatly influenced by the plate bending stiffness when the point force acts on the beam. Therefore, the lower bound of the frequency averaged input mobility of the ribbed plate can no longer be represented by that of the corresponding infinite beam for this case. It is noted that the observations made here are independent of the y-coordinate of the source location when the source is applied at more than a quarter wavelength away from the plate edges in this direction.

b) Moment input mobility

The input mobilities of the ribbed plate to bending ($\varphi = 0^0$) and torsional moment ($\varphi = 90^0$) excitations are considered separately where only the principal component of the moment input mobility (the component that shares the same axis with the external moment) is examined.

Figure 3.6 shows the torsional moment input mobilities of the ribbed plate together with those of the corresponding uncoupled plate of finite and infinite extents. It is found that the input mobility of the ribbed plate for this excitation case does not vary much from that of the corresponding uncoupled plate regardless of the location of the stiffened beam. This is because the stiffness term of the input mobility for this excitation case is dominated by the plate bending stiffness, which is much greater than the beam torsional stiffness ($\frac{D}{T} > 60$). It is illustrated that for all of the three beam/plate configurations in this simulation, the frequency averaged input mobilities increase with increasing frequency, which can be well represented by the input mobility of the corresponding infinite plate.

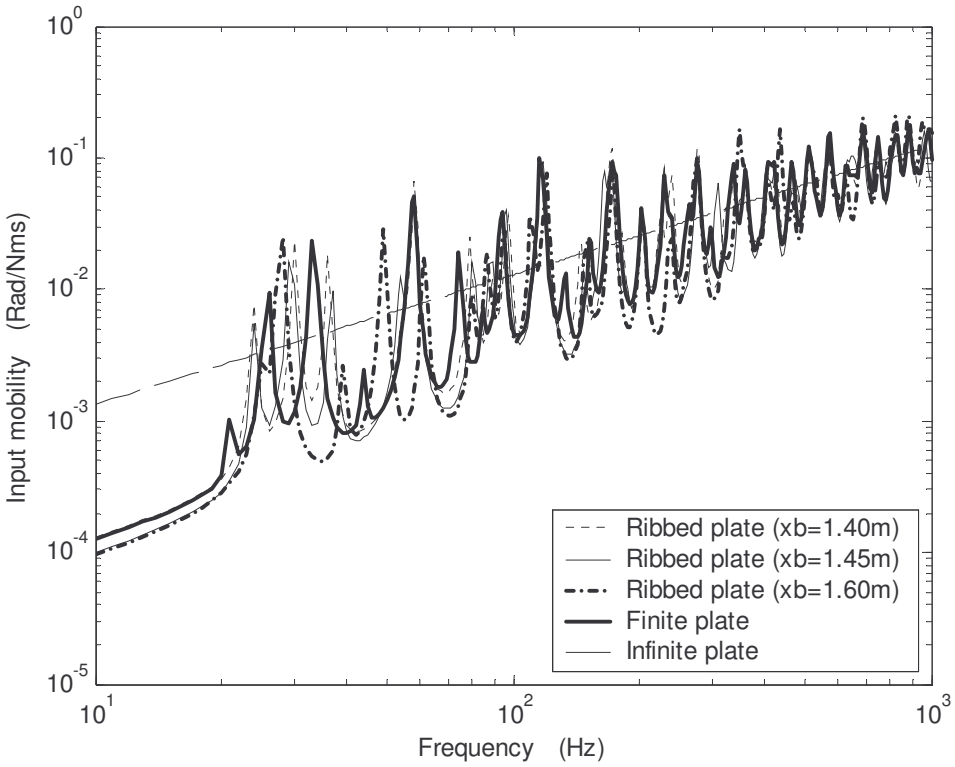

Figure 3.6. Input mobility of the ribbed plate to torsional moment excitations.

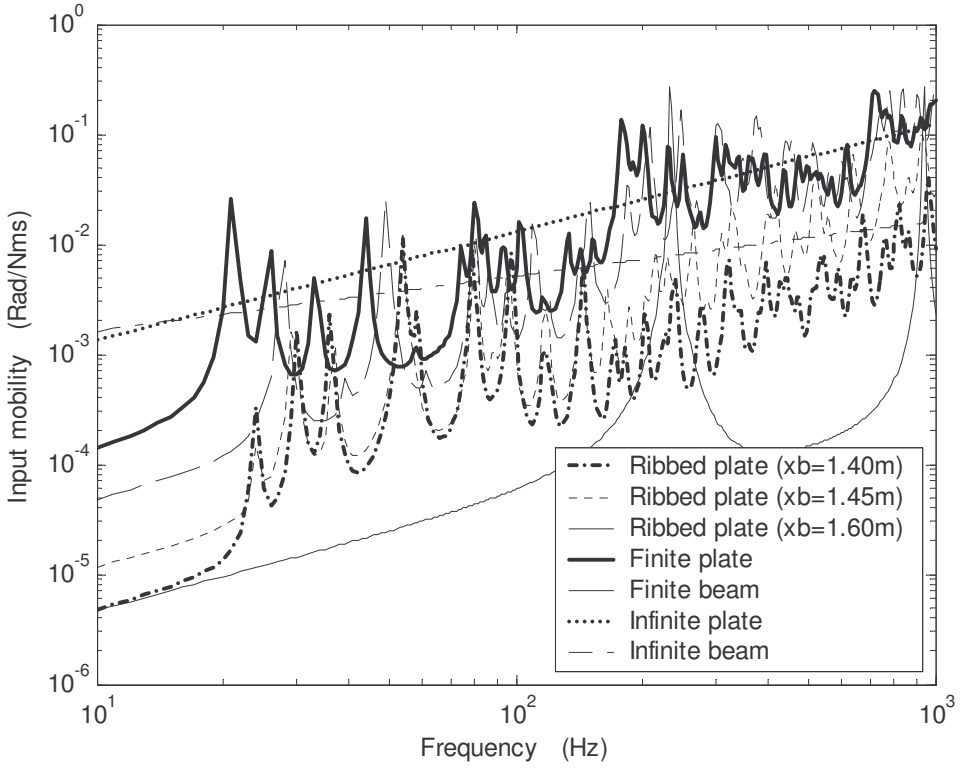

Figure 3.7. Input mobility of the ribbed plate to bending moment excitations.

Similar to what was found in point force excitation cases, the bending moment input mobilities of the ribbed plate are also bounded by the input mobilities of the corresponding uncoupled plate and beam as shown in Figure 3.7. The frequency averaged input mobilities increase with increasing frequency and can be represented by the input mobility of the corresponding infinite plate when the beam is more than a quarter wavelength away from the source.

3.4.3 Beam insertion loss to the plate response

The reduction of the plate response due to the insertion of a stiffened beam may be measured by using the concept of insertion loss as defined in room acoustics [53]. This is given as:

$$IL = 10\log_{10}\frac{\left\langle \overline{T} \right\rangle_P^0}{\left\langle \overline{T} \right\rangle_P}, \tag{3.28}$$

where $\left\langle \overline{T} \right\rangle_P$ is the plate kinetic energy of the ribbed plate given by Equation (3.25) and $\left\langle \overline{T} \right\rangle_P^0$ is the kinetic energy of the corresponding uncoupled plate for the same excitation.

The insertion losses corresponding to the three beam locations for cases of point force excitation on the plate are shown in Figure 3.8. It is found that large vibration energy reductions can be achieved at low frequencies when the beam is inserted directly between the source and the plate or very close to the source. However, negative reduction is possible even at low frequencies due to the small beam/plate flexural stiffness ratio and the shifted resonant frequencies of the structure after beam insertion. When the stiffened beam is attached to the plate away from the source, the vibration reduction will depend on the distance between the beam and the source. By moving the beam away from the source, the overall insertion loss decreases due to

the decreasing influence of beam stiffness to the input mobility. The band averaged vibration reduction at high frequencies tends to zero when the beam is more than a quarter wavelength away from the source (i.e. at frequencies greater than 120Hz for the beam location at $x_b = 1.6m$).

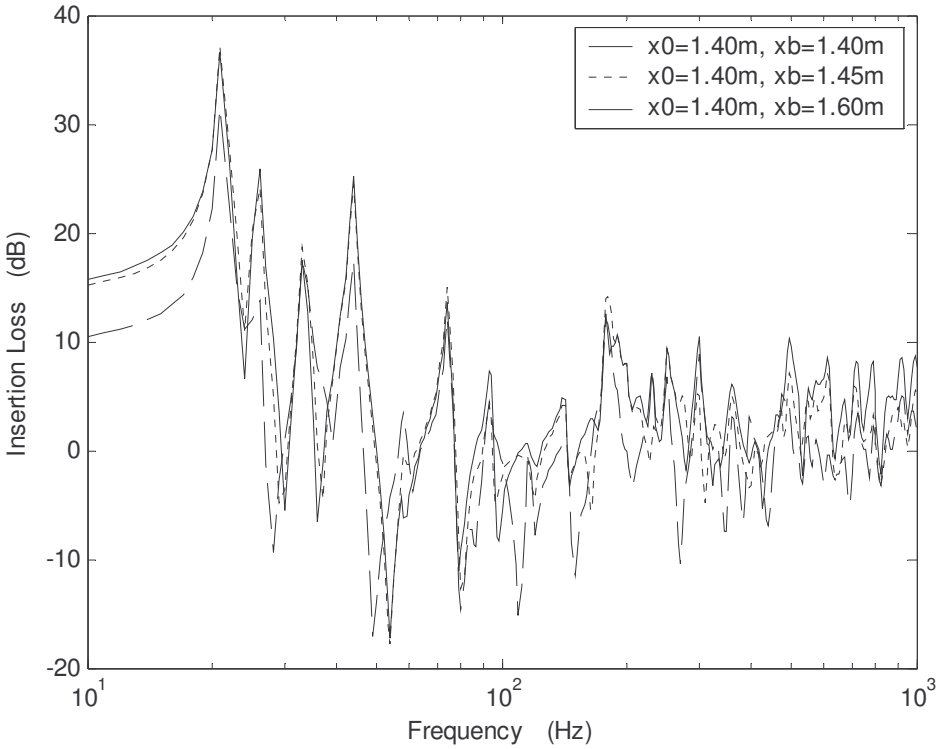

Figure 3.8. Beam insertion losses on plate vibration energy in point force excitation case.

The beam insertion losses in the bending moment excitation case are similar to those of the point force excitation case, and are not shown here. On the other hand, Figure 3.9 shows the beam insertion losses in the torsional moment excitation case. It is found that vibration reduction at frequencies below the first system resonant frequency after beam insertion is eventually zero because of the large plate bending to beam torsional stiffness ratio. The reduction also tends to zero at high frequencies. In between, general reductions are observed at frequencies corresponding to the

uncoupled plate natural frequencies while negative reductions are found at frequencies corresponding to the shifted peak frequencies after beam insertion. In general, the insertion of the stiffened beam on the plate in torsional excitation cases only changes the peak response frequencies but not the overall frequency averaged plate vibration energy.

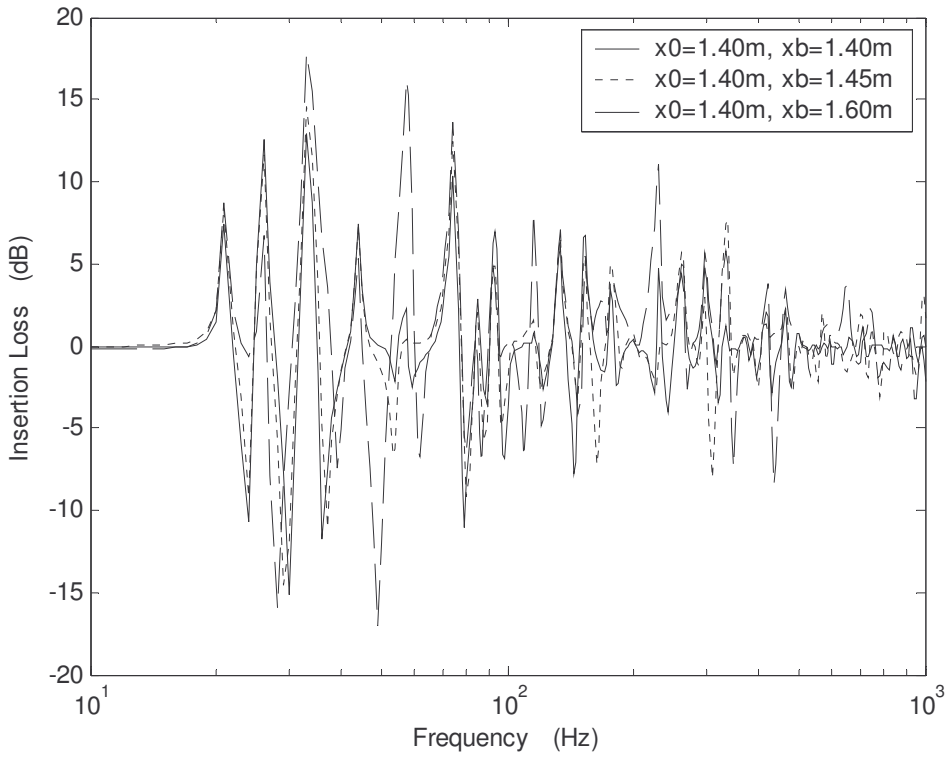

Figure 3.9. Beam insertion losses on plate vibration energy in torsional moment excitation cases.

3.5 Conclusion

A modal expansion technique is employed in this chapter to obtain closed form solutions for predicting the vibration response of a finite ribbed plate to point force and moment excitations. It is found that the point force and bending moment input mobilities of the ribbed plate are bounded by those of the corresponding uncoupled plate and beam forming the ribbed plate system. They are controlled by the plate

bending stiffness when the source location is more than a quarter of plate bending wavelength away from the beam and are mainly dominated by the beam flexural stiffness when the source acts on the beam or very close to the beam. It is also shown that the torsional moment input mobility of the ribbed plate does not vary much from that of the corresponding uncoupled plate.

Large plate vibration reductions can be found at low frequencies after the insertion of the stiffened beam on the plate in the cases of point force and bending moment excitations. Negative reduction can be observed in the frequency bands associated with some of the shifted peak frequencies after beam insertion. The vibration reduction tends to zero at high frequencies when the beam is more than a quarter wavelength away from the source. In contrast, the insertion of the beam in torsional excitation case only changes the peak response frequencies but not the overall frequency averaged plate vibration energy.

A major advantage of the method presented in this chapter is that the ribbed plate response can be expressed in simple closed form solutions to provide a direct physical understanding of the relationship between the response and the excitation as well as the properties of the plate and the beam. Another advantage of the method is that it can be easily extended to deal with ribbed plate structures reinforced by a large number of stiffened beams. One major drawback of the method is that the solution is only valid for narrow beam cases although approximate solutions could still be obtained when the excitation is not a torsional moment, and is applied on the beam or on the plate at more than a quarter wavelength away from the beam.

Chapter 4

A study of vibration characteristics of finite periodic and irregular ribbed plates

4.1 Introduction

Analytical approaches were presented in Chapters 2 and 3 for predicting the vibration responses of finite rectangular plates reinforced by a single stiffened beam. These approaches can be readily extended to the analysis of vibration response of finite plates reinforced by multiple stiffened beams. For a plate reinforced by heavy beams, the wave guide approach is a more suitable approach since the coupling moment and force on each side of the interfaces are formulated separately. For plate reinforced by narrow beams, the modal expansion solution provides a simpler and faster solution for the vibration response of the ribbed plate. This approach is utilized in this chapter to study the characteristics of wave propagation in finite periodic ribbed plates as well as the phenomena of vibration confinement in a finite irregular ribbed plate.

4.2 Literature review

Vibration characteristics of periodic structures have been a long-standing research topic for many decades due to its broad applications and interesting wave phenomena. Mead [54] provided a comprehensive review of the research methods developed at the University of Southampton for analyzing the free and forced wave motions in periodic structures for over three decades in the last century (1964 – 1995). Keane and Price [55] also reviewed some commonly used methods in the periodic theory.

Traditionally, the vibration of a periodic structure is analyzed by solving each section (bay) of the periodic system successively. The most common approaches are propagation wave approaches [56-59] and transfer matrix methods [60-63]. The propagation wave approach is associated with the development of the Bloch theorem in solid state physics [64], which can be applied most efficiently to infinite or semi-infinite periodic systems. On the other hand, the transfer matrix method provides a more convenient approach for the analysis of finite periodic structures because boundary conditions of the finite periodic system can be easily incorporated into the transfer matrix. Other methods, such as Z-transform [65] and energy [66] methods have also been developed. Moreover, Mead [45] provided an analytical solution to predict wave propagation in an infinite periodic beam and plate by using phased array receptance functions and obtained analytical equations for calculating the wave propagation constants. The above work has greatly improved the understanding of wave propagation characteristics of periodic structures. However, a common assumption made by this work is that the periodic system is formed by identical periodic elements. In contrast, disorders due to manufacturing imperfections or installation errors, or directly from the design of a structure are common for most practical periodic systems.

Wave propagation in disordered periodic systems has attracted more and more attentions because of its growing importance in passive vibration control of engineering structures. Mead and Bansal [67, 68] studied free and forced wave motions in an infinite mono-coupled periodic system with single disorder by utilizing the end receptance of the disorder and the characteristic wave receptance of the periodic system. The disorder of the infinite periodic system is considered as two semi-infinite periodic systems connecting through the disordered element. Hodges [69] first introduced the Anderson localization phenomenon [9] discovered originally

for solid state physics to acoustic contexts and showed that vibration localization could be produced in a one-dimension structure depending upon the effective dimension of the structure and the extent of structural irregularities. Hodges and Woodhouse [70] studied the phenomenon further in a weakly disordered one-dimension chain of oscillators. Their experimental investigation on a vibrating string with irregular spaced attaching masses shows good agreement with that of the theoretical prediction. Single and multiple weak disorders in a mono-coupled periodic system were also studied by Keane and Price [55].

Photiadis [71] studied the Anderson localization in an infinite fluid loaded plate with an irregularity array of line attachments by applying the Green's function. Only shear force couplings between the ribs and the plate were considered in his analysis. In about the same era, Sobnack and Crighton [72] examined the Anderson localization effect on wave transmission in an infinite fluid-loaded membrane supported by a number of irregular spaced ribs by employing the Green's function and statistical methods. The localization lengths for both small and large disorder limits were calculated and discussed. Nevertheless, because the moment couplings between the ribs and the plate were not considered in their analysis, the vibration localization phenomenon observed in their analysis is only valid for one group of modes associated with the shear force couplings at the interfaces of a ribbed plate.

In this study, by considering both shear force and moment couplings and including the beam characteristic functions in the formulation, a simple analytical method is obtained to predict the vibration response of a finite periodic or irregular ribbed plate by employing the modal expansion solution similar to that described in Chapter 3. The excitations to the system can be either force or moment excitations and can be applied either on the plate or on the beams. In contrast to the conventional

approaches where each periodic section is solved successively, the entire plate in this analysis is considered as a single entity where the stiffened beams are subsequently added onto the plate via the force and moment couplings at the beam/plate interfaces. One advantage of the proposed method is that both periodic and periodic disordered systems can be solved by using the same matrix formulation without altering the solution procedure.

As a result, progress has been made into more detailed understanding towards the band pass/stop properties of a periodic ribbed plate and the vibration confinement phenomenon when structural irregularities are introduced. For the first case, the modal vibration and wave matching characteristics of the pass bands are studied. For the latter case, we found that the existence of the vibration confinement is dependent on the nature of beam/plate couplings. The irregular beam spacing is only effective in generating vibration confinement to those waves dominated by the flexural/flexural couplings between the beams and the plate. While confinements for the group of waves dominated by the torsional/flexural couplings at the beam/plate interfaces rely on torsional stiffness irregularity of the stiffened beams.

4.3 General formulations

A finite multiple ribbed plate model is shown in Figure 4.1 where a rectangular plate is simply supported on all its edges and is reinforced by N stiffened beams, which are either periodic or irregular distributed on the plate surface and with their neutral axis parallel to a pair of the plate edges. It is assumed that all the stiffened beams are also simply supported and are firmly attached to the plate where the beam/plate interfaces can be considered as non-slip line connections.

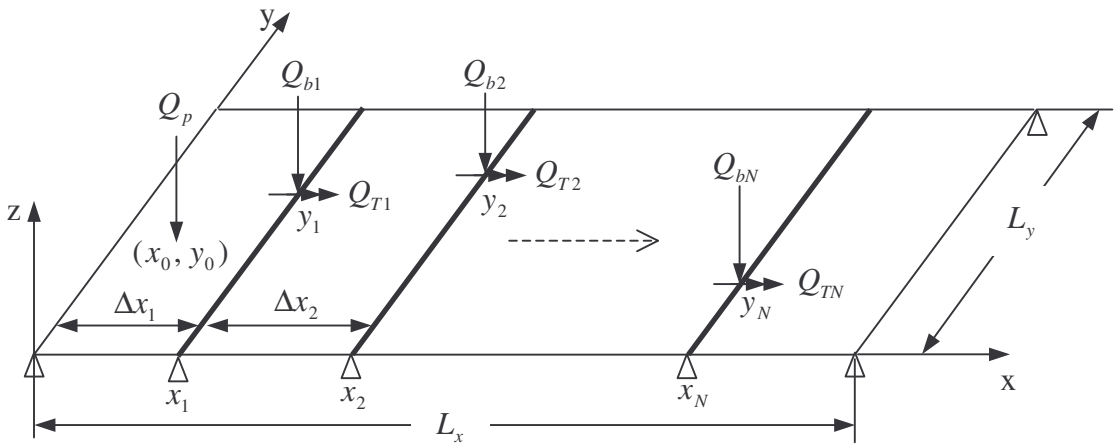

Figure 4.1 Model description and the coordinate system of the finite ribbed plate.

By including all the coupling forces and moments into the plate equation, Equation (3.1) is rewritten here as:

$$\nabla^4 W - k_p^4 W = \frac{Q_p}{D} - \sum_{i=1}^{N} \frac{q_i}{D} \delta(x - x_i) - \sum_{i=1}^{N} \frac{m_i}{D} \delta'(x - x_i), \tag{4.1}$$

where q_i and m_i are the coupling force and moment per unit length at the i^{th} beam/plate interface, x_i is the location of the i^{th} beam on the plate.

For uncoupled beam flexural and torsional motions, the governing equations of the flexural and torsional displacements of the i^{th} beam (U_i, θ_i) are given by:

$$\frac{\partial^4 U_i}{\partial y^4} - k_{bi}^4 U_i = \frac{Q_{bi}}{B_{bi}} \delta(y - y_i) + \frac{q_i}{B_{bi}}, \quad i = 1,2,...,N, \tag{4.2}$$

and

$$\frac{\partial^2 \theta_i}{\partial y^2} + k_{ti}^2 \theta_i - R_i \frac{\partial^4 \theta_i}{\partial y^4} = \frac{Q_{T_i}}{T_i} + \frac{m_i}{T_i}, \quad i = 1,2,...,N, \tag{4.3}$$

where the symbols are similarly defined as in Chapter 3.

The modal expansion solution of the plate response gives:

$$w_{m,n} = \frac{1}{G_{m,n}} \int_S Q_p \phi_m(x) \phi_n(y) dS - \sum_{i=1}^{N} \frac{\phi_m(x_i)}{G_{m,n}} Q_i - \sum_{i=1}^{N} \frac{\phi_m'(x_i)}{G_{m,n}} M_i , \quad (4.4)$$

where $Q_i = \int_0^{Ly} q_i \phi_n(y) dy$ and $M_i = \int_0^{Ly} m_i \phi_n(y) dy$ are the modal coupling force and moment at the i^{th} beam/plate interface.

The modal expansion solutions of the beam flexural and torsional vibrations provide:

$$u_{ni} = F_i + \frac{1}{G_{ni}} Q_i, \quad i = 1,2,...,N , \quad (4.5)$$

and

$$\theta_{ni} = -M_{Ti} - \frac{1}{G_{Tni}} M_i, \quad i = 1,2,...,N , \quad (4.6)$$

where $G_{ni} = B_{bi} \Lambda_n (k_n^4 - k_{bi}^4)$, $G_{Tni} = T_i \Lambda_n (R_i k_n^4 + k_n^2 - k_{ti}^2)$. $F_i = \frac{1}{G_{ni}} \int_0^{Ly} Q_{bi} \phi_n(y) dy$ and $M_{Ti} = \frac{1}{G_{Tni}} \int_0^{Ly} Q_{Ti} \phi_n(y) dy$ are the modal components of the external force and moment applied on the i^{th} beam.

Although both external force and moment excitations are included in the above equations, for simplicity, only the response of the ribbed plate to point force excitations is discussed in the subsequent analysis.

4.4 Vibration response of finite ribbed plates to point force excitations

For this excitation case, $Q_P = F_0 \delta(x - x_0) \delta(y - y_0)$ and $Q_{Bi} = F_{Bi} \delta(y - y_i)$ where F_0 is the external point force applied on the plate and F_{Bi} is the external point force

applied on the i^{th} beam. Applying the compatibility conditions at the beam/plate interfaces and using Equations (4.4) – (4.6), for each modal index n, one has:

$$\begin{Bmatrix} \{Q\} \\ \{M\} \end{Bmatrix}_n = \begin{bmatrix} [A] & [C] \\ [C]^T & [B] \end{bmatrix}_n^{-1} \begin{Bmatrix} F_0\phi_n(y_0)\{H^{ss}\} - \{F\} \\ F_0\phi_n(y_0)\{H^{sc}\} \end{Bmatrix}_n, \tag{4.7}$$

where the superscript T indicates matrix transpose.

$$\{Q\} = \lfloor Q_1 \quad Q_2 \quad \ldots \quad Q_{N-1} \quad Q_N \rfloor^T, \tag{4.8}$$

and

$$\{M\} = \lfloor M_1 \quad M_2 \quad \ldots \quad M_{N-1} \quad M_N \rfloor^T, \tag{4.9}$$

are respectively the modal coupling force and moment vectors which are to be determined.

In Equation (4.7), $[A]$ is a $N \times N$ square sub-matrix relating to the interactions of the shear force couplings at the beam/plate interfaces, whose elements are given by:

$$A_{i,j} = \sum_m \frac{\phi_m(x_i)\phi_m(x_j)}{G_{m,n}},\ A_{i,i} = \sum_m \frac{\phi_m^2(x_i)}{G_{m,n}} + \frac{1}{G_{ni}}, \quad i, j = 1,2,\ldots,N. \tag{4.10}$$

$[B]$ is a $N \times N$ square sub-matrix relating to the interactions of the moment couplings at the beam/plate interfaces, whose elements are given by:

$$B_{i,j} = \sum_m \frac{\phi_m'(x_i)\phi_m'(x_j)}{G_{m,n}},\ B_{i,i} = \sum_m \frac{\phi_m'^2(x_i)}{G_{m,n}} - \frac{1}{G_{Tni}}, \quad i, j = 1,2,\ldots,N. \tag{4.11}$$

While $[C]$ is a $N \times N$ cross coupling sub-matrix, whose elements are given by:

$$C_{i,j} = \sum_m \frac{\phi_m(x_i)\phi_m'(x_j)}{G_{m,n}}, \quad i, j = 1,2,\ldots,N. \tag{4.12}$$

The elements in the external force vector on the right hand side of Equation (4.7) are given respectively by:

$$H_i^{ss} = \sum_m \frac{\phi_m(x_0)\phi_m(x_i)}{G_{m,n}}, \quad i = 1,2,\ldots,N, \tag{4.13}$$

$$H_i^{sc} = \sum_m \frac{\phi_m(x_0)\phi'_m(x_i)}{G_{m,n}}, \quad i = 1,2,...,N\ . \tag{4.14}$$

The elements in $\{F\}$ are given by:

$$F_i = \frac{F_{bi}}{G_{ni}}\phi_n(y_i), \quad i = 1,2,...,N\ . \tag{4.15}$$

Once the modal coupling forces and moments are determined, the modal coefficient of the plate vibration response can be calculated from Equation (4.4) as:

$$w_{m,n} = \frac{F_0\phi_m(x_0)\phi_n(y_0) - \sum_{i=1}^{N}[\phi_m(x_i)Q_i + \phi'_m(x_i)M_i]}{G_{m,n}}\ . \tag{4.16}$$

The first term in Equation (4.16) is the modal response of the corresponding un-ribbed plate to the same excitation and the summation term is the sum of the contributions from the modal coupling forces and moments at beam/plate interfaces to the plate response.

4.5 Kinetic energy distributions

By substituting Equation (4.16) into Equation (3.31), the time-averaged, steady state kinetic energy of the plate (excluding the energy in the beams) can be determined. Conversely, the time averaged, steady state vibration energy of the i^{th} plate section (bounded by two consecutive stiffened beams) of the ribbed plate can be calculated by:

$$\left\langle \overline{T} \right\rangle_P^i = \frac{\rho_S \omega^2 \Lambda_n}{2} \sum_n \int_{x_{i-1}}^{x_i} (\sum_{m'} w_{m',n}\phi_{m'}(x))(\sum_m w_{m,n}\phi_m(x))^* dx, \quad i = 1,2,...(N+1)\,, \tag{4.17}$$

where $x_{i-1} = 0$ when $i = 1$ and $x_i = L_x$ when $i = (N+1)$. For simply supported boundary conditions, the integral in Equation (4.17) can be solved analytically.

If we consider the i^{th} bay of the ribbed plate consisting of the i^{th} plate section and the i^{th} beam (see Figure 4.1), the total kinetic energy of the bay is:

$$\left\langle \overline{T} \right\rangle^{i} = \left\langle \overline{T} \right\rangle_{P}^{i} + \left\langle \overline{T} \right\rangle_{B}^{i} + \left\langle \overline{T} \right\rangle_{T}^{i}, \quad i = 1,2,...,(N+1), \tag{4.18}$$

where

$$\left\langle \overline{T} \right\rangle_{B}^{i} = \frac{1}{2}\int_{0}^{Ly} \rho_{Li}\dot{U}_i\dot{U}_i^{*}dy = \frac{\rho_{Li}\omega^2\Lambda_n}{2}\sum_n \left|\sum_m w_{m,n}\phi_m(x_i)\right|^2, \quad i = 1,2,3,...,N, \tag{4.19}$$

is the flexural vibration energy of the i^{th} beam, and

$$\left\langle \overline{T} \right\rangle_{T}^{i} = \frac{1}{2}\int_{0}^{Ly} \rho_{bi}I_{Pi}\dot{\theta}_i\dot{\theta}_i^{*}dy = \frac{\rho_{bi}I_{Pi}\Lambda_n\omega^2}{2}\sum_n \left|\sum_m w_{m,n}\phi'_m(x_i)\right|^2, \quad i = 1,2,3,...,N, \tag{4.20}$$

is the torsional vibration energy of the i^{th} beam, $\left\langle \overline{T} \right\rangle_{B}^{N+1} = \left\langle \overline{T} \right\rangle_{T}^{N+1} = 0$. ρ_{Li} is the mass per unit beam length and $\rho_{bi}I_{pi}$ is the mass moment of inertia per unit length of the i^{th} beam.

For periodic ribbed plates where the beams are well separated from each other, the vibration energy of each stiffened beam is only a very small part of the total vibration energy of the associated periodic bay. Therefore, the beam vibration energies are not included in the kinetic energy distribution of the corresponding periodic bay in the subsequent analyses.

4.6 Results and discussion

The finite periodic ribbed plate used in this simulation is composed of a simply supported rectangular plate with eight stiffened beams ($N = 8$), which are periodically distributed on the plate surface. The rectangular plate has a surface area of $S = 4.5 \times 1m^2$ and is $8mm$ thick. The beams have the uniform cross sectional area of $A_{bi} = b_i \times t_i = 50 \times 5mm^2$. A unit point force is applied at plate location

$(x_0, y_0) = (0.20m, 0.30m)$ in the first section (the source section) of the periodic ribbed plate. This excitation location is also used in all other simulations throughout this chapter. For better illustration of the "stop/pass band" characteristics of periodic systems, it is further assumed that the structural damping for the plate and the beams is negligible except in the calculation of input mobility of the periodic ribbed plate where a moderate damping value ($\eta = 0.03$) is assumed. The accuracy of the analytical solution is evaluated by comparing the predicted input mobility to that obtained from FEA analysis. Good agreement is found in the whole frequency range investigated (up to 1000Hz), which is shown in Figure 4.2.

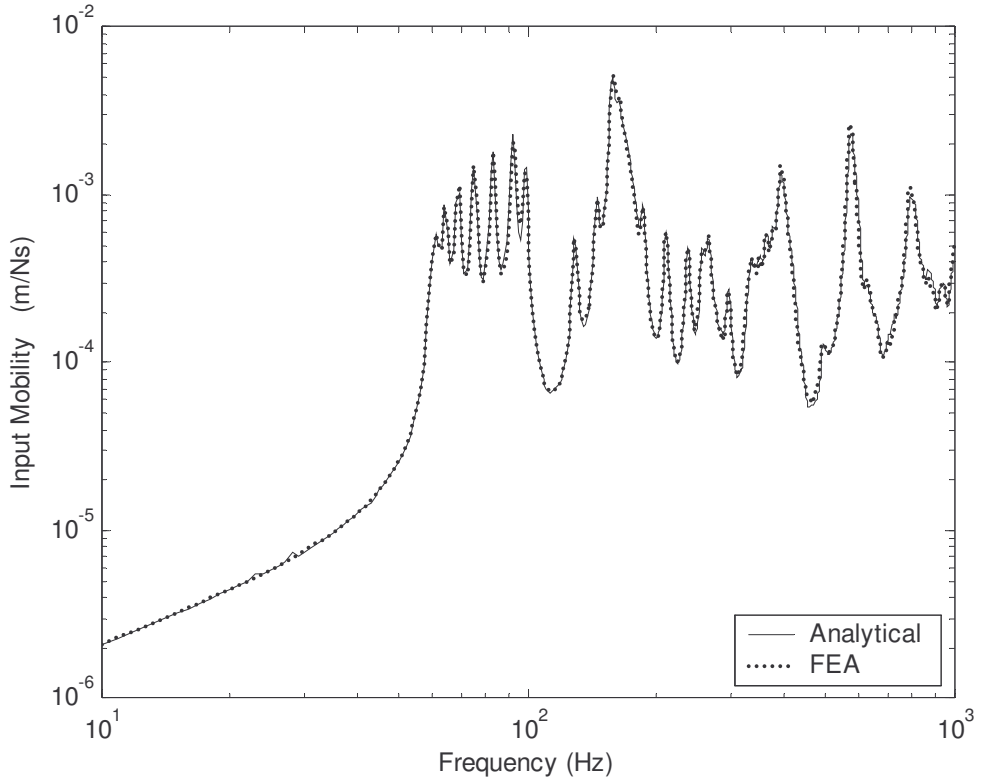

Figure 4.2. Point force input mobility of the finite periodic ribbed plate.

4.6.1 Vibration characteristics of finite periodic ribbed plates

Vibration characteristics of the finite periodic ribbed plate are studied by the kinetic energy distributions of periodic sections as shown in Figure 4.3. For clarity, only kinetic energy distributions of the odd number periodic bays are shown in the figure. Modal index numbers corresponding to peak responses in the enclosed pass bands of the ribbed plates are also given and shown in the figure for better understanding of vibration properties of the pass bands. There are two sets of wave propagation zones for the periodic ribbed plate due to the two coupling mechanisms (shear force and moment couplings) considered for the ribbed plate in the study (a so-called bi-coupled periodic system [45, 59]). The set associated with the shear force couplings at the interfaces is termed as ***F/F*** wave propagation zones. The other set (associated with the moment couplings) is termed as ***T/F*** wave propagation zones.

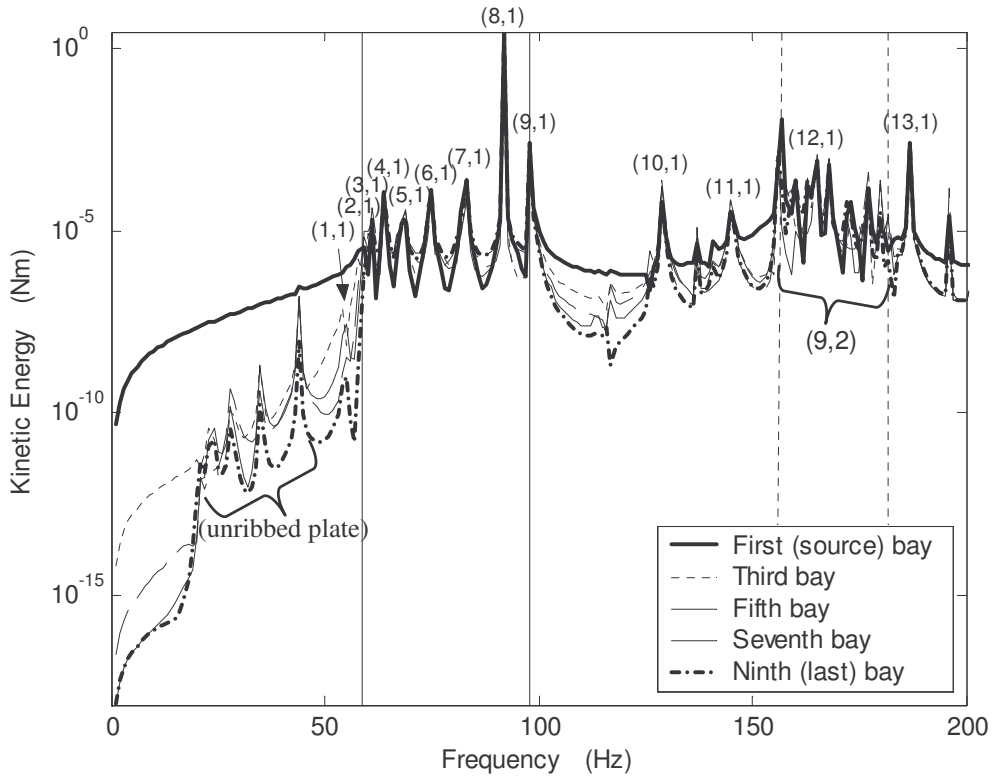

Figure 4.3. Vibration energy distributions of the odd number bays of the finite periodic ribbed plate.

It is found that each ***F/F*** propagation zone is characterized by one of the beam flexural modes. For example, the zones enclosed by the two vertical solid lines and the two vertical dotted lines are the first and the second ***F/F*** zones, which are governed respectively by $n = 1$ and $n = 2$ beam flexural modes. Modes in the first ***T/F*** zone are found to spread across the first ***F/F*** zone but below the lower bounding frequency of the second ***F/F*** zone attributed to the relatively small torsional stiffness of the ribs (i.e. a wider frequency band [45] of the ***T/F*** propagation zone). This group of modes can be identified by comparing the energy distribution of the last section of the periodic ribbed plate to that of the corresponding mono-coupled periodic ribbed plate (considering only shear force couplings at the interfaces by letting sub-matrices $[B]$ and $[C]$ in Equation (4.7) equal to zero) as shown in Figure 4.4.

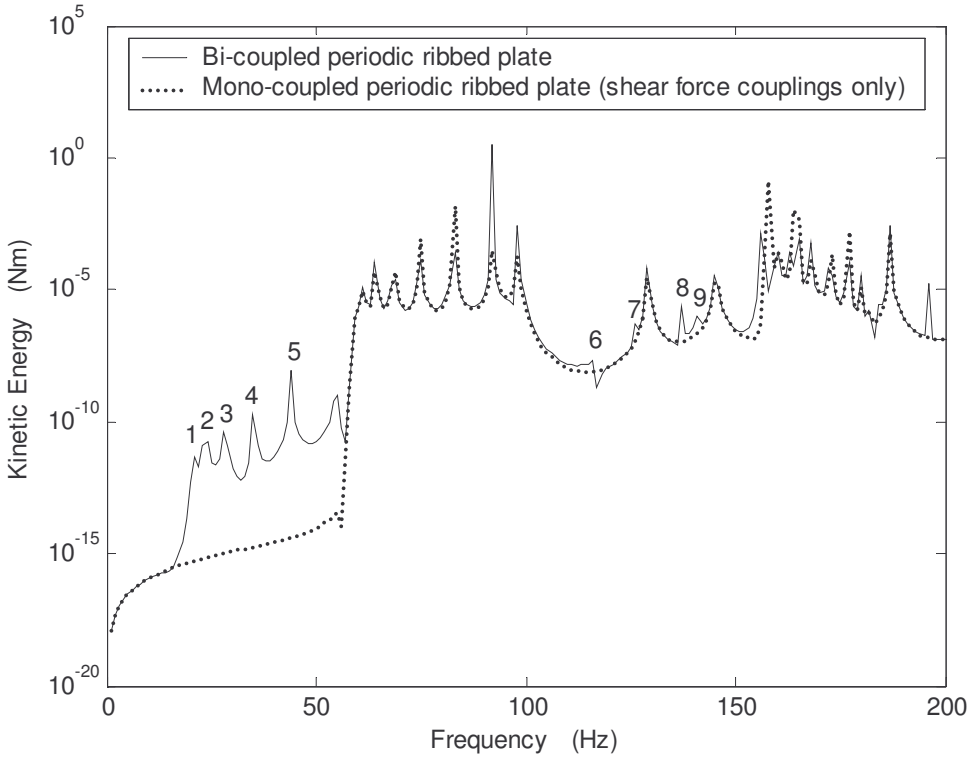

Figure 4.4. Kinetic energy distribution of the last plate section of the bi-coupled and the corresponding mono-coupled (shear force couplings only) periodic

There are eight peaks enclosed in the first $(n=1)$ ***F/F*** propagation zone (bounded by the two solid lines in Figure 4.3) with an addition peak lies just below the lower bounding frequency of the zone. This is typical for asymmetrical periodic systems [58, 59] (asymmetrical mass and stiffness distributions on the end boundaries of a periodic section with respect to the centre of the section). The peak lies outside of this zone is found to be a non-propagating mode corresponding to the trace wave number $k_{m'(m'=1)}$ where most vibration energy of the mode is confined in the source section of the periodic plate. On the other hand, the eight peaks enclosed in this zone can be approximated by modes of the corresponding orthotropic plate. For instance, these peak responses have the mode shape distributions of distorted sine waves corresponding to the trace wave number $k_{m'}$ ($m' = 2,3,...,9$) where m' is the number of distorted half wavelength along the plate edge L_x. An approximation method for representing the resonant modes of a finite periodic ribbed plate by those of an equivalent orthotropic plate is given by Wah [31]. It is worth noting that the resonant frequency for the peak at the upper bounding frequency of the zone ($k_{m'(m'=9)}$) overlaps with the frequency of the coincidence condition between the plate trace wavelength λ_x and the span of the periodic section Δx_i ($\lambda_{x(n=1)} = 2\Delta x_i$), where the plate trace wavelength λ_x is related to the trace wave number $k_x = \sqrt{k_p^2 - k_n^2}$ by $\lambda_x = \frac{2\pi}{k_x}$. For this mode, all stiffened beams are located exactly at the nodal locations of the mode so that effects of the beam flexural stiffness to the modal vibration of the plate are negligible. Therefore, the modal vibration (including both mode shape and resonance frequency) of the periodic ribbed plate at this peak frequency is identical to that of the corresponding un-ribbed plate.

There are nine peaks enclosed in the second ***F/F*** wave propagation zone (bounded by the two dotted vertical lines). All peaks in this zone have similar mode shape distribution with the distorted modal wave number $(m', n) = (9,2)$ except for the fourth peak, which has the modal wave number of $(m', n) = (12,1)$ as indicated in Figure 4.3. This mode and the other three modes ($(m', n) = (10,1), (11,1)$ and $(13,1)$) shown in Figure 4.3 are the higher order orthogonal plate modes after the modes in the first ***F/F*** zone, which do not belong to any pass bands defined by the classical periodic theory. Therefore, both periodic theory and orthogonal plate approximation are required for better explanation of modal response of finite periodic ribbed plates.

On the other hand, the modal frequencies of the nine peak responses marked by the serial numbers in Figure 4.4 are near the resonant frequencies of the corresponding un-ribbed plate. For instance, the frequencies of the first five peak responses of the periodic ribbed plate (marked by 1-5 in Figure 4.4) match the first five fundamental resonance frequencies of the corresponding un-ribbed plate. This is attributed to the inclusion of moment couplings in the mathematical model of the finite periodic ribbed plate, which results in the non-zero numerator in Equation (4.16) when $G_{m,n}$ goes to zero (i.e. the resonance of the corresponding un-ribbed plate). In contrast, the numerator in Equation (4.16) would also tend to zero when $G_{m,n}$ goes to zero if only shear force couplings are considered (with the exception where all beams are located at the nodal positions of the vibrating modes of the un-ribbed plate). Therefore, for a mono-coupled periodic ribbed plate considering only shear force couplings at the interfaces, peak responses would not be formed at these frequencies resulting from the l'Hospital's rule (see Figure 4.4).

By definitions, the marked peak responses in Figure 4.4 constitute to the first ***T/F*** wave propagation zone of the finite periodic ribbed plate because wave propagation

for these peak responses is governed by moment couplings at the interfaces. The mode shape distributions for some of these peak responses can be traced back to the modal responses of the corresponding un-ribbed plate at the same frequencies. Others are largely distorted from those of the corresponding un-ribbed plate, which are difficult to describe by numerical modal indices. For peak responses in ***T/F*** wave propagation zones, the modal vibration energy is largely confined in the source section of the ribbed plate attributed to the attenuation of the plate bending wave when it propagates through the rib at the section's boundary (i.e. large beam flexural stiffness at low frequencies). The remaining part of vibration energy after the attenuation can propagate freely to other sections of the periodic ribbed plate via moment couplings at the interfaces (wave propagates at same incident angles).

4.6.2 Vibration confinements

Vibration confinement of finite periodic disorder ribbed plates is studied here for three cases: (a) single beam spacing disorder to simulate the disorder of the periodic ribbed plate resulting from installation errors; (b) single beam cross section disorder to simulate the disorder of periodic ribbed plates due to manufacturing imperfections and (c) random beam spacing irregularity for better understanding of vibration localization of irregular ribbed plates.

a) Single beam spacing disorder

In this simulation, the location of the first beam of the ribbed plate is shifted from $x_1 = 0.5m$ to two disorder locations at $x_1 = 0.3m$ and $x_1 = 0.7m$ in two separate calculations. The other properties of the ribbed plate remain the same as in the periodic case. Effects of the disorders to vibration energy propagation of the ribbed

plate are studied by comparing the kinetic energy distributions of the last plate section for both periodic and disorder cases, which are shown in Figure 4.5.

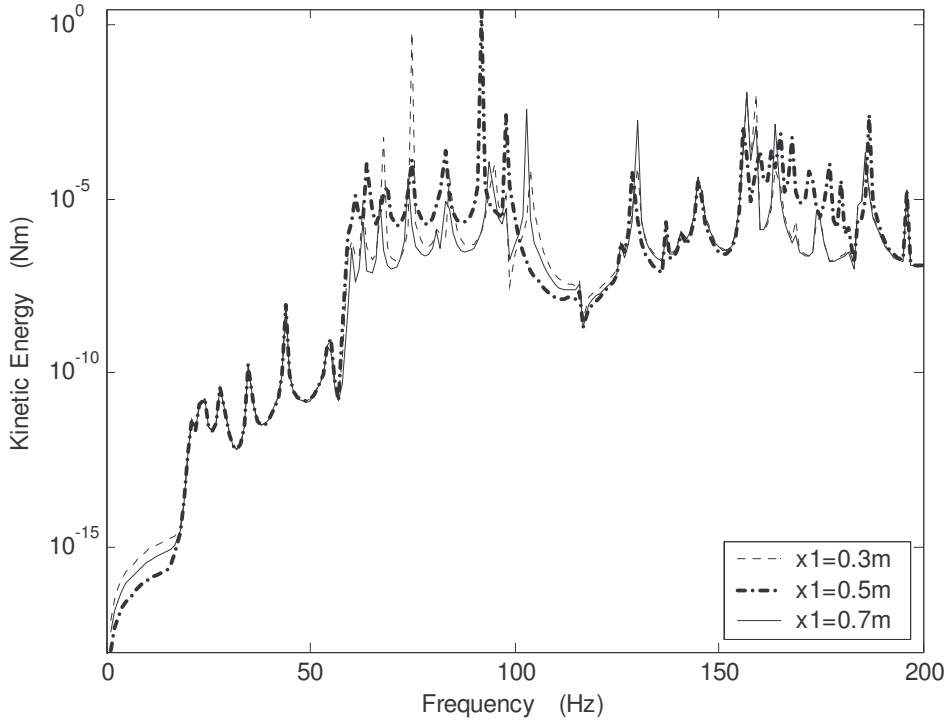

Figure 4.5. Kinetic energy distributions of the last plate section of the finite periodic and disordered ribbed plates.

It is shown that the disorder mainly affects the vibration response of the ***F/F*** propagation zones of the ribbed plate. Although it leads to general vibration reduction in the ***F/F*** zones, it also causes increase modal amplitude for some individual peaks in the zones. Such interesting phenomenon is attributed to the effect of beam locations on the modal vibration of the ribbed plate. For example, when the location of the disordered beam is moved to or close to the anti-nodal position(s) of a resonant mode, the flexural stiffness of the disordered beam would have greater influence on the modal stiffness of the mode, which increases the resonance frequency and decreases the response amplitude of the mode. On the contrary, when the location of the disordered beam is shifted to the nodal position of the vibrating

mode, the modal stiffness of a mode would decrease correspondingly. One example given here is the peak with the largest vibration amplitude in the first ***F/F*** propagation zone for the periodic case (The peak marked by $(8,1)$ in Figure 4.3). The mode shape distribution of this mode (calculated at $y = 0.3m$) in the periodic case is shown in Figure 4.6(a), which is corresponding to the $(8,1)^{th}$ mode of an equivalent orthotropic plate. The mode shape distributions of this mode in the disorder cases are shown in Figure 4.6(b). It is illustrated that the resonance frequency of the mode increases respectively from $92Hz$ to $95Hz$ and $94Hz$ in the two disorder cases because the location of the disordered beam is shifted from the position closed to the nodal location to positions closed to the anti-nodal position of the mode. Concurrently, the vibration amplitude of the mode decreases significantly from that in the periodic case. The frequency bandwidth of the ***F/F*** zone also increases after the disorder due to the same effect. For instance, because the flexural stiffness of the disordered beam also contributes to the modal vibration of the $(m', n) = (9,1)$ mode after the disorder, the upper bounding frequency of the zone increase following the increase resonance frequency of the mode. The vibration amplitude of a mode usually decreases following the increase modal stiffness, however, this is not always the case for the disorder periodic ribbed plate as illustrated in Figure 4.5. Moving the position of the first beam away from the corresponding periodic location not only changes the modal stiffness of the ribbed plate (a global stiffness quantity) but also changes the local stiffness of the source plate section. For instance, the bending rigidity of the first plate section decreases due to the increase area of the section after moving the position of the first beam from $x_1 = 0.5m$ to $x_1 = 0.7m$. This changes the ability of the source plate section in accepting the power injected by the point force. As a result, the input power by the point force increases attributed to the decrease bending rigidity of the section. The increase input power then propagates to the

energy flow to the other plate sections of the ribbed plate, which results to the increase kinetic energy of last plate section.

On the contrary, it is found that the disorder has little effects on the vibration response for modes in ***T/F*** zones since wave propagation for modes in these zones is governed by moment coupling mechanism at the interfaces, which is not affected by the disorders. The discussions presented herein shed some lights on the principle of vibration confinement in periodic ribbed plates. However, vibration localization is not well illustrated, which is discussed further in the subsequent analysis.

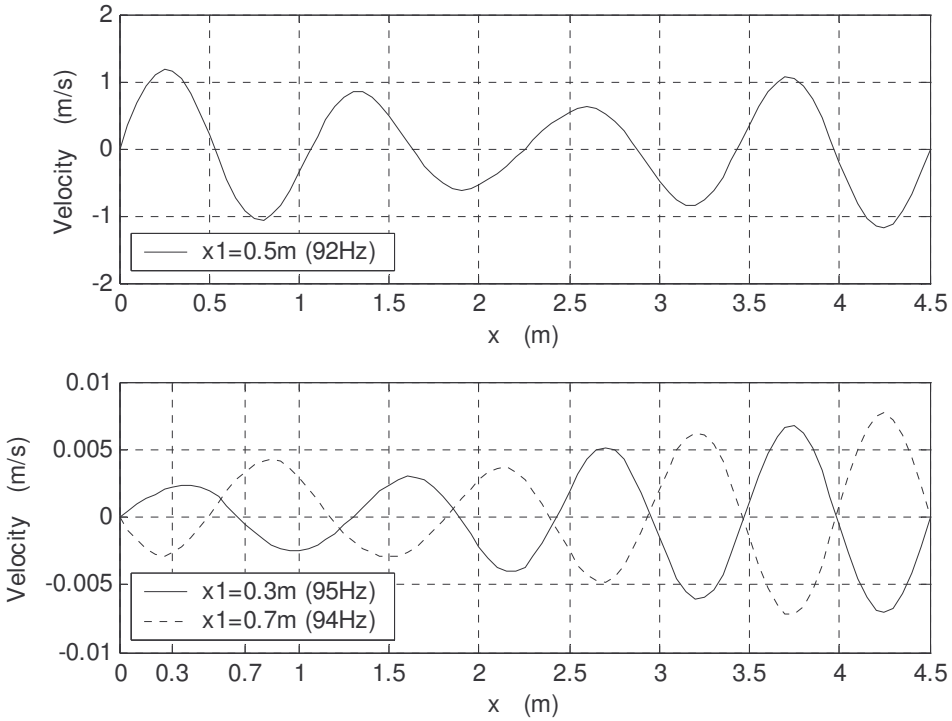

Figure 4.6. Mode shape distribution of the vibration mode $(m', n) = (8, 1)$ of the ribbed plate calculated at $y = 0.3m$. Top: periodic; Bottom: disordered.

a) Single beam cross section disorder

The cross section area of the first beam (at x_1) of the finite periodic ribbed plate is replaced by $A_{b1} = 80 \times 5mm^2$ and $A_{b1} = 30 \times 5mm^2$ in two separate calculations while the other properties of the ribbed plate remain the same as in the periodic case. The

kinetic energy distributions of the last plate section for both periodic and disorder cases are shown in Figure 4.7. It is found that effects of the disorder to vibration response of the ribbed plate are more significant by increasing the cross section area of the disordered beam. Besides the vibration reduction found in previous disorder case, vibration reduction resulting from beam cross section area disorder also extends to modes in the ***T/F*** propagation zones attributed to beam torsional stiffness irregularity of the ribbed plate. It is also noted that the upper bounding frequency of the first ***F/F*** propagation zone is not affected by the disorder since the modal response of the $(m', n) = (9,1)$ mode is not affected by changing the flexural and torsional stiffness of the beams.

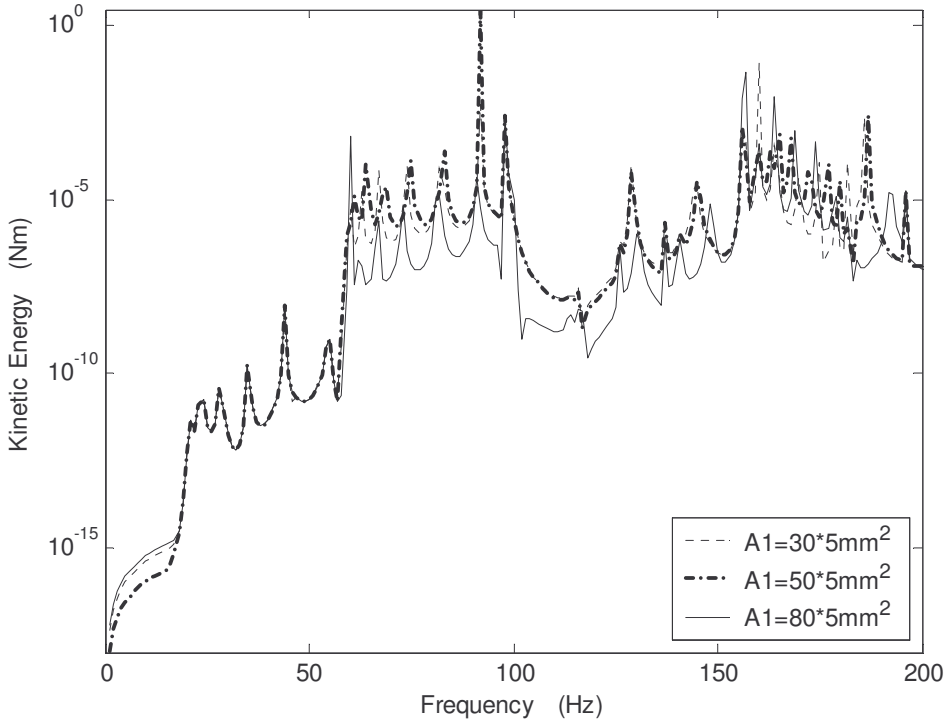

Figure 4.7. Vibration energy distributions of the last section of the finite periodic and disordered ribbed plates.

b) Irregular beam spacing

For better illustration of the Anderson localization phenomenon in a finite ribbed plate, the surface area of the plate is enlarged to $S = 36 \times 1m^2$ while the eight

stiffened beams are irregularly distributed on the plate surface and have a mean beam spacing of $4m$. The fluctuations of the beam locations are restricted to no more than half of the mean beam spacing away from the periodic locations and to ensure a random phase factors $\exp(jk_p\Delta x_i)$ [69] in the simulation. The exact locations of the beams in the simulation are shown in the mode shape plots in Figures 4.9 and 4.10. Furthermore, the span of the last plate section of the irregularly ribbed plate is deliberately kept to be the same as in the periodic case so that the energy distributions of this section for both periodic and irregular cases are comparable, which are shown in Figure 4.8.

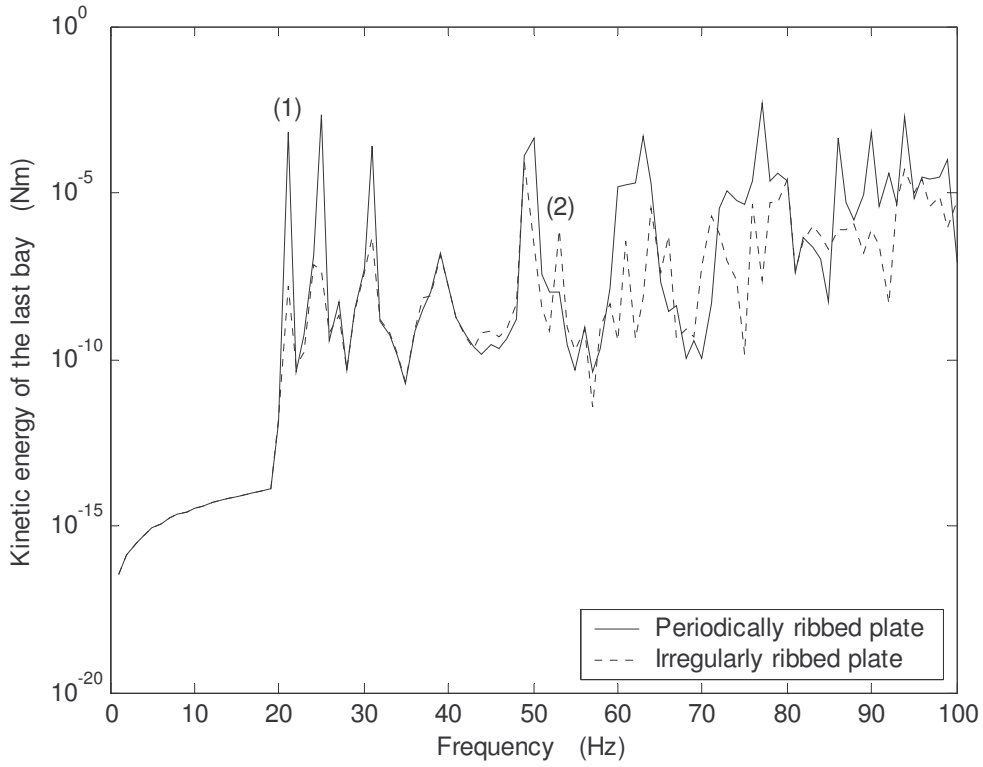

Figure 4.8. Kinetic energy distributions of the last plate section for the periodically and the irregularly ribbed plates.

It is showed that the irregularity has resulted in vibration localization for most of the modes in this frequency range. The modes localized by the irregularity are found to be modes in the ***F/F*** wave propagation zones and the unconfined modes are modes

in the ***T/F*** wave propagation zones. This is because only modes in the ***F/F*** zones depend upon beam locations and the beam flexural stiffness but not the modes in the ***T/F*** zones whose modal vibration depends only on the moment couplings at the beam/plate interfaces.

The mode shape distributions for the two modes marked in Figure 4.8 are shown in Figures 4.9 and 4.10 to provide further explanations of the phenomenon. It is illustrated in Figure 4.9 that the modal vibration of the first selected mode (marked by (1) in Figure 4.8) is largely confined in the source section of the ribbed plate by the irregularity since the mode is in ***F/F*** zones. In contrast, it is shown in Figure 4.10 that the vibration of the other selected mode (marked by (2) in Figure 4.8) is not localized by the irregularity since they are modes in the ***T/F*** zones. For modes in the ***T/F*** zones, the vibration energy can propagate over a long distance via the moment couplings at the beam/plate interfaces and is independent of the beam spacing. Furthermore, because of local resonance [69] resulting from the spatial matching between the plate trace wavelength λ_x and the span of a plate section, the plate section away from the source section in the irregularly cases can have higher modal energy than those of plate sections closer to the source. This explains why the last section of the irregularly ribbed plate can have higher modal energy than that of the corresponding plate section in the periodic case for modes in ***T/F*** zones as indicated in Figure 4.8.

Therefore, it can be concluded that random beam spacing irregularity on a ribbed plate can only generate vibration localization for modes in the ***F/F*** wave propagation zones but not for modes in the ***T/F*** wave propagation zones. To localize the modes in the ***T/F*** wave propagation zones, torsional stiffness irregularity of the beams needs also be imposed.

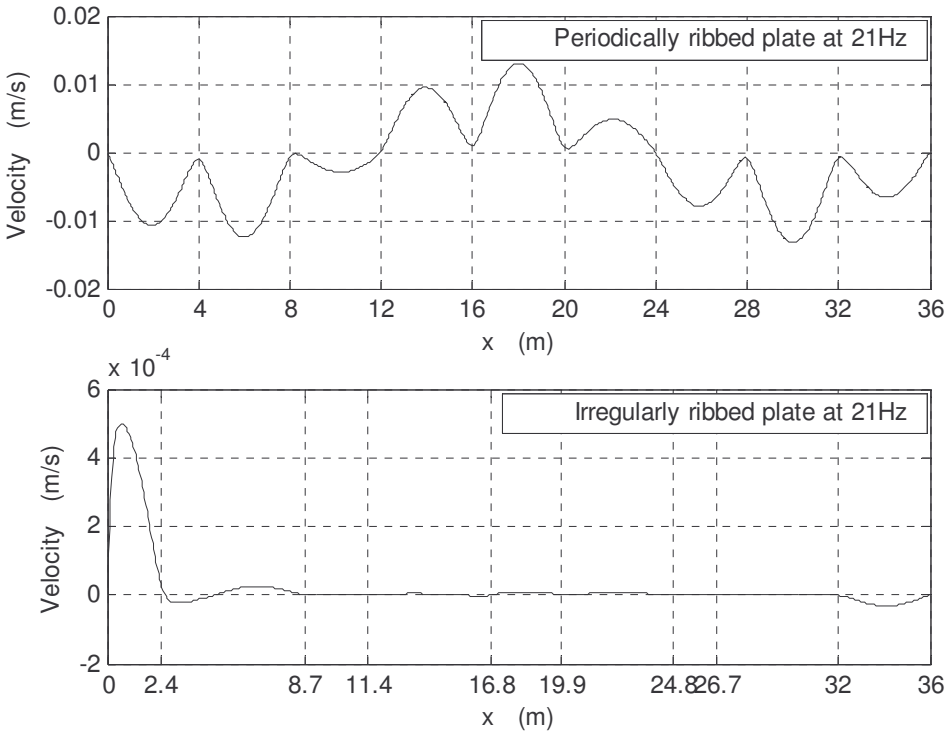

Figure 4.9. Mode shape distributions of the ribbed plate at 21Hz calculated at $y = 0.3m$. Top: periodic ribbed plate; Bottom: irregularly beam spacing ribbed plate.

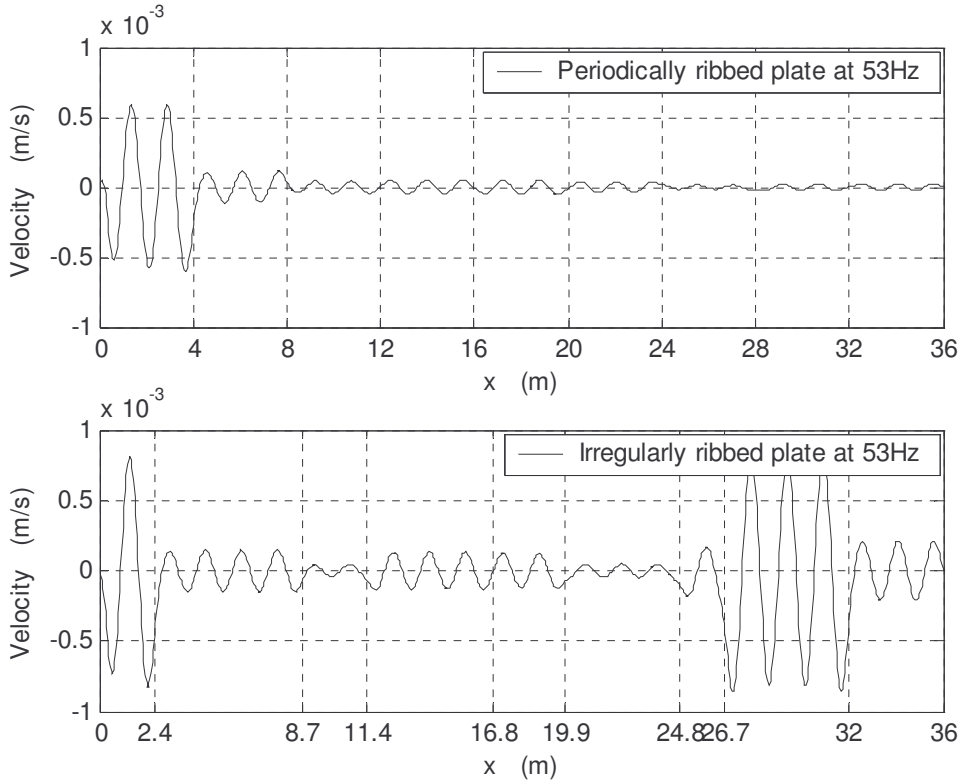

Figure 4.10. Mode shape distributions of the ribbed plate at 53Hz calculated at $y = 0.3m$. Top: periodic ribbed plate; Bottom: irregularly beam spacing ribbed plate.

4.7 Conclusion

An analytical solution is obtained in this chapter to predict the vibration response of finite periodic and irregular ribbed plates to point force excitations by employing the well-known modal expansion solution. The solution is then used to study the general properties of the finite periodic ribbed plate and vibration confinement of finite periodic disorder and irregular ribbed plates.

Physical interpretation is given to the bounding frequencies and peak responses in the pass bands of the finite periodic ribbed plate. It is found that each ***F/F*** wave propagation zone is dominated by one beam flexural wave number (k_n). Modes in the first (***F/F***) pass band ($n=1$) can be approximated by those of the corresponding orthotropic plate while modes in the second (***F/F***) pass band ($n=2$) all have similar mode shape distribution corresponding to the modal wave number $(m',n)=(9,2)$. The resonance frequencies for modes in the ***T/F*** bands are closed to the resonances frequencies of the corresponding un-ribbed plate although mode shape distributions for this group of modes are often difficult to describe by numerical modal indices.

The study also shows that general vibration reduction can be achieved by imposing a single periodic disorder to the ribbed plate attributed to the effect of disorders on the modal responses of the ribbed plate. It is illustrated that the random beam spacing irregularity of a ribbed plate can only localize the modes associated with the flexural couplings at the beam/plate interfaces but not the modes associated with the torsional couplings at the interfaces of the ribbed plate. To localize the modes in the latter group, one needs to apply torsional stiffness irregularity to the stiffened beams.

Chapter 5

Closed form solutions for the vibration response of an L-shaped plate

5.1 Introduction

In previous chapters, only one category of structural couplings, i.e. beam/plate couplings were considered in the analysis of vibration response of coupled structures. Nevertheless, another type of structural couplings, i.e. plate/plate couplings are equally important in engineering applications such as in the ship building industry. The plate/plate coupling is considered in this chapter through the study of vibration response of an L-shaped plate.

A common approach for vibration analysis of plate/plate coupling structures is SEA when the band-averaged quantities are the main concern. However, the validity of SEA is often questionable in the low and medium frequency ranges where modal overlap is low. Furthermore, SEA also assumes broadband random excitations of statistically independent forces while in practical applications, excitation forces often appear in deterministic forms. For coupled structures under deterministic force excitations, there is a great tendency nowadays to use the numerical method of FEA analysis. The disadvantage of FEA analysis is that it provides no explicit understanding of the structural response in relation to structural properties and the excitations. In addition, FEA analysis becomes extremely cumbersome in the medium and high frequency ranges where large numbers of modes are required in the calculation and the detailed information of boundary conditions is difficult to obtain. Besides SEA and FEA analysis, other analytical methods have also been developed, which are briefly reviewed in the following section.

5.2 Literature review

Plate/plate coupled structures are often encountered in engineering applications where plates are coupled to form an integral engineering structure, such as a ship hull or a transformer. Guyader and co-workers [73, 74] studied the vibration response of finite plates coupled at L, T and cross junctions by the wave guide approach. The wave coefficients from propagation wave solutions are determined from matrix inversions. Cuschieri [75] obtained a closed form solution to predict the coupled power transmission of an L-shaped plate using a mobility power flow approach. By including the in-plane waves in plates, Cuschieri and McCollum [76] expanded the analysis further by studying the vibration response of an L-shaped plate in both thin and thick plate models. Kessissoglou [77] investigated the vibration response of coupled plate structures by employing the wave guide approach where the in-plane contributions to the power flow of the coupled plate structure in the low and in the high frequency ranges were discussed. She observed that at low frequencies, the inclusion of in-plane waves has the effect of increasing the total power at structural resonances. Effects of in-plane waves to the total power increase as frequency increases where in-plane waves can act as efficient transmitters of flexural energy through plate/plate junctions. By employing propagation wave approaches, Wester and Mace [78] studied the validity of SEA in a wave guide system comprising two coupled simply supported rectangular plates. Two wave parameters (reflectance and transmission coefficients) were found to quantify the coupling strength between plates as weak, strong and very strong. It was found that the coupling loss factor estimated based on the classical SEA assumptions of semi-infinite subsystems and diffuse field only holds for the finite coupled system when the coupling strength is weak. It was noted that the coupling strength and the accuracy of coupling loss factor between two finite coupled plates could not be indicated by modal overlap of the system.

By assuming that all of the plate edges including the coupled plate/plate junction are simply supported, Dimitriadis and Pierce [79] obtained a closed form solution for the vibration response of two rectangular plates coupled at right angles by utilizing the modal expansion method (MEM). The solution was then used to extract the 'apparent' quantities that correspond to the coupling loss factor and modal density ratio used in SEA.

By including both in-plane and flexural vibrations of plates in the analysis, Rebillard and Guyader [80] obtained an analytical solution for predicting the response of finite plates coupled at arbitrary angles by using the wave guide approach. They showed that the effect of angular defects on the vibration behaviours of coupled plate structures depends on the value of coupling angles. A small angle defect can lead to a large variation of response when the angle between two coupled plates is small. On the contrary, large modification of the angle has little effect on the response when the angle of two coupled plates is large. By employing modal receptance formulations, Farag and Pan [81], Farag [82] studied the vibration response of two finite plates coupled at arbitrary angles where the flexural, shear and in-plane wave components of the plates were included in a single matrix formulation. They observed that the coupling of the two plates is dominated by the moment coupling at frequencies up to the cut-off frequency of the first in-plane mode and is controlled by out-of-plane shear and in-plane vibrations at frequencies above this frequency. Most recently, Wang et al [83] employed an approach similar to Farag and Pan [81] for solving the dynamic response of an L-shaped plate to point force excitation. They studied the power flow characteristics of the L-shaped plate and found that the energy flow from the source to the receiving plate along the coupling edge is not always positive. The

direction of energy flow at different locations on the coupling edge depends upon the relative phase between the internal force and velocity response at the location.

Although some typical SEA parameters of coupled plate structures have been evaluated in the literature [78, 79], the validity of SEA in the prediction of vibration response of plate/plate coupling structures due to deterministic force excitations has never been examined, which forms the main objective of this study.

Vibration of plate/plates coupled structures by including both in-plane and flexural wave motions in the analysis has been reported in many literatures [76, 77, 80-82]. It was found that the contribution of in-plane vibration to the power transmission of an L-shaped plate is only significant at higher frequencies [76, 77]. In-plane wave motions were also ignored by Nilsson [84] in the study of wave propagation in a scaled model of ship structures where only flexural wave propagation in ship structures was considered. The calculation results agreed well with experiment. Bercin [85] also showed that in-plane contributions to energy flow of simple coupled plate structures, i.e. an L-shape plate is insignificant. As a result, in-plane vibration of the plates is not considered in this study where the shear force coupling at the plate/plate junction is ignored. The analysis then focuses on the derivation of a simple closed form solution to predict the vibration response of two rectangular plates coupled at right angles (an L-shaped plate) due to point force or moment excitations. The solutions are used to examine the validity of SEA in the prediction of the vibration response and coupling energy flow of a plate/plate coupled structure under deterministic force excitations.

5.3 Closed form solutions

5.3.1 Formulation

The L-shaped plate and the associated coordinate system are shown in Figure 5.1. It is assumed that all of the plate edges other than the coupled plate/plate junction are simply supported. Using thin plate vibration models, the governing equations for the flexural displacements (W ,U) of the source and the receiving plates to a point force excitation (F_p) applied at plate location (x_0, y_0) are given by:

$$\nabla^4 W + k_{p1}^4 W = \frac{F_p}{D_1}\delta(x - x_0)\delta(y - y_0), \tag{5.1}$$

and

$$\nabla^4 U + k_{p2}^4 U = 0, \tag{5.2}$$

where k_{p1} and k_{p2} are respectively the bending wave numbers, D_1 and D_2 are the bending rigidity of the source and the receiving plates.

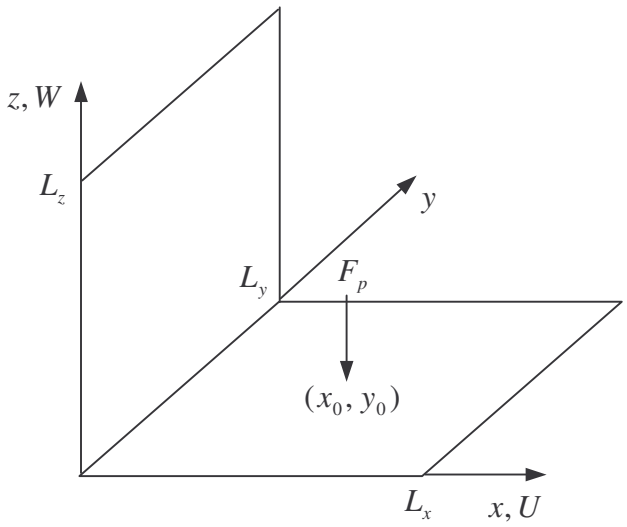

Figure 5.1. Model description and the coordinate system of the L-shaped plate.

Equations (5.1) and (5.2) can be solved by wave guide approaches similar to that described in Chapter 2. However, when the calculation domain of the source plate is

large (i.e. L_x is large), the exponential terms associated with the travelling wave solutions of the source plate can have extremely large or small values, which can lead to numerical overflow problems [80]. To overcome such problems, the sub-domain method suggested by Rebillard and Guyader [80] is also adopted in this analysis where the source plate is partitioned into three sub-domains as shown in Figure 5.2. After partitioning, the source location becomes (x_0^a, y_0) in the local coordinate system of the source plate section.

The wave-guide solutions for the flexural displacements of the three calculation sub-domains of the source plate give:

$$W_1 = \sum_n (A_{1n}e^{-k_{n1}(L_{x1}-x_I)} + A_{2n}e^{-k_{n1}x_I} + A_{3n}e^{-k_{n2}(L_{x1}-x_I)} + A_{4n}e^{-k_{n2}x_I})\phi_n(y), \quad 0 \le x_I \le L_{x1}, \tag{5.3}$$

$$W_{2_I} = \sum_n (A_{5n}e^{-k_{n1}(L_{x2}-x_{II})} + A_{6n}e^{-k_{n1}x_{II}} + A_{7n}e^{-k_{n2}(L_{x2}-x_{II})} + A_{8n}e^{-k_{n2}x_{II}})\phi_n(y), \quad 0 \le x_{II} \le x_0^a, \tag{5.4}$$

$$W_{2_{II}} = \sum_n (A_{9n}e^{-k_{n1}(L_{x2}-x_{II})} + A_{10n}e^{-k_{n1}x_{II}} + A_{11n}e^{-k_{n2}(L_{x2}-x_{II})} + A_{12n}e^{-k_{n2}x_{II}})\phi_n(y), \quad x_0^a \le x_{II} \le L_{x2}, \tag{5.5}$$

and

$$W_3 = \sum_n (A_{13n}e^{-k_{n1}(L_{x3}-x_{III})} + A_{14n}e^{-k_{n1}x_{III}} + A_{15n}e^{-k_{n2}(L_{x3}-x_{III})} + A_{16n}e^{-k_{n2}x_{III}})\phi_n(y), \quad 0 \le x_{III} \le L_{x3}, \tag{5.6}$$

where $\phi_n(y) = \sin(k_n y)$, $k_{n1} = \sqrt{k_n^2 + k_{p1}^2}$ and $k_{n2} = \sqrt{k_n^2 - k_{p1}^2}$.

Similarly, the wave-guide solution for the flexural displacement of the receiving plate gives:

$$U = \sum_n (A_{17n}e^{-k_{n3}(L_z-z)} + A_{18n}e^{-k_{n3}z} + A_{19n}e^{-k_{n4}(L_z-z)} + A_{20n}e^{-k_{n4}z})\phi_n(y), \quad 0 \le z \le L_z, \tag{5.7}$$

where $k_{n3} = \sqrt{k_n^2 + k_{p2}^2}$, $k_{n4} = \sqrt{k_n^2 - k_{p2}^2}$.

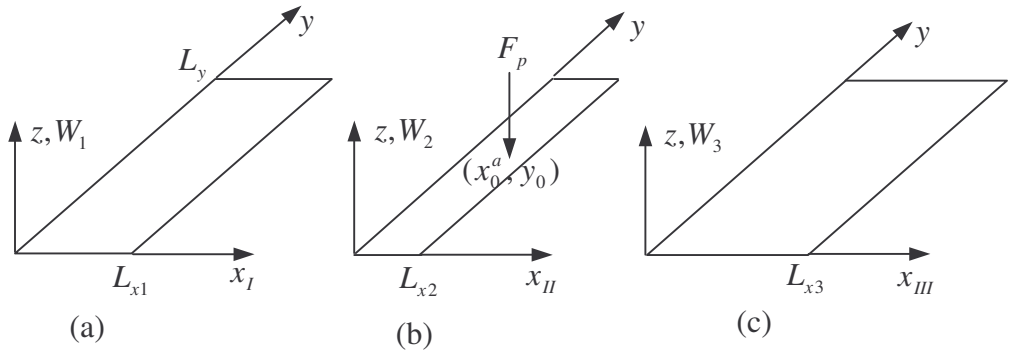

Figure 5.2. The three sub-domains of the source plate after partitioned.

5.3.2 Point force excitation

Traditionally, the wave coefficients from travelling wave solutions are determined via matrix inversions [73, 80]. In contrast, they are given by analytical expressions in this study so that vibration responses of the coupled structure can be expressed explicitly in terms of structural properties of the coupled structure and the driving force, with no matrix inversion required in the solution.

a) Analytical expressions for the wave coefficients

To derive analytical expressions for the wave coefficients, it is convenient to replace the receiving plate with a coupling boundary condition on the source plate. This is done by first utilizing the simply supported boundary conditions at $z = L_z$ and the zero flexural displacement of the receiving plate at the plate/plate coupling junction ($z = 0$) so that the first three wave coefficients in Equation (5.7) can be expressed in terms of the fourth wave coefficient of the receiving plate as:

$$A_{17n} = c_{21}\beta A_{20n},\ A_{18n} = -\beta A_{20n},\ A_{19n} = -c_{22}A_{20n}, \tag{5.8}$$

where $\beta = \dfrac{1-c_{22}^2}{1-c_{21}^2}$, $c_{21} = e^{-k_{n3}L_z}$ and $c_{22} = e^{-k_{n4}L_z}$ are the exponential wave constants for given frequencies and component wave number k_n.

Furthermore, by using the two coupled boundary conditions at the plate/plate junction ($\left.\frac{\partial W_1}{\partial x_I}\right|_{x_I=0} = \left.\frac{\partial U}{\partial z}\right|_{z=0}, \left.\left(\frac{\partial^2 W_1}{\partial x_I^2} + \nu\frac{\partial^2 W_1}{\partial y^2}\right)\right|_{x_I=0} = -r\left.\left(\frac{\partial^2 U}{\partial z^2} + \nu\frac{\partial^2 U}{\partial y^2}\right)\right|_{z=0}$, $r = \frac{D_2}{D_1}$), the fourth wave coefficient of the receiving plate can be cancelled out to form a new boundary condition in terms of the wave coefficients of the source plate only, which is given by:

$$(\Delta_2 - \Delta_1)A_{1n}c_1 - (\Delta_2 + \Delta_1)A_{2n} + (\Delta_2 H_1 - \Delta_1 H_1^2)A_{3n}c_2 - (\Delta_2 H_1 + \Delta_1 H_1^2)A_{4n} = 0, \quad (5.9)$$

where $\Delta_1 = [H_3\beta(1+c_{21}^2) - H_4(1+c_{22}^2)]$, $\Delta_2 = r(H_3^2 + H_4^2)(1-c_{22}^2)$. The exponential wave constants c_1 and c_2 are the same as defined in Chapter 2, $H_1 = \frac{k_{n2}}{k_{n1}}$, $H_2 = \frac{k_{n4}}{k_{n3}}$, $H_3 = \frac{k_{n3}}{k_{n1}}$ and $H_4 = \frac{k_{n4}}{k_{n1}}$ are the wave number ratios.

Equation (5.9) together with the boundary condition ($W_{1(x_I=0)} = 0$) at the plate/plate junction provides the two essential boundary conditions for the plate edge of the source plate at $x_I = 0$. Combining Equation (5.9) with other boundary conditions of the source plate (see *Appendix C*), and after some tedious mathematical manipulations, one has:

$$A_{3n} = \frac{\alpha_2\gamma_2 - \alpha_3\gamma_1}{\alpha_2 - \alpha_1\alpha_3}F_n, \quad (5.10)$$

and

$$A_{4n} = \frac{\gamma_1 - \alpha_1\gamma_2}{\alpha_2 - \alpha_1\alpha_3}F_n, \quad (5.11)$$

where $F_n = \frac{F_p\phi_n(y_0)}{4D_1\Lambda_n k_{n1}k_{p1}^2}$, $\gamma_1 = c_6 - \frac{c_3^2c_9^2}{c_6}$, $\gamma_2 = \frac{c_8}{H_1} - \frac{c_4^2c_{10}^2}{c_8H_1}$, $\alpha_1 = \Theta_1 + c_1c_3^2c_9^2\Theta_3$, $\alpha_2 = \Theta_2 + c_1c_3^2c_9^2\Theta_4$, $\alpha_3 = c_2c_4^2c_{10}^2$. The constants c_3 and c_4 are the same as defined in

Chapter 2 while $c_5 = e^{-k_{n1}(L_{x2}-x_0^a)}$, $c_6 = e^{-k_{n1}x_0^a}$, $c_7 = e^{-k_{n2}(L_{x2}-x_0^a)}$, $c_8 = e^{-k_{n2}x_0^a}$, $c_9 = e^{-k_{n1}L_{x3}}$ and $c_{10} = e^{-k_{n2}L_{x3}}$. The other four constants are defined by:

$$\Theta_1 = \frac{(1+H_1)[\Delta_2 + \Delta_1(1-H_1)]\,c_2}{2\Delta_2 c_1},\ \Theta_2 = \frac{(1-H_1)[\Delta_2 + \Delta_1(1+H_1)]}{2\Delta_2 c_1},$$

$$\Theta_3 = \frac{(1-H_1)[\Delta_2 - \Delta_1(1+H_1)]\,c_2}{2\Delta_2},\ \Theta_4 = \frac{(1+H_1)[\Delta_2 - \Delta_1(1-H_1)]}{2\Delta_2}. \tag{5.12}$$

Analytical expressions for other wave coefficients can be obtained by utilizing the inter-relationships between the wave coefficients as well as Equations (5.10) and (5.11) and are given in *Appendix C*.

b) Input mobility

The point force input mobility of the L-shaped plate can be calculated directly from Equation (5.4). It is given here in terms of the first four wave coefficients of the source plate as:

$$Y_{in}^F = j\omega\frac{W(x_0,y_0)}{F_p} = \frac{j\omega}{F_p}\sum_n\left(\frac{1}{c_6}A_{1n} + c_1c_6A_{2n} + \frac{1}{c_8}A_{3n} + c_2c_8A_{4n}\right)\phi_n(y_0). \tag{5.13}$$

Alternatively, the input mobility can be expressed in terms of structural properties of the coupled plates by substituting the analytical expressions of the wave coefficients into Equation (5.13) to give:

$$Y_{in}^F = \frac{j\omega}{4D_1\Lambda_n k_{p1}^2}\sum_n\frac{\phi_n^2(y_0)}{k_{n1}}\left(\frac{\alpha_2\gamma_2 - \alpha_3\gamma_1}{\alpha_2 - \alpha_1\alpha_3}R_1 + \frac{\gamma_1 - \alpha_1\gamma_2}{\alpha_2 - \alpha_1\alpha_3}R_2\right), \tag{5.14}$$

where $R_1 = \frac{1}{c_8} - \left(\frac{1}{c_6}\Theta_1 + c_1c_6\Theta_3\right)$, $R_2 = c_2c_8 - \left(\frac{1}{c_6}\Theta_2 + c_1c_6\Theta_4\right)$.

c) Vibration energy flow

The power injection to the system by the point force can be calculated from Equation (5.14) as:

$$\left\langle \overline{P}_{in} \right\rangle = \frac{\left|F_p\right|^2}{2}\mathrm{Re}(Y_{in}^F) = -\frac{\omega\left|F_p\right|^2}{8\Lambda_n}\mathrm{Im}[\frac{1}{D_1 k_{p1}^2}\sum_n \frac{\phi_n^2(y_0)}{k_{n1}}(\frac{\alpha_2\gamma_2-\alpha_3\gamma_1}{\alpha_2-\alpha_1\alpha_3}R_1+\frac{\gamma_1-\alpha_1\gamma_2}{\alpha_2-\alpha_1\alpha_3}R_2)]. \tag{5.15}$$

It is illustrated in Equation (5.15) that input power of the L-shaped plate is mainly controlled by structural properties of the source plate.

The time averaged, steady state energy flow from the source plate to the receiving plate can be calculated by:

$$\left\langle \overline{P}_{12} \right\rangle = \frac{1}{2}\mathrm{Re}\int_0^{Ly} M_y(0,y)\dot{\theta}_y^*(0,y)\,dy, \tag{5.16}$$

where M_y and $\dot{\theta}_y$ are respectively the moment and angular velocity distributions along the plate/plate junction.

Moreover, the moment distribution at the plate/plate junction is evaluated by:

$$\begin{aligned} M_y(0,y) &= D_1(\frac{\partial^2 W}{\partial x_I^2}+\nu\frac{\partial^2 W}{\partial y^2})_{x_I=0} \\ &= -\frac{F_p}{2\Lambda_n}\sum_n \frac{\phi_n(y_0)}{k_{n1}}(\frac{1-c_2\alpha_3}{\alpha_2-\alpha_1\alpha_3}\gamma_1+\frac{c_2\alpha_2-\alpha_1}{\alpha_2-\alpha_1\alpha_3}\gamma_2)\phi_n(y) \end{aligned}. \tag{5.17}$$

While the angular velocity distribution at the plate/plate junction is given by:

$$\begin{aligned} \dot{\theta}_y(0,y) &= j\omega\sum_n [k_{n1}(A_{1n}c_1-A_{2n})+k_{n2}(A_{3n}c_2-A_{4n})]\phi_n(y) \\ &= -\frac{j\omega F_p}{2D_1\Lambda_n}\sum_n \frac{\phi_n(y_0)}{k_{n1}^2}(\frac{1-c_2\alpha_3}{\alpha_2-\alpha_1\alpha_3}\gamma_1+\frac{c_2\alpha_2-\alpha_1}{\alpha_2-\alpha_1\alpha_3}\gamma_2)\frac{\Delta_1}{\Delta_2}\phi_n(y) \end{aligned}. \tag{5.18}$$

Substituting Equations (5.17) and (5.18) into Equation (5.16) gives:

$$\left\langle \overline{P}_{12} \right\rangle = -\frac{\omega\left|F_p\right|^2}{8\Lambda_n}\mathrm{Im}[\frac{1}{D_1^*}\sum_n \frac{\phi_n^2(y)}{\left|k_{n1}\right|^2 k_{n1}^*}\left|\frac{(1-c_2\alpha_3)\gamma_1+(c_2\alpha_2-\alpha_1)\gamma_2}{\alpha_2-\alpha_1\alpha_3}\right|^2(\frac{\Delta_1}{\Delta_2})^*]. \tag{5.19}$$

In contrast to the input power, the energy flow from the source to the receiving plate is not only governed by the source plate stiffness D_1 but is also affected by the receiving plate stiffness D_2 via the stiffness ratio r in the coupling term $\frac{\Delta_1}{\Delta_2}$. Furthermore, it is also a function of the wave number ratios between the source and the receiving plates.

5.3.3 Moment excitation

For moment excitations, the source term in Equation (5.1) is replaced by [51]:

$$M_0 \sin\varphi \frac{\partial \delta(x-x_0, y-y_0)}{\partial x} - M_0 \cos\varphi \frac{\partial \delta(x-x_0, y-y_0)}{\partial y}, \tag{5.20}$$

where M_0 and φ are similarly defined as in Chapter 3.

Following the same procedure as described in Section 5.3.2, one has:

$$A_{3n} = \frac{\alpha_2\gamma_4 - \alpha_3\gamma_3}{\alpha_2 - \alpha_1\alpha_3} M_n^x + \frac{\alpha_2\gamma_2 - \alpha_3\gamma_1}{\alpha_2 - \alpha_1\alpha_3} M_n^y, \tag{5.21}$$

and

$$A_{4n} = \frac{\gamma_3 - \alpha_1\gamma_4}{\alpha_2 - \alpha_1\alpha_3} M_n^x + \frac{\gamma_1 - \alpha_1\gamma_2}{\alpha_2 - \alpha_1\alpha_3} M_n^y, \tag{5.22}$$

where $M_n^x = \frac{M_0 \sin\varphi \phi_n(y_0)}{4D_1\Lambda_n k_{p1}^2}$, $M_n^y = \frac{M_0 \cos\varphi \phi_n'(y_0)}{4D_1\Lambda_n k_{p1}^2 k_{n1}}$, $\gamma_3 = c_6 + \frac{c_3^2 c_9^2}{c_6}$, $\gamma_4 = c_8 + \frac{c_4^2 c_{10}^2}{c_8}$.

The inter-relationships between the wave coefficients for this excitation case are the same as those described in the point force excitation case except for those coefficients directly associated with the moment source ($A_{5n} - A_{12n}$). The inter-relationships of these wave coefficients are also given in *Appendix C*.

a) Input mobility

There are two components of moment input mobility, each associated with one of the two angular velocity components at the source location. These two components of input mobility are given respectively by:

$$Y_{in}^{x}=\frac{\left.\frac{\partial \dot{W}_2}{\partial y}\right|_{(x_0^a,y_0)}}{M_0}=\frac{j\omega}{4D_1\Lambda_n k_{p1}^2}\sum_n[\phi_n(y_0)\phi_n'(y_0)\sin\varphi(\frac{\alpha_2\gamma_4-\alpha_3\gamma_3}{\alpha_2-\alpha_1\alpha_3}R_1 \quad , \tag{5.23}$$
$$+\frac{\gamma_3-\alpha_1\gamma_4}{\alpha_2-\alpha_1\alpha_3}R_2)-\frac{\phi_n'^2(y_0)\cos\varphi}{k_{n1}}(\frac{\alpha_2\gamma_2-\alpha_3\gamma_1}{\alpha_2-\alpha_1\alpha_3}R_1+\frac{\gamma_1-\alpha_1\gamma_2}{\alpha_2-\alpha_1\alpha_3}R_2)]$$

and

$$Y_{in}^{y}=\frac{\left.\frac{\partial \dot{W}_2}{\partial x_{II}}\right|_{(x_0^a,y_0)}}{M_0}=\frac{j\omega}{4D_1\Lambda_n k_{p1}^2}\sum_n[\phi_n^2(y_0)\sin\varphi(\frac{\alpha_2\gamma_4-\alpha_3\gamma_3}{\alpha_2-\alpha_1\alpha_3}R_3+\frac{\gamma_3-\alpha_1\gamma_4}{\alpha_2-\alpha_1\alpha_3}R_4), \tag{5.24}$$
$$-\frac{\phi_n(y_0)\phi_n'(y_0)\cos\varphi}{k_{n1}}(\frac{\alpha_2\gamma_2-\alpha_3\gamma_1}{\alpha_2-\alpha_1\alpha_3}R_3+\frac{\gamma_1-\alpha_1\gamma_2}{\alpha_2-\alpha_1\alpha_3}R_4)]$$

where $R_3=k_{n1}(c_1c_6\Theta_3-\frac{1}{c_6}\Theta_1)+\frac{1}{c_8}k_{n2}$, $R_4=k_{n1}(c_1c_6\Theta_4-\frac{1}{c_6}\Theta_2)-c_2c_8k_{n2}$.

Once the input mobility is known, the input power of the moment excitation can be calculated accordingly.

b) Vibration energy flow

The moment distribution at the plate/plate junction for this excitation is given by:

$$M_y(0,y)=\frac{-M_0}{2\Lambda_n}\sum_n[\phi_n(y_0)\sin\varphi(\sigma_1\gamma_3+\sigma_2\gamma_4)-\frac{\phi_n'(y_0)\cos\varphi}{k_{n1}}(\sigma_1\gamma_1+\sigma_2\gamma_2)]\phi_n(y), \tag{5.25}$$

where $\sigma_1=\frac{1-\alpha_3c_2}{\alpha_2-\alpha_1\alpha_3}$ and $\sigma_2=\frac{\alpha_2c_2-\alpha_1}{\alpha_2-\alpha_1\alpha_3}$.

The angular velocity distribution at the junction is determined by:

$$\dot{\theta}_y(0,y) = \frac{-j\omega M_0}{2D_1\Lambda_n}\sum_n [\frac{\phi_n(y_0)\sin\varphi}{k_{n1}}(\sigma_1\gamma_3+\sigma_2\gamma_4) - \frac{\phi_n'(y_0)\cos\varphi}{k_{n1}^2}(\sigma_1\gamma_1+\sigma_2\gamma_2)]\frac{\Delta_1}{\Delta_2}\phi_n(y)\,. \tag{5.26}$$

Substituting Equations (5.25) and (5.26) into Equation (5.16) gives:

$$\left\langle \overline{P}_{12} \right\rangle = -\frac{\omega|M_0|^2}{8\Lambda_n}\mathrm{Im}[\frac{1}{D_1^*}\sum_n \frac{1}{k_{n1}^*}\left|\phi_n(y_0)\sin\varphi(\sigma_1\gamma_3+\sigma_2\gamma_4) - \frac{\phi_n'(y_0)\cos\varphi}{k_{n1}}(\sigma_1\gamma_1+\sigma_2\gamma_2)\right|^2 (\frac{\Delta_1}{\Delta_2})^*]\,. \tag{5.27}$$

5.3.4 Kinetic energy distributions

For both excitation cases, the time averaged, steady state kinetic energy distribution of the source plate is given by:

$$\left\langle \overline{T} \right\rangle_{P1} = \frac{1}{2}\int_{S_1}\rho_{s1}\dot{W}\dot{W}^* dS = \frac{\rho_{s1}\Lambda_n\omega^2}{2}\sum_{i=1}^{4} T_i\,, \tag{5.28}$$

where T_i is the energy coefficient obtained by integrating over the surface area of i^{th} calculation sub-domain of the source plate. The analytical expressions for the energy coefficients of the source plate are given by Equations (C20) – (C23) in *Appendix C*.

Similarly, the time averaged, steady state kinetic energy distribution of the receiving plate is given by:

$$\begin{aligned}\left\langle \overline{T} \right\rangle_{P2} = \frac{\rho_{s2}\Lambda_n\omega^2}{2}\sum_n \{&\frac{|A_{17n}|^2+|A_{18n}|^2}{2\,\mathrm{Re}(k_{n3})}(1-|c_{21}|^2) + \frac{|A_{19n}|^2+|A_{20n}|^2}{2\,\mathrm{Re}(k_{n4})}(1-|c_{22}|^2) - \\ &\frac{2\,\mathrm{Re}(A_{17n}^*A_{18n})\,\mathrm{Im}(c_{21})}{\mathrm{Im}(k_{n3})} - \frac{2\,\mathrm{Re}(A_{19n}^*A_{20n})\,\mathrm{Im}(c_{22})}{\mathrm{Im}(k_{n4})} + \\ &2\,\mathrm{Re}[\frac{A_{17n}^*A_{20n}+A_{18n}^*A_{19n}}{k_{n3}^*-k_{n4}}(c_{22}-c_{21}^*) + \frac{A_{17n}^*A_{19n}+A_{18n}^*A_{20n}}{k_{n3}^*+k_{n4}}(1-c_{21}^*c_{22})]\}\end{aligned}\,. \tag{5.29}$$

5.4 Results and discussion

In this simulation, both the source and the receiving plates are assumed to be aluminum plates and to have the same plate thickness of $8mm$. The source plate has $S_1 = 3.6 \times 1m^2$ in surface area while the receiving plate has $S_2 = 1 \times 1m^2$. A constant internal loss factor $\eta = 0.01$ is assumed for both plates. Because the real part of input mobilities is directly related to the input power, only real parts of the input mobilities are shown on the figures in the subsequent analysis.

5.4.1 Input mobilities

The input mobilities of the L-shaped plate to point force and moment ($\varphi = 0^o$) excitations at plate location $(x_0, y_0) = (1.2m, 0.32m)$ are shown in Figures 5.3 and 5.4 together with those obtained by finite element analysis (FEA) and statistical energy analysis (SEA). In SEA analysis, the input mobilities of the corresponding infinite plate [1] are utilized. General good agreement is found in results over the whole frequency range of interest, for all methods. The proposed method not only provides a better and explicit understanding for the vibration response of L-shaped plates when compared to other methods, it is also more computationally efficient and cost effective than other analytical approaches discussed in the literature review since no matrix inversion is required in the solution. In addition, only a few trace modes are required in the modal summation to achieve good convergent results.

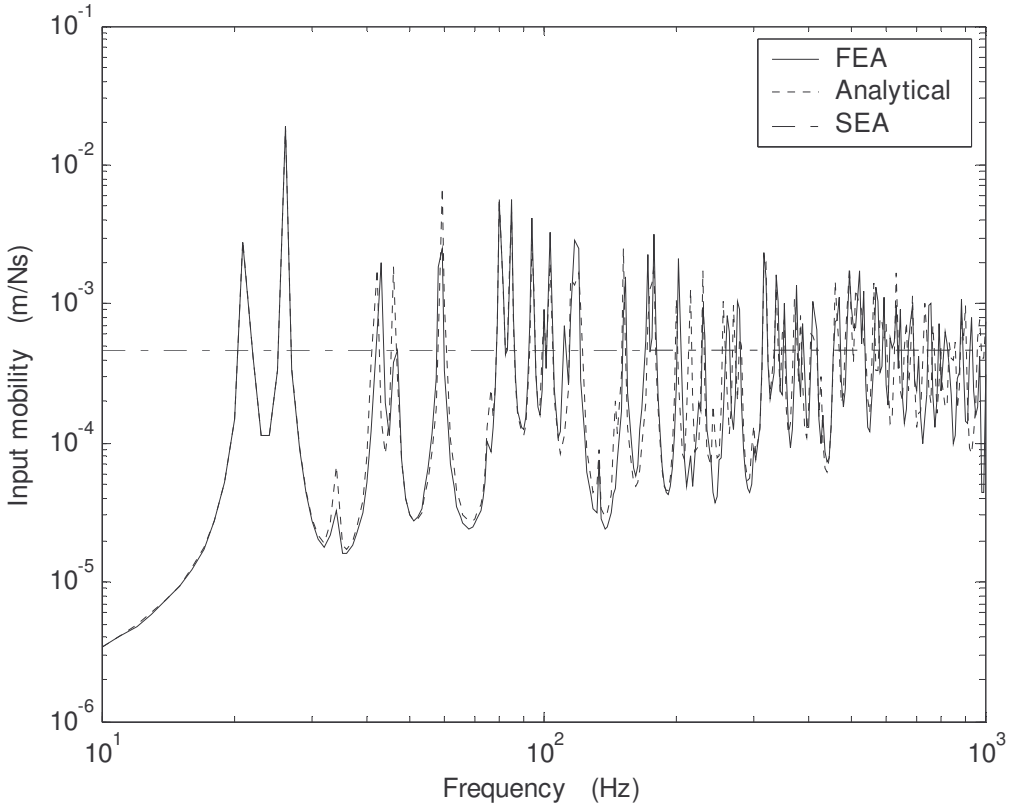

Figure 5.3. Input mobility of the L-shaped plate to point force excitation.

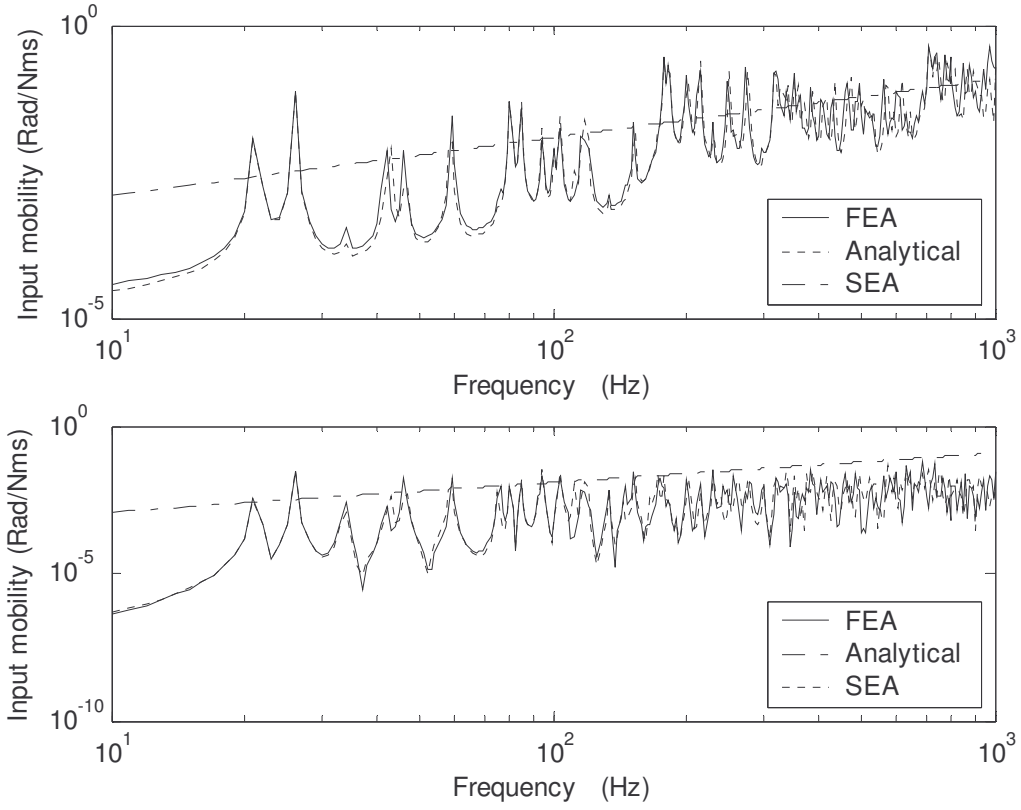

Figure 5.4. Input mobility of the L-shaped plate to moment excitation ($\varphi = 0^0$). Top, x component; Bottom, y component.

5.4.2 Test of SEA in point force excitation case

In this simulation, the vibration response of the L-shaped plate is calculated for three excitation locations at $(x_0, y_0) = (0.01, 0.32)$, $(0.07, 0.32)$ and $(0.22, 0.32)$ in three separate calculations. The predicted input mobilities for these three excitations are shown in Figure 5.5 together with that of SEA prediction. The kinetic energy distributions of the source and the receiving plates for these excitations are shown in Figure 5.6.

It is shown in Figure 5.5 that SEA analysis over predicts the vibration response of the coupled plates when the source location is less than a quarter of plate bending wavelength away from the coupling edge (i.e. the first and the second excitations). Similar results can be obtained when the source location is less than a quarter wavelength away from the other edges of the source plate. This is attributed to the effect of the boundary stiffness of the source plate on the stiffness term of the point force input mobility when the source location is less than a quarter wavelength away from the plate edges. This finding is similar to that observed on the characteristics of input mobilities of finite beam stiffened plates (see Section 3.4.2). In contrast, the source plate bending stiffness controls the stiffness term of the input mobility when the source location is more than a quarter wavelength away from the plate edges where the frequency averaged input mobility can be represented well by that of the corresponding infinite plate. For example, when the point force location is $0.22m$ (corresponding to a quarter bending wavelength at $100Hz$) away from the coupling plate edge, the frequency averaged input mobilities, the kinetic energy distributions of the source and the receiving plates can all be represented well by those of SEA predictions at frequencies greater than 100Hz.

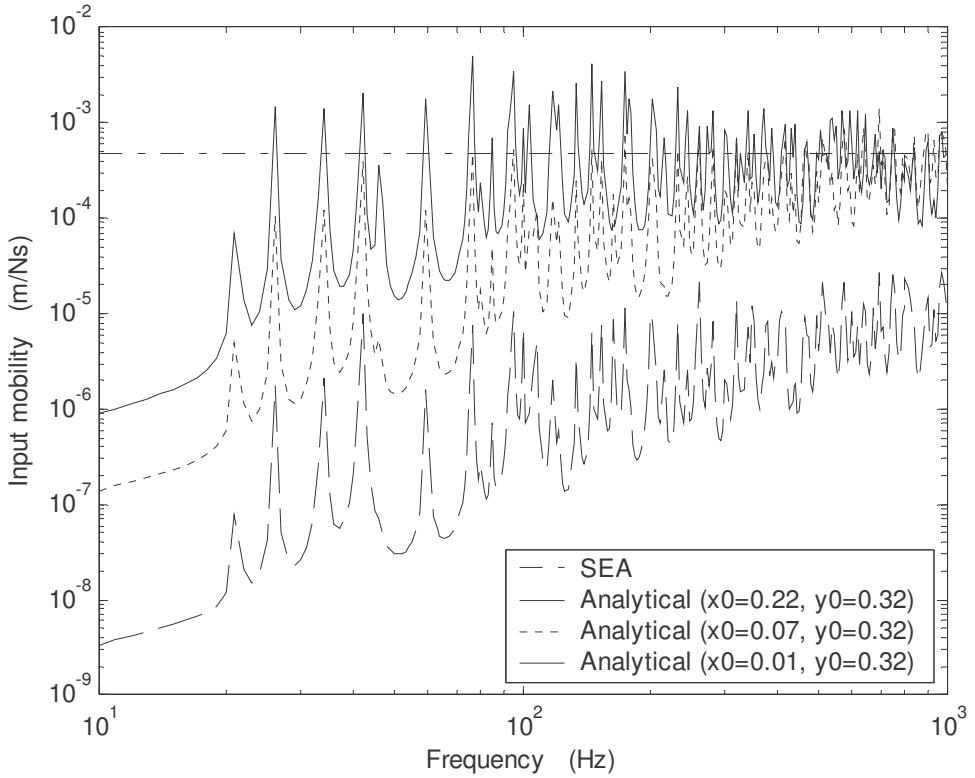

Figure 5.5. Input mobility of the L-shaped plate to point force excitation at different locations away from the coupling edge.

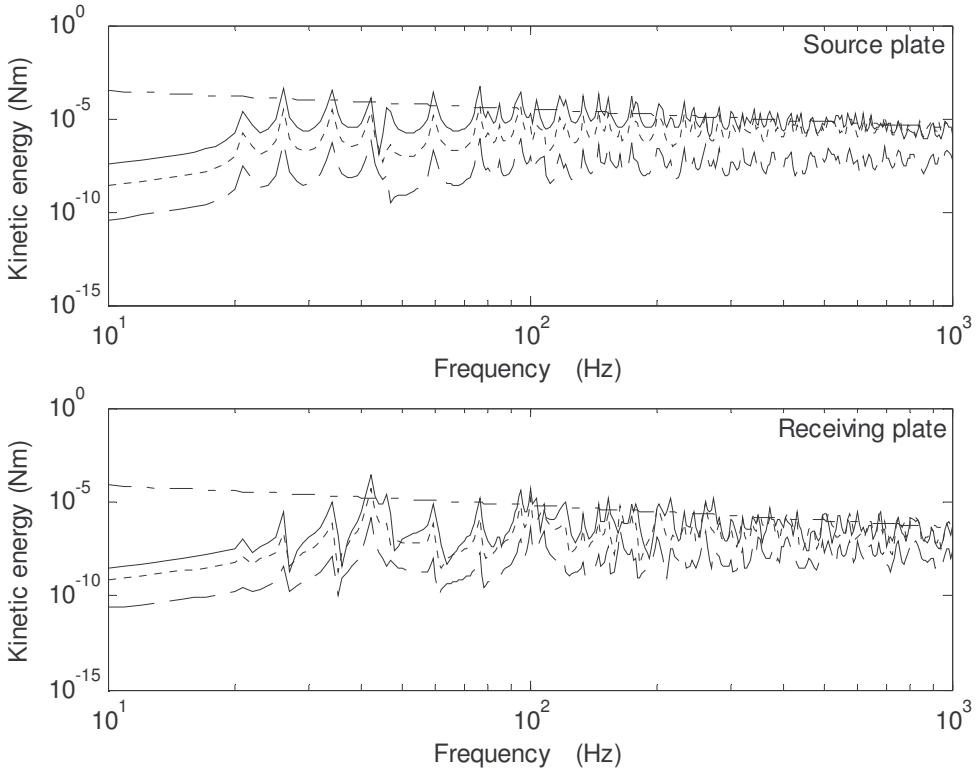

Figure 5.6. Kinetic energy distributions of the L-shaped plate to point force excitation at different locations on the plate. The legends are the same as used in Figure 5.5.

5.4.3 Test of SEA in moment excitation case

The input mobilities of the L-shaped plate to a bending moment excitation ($\varphi = 0^o$) applied at different locations on the source plate are shown in Figures 5.7 and 5.8. Attributed to the directional characteristics of moment excitations, only the boundary stiffness of the pair of the simply supported source plate edges perpendicular to the moment axis can have large effects on the input mobilities and structure responses of the L-shaped plate when the source location is less than a quarter of plate bending wavelength away from this pair of plate edges. Effects of boundary stiffness on the moment input mobility of the L-shaped plate diminish when the source location is greater than a quarter of plate bending wavelength away from the source plate edges. At this condition, the frequency averaged moment input mobilities, kinetic energy distributions of the L-shaped plate could be approximated by those of the corresponding infinite plate. Similar results can also be obtained when the L-shaped plate is excited by a torsional moment ($\varphi = 90^o$).

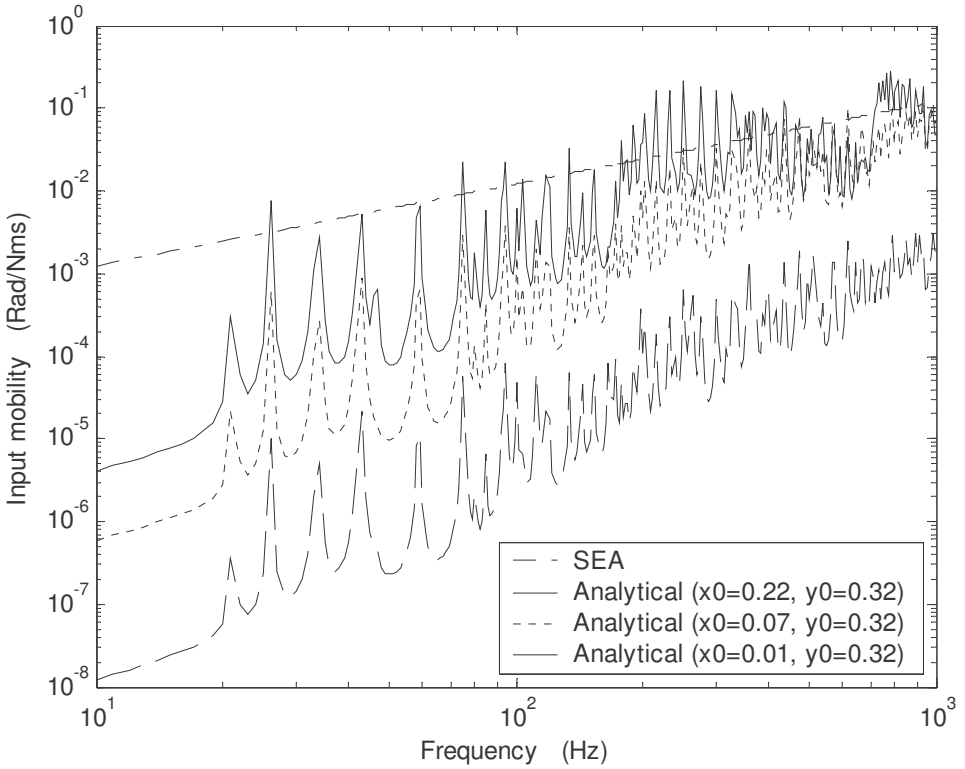

Figure 5.7. Input mobility of the L-shaped plate to bending moment excitation ($\varphi = 0^o$) at different plate locations away from the coupling edge.

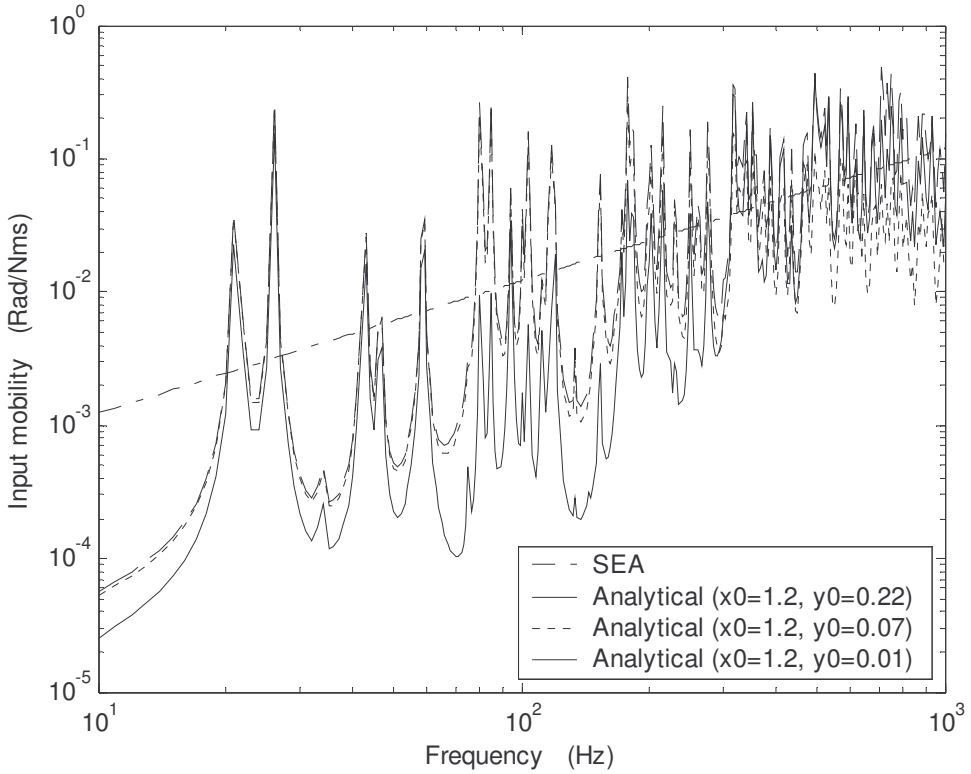

Figure 5.8. Input mobility of the L-shaped plate to bending moment excitation ($\varphi = 0^o$) at different plate locations away from the plate edges perpendicular the coupling edge.

5.5 Conclusion

Closed form solutions are obtained in this chapter for predicting the vibration response of an L-shaped plate to point force and moment excitations by utilizing the wave-guide approach where input mobilities, energy flow and kinetic energy distributions of the L-shaped plate are either expressed in terms of wave coefficients or in terms of mechanical properties of the structure.

The solutions are utilized to examine the validity of SEA for the prediction of vibration response of L-shaped plates in deterministic force and moment excitation cases. It is found that SEA can be employed to predict the frequency averaged

vibration response of L-shaped plates in point force excitation cases providing that the source location is more than a quarter of plate bending wavelength away from the source plate edges. This limitation is relaxed further in moment excitation cases where the accuracy of the SEA in predicting the L-shaped response is only affected by the distance between the source location and a pair of the source plate edges (the edges perpendicular to the moment axis).

Chapter 6

Dynamic response of two finite periodic or irregular ribbed plates coupled at right angles

6.1 Introduction

Beam/plate couplings were considered in Chapters 2 – 4 while plate/plate couplings were considered in Chapter 5. However, quite often, one has to deal with complex structures comprising both types of structural couplings in practical applications such as in ship hull structures. For such structures, the analysis presented in previous chapters is inadequate. This forms the basis of the analysis presented in this chapter where a coupled system consisting of two finite periodic or irregular ribbed plates is considered. Similar to that in Chapter 5, the in-plane plate vibration is also ignored in this analysis.

The literature for works on vibration analysis of ribbed plate structures was reviewed in Chapters 2 and 4 while the literature for works on vibration analysis of plate/plate coupled structures was reviewed in Chapter 5. Nevertheless, the literature survey shown that little work has been done to address the vibration problem of coupled structures consisting of both beam/plate and plate/plate couplings. The analysis of vibration response for this type of coupled structures usually resorted to either numerical analysis such as FEA analysis or statistical analysis such as SEA. A typical example is the analysis of Tso and Hansen [86] who studied the averaged energy transmission from a semi-infinite uniform plate to a semi-infinite periodic ribbed plate and obtained the coupling loss factor between the two structural components from the mean transmission efficiency. However, the assumptions of

SEA are often not met in practical applications, which limit the usefulness of the method.

Extending the analysis approaches of Chapters 4 and 5, this study focuses on the derivation of an analytical solution to predict the vibration response of a coupled structure system consisting of two finite periodic or irregular ribbed plates coupled at right angles. Some interesting phenomena of the 'pass band' and 'stop band' properties of the coupled system are observed where physical interpretations are given for the bounding frequencies and the peak responses in the wave propagation zones of the coupled system. Furthermore, vibration confinement of the coupled system due to structural irregularities on the source ribbed plate is also investigated.

6.2 General formulations

The coupled structure under investigation and the associated coordinate system are shown in Figure 6.1 where the plate under direct external force excitation (source plate) is reinforced by s stiffened beams, and the other plate (receiving plate) is reinforced by r stiffened beams. The beams are either periodic or irregular distributed on each plate. The source plate is excited by a point force excitation F_p applied at plate location $\sigma_0 = (x_0, y_0)$ and point force excitations (F_{bi}) applied at $y = y_i$ on the i^{th} beam of the source plate. Simply supported boundary conditions are assumed on all plate edges and the stiffened beams.

In the analysis, the two coupled ribbed plates are considered separately where the coupling at the plate/plate junction is replaced by a pair of anti-phase distributing moments (m_c) applied on the coupling edge of each plate [79], which are illustrated in Figures 6.2(a) and 6.2(b). The validity of representing the coupled system by two

separate subsystems and a pair of anti-phase coupling moments is verified later in the analysis by comparing the predicted input mobility of the coupled system to that obtained from FEA analysis.

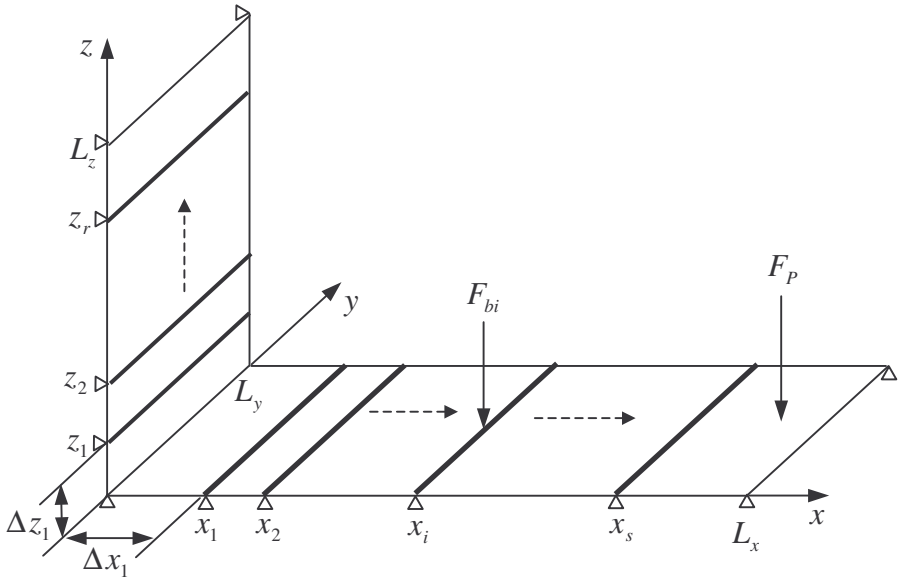

Figure 6.1. Model description and the associate coordinate system of the coupled periodically/irregularly ribbed plates.

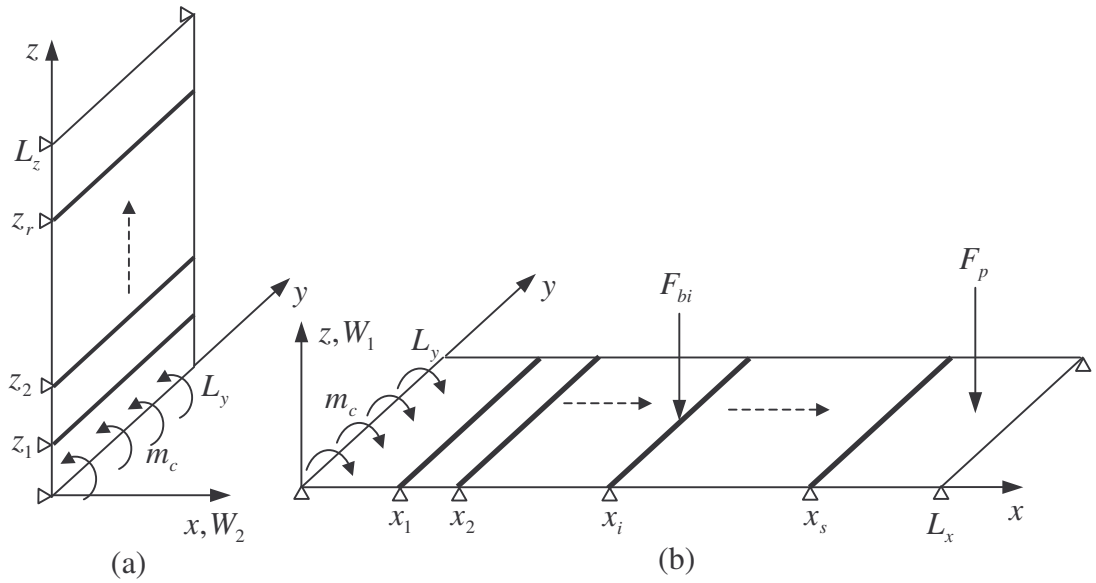

Figure 6.2. The two subsystems of the coupled structure. (a) Receiving ribbed plate; (b) Source ribbed plate.

6.2.1 Formulation

For the source ribbed plate (Figure 6.2(b)), by including the coupling moment at the plate/plate junction into the formulation, Equation (4.1) is rewritten here as:

$$\nabla^4 W_1 - k_{p1}^4 W_1 = \frac{F_p}{D_1}\delta(\sigma - \sigma_0) - \sum_{i=1}^{s}\frac{q_i}{D_1}\delta(x - x_i) - \sum_{i=1}^{s}\frac{m_i}{D_1}\delta'(x - x_i) + \frac{m_c}{D_1}\delta'(x - 0), \quad (6.1)$$

where m_c is the coupling moment per unit length on the plate/plate junction, $\sigma_0 = (x_0, y_0)$ is the source location on the plate, W_1 is the bending displacement of the source plate.

The governing equation of the flexural displacement for the receiving plate is:

$$\nabla^4 W_2 - k_{p2}^4 W_2 = -\sum_{j=1}^{r}\frac{q_j}{D_2}\delta(z - z_j) - \sum_{j=1}^{r}\frac{m_j}{D_2}\delta'(z - z_j) - \frac{m_c}{D_2}\delta'(z - 0), \quad (6.2)$$

where q_j and m_j are the coupling force and moment per unit length at the j^{th} beam/plate interface on the receiving plate.

The governing equations for the flexural and torsional displacements of the stiffened beams on both plates are similar to those given by Equations (4.2) and (4.3), which will not be repeated here. By employing modal expansion solutions for the bending displacements of both plates as well as the flexural and torsional displacements of the stiffened beams, the coupling forces and moments on the beam/plate interfaces and the plate/plate junction of the coupled system can be determined.

6.2.2 Vibration response of the coupled system

From Equations (6.1) and (6.2), there are $2(r+s)+1$ unknown modal coupling forces and moments at the interfaces of the coupled system, which can be solved by

the $2(r+s)$ continuity conditions at the beam/plate interfaces and the continuity condition at the plate/plate junction. For each modal index m, we have:

$$\begin{bmatrix} [A^I] & [C^I] & [0] & [0] & -\{L^I\} \\ [C^I]^T & [B^I] & [0] & [0] & -\{L^{II}\} \\ [0]^T & [0]^T & [A^{II}] & [C^{II}] & \{N^I\} \\ [0]^T & [0]^T & [C^{II}]^T & [B^{II}] & \{N^{II}\} \\ \{L^I\}^T & \{L^{II}\}^T & -\{N^I\}^T & -\{N^{II}\}^T & -(\sum_l \frac{k_l^2}{G_{l,m}} + \sum_n \frac{k_n^2}{G_{m,n}}) \end{bmatrix} \begin{Bmatrix} \{Q^I\} \\ \{M^I\} \\ \{Q^{II}\} \\ \{M^{II}\} \\ M_c \end{Bmatrix} = F_0 \phi_m(y_0) \begin{Bmatrix} \{H^{ss}\} \\ \{H^{sc}\} \\ \{0\} \\ \{0\} \\ \sum_l \frac{k_l \phi_l(x_0)}{G_{l,m}} \end{Bmatrix} - \begin{Bmatrix} \{F\} \\ \{0\} \\ \{0\} \\ \{0\} \\ 0 \end{Bmatrix}. \tag{6.3}$$

The assembly of the sub-matrices $[A^I]$, $[B^I]$ and $[C^I]$ of the source ribbed plate and the sub-matrices $[A^{II}]$, $[B^{II}]$ and $[C^{II}]$ of the receiving ribbed plate are similar to those described by Equations (4.10) – (4.12). $[0]$ is a $s \times r$ null sub-matrix.

The other elements in the square matrix of Equation (6.3) are given by:

$$L_i^I = \sum_l \frac{k_l \phi_l(x_i)}{G_{l,m}}, \quad i = 1,2,...,s, \tag{6.4}$$

$$L_i^{II} = \sum_l \frac{k_l \phi_l'(x_i)}{G_{l,m}}, \quad i = 1,2,...,s, \tag{6.5}$$

$$N_j^I = \sum_n \frac{k_n \phi_n(z_i)}{G_{m,n}}, \quad j = 1,2,...,r, \tag{6.6}$$

and

$$N_j^{II} = \sum_n \frac{k_n \phi_n'(z_i)}{G_{m,n}}, \quad j = 1,2,...,r. \tag{6.7}$$

Equations (6.4) – (6.7) describe the interactions of the shear force and moment couplings at the beam/plate interfaces of the source and the receiving plates to the moment coupling at the plate/plate junction.

The elements of the unknown modal coupling force and moment vectors are:

$$Q_i^I = Q_i, \quad i = 1,2,...,s, \tag{6.8}$$

$$M_i^I = M_i, \quad i = 1,2,...,s, \tag{6.9}$$

$$Q_j^{II} = Q_j, \quad j = 1,2,...,r, \tag{6.10}$$

and

$$M_j^{II} = M_j, \quad j = 1,2,...,r. \tag{6.11}$$

The elements of the external force vectors on the right hand side of Equation (6.3) are the same as described by Equations (4.13) – (4.15) where the modal index m is replaced by l and n by m.

Once the modal coupling forces and moments at the beam/plate interfaces and the plate/plate junction are known, the modal coefficients of the source and the receiving ribbed plates can be calculated respectively by:

$$w_{l,m} = \frac{F_p \phi_l(x_0)\phi_m(y_0) - \sum_{i=1}^{s} \phi_l(x_i) Q_i - \sum_{i=1}^{s} \phi_l'(x_i) M_i + k_l M_c}{G_{l,m}}, \tag{6.12}$$

and

$$w_{m,n} = \frac{-\sum_{j=1}^{r} \phi_n(z_j) Q_j - \sum_{j=1}^{r} \phi_n'(z_j) M_j - k_n M_c}{G_{m,n}}. \tag{6.13}$$

6.3 Vibration energy distribution

The time and space averaged kinetic energy distributions of the source and the receiving plates (excluding the energies in the beams) are given respectively by:

$$\left\langle \overline{T} \right\rangle_{P1} = \frac{1}{2} \int_{S_1} \rho_{s1} \dot{W}_1 \dot{W}_1^* dS_1 = \frac{\rho_{s1} \Lambda_{l,m} \omega^2}{2} \sum_l \sum_m \left| w_{l,m} \right|^2, \tag{6.14}$$

and

$$\left\langle \overline{T} \right\rangle_{P2} = \frac{1}{2}\int_{S_2} \rho_{s2} \dot{W}_2 \dot{W}_2^{*} dS_2 = \frac{\rho_{s2}\Lambda_{m,n}\omega^2}{2}\sum_m \sum_n \left| w_{m,n} \right|^2 . \tag{6.15}$$

On the other hand, Equation (4.17) can be utilized to calculate the kinetic energy distribution of each plate section of the source and the receiving plates, while Equations (4.19) and (4.20) can be employed to calculate the flexural and torsional vibration energies of the beams.

6.4 Results and discussion

In this simulation, both the source and the receiving plates are assumed to be aluminum plates having the same plate thickness ($h_1 = h_2 = 8mm$) and same surface area ($S_1 = S_2 = 4.5 \times 1m^2$). Initially, the source plate is reinforced periodic by eight stiffened beams ($s = 8$) while the receiving plate is reinforced periodic by four stiffened beams ($r = 4$). All of the stiffened beams are aluminum beams and have the same cross sectional area of $A_b = 50mm \times 5mm$. Initially, an internal loss factor $\eta_p = 0.03$ is assumed for all structural components in the calculation of input mobilities while zero damping is assumed for all structural components in the calculation of energy propagation of the coupled system.

6.4.1 Accuracy assessment

To justify the validity of representing the coupled structure by two separated ribbed plates and a pair of anti-phase distributing moments on the plate/plate junction, the input mobilities of the coupled structure predicted by the current analytical approach is compared to those obtained from FEA analysis in this study. The input mobilities of the coupled system are calculated for two cases, point force applied on the plate at location $(x_0, y_0) = (4.3m, 0.2m)$ and point force applied on the beam at location

$(x_8, y_8) = (4.0m, 0.2m)$. The first excitation case is also used for all other calculations in this chapter.

The input mobilities of the coupled structure for these two excitation cases are shown in Figures 6.3 and 6.4 respectively together with those obtained from FEA analysis. Good agreements are found between the results in the whole frequency range of investigation. Additionally, the input mobility of the coupled structure for the first excitation case is also compared to that of the corresponding periodic ribbed plate given in Chapter 4 to the same excitation. It is found that the input mobility of the periodic ribbed plate only changes slightly when coupled to another periodic ribbed plate, which indicates that the input mobility of the coupled system is mainly dominated by the flexural stiffness of the source periodic ribbed plate.

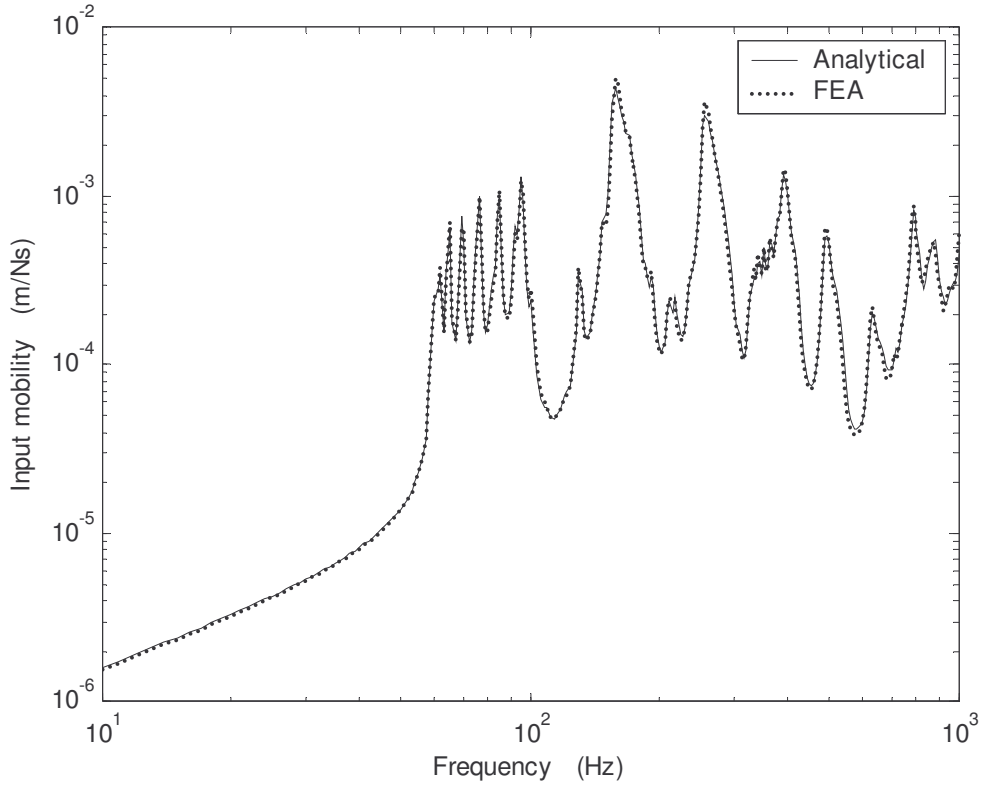

Figure 6.3. Input mobility of the coupled system to point force excitation applied on the plate at location $(x_0, y_0) = (4.3m, 0.2m)$.

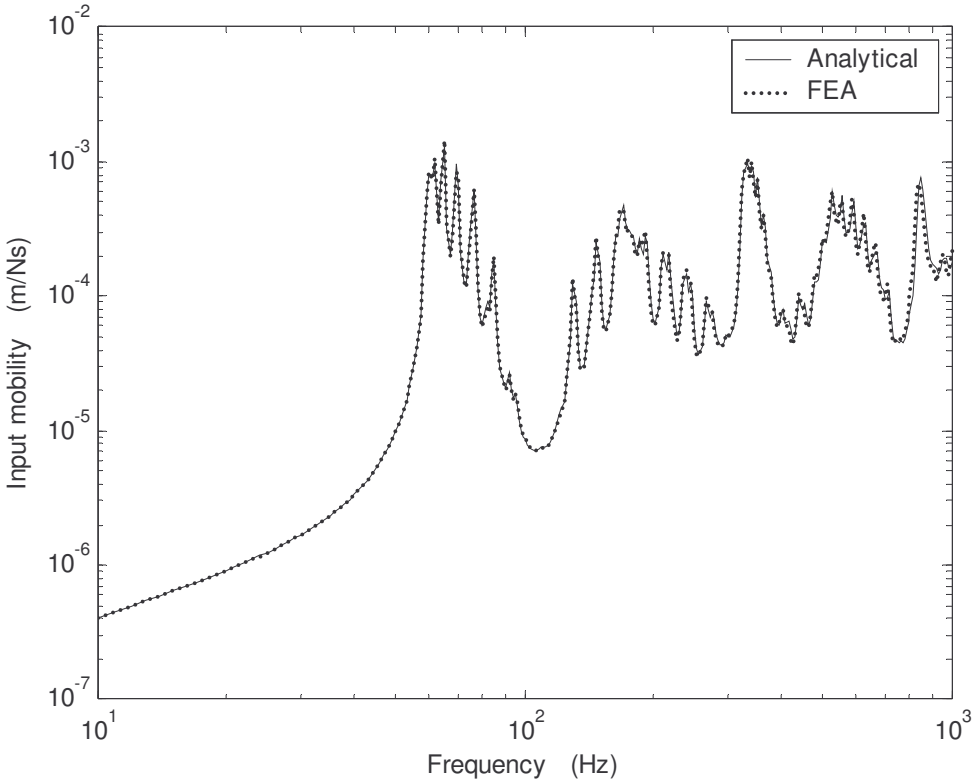

Figure 6.4. Input mobility of the coupled system to point force excitation applied on the beam at location $(x_8, y_8) = (4.0m, 0.2m)$.

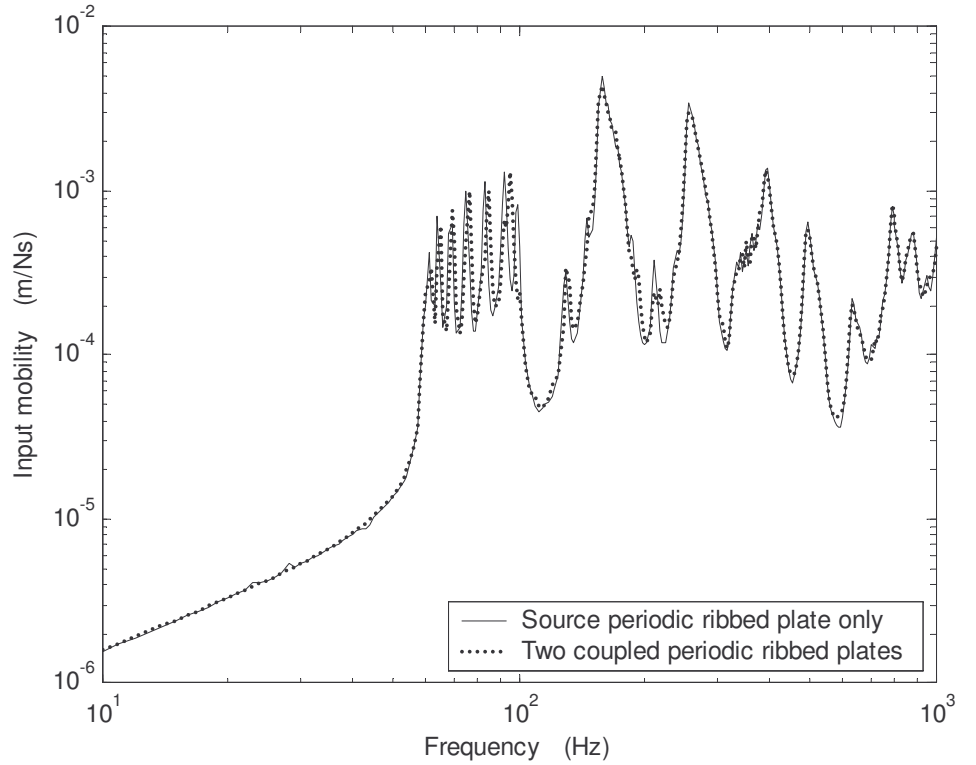

Figure 6.5. Comparison between the input mobility of the coupled system and that of the source ribbed plate when detached from the reciving ribbed plate.

6.4.2 Vibration energy attenuation

For reasons of clarification, the frequency range in this simulation is confined in the lower frequency region but enveloped at least one of the ***F/F*** wave propagation zones. Zero damping is assumed for all structural components in this simulation. Furthermore, beam vibration energies are not included in the energy calculation.

The kinetic energy distributions of the source and the receiving periodic ribbed plates are shown in Figure 6.6. It is found that the number of peaks enclosed in each wave propagation zone of the coupled system is the superposition of the peaks in the corresponding propagation zones of the two periodic ribbed plates when detached from each other. However, because of the overlapping of frequency bands of the peak responses, the number of peaks in each propagation zone of the coupled system is usually less than the sum of the peaks in the corresponding zones of the two periodic ribbed plates when detached. It is found that the receiving plate has much less modal energy than the source plate for peaks in the ***F/F*** propagation zones that correspond to the resonant responses of the source plate and vice versa. A separate calculation also shows that when the two coupled ribbed plates are identical, the receiving plate would share a similar amount of modal energy to that of the source ribbed plate for modes other than the non-propagating modes.

It is illustrated in Figure 6.6 that the lower bounding frequency of the first ***F/F*** propagation zone of the coupled system (bounded by the two straight dot lines) is almost unchanged from that of the source periodic ribbed plate when detached. This is because the stiffness term of input mobility of the coupled system is primarily controlled by the flexural stiffness of the source periodic ribbed plate. On the other hand, because of modal interactions between the source and the receiving periodic ribbed plates and the addition peak responses contributed by the receiving plates, the

upper bounding frequency of the first ***F/F*** zone shifts up by about 3Hz, which is no longer governed by the wave matching condition $\lambda_{x(m=1)} = 2\Delta x_i$. The mode shape distributions of the source ribbed plate for peaks enclosed in this propagation zone are much more complex than those of the corresponding orthogonal plate (see discussions in Chapter 4) due to the modal interaction of the two ribbed plates.

It is observed that there are two weak response peaks in the energy distribution curve of the receiving plate at frequencies below the lower bounding frequency of the first ***F/F*** propagation zone. These peaks are the non-propagation modes typical for asymmetrical periodic systems [59], one for each of the two finite periodic ribbed plates. The first peak is the non-propagation mode of the source periodic plate corresponding to $k_{l'(l'=1)}$. However, because the trace bending wavelength (λ_z) of the receiving plate also matches the span of the periodic sections (Δz_j) of the receiving plate at this frequency ($\frac{\lambda_{z(m=1)}}{\Delta z_j} = 2$), a weak resonant peak is formed in the response of the receiving plate. The latter peak is the non-propagation mode of the receiving plate corresponding to $k_{n(n=1)}$. For this mode, the source plate also has the same non-propagating mode shape distribution corresponding to $k_{l'(l'=1)}$ so that most of the modal energy is confined in the source section of the source plate rather than in the receiving plate.

It is noted that the response peaks at the resonance frequencies of the corresponding un-ribbed source plate (see discussions in Section 4.6.1) are not shown in the kinetic energy plots for both source and the receiving plates attributed to the additional plate/plate coupled term ($k_l M_c$) in Equation (6.12), which results to zero numerator

when $G_{m,n}$ goes to zero (resonance of the un-ribbed plate). Therefore, peak responses are not formed at these frequencies according to the l'Hospital's rule.

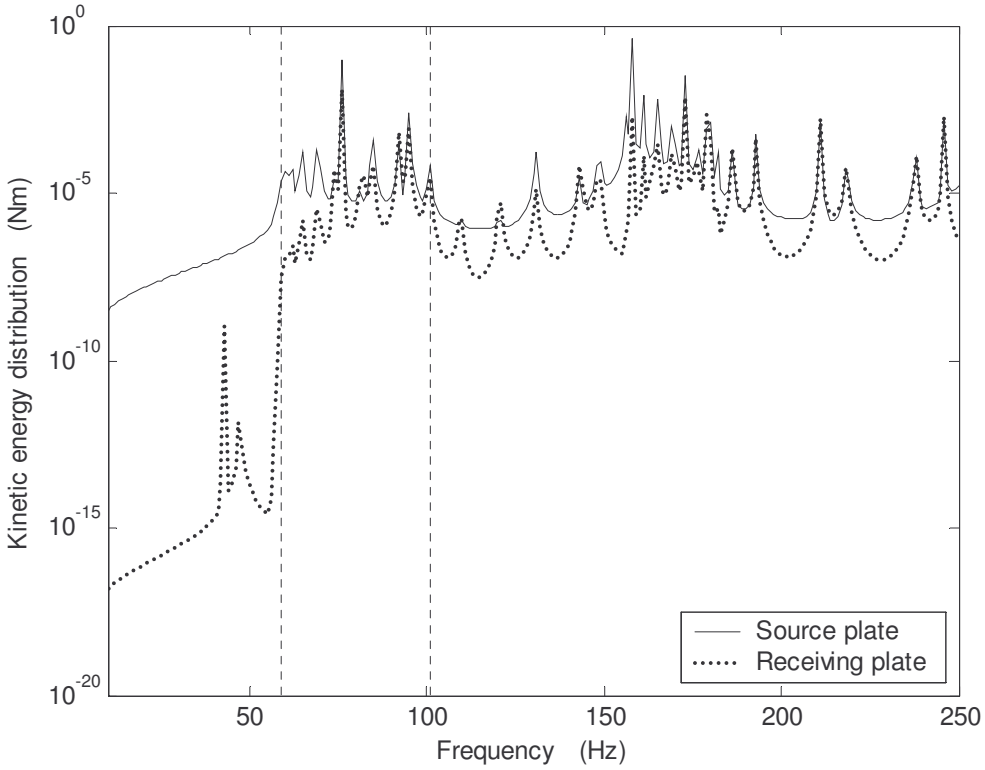

Figure 6.6. Kinetic energy distributions of the coupled system.

6.4.3 Vibration confinement by structural irregularities

Structural irregularities are common in periodic ribbed plate structures either due to manufacturing/installation errors or directly from the design of the structures. Some typical examples have been discussed in Chapter 4. The study of vibration confinement is extended to the coupled system consisting of two ribbed plates in this section by imposing structural irregularities on the source ribbed plate. Two cases of irregularities are studied: (a) beam spacing irregularity; and (b) beam property irregularity. Both source and receiving plates are assumed to have the same number of reinforced beams ($s = r = 4$) in the simulation.

a) Beam spacing irregularity

The exact beam locations on the source plate in this simulation are shown in the subsequent mode shape plot where the variations of beam locations are restricted to less than half of the mean beam spacing. Because the energy propagated to the receiving ribbed plate is of more concern, only the kinetic energy in the receiver plate is shown. It is illustrated in Figure 6.7 that the beam spacing irregularity on the source plate only affects the propagation of modal energy for modes in the ***F/F*** zones and corresponding to the resonant responses of the source plate. In contrast, modes in ***F/F*** zones but corresponding to the resonant responses of the receiving plate are not localized by the irregularity. So are modes in ***T/F*** wave propagation zones. Such interesting phenomena are examined further by mode shape plots of the selected peak responses shown in Figure 6.7.

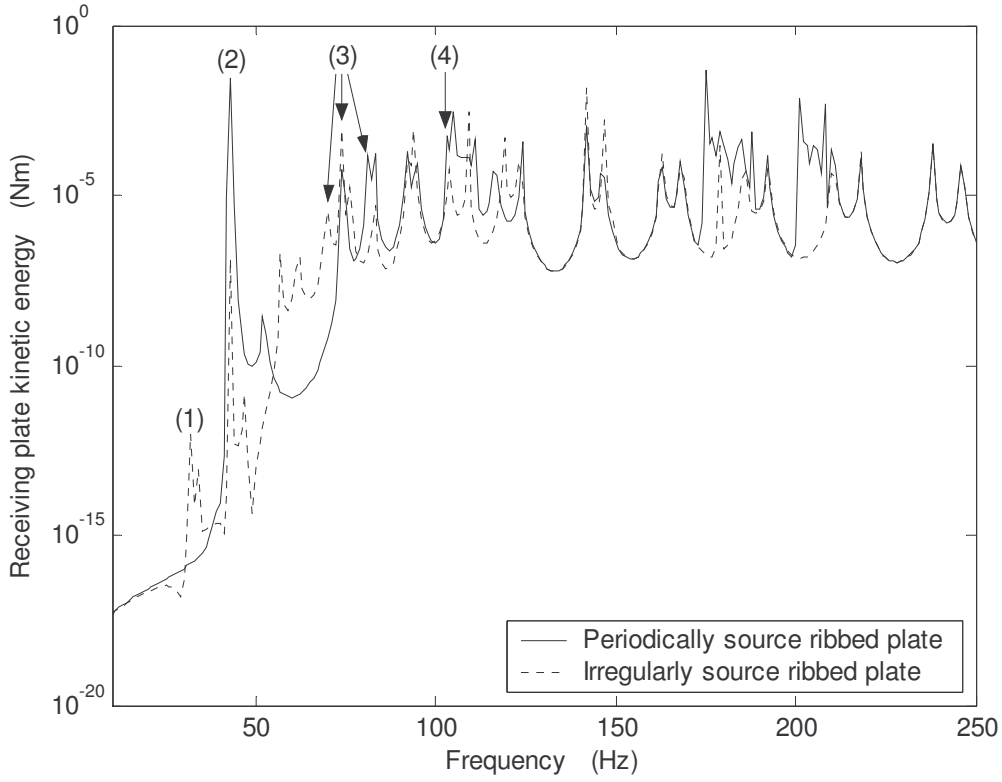

Figure 6.7. Kinetic energy distribution of the receiving plate.

The mode shape distributions of the first selected peak (calculated at $y = 0.2m$) are shown in Figure 6.8. The mode is a non-propagating mode for both periodic and irregular cases. However, because of the local resonance of the plate section next to the source bay (attributed to the 'trace-matching' condition between the span of the section (Δx_4) and the plate trace wavelength (λ_x) where $\frac{\lambda_{x(m=1)}}{\Delta x_4} = 2$) in the irregular case, the modal energy of the source plate increases significantly from that in the periodic case. As a result, the energy propagated to the receiving plate also increases, which leads to the peak response of the receiving plate at this frequency.

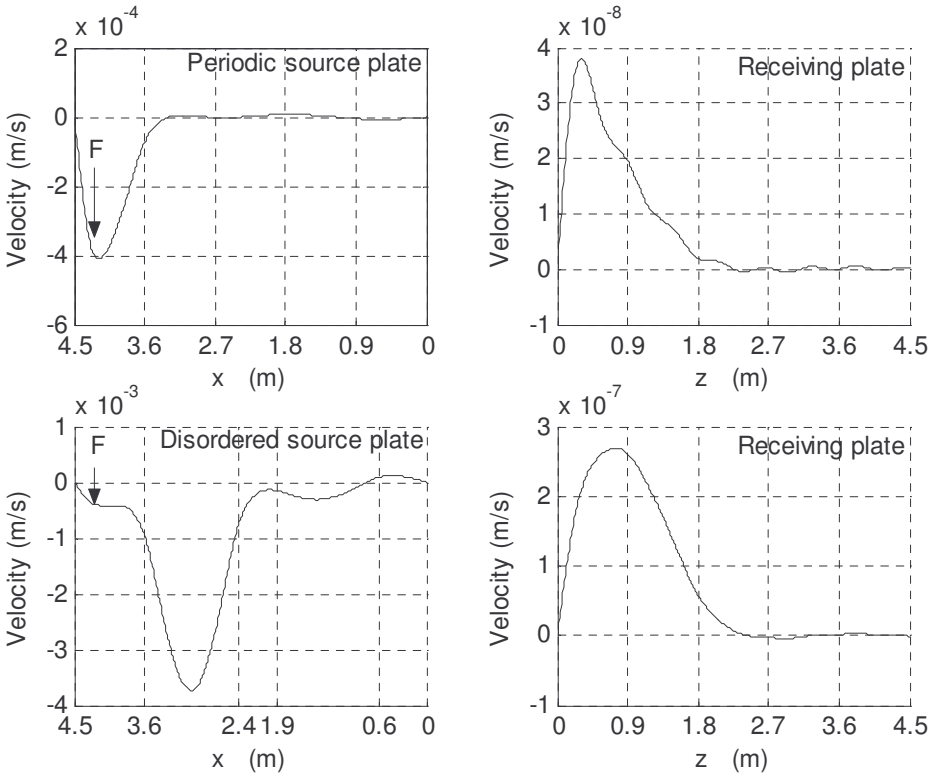

Figure 6.8. Mode shape distribution of the coupled system at 34Hz (calculated at $y = 0.2m$).

The mode shape distributions of the second selected peak are shown in Figure 6.9. It is found for this mode, the receiving plate has similar modal energy as that of the

source plate in the periodic case because of the 'trace-matching' condition between the plate trace wavelengths ($\lambda_{x(m=1)} = \lambda_{z(m=1)}$) and the spans of the periodic sections ($\Delta x_i, \Delta z_j$). While in the irregular case, the mode shape distribution of this mode is mainly confined in the source section where little energy is propagated to the receiving plate. This is because the energy propagation of this mode is governed by shear force couplings at the beam/plate interfaces (in ***F/F*** zones) that correspond to the resonant response of the source plate. Therefore, the modal response is controlled by the source plate flexural stiffness, which depends on the beam locations of the source plate. For this mode, little modal energy is propagated to the receiving plate after the irregularity.

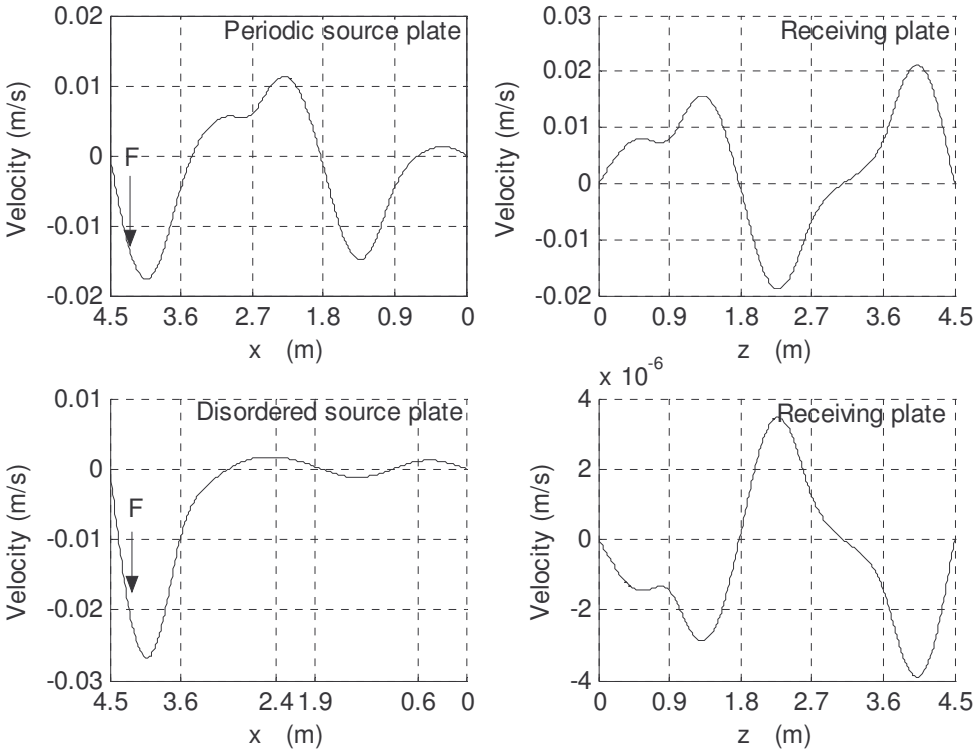

Figure 6.9. Mode shape distribution of the coupled system at 43Hz (calculated at $y = 0.2m$).

The peaks at 74Hz for both periodic and irregular cases are referred to two different modes. The mode shape distributions of these two modes are shown in Figures 6.10

and 6.11 respectively. It is found that the resonance frequency of the mode (at 74Hz) in the periodic case decreases to 70Hz in the irregular case. The mode at 74Hz in the irregular case is originated from the mode at 81Hz in the periodic case. The decrease modal frequencies for these two modes after the irregularity are due to the decrease flexural stiffness of the source ribbed plate when the beams are moved away from the positions close to the anti-nodal locations to positions close to the nodal locations of the modes. The decrease modal stiffness also leads to higher modal amplitudes. However, it is shown in Figure 6.7 that only the latter of the two modes has increase modal energy distribution on the receiving plate. For the first of the two modes, the decreasing modal energy on the receiving plate after the irregularity is due to the attenuated mode shape distribution of the receiving plate. For the latter of the two modes, the modal energy in the source ribbed plate increases significantly after the irregularity due to the local resonance of the plate section next to the source bay ($\frac{\lambda_x}{\Delta x_4} = 1$), the energy propagated to the receiving plate also increases.

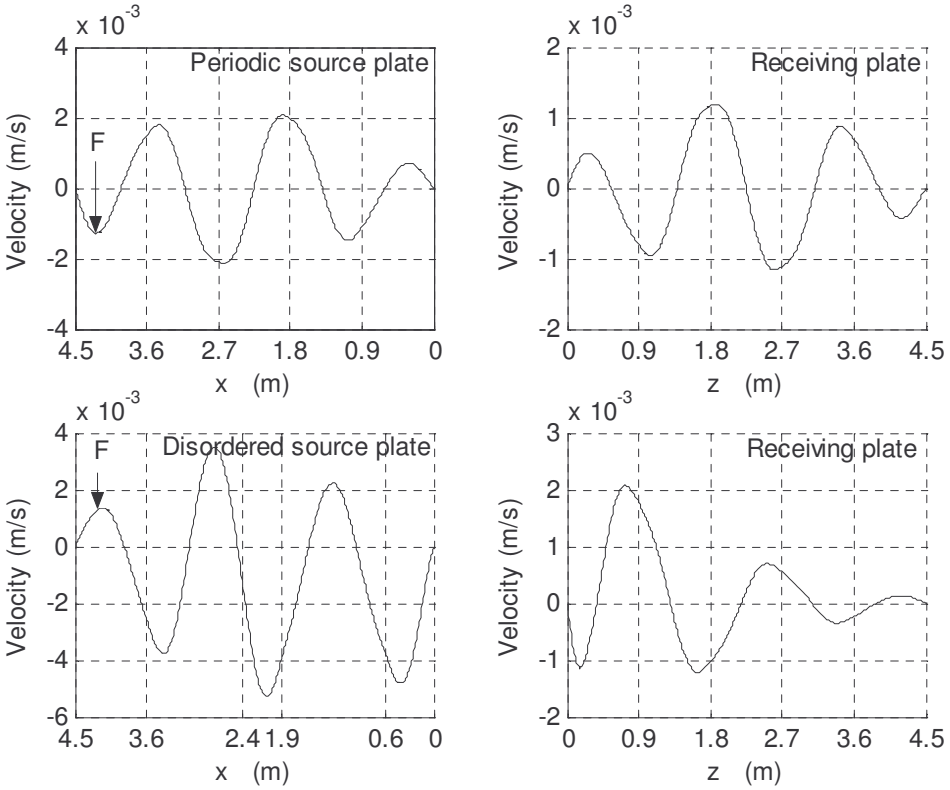

Figure 6.10. Mode shape distribution of the coupled ribbed plates (calculated at $y = 0.2m$); top: at 74Hz; bottom: at 70Hz.

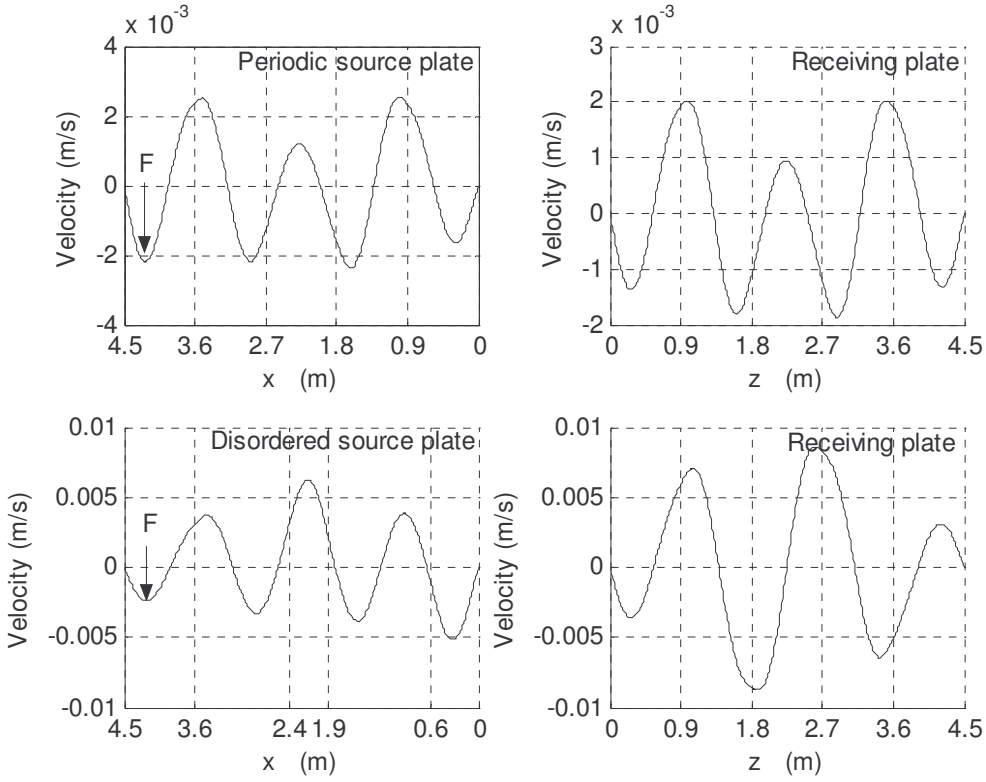

Figure 6.11. Mode shape distribution of the coupled ribbed plates (calculated at $y = 0.2m$); top: at 81Hz; bottom: at 74Hz.

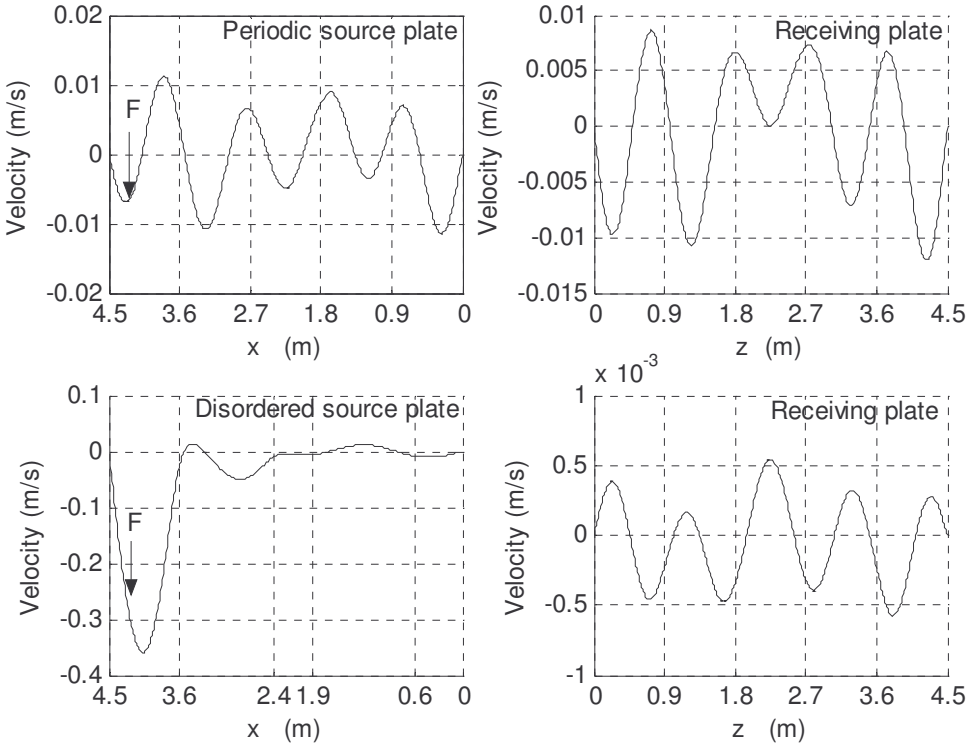

Figure 6.12. Mode shape distribution of the coupled ribbed plates at 105Hz (calculated at $y = 0.2m$).

The mode shape distributions of the last selected peak for both periodic and irregular cases are shown in Figure 6.12. It is found that for this mode, most of the modal energy is confined in the source section after the irregularity, which is typical for vibration localizations. Therefore, little modal energy is propagated to the receiving plate.

b) Beam property irregularity

In this simulation, the stiffened beams are assumed to be distributed periodically on both source and receiving plates. It is further assumed that beams on the receiving plate have the uniform cross sectional area of $A_{bj} = 50 \times 5mm^2$. While the cross sectional areas for beams on the source plate vary from $A_{bi} = 80 \times 8mm^2$ to $A_{bi} = 30 \times 3mm^2$. The energy distributions of the receiving plate for both periodic and irregular cases are shown in Figure 6.13.

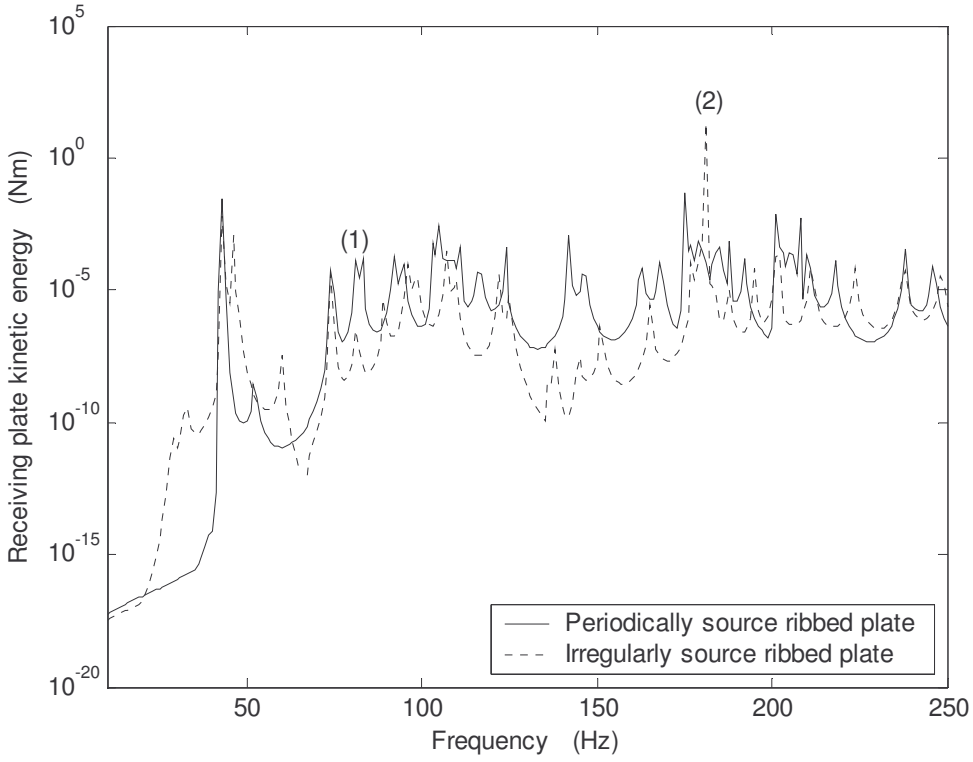

Figure 6.13. Kinetic energy distribution of the receiving ribbed plate.

Similar to that discussed in Chapter 4, it is found that the beam cross section area irregularity is more effective to generate vibration confinement for modes of the coupled ribbed plate system across the frequency bands. Two response peaks are selected to explain the vibration localization phenomenon.

The mode shape distribution of the first selected mode for both periodic and irregular cases (both at 81Hz) is shown in Figure 6.14. It is illustrated that the modal energy propagated to the receiving plate is significantly less than that in the periodic case after the irregularity due to vibration confinement of the source plate.

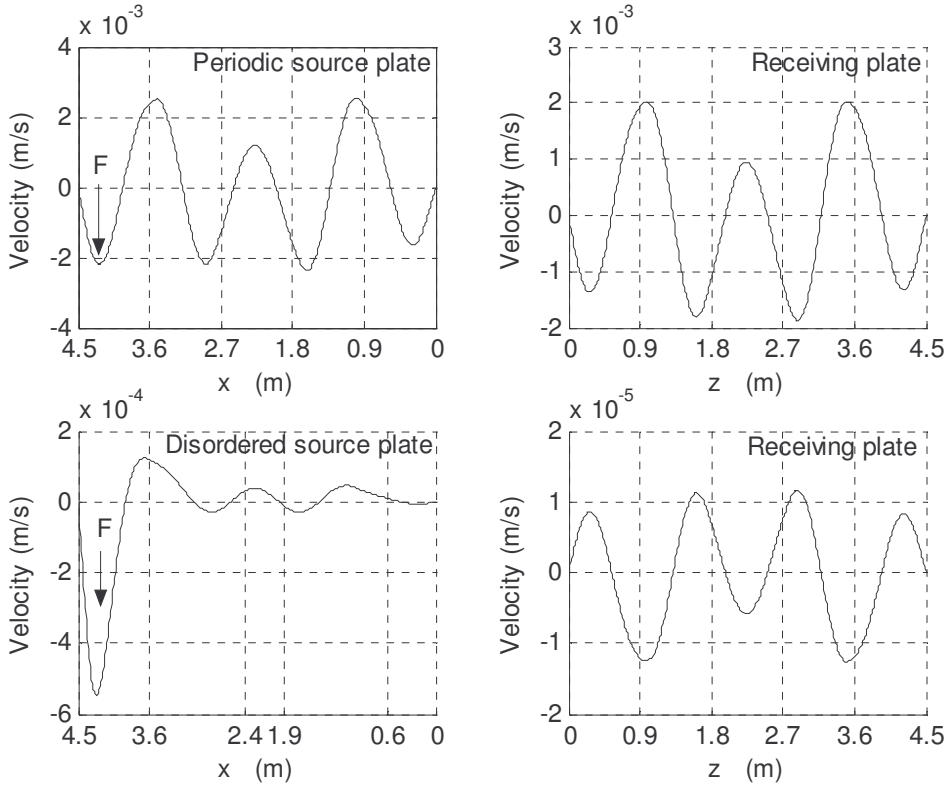

Figure 6.14. Mode shape distribution of the coupled system at 81Hz (calculated at $y = 0.3m$).

Nevertheless, because of the 'trace-matching' conditions between the plate bending and the flexural/torsional waves of the irregular beams, new response peaks are

formed at the corresponding frequencies, which results to the new response peaks in the irregular case. For instance, because of the trace matching condition between the plate bending wave and the flexural wavelength of the third stiffened beam on the source plate ($A_{b3} = 40 \times 4mm^2$), a large response peak is formed at the corresponding frequency (the peak marked by (2) in Figure 6.13).

6.5 Conclusion

An analytical solution is presented in this chapter to predict the vibration response of a coupled system consisting of two finite periodic/irregular ribbed plates coupled at right angles. It is shown that the input mobility of the coupled system is mainly dominated by the flexural stiffness of the source ribbed plate where the lower bounding frequencies of the ***F/F*** propagation zones of the coupled structure remain unchanged from those of the corresponding single (source) periodic ribbed plate. It is found that the number of peaks in each ***F/F*** wave propagation zone of the coupled system is the superposition of the peaks in the corresponding propagation zones of the two periodic ribbed plates when detached from each other. As a result, the upper bounding frequencies and the bandwidthes of wave propagation zones increase slightly from those of the corresponding periodic ribbed plate. Furthermore, the receiving plate would have less modal energy than that of the source plate for peaks in the ***F/F*** zones and corresponding to the resonant responses of the source ribbed plate. It would have higher modal energy than that of the source plate for peaks in the ***F/F*** zones but corresponding to the resonant responses of the receiving plate. It is found that the mode shape distributions for modes in ***F/F*** zones are more complex than those of the corresponding orthogonal plate due to modal interactions between the source and the receiving ribbed plates.

Only modes in the ***F/F*** wave propagation zones and corresponding to the resonant responses of the source plate are localized by beam spacing irregularity imposed on the source plate. The modes in ***F/F*** zones but corresponding to the resonant responses of the receiving plate are not localized by the irregularity. On the contrary, most modes of the coupled system are localized when cross section areas of the beams on the source plate are not uniform. Higher modal amplitudes are also found at frequencies corresponding to the 'trace-matching' conditions between the plate bending and the flexural/torsional waves of the irregular beams.

Chapter 7

Vibration response of a clamped-clamped ribbed plate: Analytical Solution and Experiment

7.1 Introduction

Analytical solutions were presented in Chapters 2 – 6 for the prediction of vibration response of finite coupled structures typical for ship constructions. The accuracies of the analytical solutions were evaluated by comparing the analytical results to those predicted by FEA analysis. Nonetheless, both analytical and FEA models were all based on ideal systems, which did not take into account the variation of coupling interfaces, boundary conditions and material properties of the structures. Yet structural imperfections due to manufacturing or installation errors are common for practical coupled structures. Thus, besides analytical solutions, experimental investigation is also vital for engineering applications, which forms the subject of this chapter.

A clamped-clamped ribbed plate is chosen in this study based on two reasons. Firstly, a clamped boundary condition is relatively easy to implement in the laboratory. Secondly, clamped boundary conditions are often assumed in vibration analysis of ship structures [84, 87]. The literature survey shows that little work has been done in the study of vibration response of clamped-clamped ribbed plates except for an early work by Olson and Hazell [88] who studied the free vibration of four clamped-clamped ribbed plates by experimental measurements. In their work, the vibration mode shapes of four integrally machined clamped-clamped ribbed plates were measured using Laser holographic, which were then compared to those

predicted by FEA analysis. Good agreements were found between the measured results and the FEA predictions. Nevertheless, they provided only a numerical solution rather than a more comprehensive analytical solution. In addition, their experimental measurement required elaborate laboratory setup and expensive equipment.

The study in this chapter is divided into two parts. In the first part, the study aims at the derivation of an analytical solution to predict the vibration response of clamped-clamped ribbed plates. The second part concentrates on the measurement of the vibration response of a clamped-clamped ribbed plate so that vibration characteristics of the ribbed plate predicted by the analytical solution can be verified experimentally. For this reason, a simple test-rig including a solid steel base, a steel plate and a narrow steel beam is assembled in the laboratory. Standard noise and vibration instruments, such as shaker, accelerometers are utilized in the measurement of vibration response of the test-rig.

7.2 Analytical approach

A clamped-clamped ribbed plate and the associated coordinate system are shown in Figure 7.1. It is assumed that the beam is firmly attached to the plate at location $x = x_b$, which is also clamped on both ends.

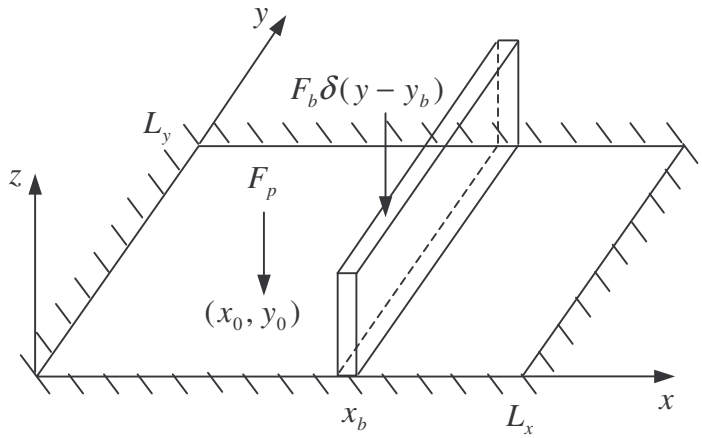

Figure 7.1. Model description of the clamped-clamped ribbed plate.

The analytical solution for the vibration response of the clamped-clamped ribbed plate can be obtained by employing the wave guide approach similar to that described in Chapter 2 where a clamped-clamped beam mode shape function is used in the semi-modal decomposition. The mode shape function of a clamped-clamped beam is given by Equation (A.4) in *Appendix A*, which is rewritten here as:

$$\phi_n(y) = \sinh(k_n y) - \sin(k_n y) - \beta_n[\cosh(k_n y) - \cos(k_n y)], \tag{7.1}$$

where $\beta_n = \dfrac{\sinh(k_n L_y) - \sin(k_n L_y)}{\cosh(k_n L_y) - \cos(k_n L_y)}$ is the modal constant of the clamped-clamped beam. The modal wave number k_n of the clamped-clamped beam is given by Equation (A.5) in *Appendix A*.

Following the same procedure as in Section 2.3 and using the clamped-clamped beam function in the semi-modal decomposition, Equation (2.6) becomes:

$$\frac{\partial^4 w_{1n}}{\partial x_I^4} + 2\alpha_n k_n^2 \frac{\partial^2 w_{1n}}{\partial x_I^2} + (k_n^4 - k_p^4) w_{1n} = -\frac{F_p \phi_n(y_0)}{D\Lambda_n^c} \delta(x_I - x_0), \tag{7.2}$$

where $\alpha_n = \dfrac{\Lambda_n^*}{\Lambda_n^c}$. Λ_n^c and Λ_n^* are the modal constants of the clamped-clamped beam, which are given by (also see Equations (A.9) and (A.20) in *Appendix A*):

$$\Lambda_n^c = \int_0^{Ly} \phi_n^2(y)dy = \beta_n^2 L_y + \frac{1}{2k_n}\{(1+\beta_n^2)\cosh(k_n L_y)[\sinh(k_n L_y) - 2(-1)^n] + 2\beta_n[2(-1)^n \sinh(k_n L_y) - \cosh^2(k_n L_y)]\}, \tag{7.3}$$

and

$$\Lambda_n^* = \int_0^{Ly} \phi_n^*(y)\phi_n(y)\,dy = -L_y + \frac{1}{2k_n}[(1+\beta_n^2)\sinh(k_n L_y)\cosh(k_n L_y) - 2\beta_n \sinh^2(k_n L_y) + 2\beta_n]. \tag{7.4}$$

The modal coefficients for the flexural and torsional vibrations of the clamped-clamped stiffened beam (Equations (2.7) and (2.8)) are rewritten here as:

$$v_n = -\frac{F_b}{G_n^c}\phi_n(y_b) + \frac{1}{G_n^c}(Q_{Ln} - Q_{Rn}), \tag{7.5}$$

and

$$\theta_n = -\frac{1}{G_{Tn}^c}[M_{Rn} - M_{Ln} + \frac{t}{2}(Q_{Ln} + Q_{Rn})], \tag{7.6}$$

where $G_n^c = B_b\Lambda_n^c(k_n^4 - k_b^4)$, $G_{Tn}^c = T\Lambda_n^c(Rk_n^4 + \alpha_n k_n^2 - k_t^2)$.

Similarly, from Equation (2.9), we have:

$$\frac{\partial^4 w_{2n}}{\partial x_{II}^4} + 2\alpha_n k_n^2 \frac{\partial^2 w_{2n}}{\partial x_{II}^2} + (k_n^4 - k_p^4)w_{2n} = 0. \tag{7.7}$$

Equations (7.2) and (7.7) are solved by employing travelling wave solutions similar to those described in Sections 2.4 and 2.5. The wave coefficients, as well as the coupling force and moment at the interface are again determined by a matrix equation given in the form of Equation (2.17). The square matrix $[C]_n$ for a clamped-clamped ribbed plate obtained from wave solutions is given in *Appendix D*.

7.3 Experiment measurements

7.3.1 Descriptions of the test-rig

The graphic illustration of the test-rig of the clamped-clamped ribbed plate used in the experiment is shown in Figure 7.2, where a 2.9*mm* thick flat rectangular steel plate is clamped to a very heavy solid steel base on all its four edges. The surface area of the plate after being secured on the solid steel base is measured at $S = 0.87 \times 0.618m^2$. A steel beam with rectangular cross sectional area of $A_b = 30 \times 3mm^2$ is attached (glued) on the plate surface at $x_b = 0.57m$ (measured from the original of the coordinate system as indicated in Figure 7.2). The material

properties of steel given by Norton [53] ($E = 1.95 \times 10^{11} N/m^2$, $\rho = 7700 kg/m^3$ and $\nu = 0.28$) are used for both the beam and the plate in the simulation. The reason that steel rather than aluminum is used in the experiment is because the steel panel is available at time of measurements.

Figure 7.2. Graphic illustration of the test-rig used in the measurement.

7.3.2 Instruments used in the measurement

The major instruments used in the experiment include:

1) A two-channel HP spectrum analyzer (type HP35665A)
2) A B&K vibration shaker (type 4809)
3) A B&K impedance head (type 8001)
4) A B&K vibration calibrator (type 4294)
5) Two B&K accelerometers (type 4375)
6) Two NVMS charge amplifiers
7) A Yamaha power amplifier (type AX-570)

7.3.3 Experiment setup

A schematic illustration of the power chain used in the measurement is shown in Figure 7.3. The broadband white noise signals generated by the HP analyzer are pre-amplified by the Yamaha power amplifier before being used to drive the B&K vibration shaker. The shaker is hanged vertically on a supporting wooden frame by two thin steel wires to exert a normal excitation force on the test rig. A B&K impedance head is tightly screwed on the head of the shaker, while the sensor side of the impedance head is connected to a thin steel rod (1mm in diameter), which has threads on both ends. The other end of the thin steel rod was tightly screwed on a short aluminum stud. The aluminum stud is glued on the plate surface at location $(x_0, y_0) = (0.27m, 0.15m)$. The main purpose of the thin steel rod in the setup is to eliminate the vibration forces other than the normal force generated by the vibration shaker. The surface of the plate is marked by 19×14 mesh grids before the experiment, which are used later in the mode shape measurement of the ribbed plate.

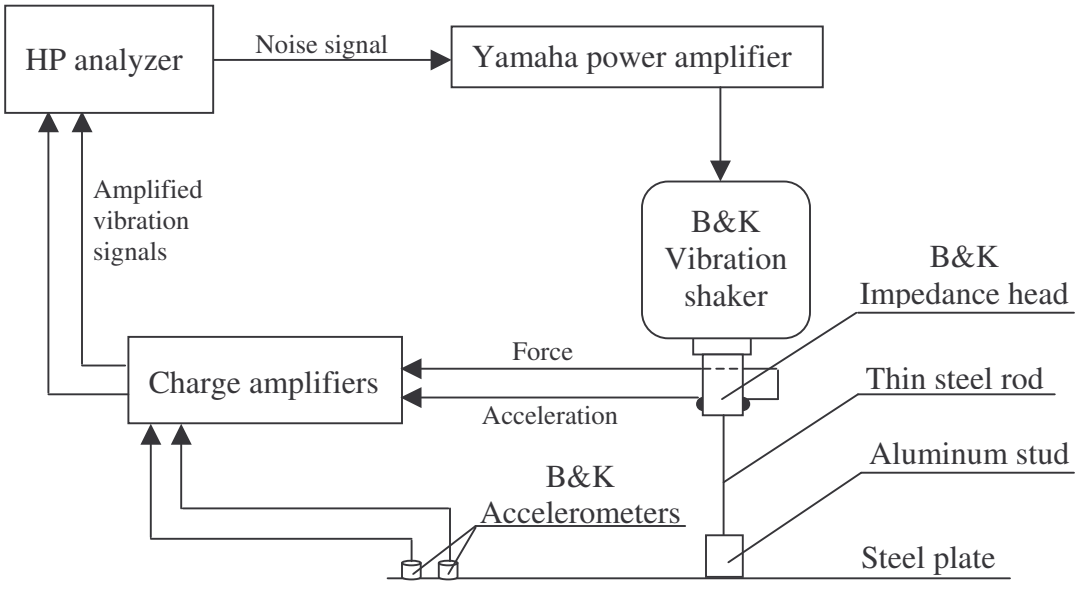

Figure 7.3. Schematic illustration of the power chain setup used in the experiment.

The frequency response function (acceleration/force) at the source location is measured directly by the impedance head. The response of the ribbed plate at locations other than the source location is measured by two B&K accelerometers. The impedance head and the accelerometers are pre-calibrated by a B&K vibration calibrator before the measurements. The vibration signal picked up by the impedance head or the accelerometers are pre-amplified by charge amplifiers and then analyzed by the HP analyzer.

7.4 Boundary conditions of the test-rig

The effective boundary conditions of the test-rig are examined prior to the attachment of the beam on the plate. This is done by comparing the peak frequencies obtained from the measured frequency response function of the un-ribbed plate to the natural frequencies of the corresponding ideal clamped-clamped plate predicted by FEA normal mode analysis. The frequency response function (acceleration/force) of the un-ribbed plate measured at the source location is shown in Figure 7.4.

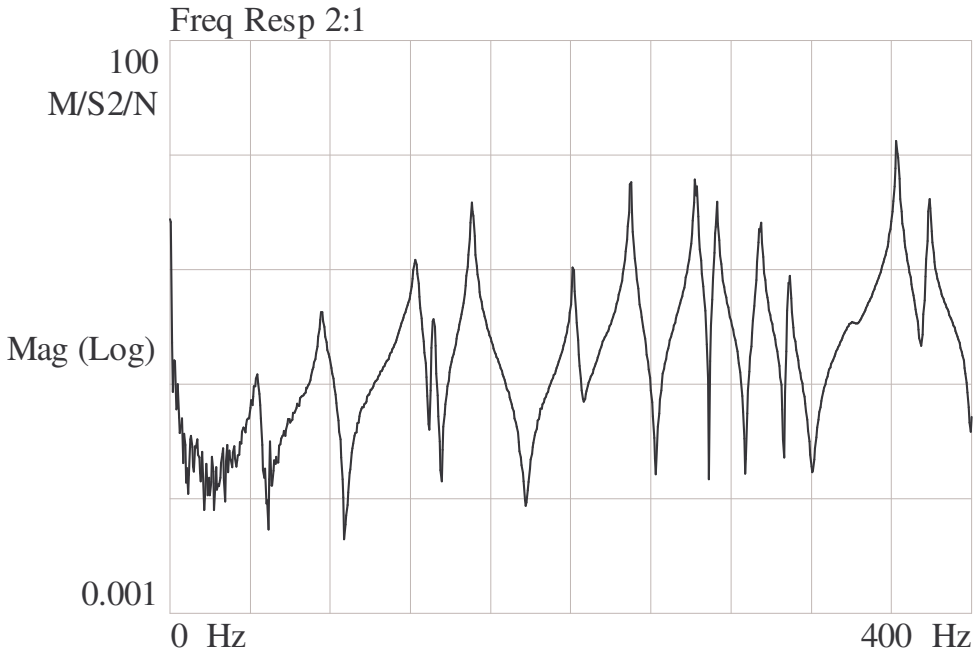

Figure 7.4. The measured frequency response function at the source location of the un-ribbed plate.

The measured peak frequencies as shown in Figure 7.4 are listed in Table 7.1 together with the natural frequencies predicted by FEA analysis. Good agreements are found between the measured and the predicted modal frequencies at frequencies above 100Hz. Nonetheless, large discrepancies are also found between the measured and the predicted modal frequencies for the first two modes at low frequencies. A separate FEA normal mode analysis indicates that the boundary condition of the test-rig at low frequencies is somewhere between the simply support and the clamped boundary conditions. It resembles the simply support boundary condition at very low frequencies and approaches the clamped boundary condition as frequency increases. The well-known numerical discrepancy of FEA analysis is also observed at higher frequencies where the modal frequencies of the clamped-clamped plate are under predicted by FEA analysis resulting from insufficient numerical discretions of the plate.

Table 7.1 Resonant frequencies of the un-ribbed plate

Experiment	Finite Element Analysis (clamped-clamped plate)	Error
43.5Hz	50.7Hz	16.55%
76.0Hz	81.6Hz	7.37%
122.5Hz	121.7Hz	-0.65%
131.5Hz	133.3Hz	1.37%
150.5Hz	149.5Hz	-0.66%
201.5Hz	196.9Hz	-2.28%
Not excited	204.3Hz	N/A
230.0HZ	229.4Hz	-0.26%
262.0Hz	255.3Hz	-2.56%
273.0Hz	263.9Hz	-3.33%
295.0Hz	293.9Hz	-0.37%
309.0Hz	299.4Hz	-3.11%
362.5Hz	350.2Hz	-2.93%
379.0Hz	362.2Hz	-3.39%
Not excited	373.1Hz	N/A

7.5 Vibration response of the ribbed plate

7.5.1 Input mobility by prediction

The input mobility of the clamped-clamped ribbed plate is calculated for two excitation cases, (a) point force excitation applied at $y_b = 0.15m$ on the beam, and (b) point force excitation applied at $(x_0, y_0) = (0.27m, 0.15m)$ on the plate. A constant damping value ($\eta = 0.01$) is assumed for both plate and beam in the simulation. To evaluate the accuracy of the proposed method in the prediction of vibration response of completely clamped-clamped ribbed plates, the real parts of the calculated input mobilities of the ribbed plate for the two excitation cases are shown in Figures 7.5 and 7.6 respectively together with those obtained from FEA analysis. Good agreements are found between the results in the whole frequency range of investigation (for frequencies up to $1000Hz$) for both excitations.

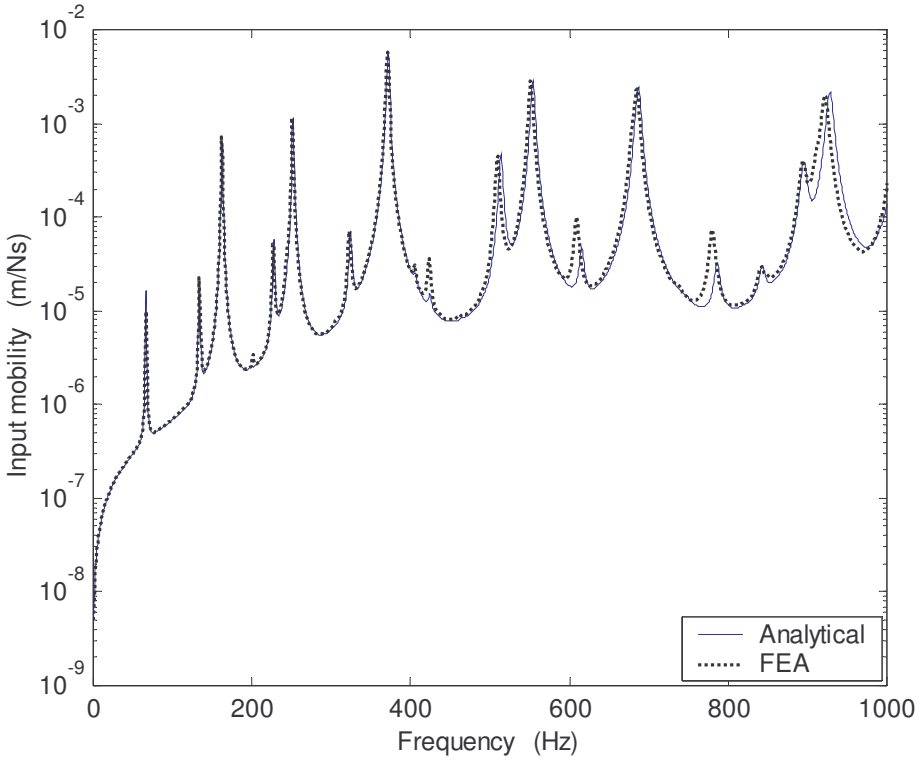

Figure 7.5. The real part of input mobility of the clamped-clamped ribbed plate to point force excitation applied on the beam.

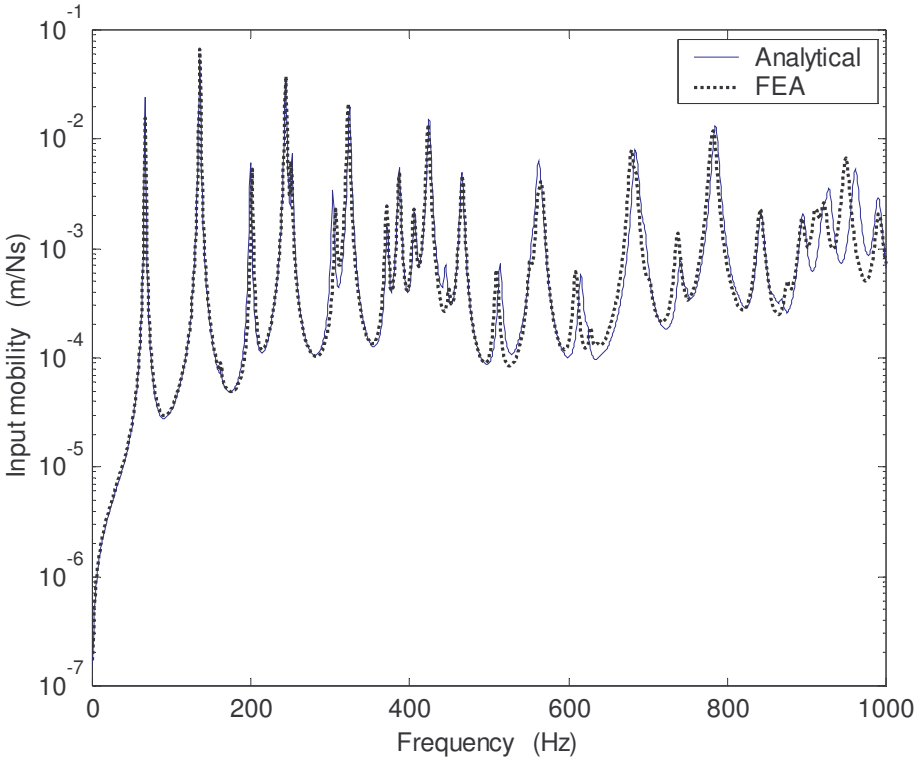

Figure 7.6. The real part of input mobility of the clamped-clamped ribbed plate to point force excitation applied on the plate.

7.5.2 Input mobility by measurement

The validity of the proposed method is also evaluated in this study by comparing the predicted input mobility of the ribbed plate to that measured experimentally. The predicted and measured input mobilities of the ribbed plate to point force excitation applied at location $(x_0, y_0) = (0.27m, 0.15m)$ on the plate are shown in Figure 7.7. To minimize the effect of phase shift caused by noise in the measurement on the display of the input mobility, magnitude rather than real part of the input mobility is shown in the figure. There is general good agreement between the predicted and the measured results. However, some discrepancies between the results are also observed at both low and higher frequency ends of the data. The discrepancy between the predicted and the measured peak amplitudes at low frequencies is mainly caused by the constant damping value ($\eta = 0.01$) used in the simulation. Such discrepancy could be prevented if modal damping values are used in the calculation.

The modal damping value of the ribbed plate can be calculated from the half power bandwidth of the modal response as:

$$\eta_n = \frac{\Delta\omega_n}{\omega_n}, \tag{7.8}$$

where the bandwidth $\Delta\omega_n$ is determined at frequencies where the modal response amplitude decreases to $\frac{1}{\sqrt{2}}$ of the peak amplitude. The modal damping value of the ribbed plate estimated from the peak frequencies of the measured frequency response function are listed in Table 7.2. The input mobility of the ribbed plate using modal damping values and constant damping value of $\eta = 0.01$ for all other non-resonant frequency bands is re-calculated, which is shown by the thick dash line in Figure 7.7.

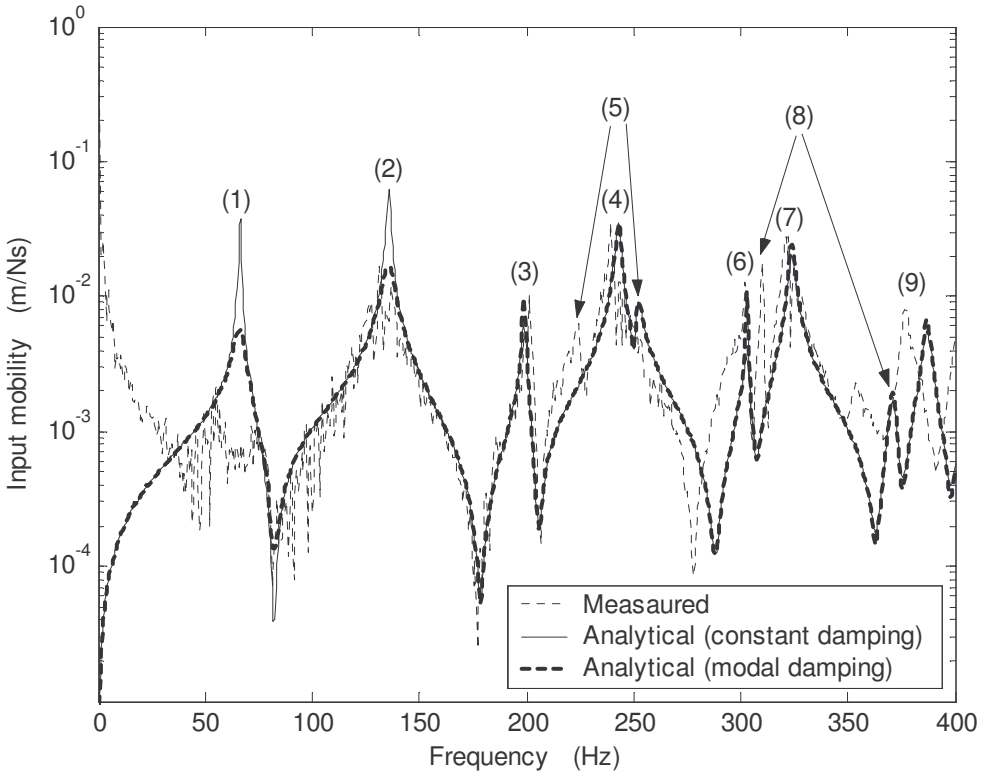

Figure 7.7. Predicted and measured input mobilities (magnitude) of the clamped-clamped ribbed plate.

Table 7.2 Estimated modal damping values of the ribbed plate

Mode number	Predicted resonant frequency (Hz)	Modal damping
#1	66	0.08
#2	136	0.04
#3	201	0.01
#4	243	0.01
#5	251	0.01
#6	307	0.01
#7	322	0.012
#8	370	0.005
#9	386	0.005

The discrepancy between the predicted and the measured peak frequencies for the two vibration modes at higher frequencies in Figure 7.7 (the peaks marked by (5) and (8)) is investigated in the subsequent analysis.

7.5.3 Mode shape measurements

In Figure 7.7, only the measured and predicted peak frequencies were compared. However, to make sure that a measured peak and a predicted peak refer to the same mode of a structure, both the peak frequencies and the mode shape distributions need to be compared.

The mode shape distributions of the ribbed plate can be obtained experimentally from the auto-spectrum measured at the grid locations on the plate when the ribbed plate is under steady state broadband noise excitation. The consistency for this set of measurement is verified by comparing the auto-spectrum at the source location prior to and after the mode shape measurements of the ribbed plate, which are shown in Figure 7.8.

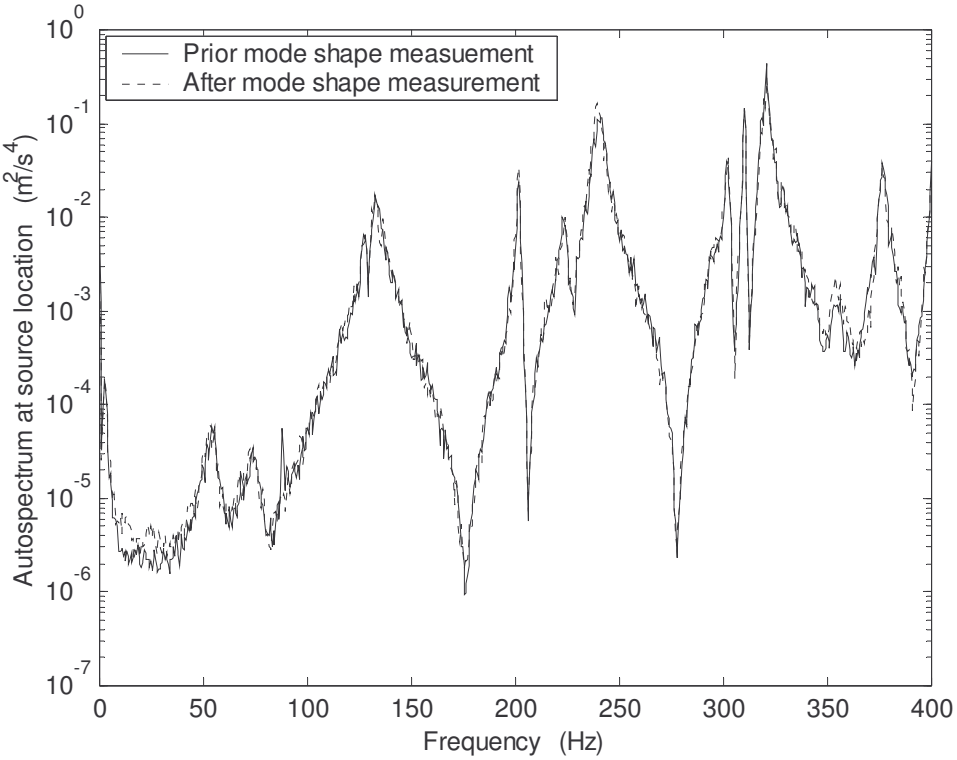

Figure 7.8. Auto-spectrum of the plate acceleration measured at the source location.

It is shown in Figure 7.7 that there are two response peaks in the measured frequency response corresponding to the first predicted response peak of the clamped-clamped ribbed plate (the peak marked by (1) in the figure), one has lower peak frequency (55Hz) and the other has a higher peak frequency (71Hz). According to the discussion on the effective boundary conditions of the test-rig in **Section 7.4**, we believe that the peak corresponding to the predicted peak should be the one at lower frequency. The comparison between the measured mode shape of this peak and the mode shape predicted by FEA at the corresponding frequency as shown in Figure 7.9 confirms that. So, how about the peak at higher frequency?

The measured mode shape of the peak at higher frequency shows that it has similar mode shape distribution as that of the peak at lower frequency. Furthermore, a separate FEA simulation shows that the peak at higher frequency matches the fundamental mode of the source plate section enclosed by the clamped boundaries of the rig and the stiffened beam in both modal frequency and mode shape. For this mode, the beam also behaves as a definite (clamped) boundary condition to the source plate section [89]. Therefore, for this mode, the modal energy is confined within the source plate section where no vibration energy is transmitted to the receiving plate section through the stiffened beam.

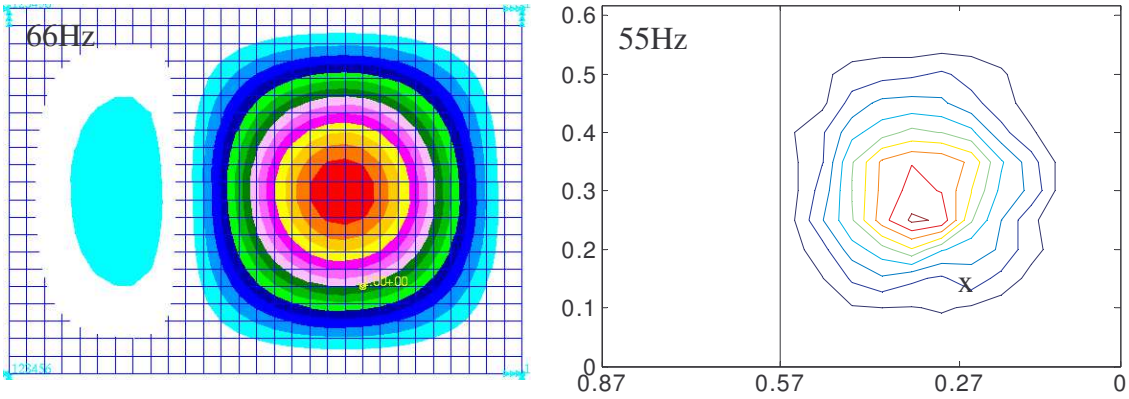

Figure 7.9. Vibration mode shape distribution of the fundamental mode of the clamped-clamped ribbed plate. (a) Predicted; (b) Measured.

Good agreements are found between the measured and the predicted mode shapes at the corresponding frequencies for all other modes as indicated in Figure 7.7. Particular interest is paid to the two structural modes marked by (5) and (8) in the figure in order to understand why there is a large difference between the measured and predicted peak frequencies for these two modes. The mode shape distributions of the two modes are shown in Figures 7.10 and 7.11. It is observed that unlike the other modes in the frequency range of investigation where the beam is located at the

nodal position of the modes, the beam is located at or close to the anti-nodal position of the modes. Therefore, the modal stiffness of these two modes is greatly affected by the flexural stiffness of the beam. Meanwhile, the flexural stiffness of the beam depends not only on the cross sectional area and material properties of the beam, but also on the beam boundary conditions. As a result, any imperfection on the beam boundary condition in the setup of the test-rig would lead to a large discrepancy between the predicted and measured modal responses for these two modes and the extra measured peak at above 350Hz. The resonance frequency for the corresponding predicted peak is out of the frequency range due to the large discrepancy.

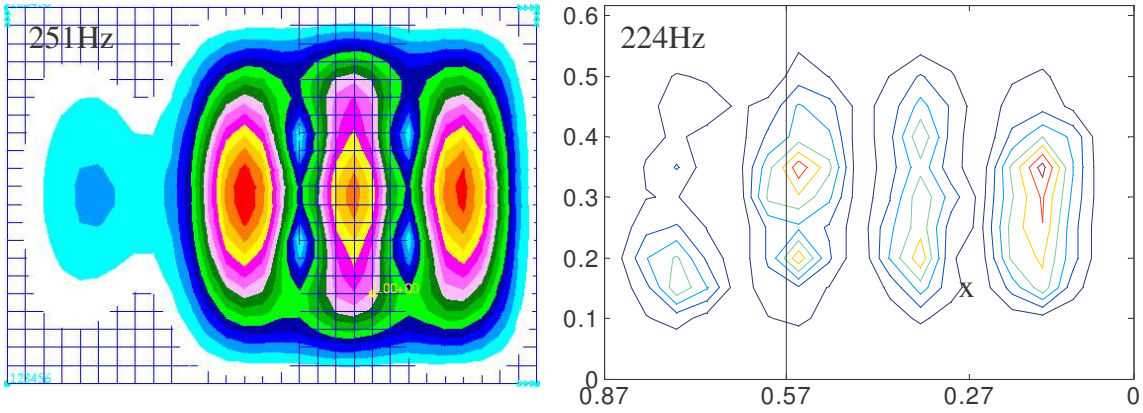

Figure 7.10. Mode shape distributions of the clamped-clamped ribbed plate. (a) Predicted ; (b) Measured.

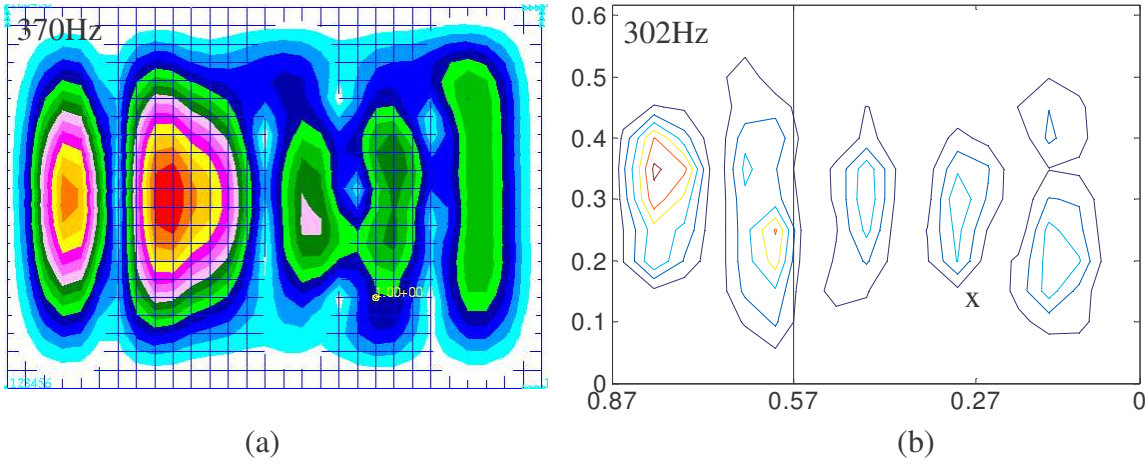

Figure 7.11. Mode shape distributions of the clamped-clamped ribbed plate. (a) Predicted; (b) Measured.

7.5.4 Effects of beam boundary conditions

The stiffened beam is assumed to be completely clamped on both ends in the simulation while it is only partly clamped on the solid steel base in the test-rig. It is found that only the lower part of the short beam edges are glued to the heavy solid steel base while the upper part of the beam edges are not attached to the test-rig because of the gaps in the setup (see Figure 7.2).

When the beam is located at or close to the nodal position of a vibrating mode, the beam flexural stiffness has little effect on the stiffness of the mode. Therefore, the vibration response of a vibrating mode would not be affected by the difference between the ideal and the practical beam boundary condition in the experiment. In contrast, the flexural stiffness of the beam plays a significant role on the vibration response of a mode when the beam is located at or close to the anti-nodal position of the mode. As a result, the difference between the practical and the ideal beam boundary conditions would result in a large discrepancy between the measured and predicted modal responses. A separate FEA calculation shows that if the two beam edges are only partly clamped in the simulation, the predicted natural frequencies of the ribbed plate for these two modes would become 217.1Hz and 299.8Hz, which agree well with the corresponding measured peak frequencies of the modes (at 224Hz and 302Hz respectively). In this FEA simulation, the beam was meshed by plate elements so that clamped boundary conditions can be assigned on part of the short beam edges.

7.5.5 Characteristics of the input mobility

The characteristics of vibration response of the clamped-clamped ribbed plate are studied by the point force input mobilities of the ribbed plate calculated at different excitation locations on the plate, which are shown in Figure 7.12. A constant

damping value ($\eta = 0.01$) is used in this simulation. It is shown that the dependency of the input mobility on the distance between the stiffened beam and the source location is similar to that found for simply supported ribbed plates (see Chapter 3). It is beam stiffness control when the source is applied on the beam or very close to the beam and is plate stiffness control when the point force is more than a quarter of plate bending wavelength away from the beam.

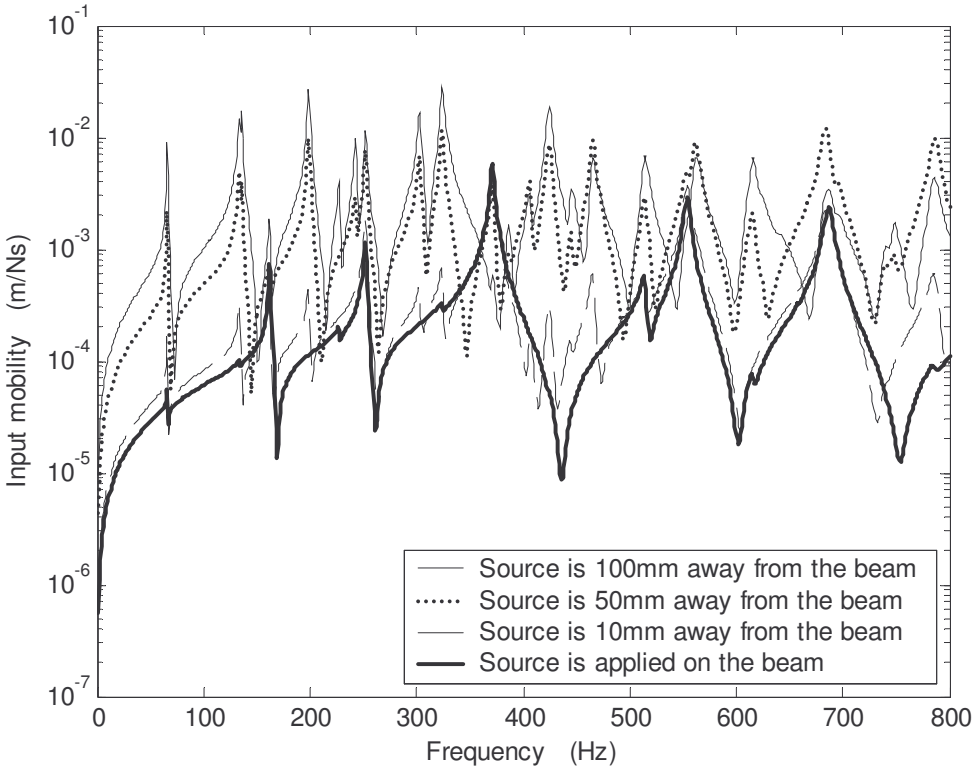

Figure 7.12. The predicted input mobilities (magnitude) of the clamped-clamped ribbed plate.

Characteristics of the input mobility of the ribbed plate are also investigated experimentally in this study, and are shown in Figure 7.13. The experimental results confirm that the input mobility of the ribbed plate is a function of the distance between the source location and the beam. Nevertheless, the dependency of the measured input mobility on the distance between the source location and the beam is

not as significant as that predicted in the analytical solution, particular when the source location is very close to the beam. This is attributed to the setup of the force excitation in the experiment where the force is applied on the plate via an aluminum stud, which is 12mm in diameter. Therefore, the excitation force is not a point force as that assumed in the analytical solution. Moreover, in the measurement, the distance between the source and the beam is measured from the centre of the stud to the mid plane of the beam. Thus, the influence of beam flexural stiffness to the measured input mobility of the ribbed plate is less significant as that in the analytical solution for the same distance, particularly when the source is close to the beam.

On the other hand, because the force signal generated by the B&K shaker is very weak at low frequencies (sensitivity range, $f > 50Hz$), the measured input mobilities at low frequency range are greatly contaminated by noise. This helps to explain why the measured input mobilities have different shapes when compared to those of the analytical predictions at low frequencies.

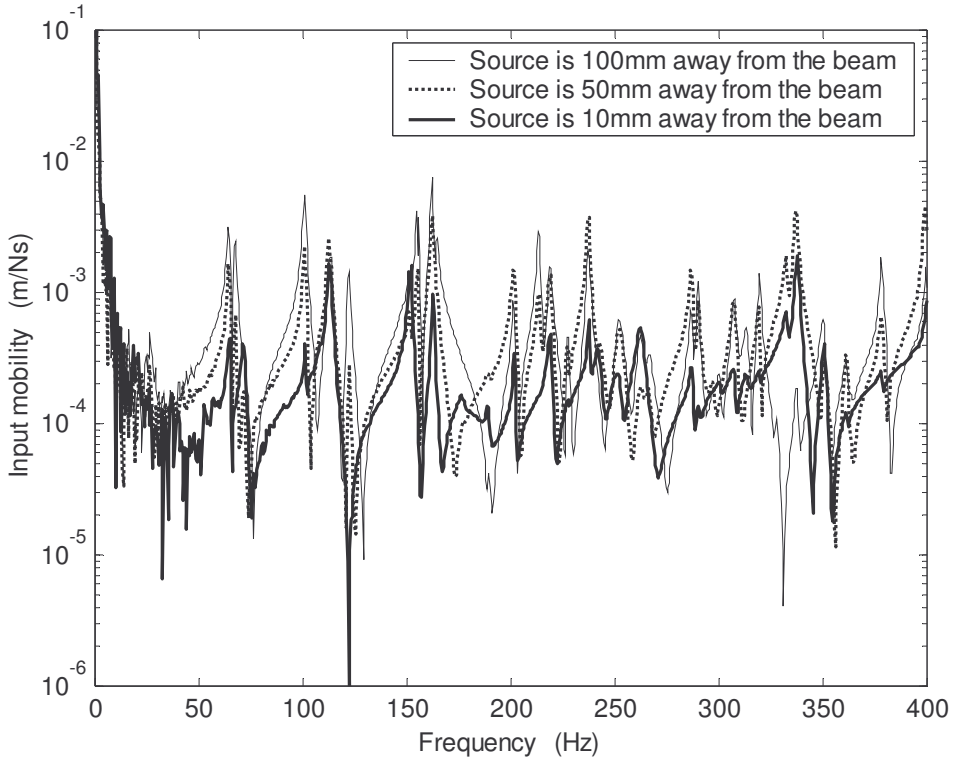

Figure 7.13. The measured input mobilities (magnitude) of the test-rig.

7.6 Conclusion

The vibration response of a clamped-clamped ribbed plate is studied both analytically and experimentally in this chapter. General good agreement is found between the experimental results and the analytical predictions. Nevertheless, some discrepancies are also observed between the results and explanations are given. The difference between the measured and predicted modal frequencies of the fundamental mode of the ribbed plate is caused by the difference between the effective boundary condition of the test-rig at low frequencies and the ideal clamped-clamped boundary condition. While the discrepancy between the measured and predicted modal frequencies for two of the modes at higher frequencies is due to the difference between the practical and the ideal clamped boundary conditions of the beam.

The dependency of the input mobility of the ribbed plate on the distance between the source location and the beam is confirmed experimentally in this study. It is beam stiffness control when the excitation location is applied at or very close to the beam and is plate stiffness when the beam is more than a quarter of plate bending wavelength away from the source.

Chapter 8

Evaluation of frequency dependent rubber mount stiffness and damping by impact test

8.1 Introduction

Rubber mounts have been used widely in the control of energy transmission from vibrating machinery to the supporting structures. Nevertheless, because of the visco-elastic behaviour of the rubber material, its dynamic properties are difficult to define. The dynamic properties of rubber materials are usually evaluated experimentally. The insufficiency of traditional methods for such measurements has prompted the development of alternative methods.

8.2 Literature review

A critical component used in machine isolators is rubber mounts. Due to the unique characteristics of rubber materials, the dynamic properties of rubber mounts are often difficult to quantify, which has posed some limitations on its applications. It has been found that, in general, rubber dynamic properties depend on static pre-load, vibration amplitude, temperature and excitation frequency [90]. Numerous studies in the last few decades have continually improved the understanding of the dynamic characteristics of rubber materials. Many different techniques have been developed to estimate the rubber dynamic properties experimentally. Servo-hydraulic systems are widely used to measure rubber static stiffness. They were also used to measure the dynamic stiffness and damping of rubber at discrete frequencies [91]. The non-linear effects of rubber dynamic stiffness have recently been investigated on a servo-hydraulic system by superimposing a noise signal on a pure tone source [92].

However, direct measurement on servo-hydraulic systems is limited to the low frequency range due to the response sensitivity of the actuator to the excitation signal. The other drawback is that the method is time consuming, let alone the limitation of the method in the measurement on real installations. Other methods, such as direct and indirect stiffness methods are widely used in the measurement of dynamic properties of rubber materials. The direct method measures the reaction force on the blocked terminal of the rubber and displacement on the rubber free end. Rubber stiffness can then be determined directly from the measured transfer function between the force and the displacement [93]. In contrast, in the indirect method, the reaction force is measured indirectly by using Newton's second law [94-96]. Alternatively, the dynamic properties of a rubber isolator can be determined by measuring its four-pole parameters [97, 98]. However, both direct and indirect methods require elaborate laboratory settings, which is often a problem in many practical measurements. In addition, bulky seismic masses are required by the indirect method.

In this chapter, an alternative simple experimental method, which adopts an impact test is proposed to evaluate the frequency dependent stiffness and damping of rubber mounts. Piecewise polynomial curve fitting is employed to estimate the frequency dependent stiffness and damping value of rubber mounts by a single test. The method differs from the traditional direct and indirect methods for such measurements. It only requires minimum experimental setup and is easy to implement. The assessment covers the frequency bands below, at and above resonance where the resonant behaviour of the test system is taken into account. The transition of the rubber mount stiffness from static to dynamic values is clarified and the static stiffness is obtained as a by-product of the method.

8.3 Theoretical formulation

A rubber-mass system is represented by a single degree of freedom (SDOF) system in this study as shown in Figure 8.1. For sufficiently small vibration amplitude (linear behaviour), the equations of motion of the rubber-mass system with frequency dependent stiffness K and damping coefficient η can be written in the frequency domain [90] as:

$$[-m\omega^2 + K(\omega)(1 + j\eta(\omega))]\tilde{x}(\omega) = \tilde{F}(\omega), \tag{8.1}$$

where the tilde (~) indicates Fourier transformation, m and $\tilde{x}$ are the mass and the displacement of the SDOF respectively, $\tilde{F}$ is the external force and ω is the angular frequency. The validity of Equation (8.1) in representing the dynamic behaviours of the SDOF system with frequency dependent stiffness and damping by impact test is examined by shaker excitation using discrete input frequencies in Section 8.6.

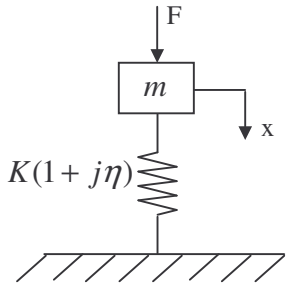

Figure 8.1. Illustration of an ideal damped SDF spring mass system.

From Equation (8.1), the complex receptance function of the system is written as:

$$\overline{R} = \frac{\tilde{x}}{\tilde{F}} = \frac{1}{K[(1 - r^2) + j\eta]}, \tag{8.2}$$

where the variable $r = \dfrac{\omega}{\omega_n}$ is the frequency ratio and $\omega_n = \sqrt{\dfrac{K}{m}}$ is the natural frequency of the SDOF system, which is determined from the measured frequency response function.

The real and imaginary parts of the complex receptance are readily available from Equation (8.2) and are given by:

$$\mathrm{Re}(\overline{R}) = \frac{1-r^2}{K[(1-r^2)^2+\eta^2]}, \tag{8.3}$$

and

$$\mathrm{Im}(\overline{R}) = \frac{-\eta}{K[(1-r^2)^2+\eta^2]}. \tag{8.4}$$

The following relations for rubber damping and stiffness as functions of frequency can be obtained from Equations (8.2), (8.3) and (8.4) as:

$$\eta = -\frac{\mathrm{Im}(\overline{R})}{\mathrm{Re}(\overline{R})}(1-r^2), \tag{8.5}$$

and

$$K = \frac{\mathrm{Re}(\overline{R})}{\left|\overline{R}\right|^2(1-r^2)}, \tag{8.6}$$

where $\left|\overline{R}\right|$ is the absolute value of the complex receptance.

$\mathrm{Re}(\overline{R})$, $\mathrm{Im}(\overline{R})$, $\left|\overline{R}\right|$ and ω_n can be obtained directly from the measured frequency response function by impact test. They are substituted into Equations (5) and (6) to obtain η and K. It has been pointed out by Ewins [99] that the natural frequency of SDOF can be obtained by the frequency of maximum response or by the frequency of peak imaginary part of the receptance function or by the frequency at zero value of the real part of the receptance function. However, care should be taken in choosing the value of ω_n since the magnitude, real and imaginary part of the measured frequency response function each gives a slightly different value of ω_n. Selecting the wrong one can have implications for the values of damping and modal constant [99] (stiffness in our case). It has been found that the correct value of ω_n is the value that gives continuity across the resonant band for the stiffness and damping

coefficient according to Equations (8.5) and (8.6). This will be explained in subsequent analysis.

It is worth noting that the singularity of $\frac{1}{\mathrm{Re}(\overline{R})}$ in Equation (8.5) and that $\frac{1}{1-r^2}$ in Equation (8.6) are exactly cancelled theoretically by the zeros in the equations. In practice, such cancellation will not be exact because of the background noise and error in the determination of the resonance frequency for r^2. Therefore, a large error may occur in the determination of η and K at these singularities. Awareness of such singularity problems and the continuation of η and K as functions of frequency suggest the use of a smooth curve fitting technique to determine η and K near the resonance frequency.

One advantage of the proposed method is that the rubber mount stiffness and damping can be determined without knowing the exact mass of the system, which is often difficult to quantify in such measurements since the rubber element has distributed mass and stiffness [98].

8.4 Experimental setup

In the experimental set up, a typical industrial machine rubber mount with an end steel cap is tightly glued to a cylindrical steel mass (~1kg) on one end and to a 10mm thick steel slab on the other end as illustrated by Figure 8.2. The thick steel slab is secured to a very heavy concrete block by screws to resemble the clamped boundary condition. In this setup, the steel mass forms the rigid mass of the SDOF system and provides static pre-load on the rubber. The rubber block provides the stiffness and damping for the SDOF system. The effect of the distributed mass of the rubber

mount was investigated in a separate Finite Element Analysis. It is found that it has little effect on the system dynamic characteristics in the low frequency range. This finding is also supported by experimental results presented in Section 8.6. Impact hammer is used to apply force along the centre of the mass while the response of the mass is measured by two accelerometers attached to the mass on each side of the disk and at the same distance away from the centre. Such arrangement will cancel, or minimize the effect of rocking motion modes on the measured frequency response function from the impact test. A soft rubber tip is chosen and attached to the impact hammer in order to generate low frequency force components. Ten averages were taken in each test to cancel the effect of random noise. A similar impact force level is applied each time to minimize the dependency of rubber dynamic properties on excitation amplitude. The dynamic properties of the rubber block are determined directly by Fast Fourier Transform (FFT) of the measured impact force and displacement at the free end of the setup.

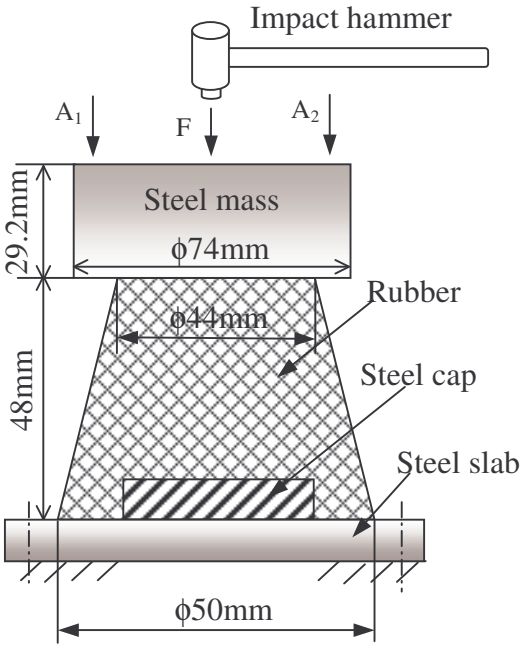

Figure 8.2. Graphic illustration of the set up for the measurement of frequency dependent rubber stiffness and damping of the machine rubber mount by impact test.

8.5 Experimental estimation of frequency dependent rubber mount stiffness and damping

In this experiment, the receptance frequency response function is measured by impact test. The natural frequency of the SDOF system is also determined from the same test. Equation (8.5) is then used to estimate the damping coefficient of the rubber mount as a function of frequency, which is shown by the dotted line in Figure 8.3. In this plot, the large variation of the damping curve at resonance is due to the fact that the real part of the measured receptance function at resonance is not exactly cancelled by the zeros in the numerator.

Although the impact test covered the frequency range from 0Hz to 800Hz where excellent coherence between the measured signals at frequencies above the resonant frequency of the rocking motion mode has been found in the test, only a portion of the calculated damping coefficients (between 100Hz and 300Hz) can be used in the least-squares curve fitting in the evaluation of the damping coefficient. This is because the measured value of the damping coefficient is sensitive to the presence of disturbances in the experimental data, such as response of the rocking motion mode at low frequencies, boundary conditions and noise at higher frequencies. A small phase shift in the measured receptance function can cause severe deviation in the calculated damping value at frequencies distance away from the resonant band. It is found that outside the chosen frequency band, the damping coefficient is affected significantly by the above-mentioned disturbances. Therefore, the measured damping coefficient is only curve fitted in the frequency range where the disturbance is small. Such curve fitted damping coefficient is also used for the reproduction of the system response in the entire frequency range of interest based on the assumption that $\eta(f)$ is a linear function of frequency. The resulting damping coefficients from least squares curve fitting is:

$$\eta(f) = 0.1512 + 1\times10^{-4} f \,, \tag{8.7}$$

where f is the frequency.

It follows that the damping coefficient approximated by the least-squares curve fitting in Equation (8.7) is non-unique since broadening or narrowing the frequency range of the curve fitting (to include or exclude more data in the least-squares curve fitting) would change the coefficients slightly. Nevertheless, it is found that fluctuation of the estimated damping coefficient is no more than 10% unless the fitting frequency range is extended to where the data is severely contaminated by noise or the neighboring modes. The damping coefficient of the rubber mount approximated by Equation (8.7) is also shown in Figure 8.3 by the solid line.

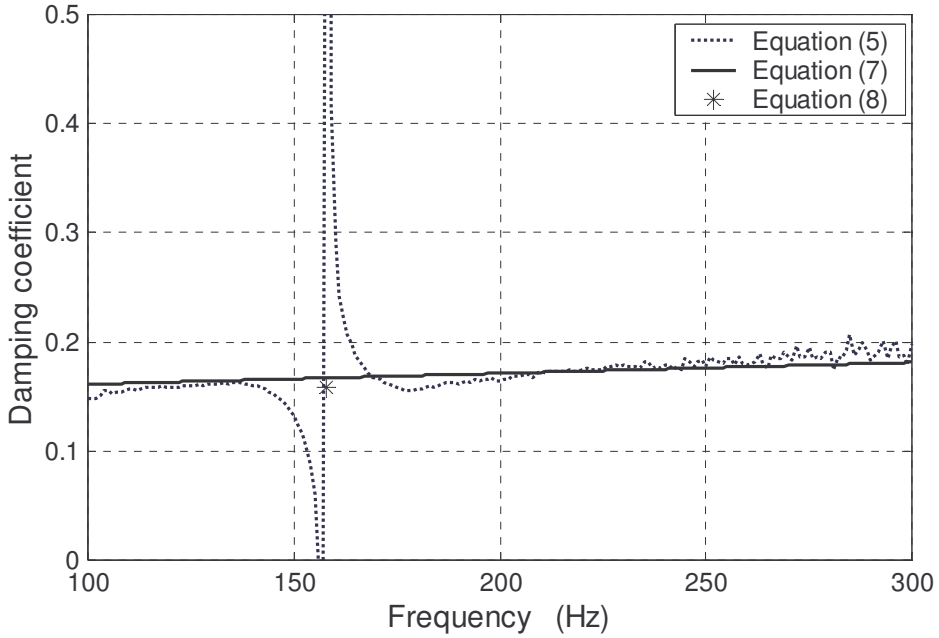

Figure 8.3. Frequency dependent damping coefficient of rubbed machine mount.

In our specific experiment, the damping coefficient at resonance can also be evaluated by the half power bandwidth method to be:

$$\eta = \frac{\Delta\omega}{\omega_n} = 0.158 . \tag{7.6}$$

The half power bandwidth $\Delta\omega = 25Hz$ in Equation (7.6) is determined from where the frequency response amplitude is $1/\sqrt{2}$ of the peak amplitude. In contrast, the damping coefficient obtained from Equation (8.7) at resonance ($f_n = 158Hz$) is $\eta = 0.167$. The difference between the damping coefficients evaluated by Equation (8.7) and Equation (7.6) is mainly due to the frequency resolution used in the measurement. Since it can be seen from Equation (7.6) that the accuracy of η from the half power bandwidth method largely depends on the accuracy of $\Delta\omega$ and ω_n, whose values differ with different frequency resolution. For example, in our case, the half power bandwidth is between $25Hz$ and $26Hz$. If $25Hz$ is used in Equation (7.6), it will give $\eta = 0.158$, if $26Hz$ is used, the equation calculates η as 0.165.

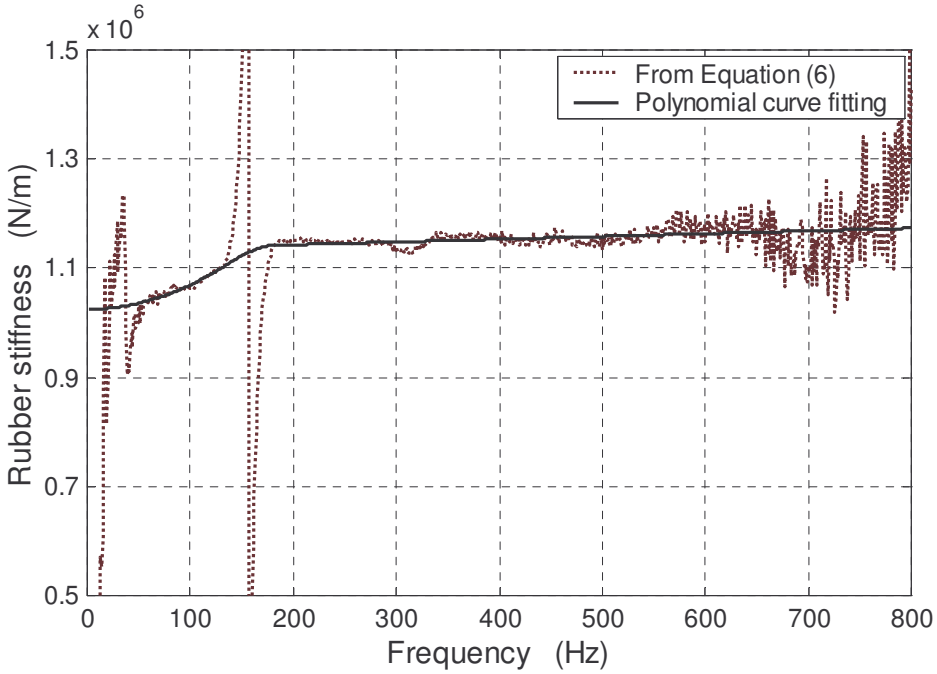

Figure 8.4. Frequency dependent rubbed stiffness of the rubbed machine mount.

The frequency dependent rubber mount stiffness calculated from Equation (8.6) is shown by the dotted line in Figure 8.4. Effect of the low frequency rocking motion

mode is evident from the discontinuity at 38Hz in the stiffness curve. This rocking motion mode at 38Hz was also verified by separate Finite Element Analysis. It occurs at such low frequency due to the slender shape of the rubber element used in the experiment. Effect of the noise in the measurement becomes severe at frequencies above 600Hz. Similar to Equation (8.5), the denominator in Equation (8.6) at resonance is not exactly cancelled by the zeros in the numerator, which causes the discontinuity in the calculated stiffness curve at frequencies around the resonance frequency.

Inspection of the calculated stiffness curve (shown by the dotted line in Figure 8.4) indicates that piecewise polynomial curve fitting is required to closely predict the rubber mount stiffness in different curve sections. The curve is then subdivided into three sections: a) below the resonant band, b) above the resonant band, and c) within the resonant band. The resonant band defined here extends the frequency bandwidth to where the response amplitude is about half of its peak value.

a) Below the resonant band

Frequency range of curve fitting: $50Hz \le f \le 135Hz$.

Data below 50Hz is ignored due to the effect of the resonant response of the rocking motion mode at 38Hz and the low frequency noise. The upper frequency is chosen at where the response amplitude is about half of the peak amplitude. It is found that this curve section exhibits clear non-linear behaviour, a non-linear function given by Equation (8.8a) is chosen to fit the curve in this section where the linear term is omitted intentionally to ensure zero slope of K at zero frequency.

$$K_1(f) = a_1 f^2 + b_1. \qquad (8.8a)$$

The two coefficients are determined from the least-squares curve fitting as $a_1 = 4.42$, $b_1 = 1.025 \times 10^6$. Value of b_1 is the static stiffness, i.e. the stiffness at zero frequency.

This means that the rubber mount static stiffness can also be evaluated by the proposed method.

b) Above the resonant band

Frequency range of curve fitting: $183Hz \le f \le 600Hz$.

The curve fitting in this section begins at 183Hz where the amplitude of the measured frequency response is about half of the peak amplitude. It ends at 600Hz where the noise contamination in the data becomes severe. The trend of the stiffness curve in this section indicate that it can be described well by a linear function, which is given by:

$$K_3(f) = a_3 f + b_3 . \tag{8.8b}$$

The coefficients are found to be $a_3 = 50.8$, $b_3 = 1.133 \times 10^6$ by least-squares curve fitting.

c) Within the resonant band

Frequency range of curve fitting: $135 < f < 183$.

In this frequency range, the dependency of the rubber mount stiffness on frequency transits from non-linear to linear. To ensure the continuity of the stiffness values and slopes across the resonant band, a four-term polynomial function is chosen to prescribe the stiffness in this frequency band as:

$$K_2(f) = a_2 f^2 + b_2 f + c_2 + d_2 \frac{1}{f} . \tag{8.8c}$$

The function is chosen such that the highest power of the variable (frequency) for the polynomial and its derivative is the minimum. The four constants can be determined uniquely from the values of stiffness and slopes on the boundaries at 135Hz and 183Hz. The values of these constants are found to be $a_2 = -31.57$, $b_2 = 1.386 \times 10^4$, $c_2 = -7.492 \times 10^5$ and $d_2 = 7.549 \times 10^7$.

By extending the application region of Equation (8.8a) to zero frequency (static state) and Equation (8.8b) to 800Hz, the complete stiffness curve can be approximated by the combination of the three fractional curve fittings, which is shown by the solid line in Figure 8.4.

8.6 Reproduction of the frequency response and damping force

The method presented in this chapter is examined by comparing the reconstructed system receptance function using the estimated frequency dependent stiffness and damping coefficient (Equations 8.7, 8.8(a)-8.8(c)) to that obtained directly from the impact test measurement. The results are shown in Figure 8.5. In addition, the receptance function of an ideal SDOF system predicted by using constant stiffness and damping coefficients is also presented. Here, the constant stiffness is determined from the known mass of the solid steel disk and the measured natural frequency, ω_n from the impact test. The constant damping coefficient is then determined by adjusting the damping value to produce the same peak frequency response amplitude to that obtained from the impact test. It is found that the constant stiffness evaluated by such approach is less than that obtained from the polynomial curve fitting in the whole frequency range of interest while the constant damping is slightly greater than that obtained from polynomial curve fitting for frequencies below and in the resonant band.

It is shown that using constant stiffness and damping coefficients slightly over predict the response by about 3% at frequencies below the resonance frequency band and over predict the response by more than 20% at frequencies above the resonance

frequency. On the other hand, using the frequency dependent stiffness and damping coefficients obtained from the proposed method, the frequency response function can be re-produced closely in the whole frequency range of interest except small deviations in peak frequency (shifts by 2Hz) and peak amplitude (less than 0.5% deviation). This is because the value of resonance frequency obtained from the real part is used in the calculation (Equation (8.2)) rather than that from the peak amplitude of the measured receptance. If the latter one is used in the calculation, the receptance can be re-produced exactly at resonance. However, it is found that using the value of resonance frequency obtained at zero value of the real part of the receptance function [99] produces better estimation of damping and stiffness using Equations (8.5) and (8.6) respectively.

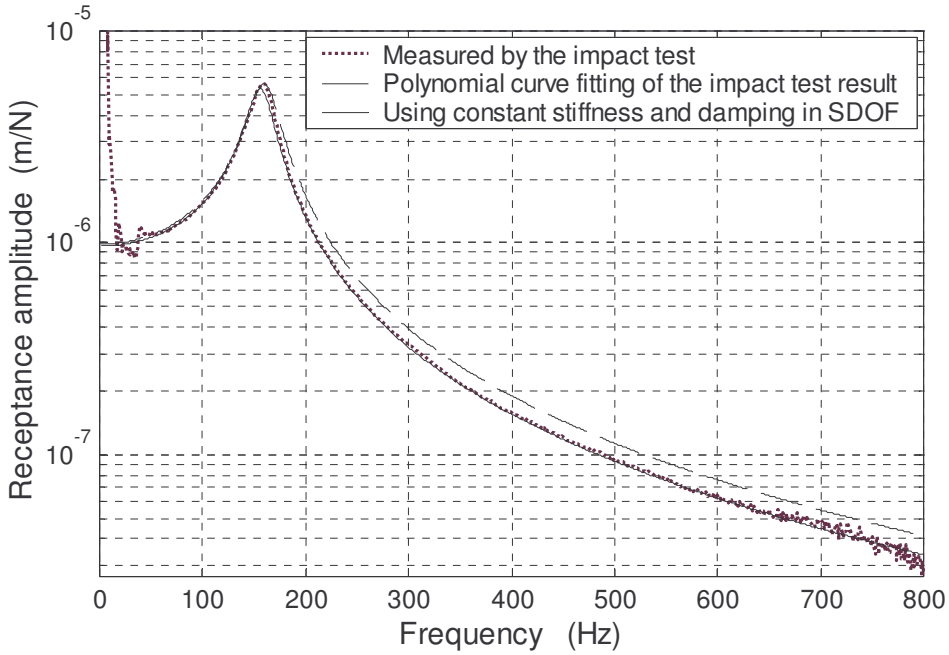

Figure 8.5. Measured and predicted frequency response function of the rubber-mass system.

Once the stiffness and damping coefficients are estimated, the amplitude of the damping force can be calculated from the relation:

$$F_d = K\eta|x|, \tag{8.9}$$

where $|x|$ is the amplitude of displacement of the rigid mass. The above relationship is based on the frequency dependent stiffness and damping model (Equation (8.1)), which assumes the damping force is proportional to the displacement and acts in the direction of velocity [90]. The damping force calculated according to Equation (8.9) is shown in Figure 8.6 together with the measured impact force for comparison. Such comparison has not been published in the literature before, which provides some useful information for the readers (particularly the relation of the two forces at resonance).

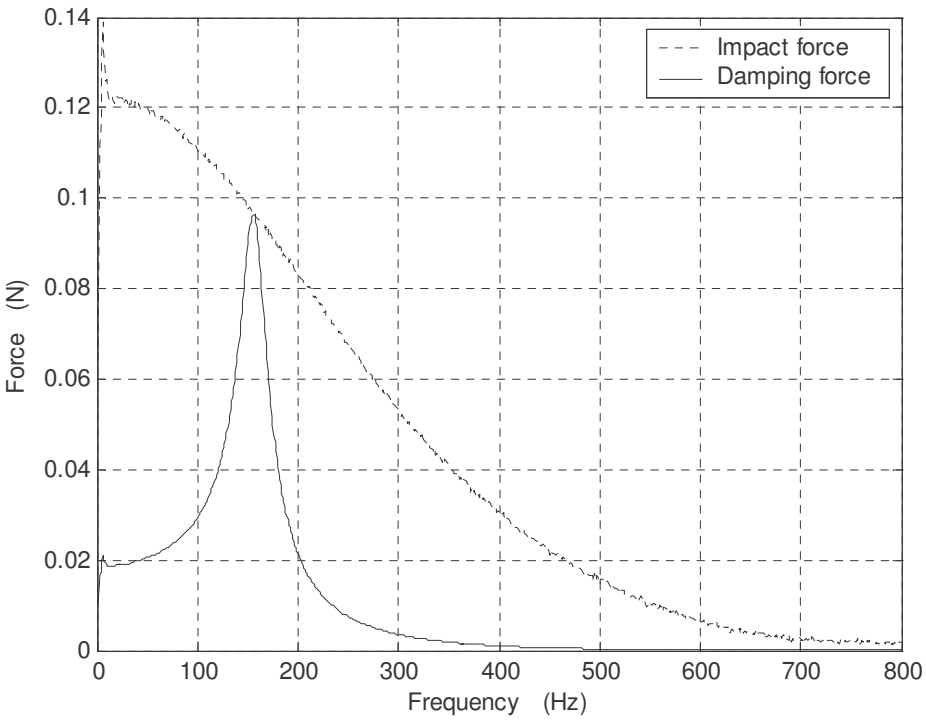

Figure 8.6. Amplitudes of the impact and damping forces.

Figure 8.6 shows that except at frequencies near the resonance, the damping force F_d is only a small fraction of the impact force. At frequencies far below the resonance frequency, the phase lag between the displacement and the impact force is small. It increases slowly with the frequency at frequencies below the resonance

frequency band. As the frequency approaches the system natural frequency, the phase lag between the displacement and the impact force increases rapidly and reaches 90^o at resonance as illustrated by the vector diagram in Figure 8.7. At resonance, the damping force and the impact force have the same magnitude but 180^o out of phase. The energy injected into the system by the impact force is dissipated completely by the rubber damping where no elastic energy is stored in the system. At frequencies higher than the system natural frequency, the displacement quickly becomes out of phase with the impact force and the displacement amplitude becomes very small. Hence, the damping force becomes negligibly small and the system response is mass controlled. The vector diagram is plotted along with the phase of the measured receptance function in Figure 8.7 to illustrate of such phenomenon.

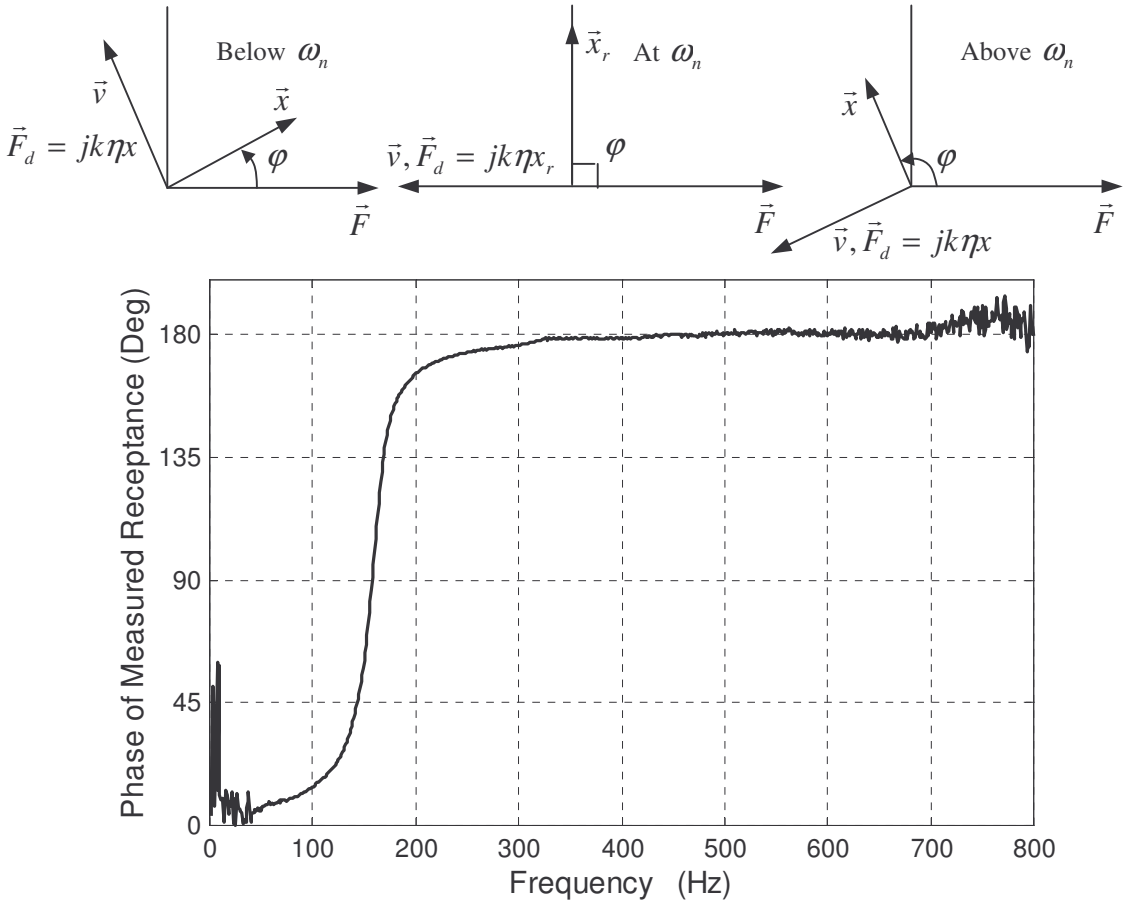

Figure 8.7. Schematic illustration and the measured phase lag between the displacement and the impact force.

In summary, the relation between the calculated damping force and the measured impact force, in conjunction with the phase relationship between the displacement and the impact force shed some light on the reason why the response displacement is very small at frequencies sufficiently higher than the resonance frequency.

8.7 Verification of the impact test method

Electromagnetic shakers are commonly used as the excitation source in rubber stiffness measurements. They are used here to verify the impact test results on the measurement of the frequency dependent rubber mount stiffness and damping coefficient. In this experimental setup, a B&K electromagnetic shaker (type 4809) is used to excite the rubber-mass system as shown in Figure 8.8. The frequency response function of the system is measured directly from an attached B&K impedance head (type 8001). The shaker is driven by broadband white noise excitation signal. The force level for the broadband noise excitation is about 50mN/Hz. In addition, pure tone signals are used to drive the shaker at discrete frequencies in order to verify the validity of the result obtained from the FFT of the response by noise excitation in the case of frequency dependent stiffness and

Figure 8.8. Graphic illustration of the experimental setup for shaker excitation of the rubber-mass system.

damping (Equation (8.1)).

The rubber stiffness estimated using the receptance functions measured by the impact test and shaker excitation (for both noise and pure tone excitations) are shown in Figure 8.9 while the damping coefficients obtained from both methods are shown in Figure 8.10. It is evident that the results obtained from both impact and shaker noise excitation agree well with each other in the frequency range of interest. The shaker pure tone excitation also produced a similar damping value to that obtained by an impact test in the frequency range of interest. However, the stiffness value obtained from the pure tone excitation is greater than that of the impact test. This is mainly due to the well-known Payne effect where rubber stiffness is high for small excitation amplitude and low for large amplitude [92]. In the pure tone excitation, the excitation amplitude is adjusted to about the same value at corresponding frequencies in broadband excitation case. Therefore, the overall excitation amplitude by pure tone excitation is much smaller than that of broadband excitation.

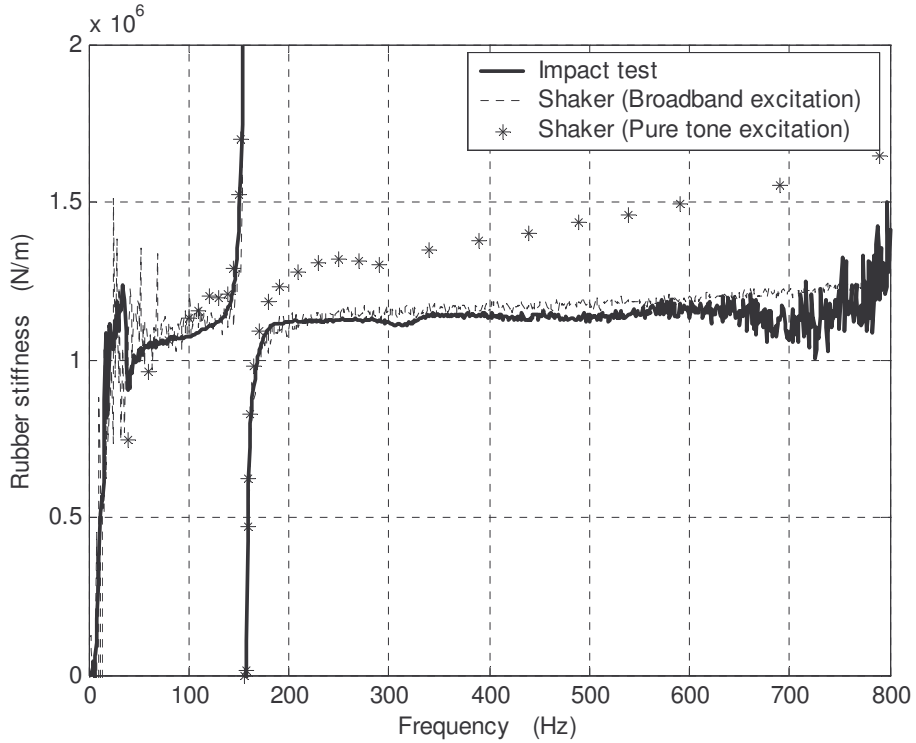

Figure 8.9. Frequency dependent rubber stiffness obtained by using impact and shaker excitations.

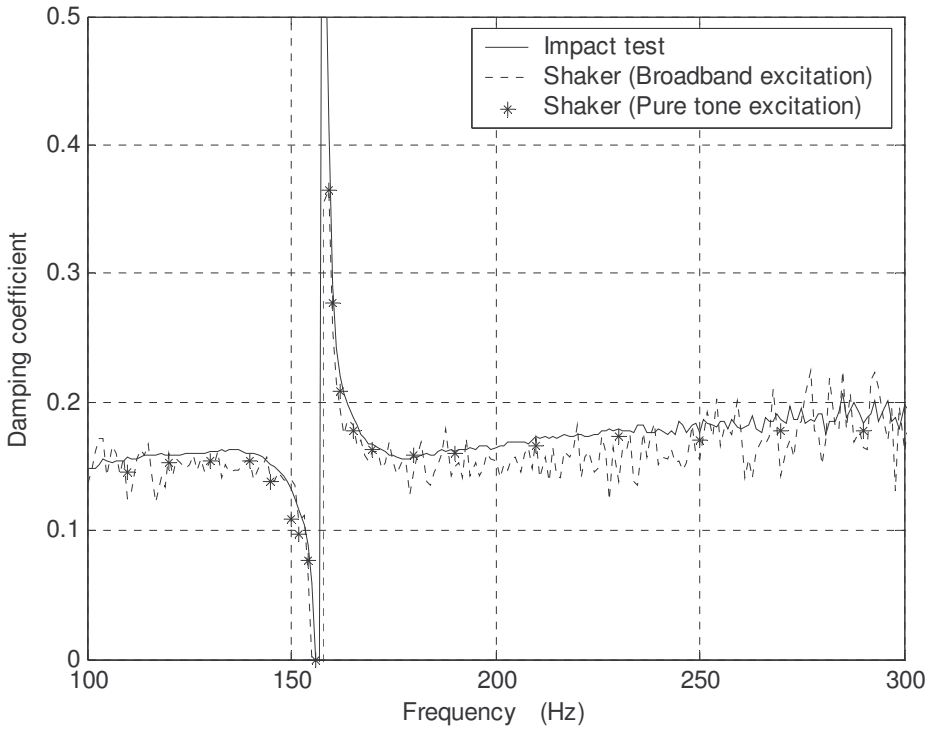

Figure 8.10. Frequency dependent rubber damping coefficient measured by using impact and shaker excitations.

In order to check the validity of representing the rubber by the mass-less spring element in the mathematical model in the frequency range of interest, blocked transfer stiffness of the rubber mount is also measured by inserting a force transducer between the steel slab and the steel cap of the rubber block as shown in Figure 8.11. Details of direct stiffness measurement using block transfer mobility are discussed in references [93] and [100], hence, they will not be repeated here. It is found that the stiffness measured by blocked transfer mobility is about the same as that obtained from the direct mobility measurement in the frequency range below 300Hz as shown in Figure 8.12. The stiffness obtained by the two methods start to deviate significantly from each other above 300Hz due to the effect of the rubber distributed mass. The damping coefficients obtained from direct and transfer mobility measurements are in close agreement with each other in the frequency range below 250Hz as shown in Figure 8.13.

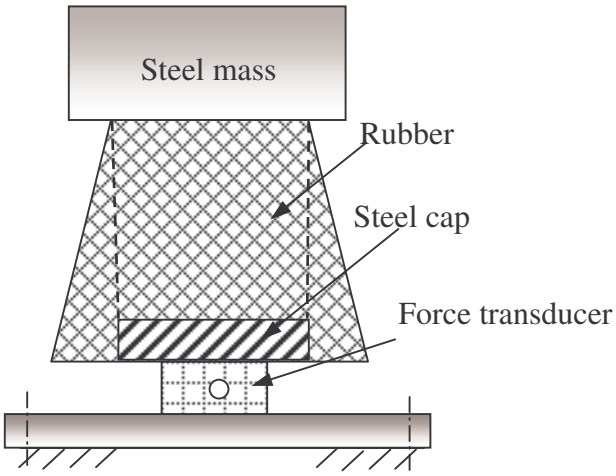

Figure 8.11. Illustration of the experimental set up for block transfer function measurement of the rubber-mass system.

It is noted that the insertion of the force transducer between the rubber steel cap and the steel slab changes the setting of the system where the measured values of damping, stiffness and resonance frequency differ from those obtained from the previous measurement. It is observed that the measured stiffness decreases by about 30% and the resonance frequency decreases by about 12% after the insertion. This is because the insertion of force transducer between the steel slab and the steel cap has reduced the effective working area of the rubber block (enclosed by the dash line, steel mass and the steel cap as shown in Figure 8.11) and therefore the stiffness decreases. On the other hand, the damping coefficient shifts up by about 25%. The deviation may have been less in value if the steel cap extends over the whole of the lower surface of the rubber block (please note that the steel cap as presented in Figures 8.2 and 8.11 is inserted into the rubber by the manufacturer to accommodate a fixing bolt for the isolator).

It has to be noted that all curves presented in Figures 8.9, 8.10, 8.12, 8.13 are obtained directly from Equations (8.5) and (8.6) by using the data from the measurements (There is no curve fitting on the data).

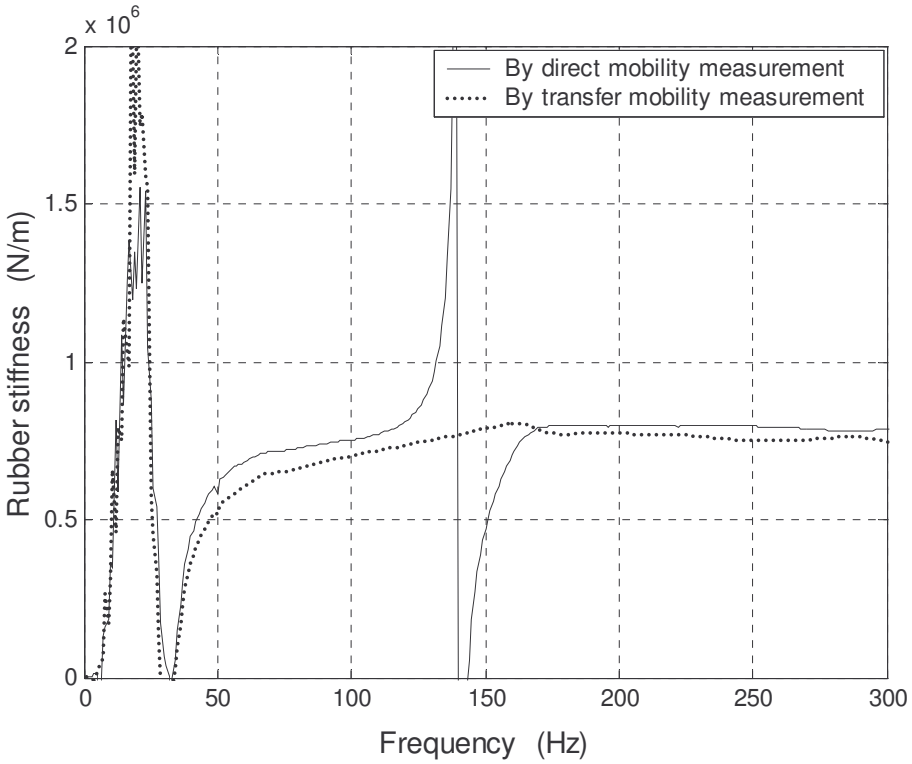

Figure 8.12. Frequency dependent rubber stiffness measured by impact test using direct and transfer mobility measurements.

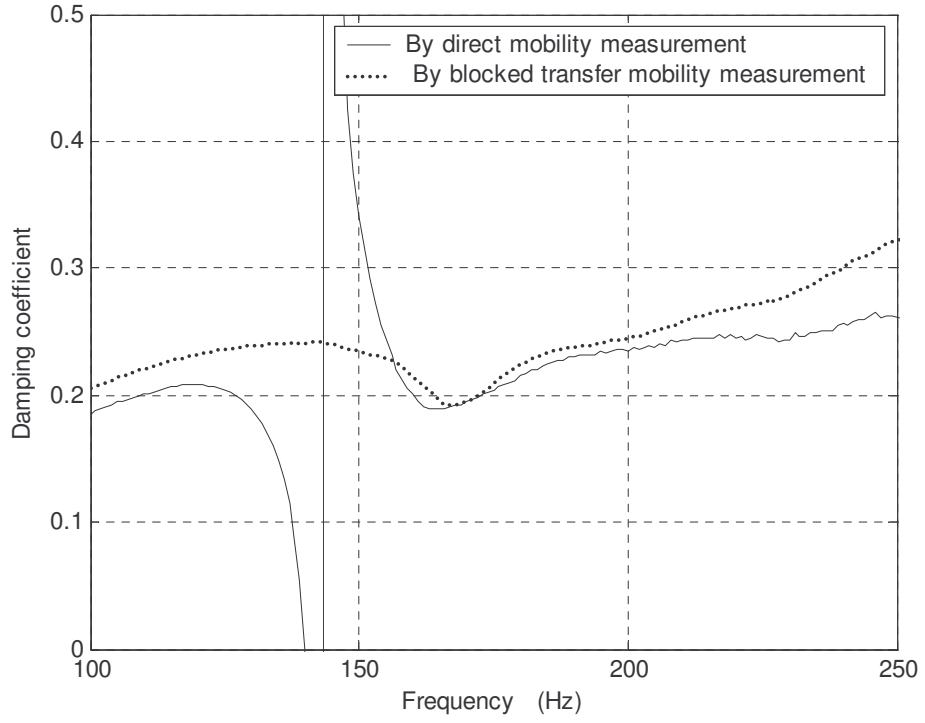

Figure 8.13. Frequency dependent rubber damping measured by impact test using direct and transfer mobility measurements.

8.8 Conclusion

The impact test technique presented in this chapter provides a quick and easy way to evaluate the frequency dependent stiffness and damping characteristics of rubber isolators. The dependency of rubber mount stiffness and damping coefficient on static pre-load and on vibration amplitude can be handled well by simply adjusting the mass and impact force amplitude. The results shown in this chapter indicate that rubber mount damping coefficient is a linear function of frequency for frequencies below, at and above the resonance frequency. It also demonstrates the non-linear dependence of the rubber mount stiffness on frequency in the low frequency range as well as in the resonance frequency band. In addition, the test results quantify the transition of the rubber mount stiffness from the static to the dynamic values and the static stiffness of the rubber element.

Chapter 9
Applications to ship structures

9.1 Introduction

In previous chapters, the vibration response of finite coupled structures typical for ship constructions were analyzed both analytically and experimentally. Some vibration characteristics of finite coupled structures were summarized. Nonetheless, the analytical models were all based on ideal systems, which did not take into consideration the structural variation and complex ship configurations. Bearing this in mind, vibration and vibration control on the ship hull structure of a 30m long crew vessel are studied and reported in this chapter by utilizing both finite element analysis and the analytical results obtained from previous chapters.

Ship vibrations can be classified generally into two major categories: (1) Global vibration where the whole hull girder is vibrating in response to the excitations at certain revolutions of main engines, propellers and auxiliary machinery or from the water wave [101]. (2) Local vibration where only an isolated part of the ship structure is in vibration (e.g. the resonance of a hull plate) [101, 102].

Traditionally, the global vibration of ships, such as natural frequencies and mode shapes of a complete ship hull structure at low frequencies are analyzed by strip theory where the natural frequencies of ships are calculated from the beam theory and the estimation of weight and moment distributions at each strip of a ship hull. A detailed description of such approach is given by Todd [101]. The wave-induced ship hull vibrations were also investigated by Gunsteren [103] who calculated the two-node ship hull vibration mode of two ship models by using modified strip theory.

Alternatively, the increasing speed and capacity of modern computers enables the analysis of a complete ship structure in a three-dimensional model by using finite element analysis (FEA). FEA analysis is increasing used in the analysis and design of complex ship structures [104]. A couple of examples are shown in references [105, 106] where the global response of ship structures were predicted.

Wave propagation and attenuation between the structural components of ship structures were investigated by Nilsson [84, 87, 107, 108], Fahy and Lindqvist [44] by employing wave guide approaches. In their analysis, the coupled structural components were assumed to share the same boundary conditions in one direction to form a wave guide model whose solution was then obtained by wave approaches. Nilsson [109] also investigated the hull plate vibration due to propeller induced fluid pressure loading by employing Green's function and the variational principle. However, in their analysis, they only considered sections of idealized ship hull structures, which did not take into account the structural variation of ships.

For better understanding of vibration response of ship hull structures, the response of a 30m long crew vessel to mechanical excitations is investigated in this chapter by employing FEA analysis. The FEA calculated results are compared to analytical solutions of the corresponding simpler structures to improve the understanding of wave propagation in ship structures. Some passive vibration control techniques on ship vibration are also explored in the study.

9.2 General descriptions of the 30m ship

The general profile of the 30m ship is shown in Figure 9.1 where the ship hull is equally divided into thirty 1m long sections by ring frames. The ship hull is made of

aluminum and is partitioned by watertight bulkheads into several functional areas, such as accommodation room, utility area, engine room, fuel tank room and rudder room. The main stiffness components of the ship hull include keel, engine beds, deck girders, bottom girders, pillars and ship frames. The details of structural arrangements of these stiffness components in the ship are shown in Figures 9.2 – 9.5. Figure 9.2 shows the structural arrangement of the deck girders while the structural arrangement of the bottom girders is shown in Figure 9.3. The structural configuration of the keel is shown in Figure 9.4 while the structural arrangements of the engine beds are shown in Figure 9.5.

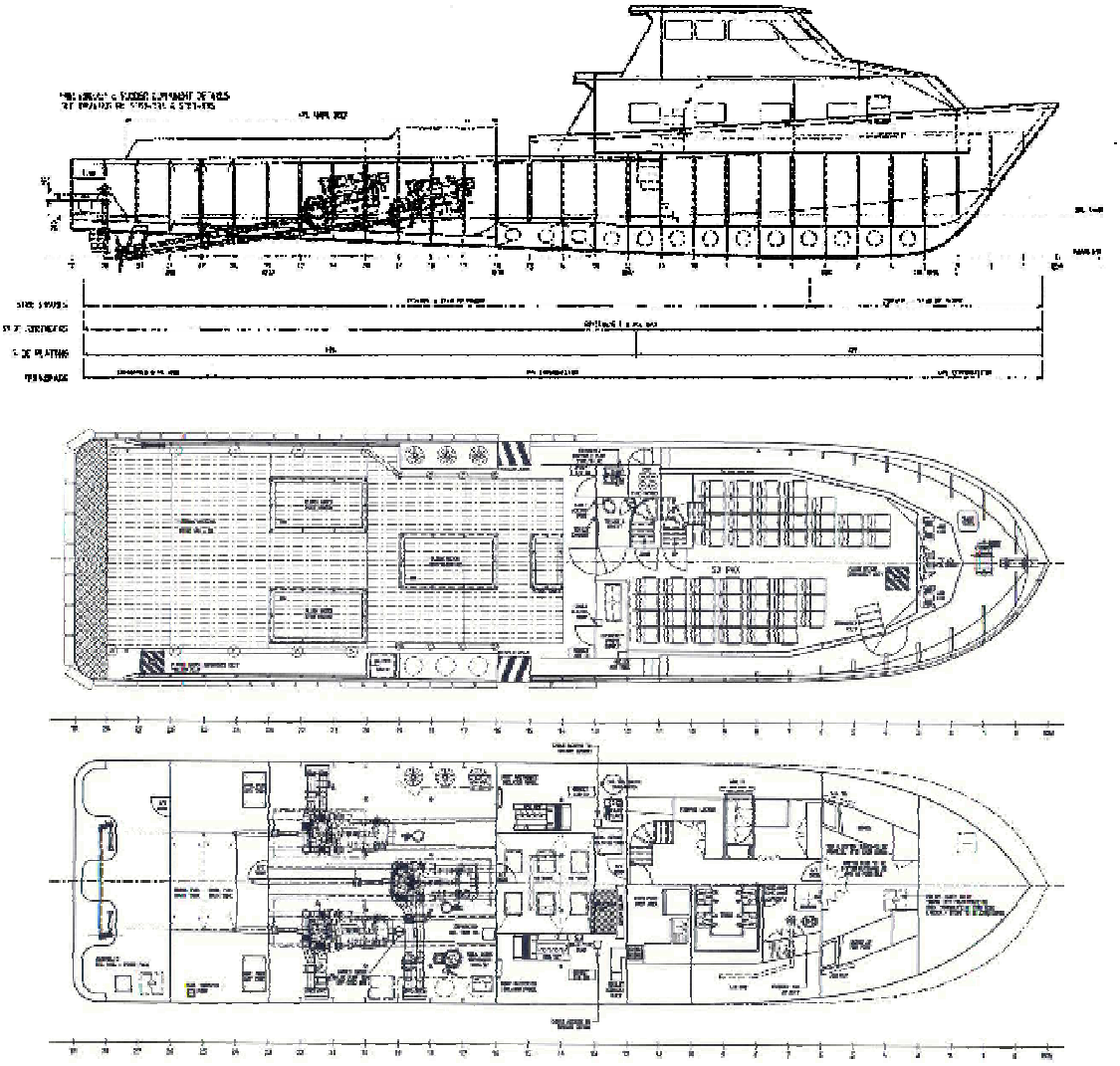

Figure 9.1 Profiles of the 30m crew vessel. Top: Main profile; Middle: Structure profile of the main deck; Bottom; Structure profile of the lower deck.

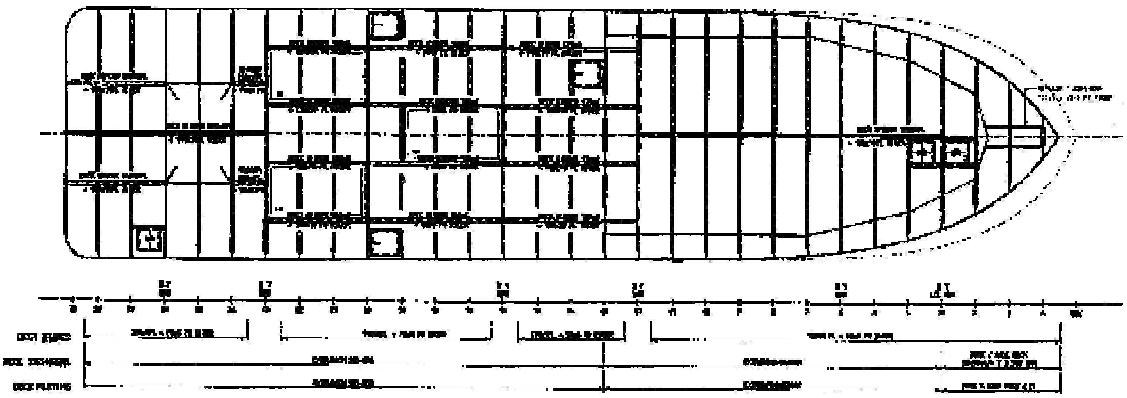

Figure 9.2. Structural (stiffness components) arrangement of the main deck plan.

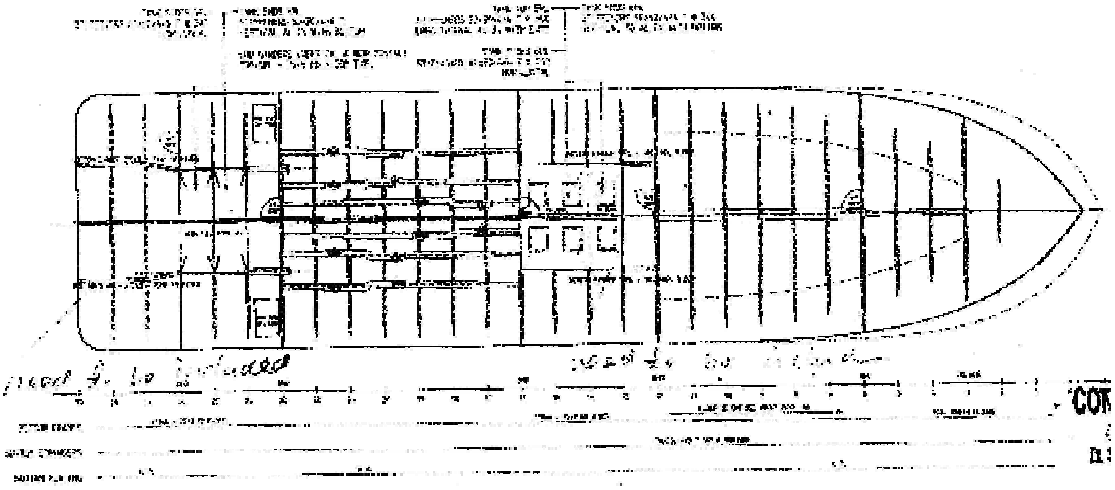

Figure 9.3. Structural (stiffness components) arrangement of the bottom plan.

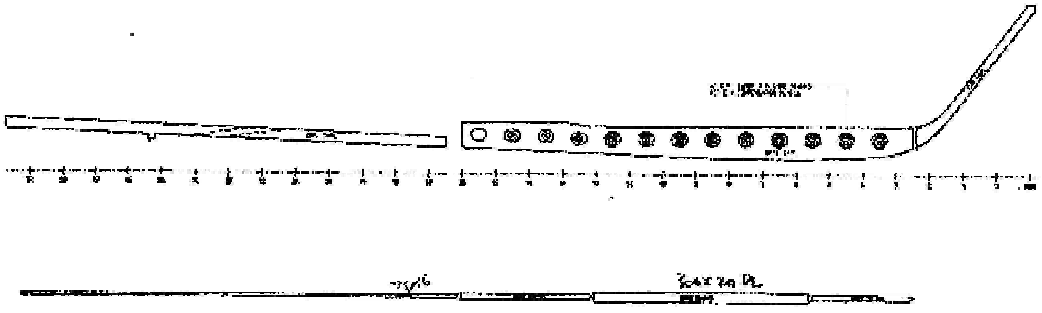

Figure 9.4. Structure profile of the keel girder, webs and rider bars.

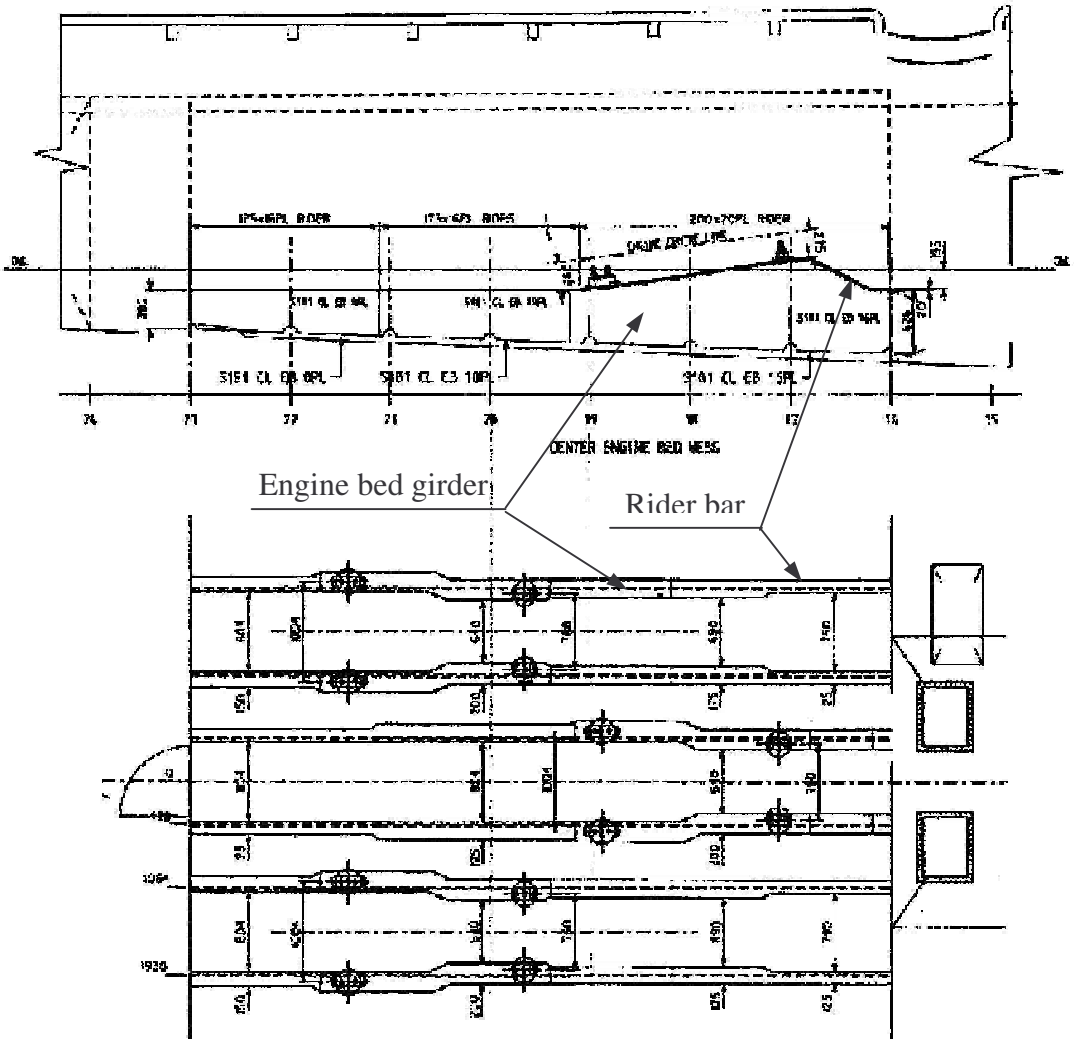

Figure 9.5. Structure profile of the engine beds and plan of rider bars.

In addition, the structures configurations for some other major ship structure components are shown in Figures 9.6 – 9.9. Figure 9.6 shows the front view of the watertight bulkhead (Frame 16) that separating the engine room with the structures enclosing the wheelhouse, passenger cabin and the accommodation area of the ship. The centre engine, the two generators and the cross section shape of their supporting engine beds are shown in Figure 9.7 together with Frame 17. Figure 9.8 shows one of the two side engines, the cross sectional shape of its supporting beds and the four

supporting pillars for this section together with Frame 20. The side view of the propeller power trains and the structural arrangement of the shafting are shown in Figure 9.9.

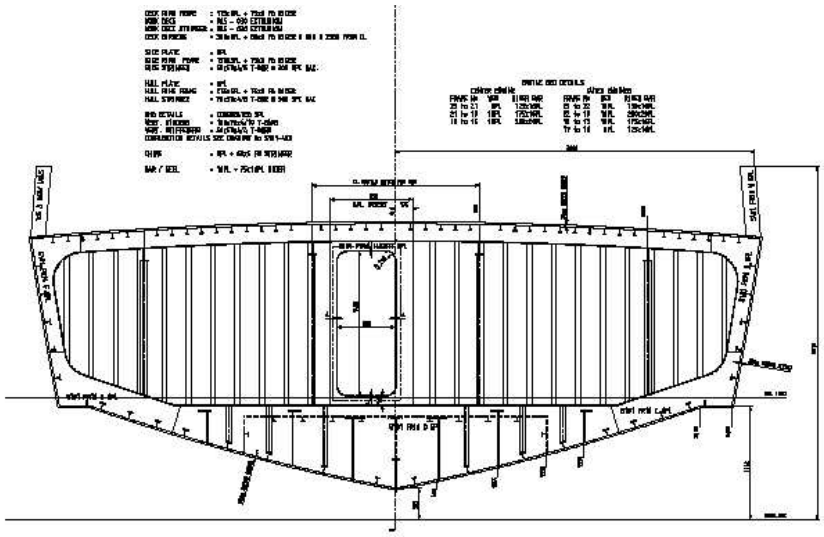

Figure 9.6. Front view of the structural configuration of the watertight bulkhead separating the engine room section and the structure components enclosing the passenger cabin and accommondation area. Looking forwards to the bow.

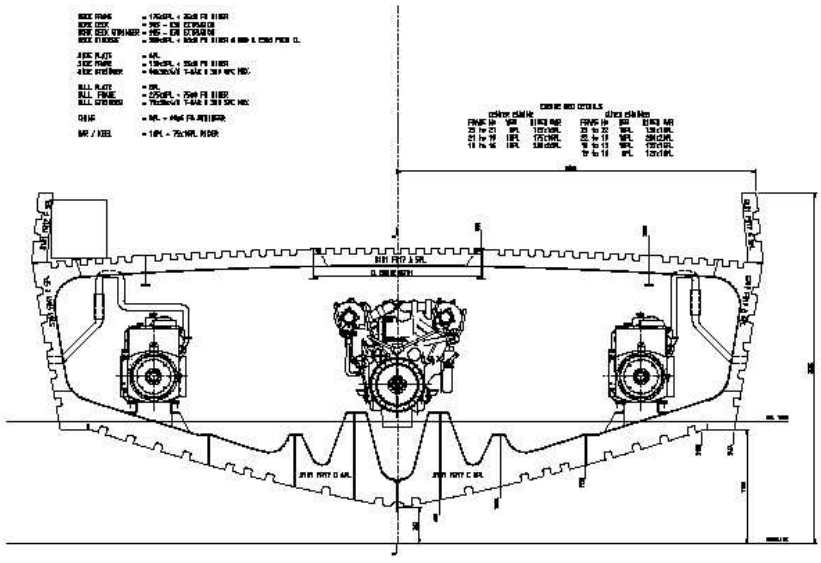

Figure 9.7. Front view of the structural arrangement of the centre engine, generators, their supporing engine beds and the associated ring frame (Frame 17). Looking forwards to the bow.

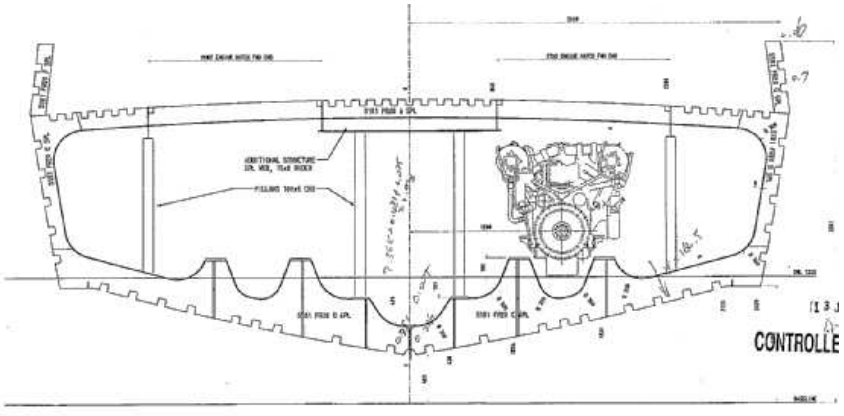

Figure 9.8. Front view of the structural arrangement of the supporting pillars, the side engines, the shape of the engine bed cross sections and the associated frame (Frame 20). Looking forwards to the bow.

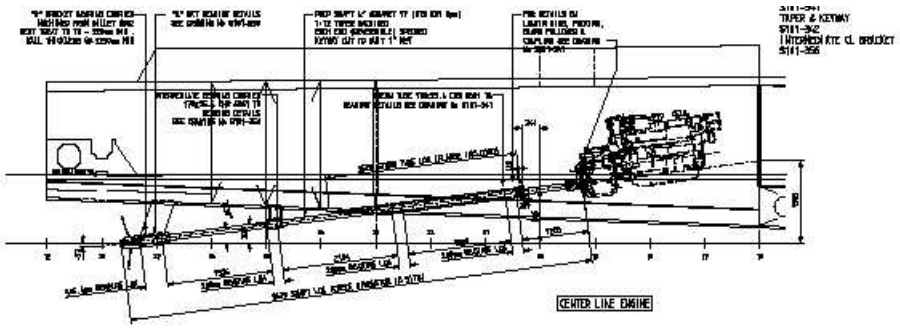

Figure 9.9. Side view of the propeller power train and the structure arrangement related to the center engine.

9.3 Finite element model of the 30m ship

The geometric configuration and the contour of the ship hull structure are well defined by the ring frames. The ring frames are 1m apart and are interconnected by keel and other major stiffness components, such as deck girders, bottom girders and engine beds. Additionally, vertical pillars are used to provide additional supports to the ship hull at Frames 5, 8, 14, 18 and 20. The ring frames are meshed by plate elements and are reinforced by rider bars (meshed by beam elements) along their inner perimeter. The other major stiffness components of the ship hull such as keel,

pillars, deck girders, bottom girders and engine beds are all meshed by beam elements in the FEA model. The structural arrangement of the stiffness components and the frames for half of the ship hull of the 30m crew vessel is shown in Figure 9.10, while the complete FEA model of the 30m crew vessel (including the hull plates and superstructure) is illustrated by Figures 9.11 and 9.12.

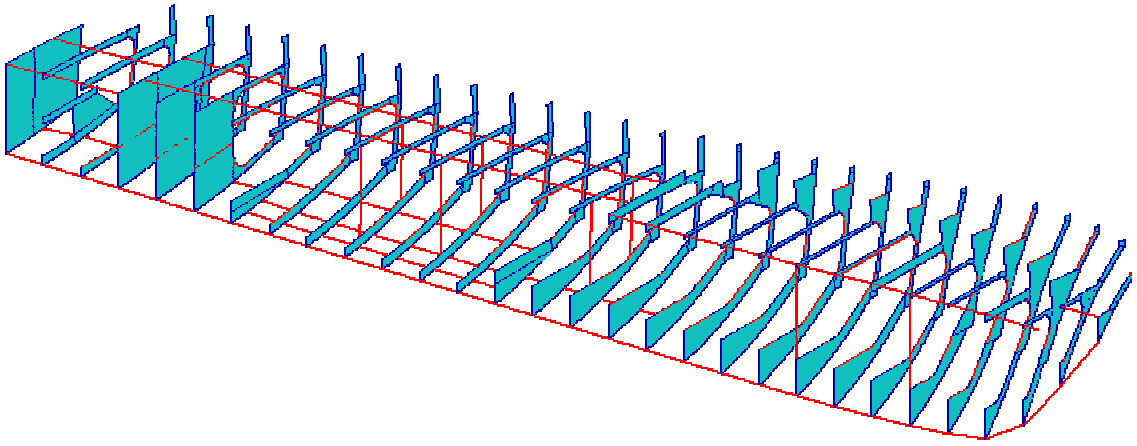

Figure 9.10. Structural arrangement of the stiffness components for half of the ship hull structure used in the FEA model.

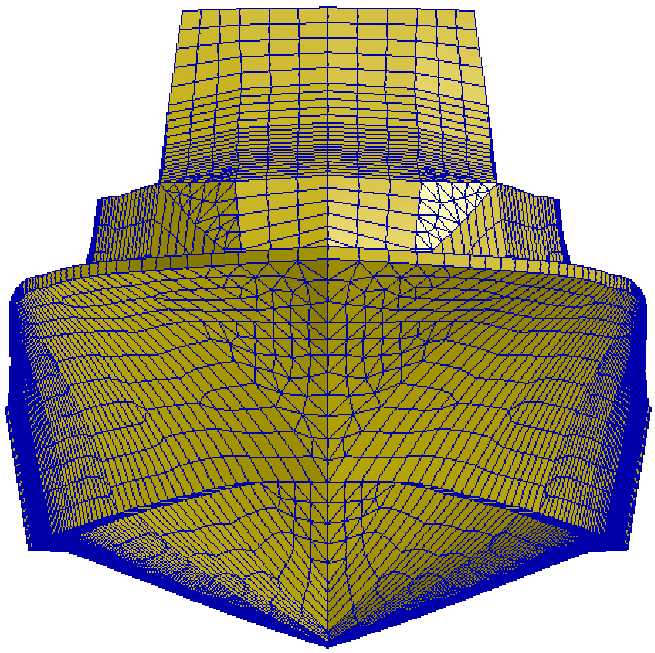

Figure 9.11. Finite element model of the 30m crew vessel. Front view.

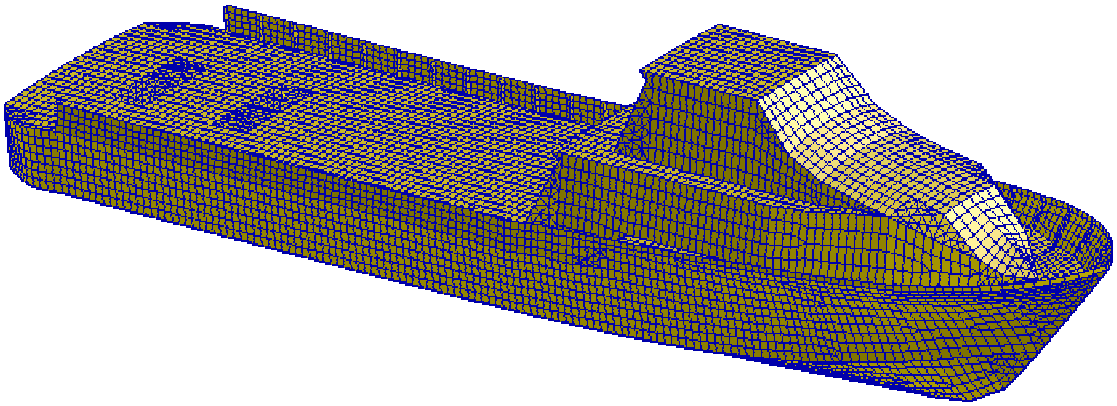

Figure 9.12. Finite element model of the 30m crew vessel. Isotropic view.

9.4 Vibration response of ship hull structures

By employing the FEA normal mode analysis provided by the commercial software – MSC/NASTRAN, the well known two-node vertical vibration mode [101, 103, 110] of the 30m crew vessel is calculated, and the mode shape distribution is shown in Figure 9.13. The natural frequency of the mode is predicted at about 13Hz for the dry ship model and is just below 4Hz when the ship is submerged in water (the water level is two meters above the baseline of the ship in the calculation). The decreasing natural frequency of the mode when the ship is submerged in water is due to the 'virtual mass" effect of the surrounding water [101, 106]. Although a detailed analysis of the global dynamic of ship structures by FEA analysis is straightforward, it is also very time consuming, particularly for the frequency response analysis, which can only be predicted at very low frequencies. In order to reduce the computation cost and to increase the frequency range of analysis, only the engine room section of the ship hull structure of the 30m crew vessel is considered in the subsequent frequency response analysis. In addition, the complete keel is included in the FEA model. The generality of the calculation results in representing the vibration response of the whole ship hull structure is illustrated later in the analysis.

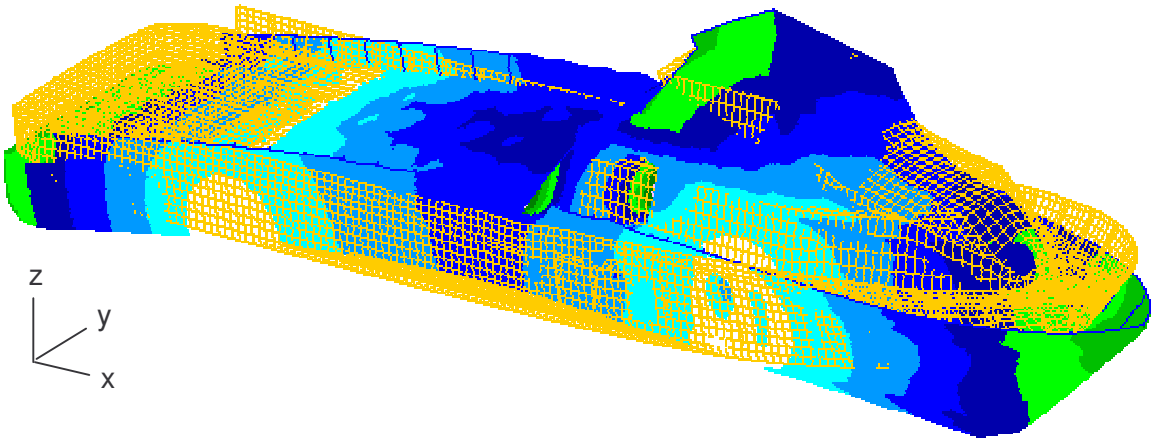

Figure 9.13. The mode shape distribution of the two-node vertical vibration mode of the 30m crew vessel.

9.4.1 Vibration response of the engine room

The engine room section of the ship structure is bounded between two watertight bulkheads – Frame 16 and Frame 23. Two FEA models are considered for this structure section in the study, one comprises only the major stiffness components of the engine room (Figure 9.14(a)) while the other includes both the stiffness components and the corresponding hull plates in the model as illustrated in Figure 9.14(b). The full length of the keel is included in both FEA models so that wave propagation from the engine room section to other sections of the ship can also be evaluated. Uniform internal loss factor ($\eta = 0.01$) is assumed for all the structural components in the simulation. No boundary constraints are imposed on the FEA models. In contrast, simply supported boundary conditions are assumed for the corresponding simple finite structural components in the analytical solutions.

Only mechanical excitations on ship structures are considered in this study. Because the wavelength of structure borne sound in the low and medium frequency ranges is much greater than the dimensions of the machine isolators and mounts, excitations from engines, generators, propellers and the auxiliary machinery on ship structures

can be well approximated by point sources. The mechanical excitations on the ship structure can be out-of-plane forces, in-plane forces, torsional moments, bending moments or their combination. For example, it has been pointed out that the engine excitations on ship hull structures are in two forms [102, 111, 112]: (a) vibrations transmitted to the foundation by the engine as a whole through engine isolators (point force excitations) and (b) torsional oscillations in the crankshaft and in the shafting of the driven machinery (moment excitations). The input mobility of the engine room due to each individual mechanical excitation is investigated separately.

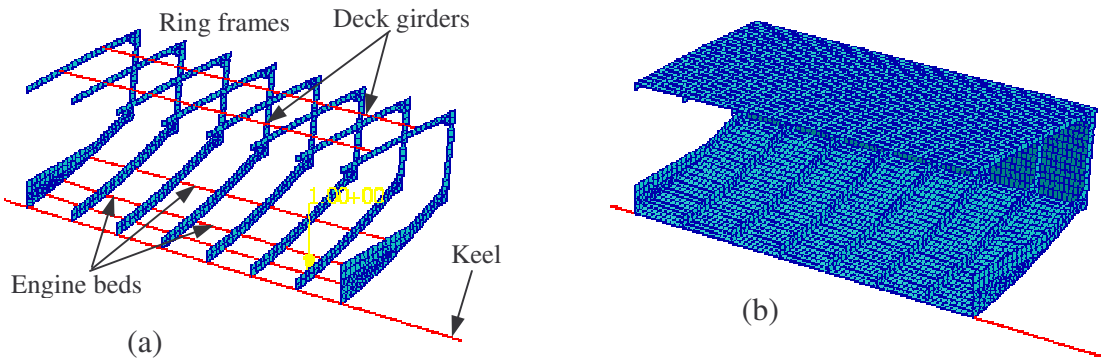

Figure 9.14. The FEA models for half of the engine room. (a) Hull and deck plates are not included; (b) Hull and deck plates included.

a) Vibration of the engine room to point force excitations

A normal point force is applied at one of the mounting positions of the engine beds as illustrated in Figure 9.14(a). The input mobility of the engine room due to this force excitation is calculated for the two FEA models. The results are shown in Figure 9.15 together with those of the corresponding beams and beam stiffened plates of finite and infinite extends.

It is illustrated that the frequency averaged input mobility of the engine room can be approximated by that of the corresponding infinite beam. This finding agrees with

that observed by Pinnington and White [113] for power transmission from vibrating machinery to supporting beams. For this excitation, the in-plane stiffness of the frames is in the same order of magnitude scale as the flexural stiffness of the engine bed so that the whole engine bed (spans between Frame 16 and Frame 23) vibrates as a non-uniform beam. The frames behave as regular stiffness and mass attachments to the flexural vibration of the engine bed. The long flexural waves of the engine bed are attenuated rapidly by short flexural waves in the plate elements of the frames. As a result, the frequency averaged input mobility of the engine bed approaches to that of the corresponding infinite beam. It is shown in the figure that the inclusion of the hull and deck plates in the FEA model does not affect the overall frequency averaged vibration response of the engine room. Therefore, they can be ignored in the analysis. This result agrees well with that observed by Grice and Pinnington [38] who showed that the short waves in the plate(s) mainly provide damping to the long wave propagation in the beam(s).

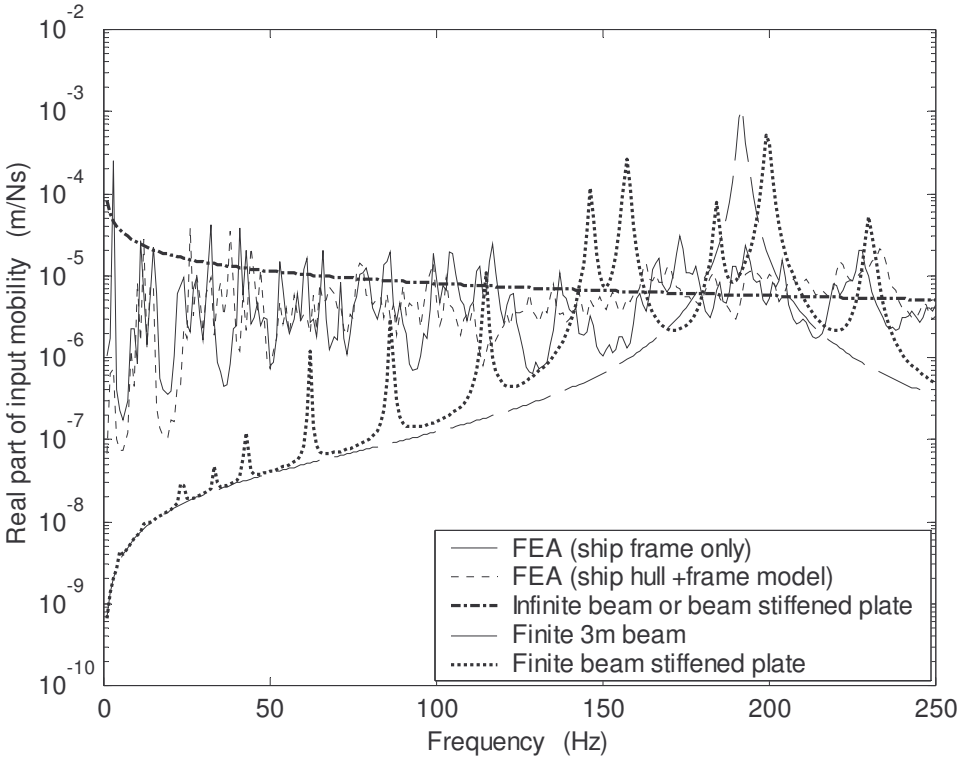

Figure 9.15. Point force input mobility of the engine room and the corresponding finite and infinite beams, beam stiffened plates.

b) Vibration of the engine room to in-plane force excitation

The real part of input mobility due to in-plane force excitation on the engine bed is shown in Figure 9.16 together with that of the corresponding beam of finite and infinite extent. It is shown that the in-plane force input mobility of the engine bed is bounded between the input mobility of the corresponding infinite beam and that of the corresponding 3m long finite beam except for a few peak responses. These peak responses are attributed to the large in-plane stiffness of the engine bed and the much smaller flexural stiffness of the frames. Therefore, these peak responses can be regarded as the resonant responses of spring-mass systems where the engine bed behaves as a rigid body mass and the flexural stiffness of the ship frames serves as the stiffness element of the spring-mass systems. Because including the hull and deck plates in the FEA model increases the modal damping and stiffness of these resonant responses, the modal amplitudes for these response peaks are largely attenuated.

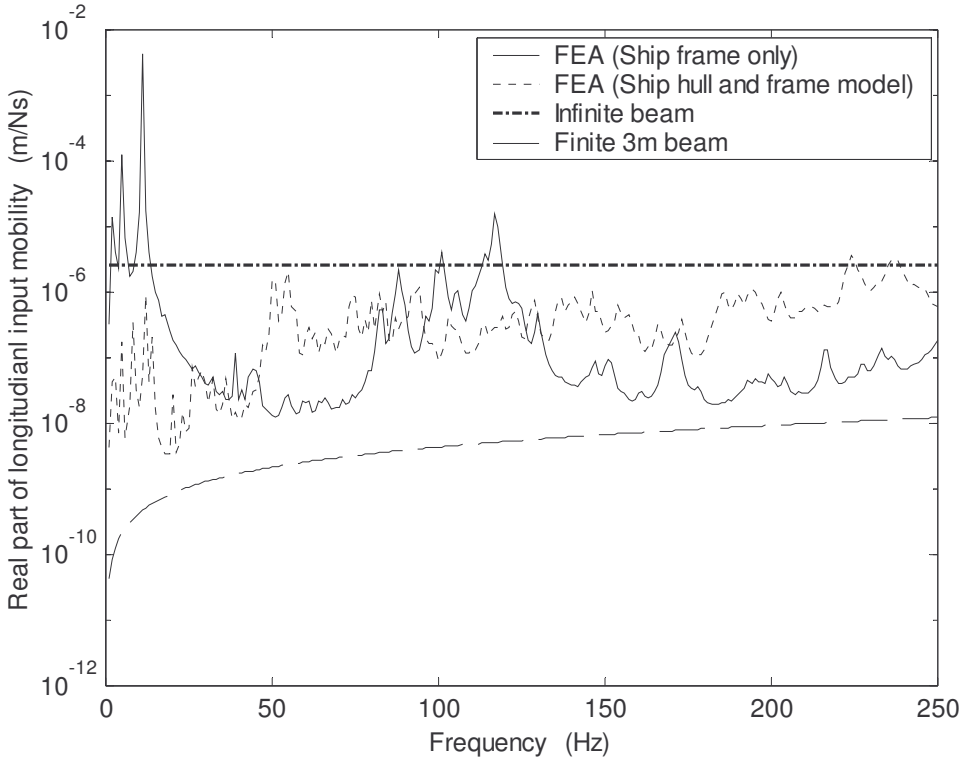

Figure 9.16. Input mobility of the engine room to in-plane force excitation at engine bed and that of the corresponding finite and infinite beam.

c) Vibration of the engine room to torsional moment excitation

Figure 9.17 shows the real part of input mobility of the engine room due to a torsional moment excitation on the engine bed together with those of the corresponding beams of finite and infinite extents. In addition, the input mobility of the corresponding finite beam stiffened plate is also shown in the figure. It is found that the input mobility of the ship structure resembles closely to that of a corresponding finite 1m beam (or a finite beam stiffened plate), particularly in the non-resonant bands of the finite beam. This is attributed to the relatively large in-plane stiffness of the frames when compared to the torsional stiffness of the engine bed. For this excitation, the two frames (Frame 17 and Frame 18) bounding the engine bed section under direct torsional moment excitation behave as end boundaries to the torsional vibration of the engine bed.

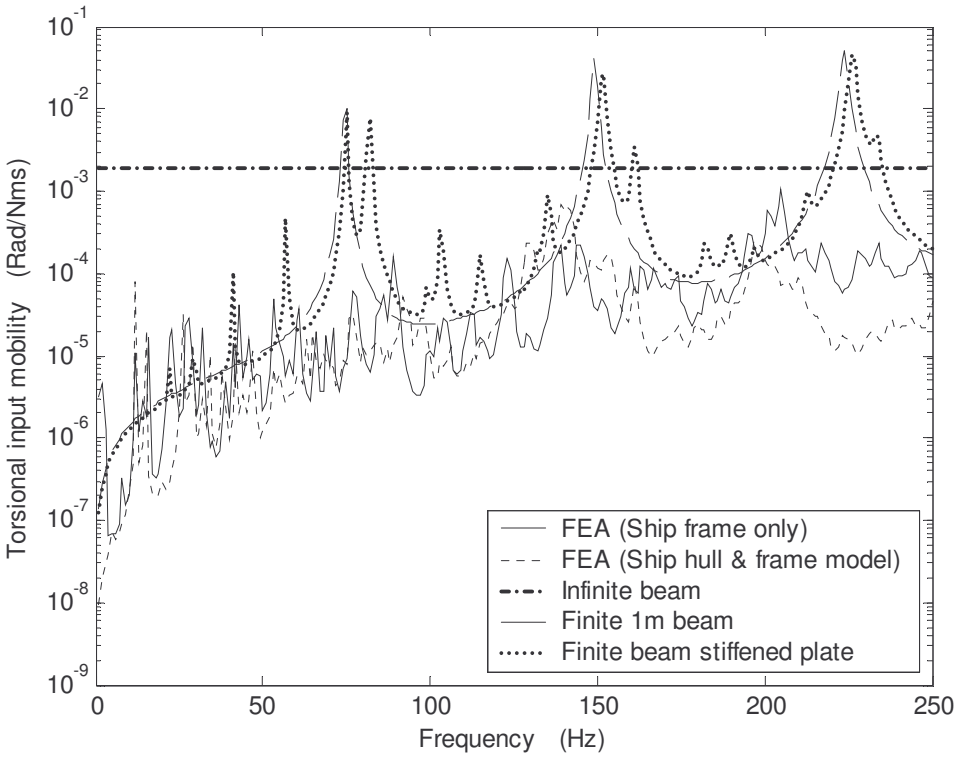

Figure 9.17. Torsional moment input mobility of the engine room and the corresponding finite, infinite beams and beam stiffened plate.

d) Vibration of the engine room to bending moment excitation

Similar to those found for finite beam stiffened plates (see Chapter 3), the input mobility of the engine room due to bending moment excitation on the engine bed also has similar characteristics to that of the point force input mobility. It is shown in Figure 9.18 that the frequency averaged input mobility of the engine room can be approximated well by that of the corresponding infinite beam in the whole frequency range of investigation.

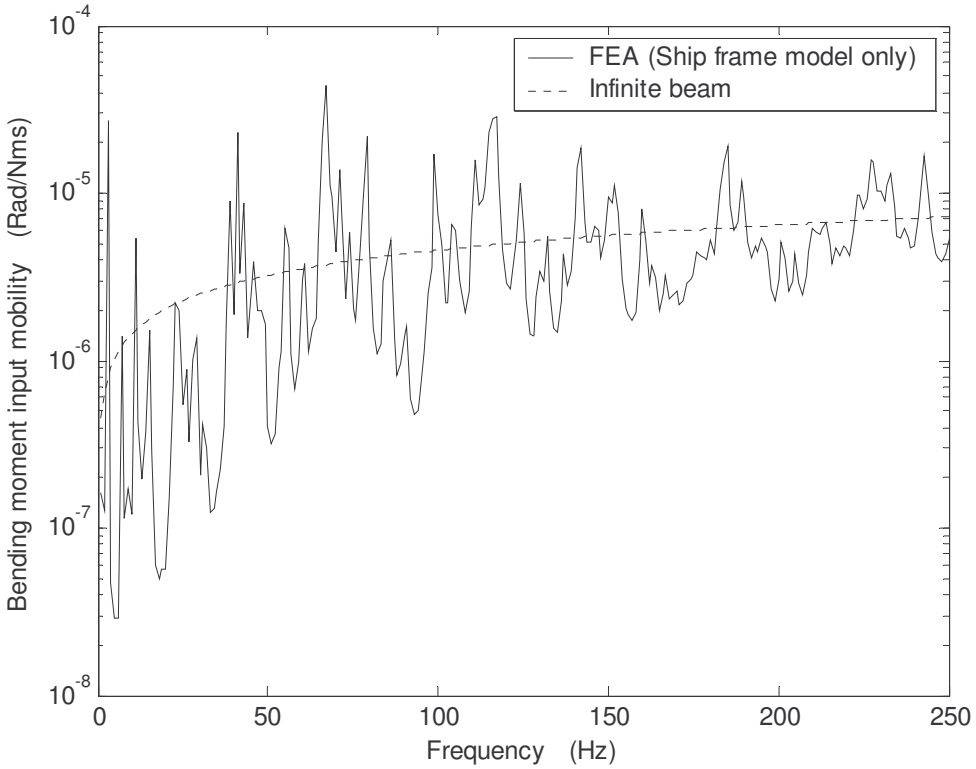

Figure 9.18. Bending moment input mobility of the engine room and that of the corresponding infinite beam.

9.4.2 Passive vibration controls of the ship structures

Passive vibration controls on ship structures can be generally classified into three categories according to the location where the control technique is applied: (a) vibration control at source locations; (b) control of wave propagation in ship

structures; and (c) vibration control at receiver locations. Vibration control at receiver locations can be achieved by applying the traditional passive control methods, such as adding damping materials on the structure or by the proper design of vibration isolators to stop the vibration from reaching the equipment at receiver locations, while vibration control at source locations (i.e. at the mounting locations of engines, generators) is usually achieved by usages of vibration isolators (i.e. machine mounts). Vibration control at source locations can also be accomplished by modifying the structure stiffness of mounting structures at source locations since power transmissions from a known vibrating source to a structure is controlled by the structure impedance at the source location. Furthermore, vibration in complex ship structures can also be controlled along the path of wave propagation. The latter two control strategies are explored in this study.

a) Vibration control by structural modifications of the engine bed

It has been illustrated in the previous sections that similar to beam stiffened plates, the input mobility of the engine room to point excitations on the engine bed(s) is mainly dominated by the stiffness of engine beds. Therefore, vibration energy transmission from main engines to ship structures could be controlled by structural modifications of engine beds. To enable structural modifications of engine beds in the FEA simulation, the engine bed section bounded by Frame 17 and Frame 18 (the section under direct point force excitation) is re-meshed by plate elements. Four structural modifications are considered in the simulation, which are illustrated in Figure 9.19. In the first modification, the girder width of the engine bed section is enlarged from 16mm to 24mm. In the second modification, two 10mm thick aluminum plates are attached on the edges of the rider bar of the engine bed to form a box shape structure. In the third modification, the two plates are attached on the junction between the rider bar and the girder of the engine bed to form a triangle

shape structure. In the fourth modification, the two plates are attached to the engine bed to form an inverse triangle shape structure.

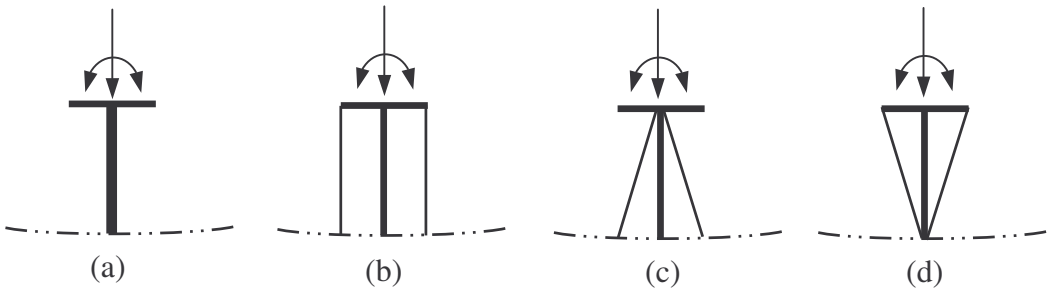

Figure 9.19. Plans of structural modifications of the engine bed section under direct force excitation. (a) Plan 1; (b) Plan 2; (c) Plan 3; (d) Plan 4.

Effects of the modifications on the input mobilities of the engine room are evaluated for both point force and torsional moment excitations. For better illustration, the results are given in one-third frequency bands and are shown in Figures 9.20 and 9.21 respectively. It is shown that effects of all proposed modifications to the vibration response of the ship structures at low frequencies are insignificant for both excitations. The control performance of the structural modifications improves as the frequency increases. Furthermore, it is observed that modification plan 2 (represented by the thin red solid curve) has the best overall control performance on the input mobilities of the engine room for both excitations. Although modification plan 4 also has good control performance in the torsional moment excitation case, its effect on the point force input mobility of the ship structure is less significant. The overall control performances of the other two modifications (Plans 1 and 3) on the input mobility of the engine bed are poor for both excitation cases.

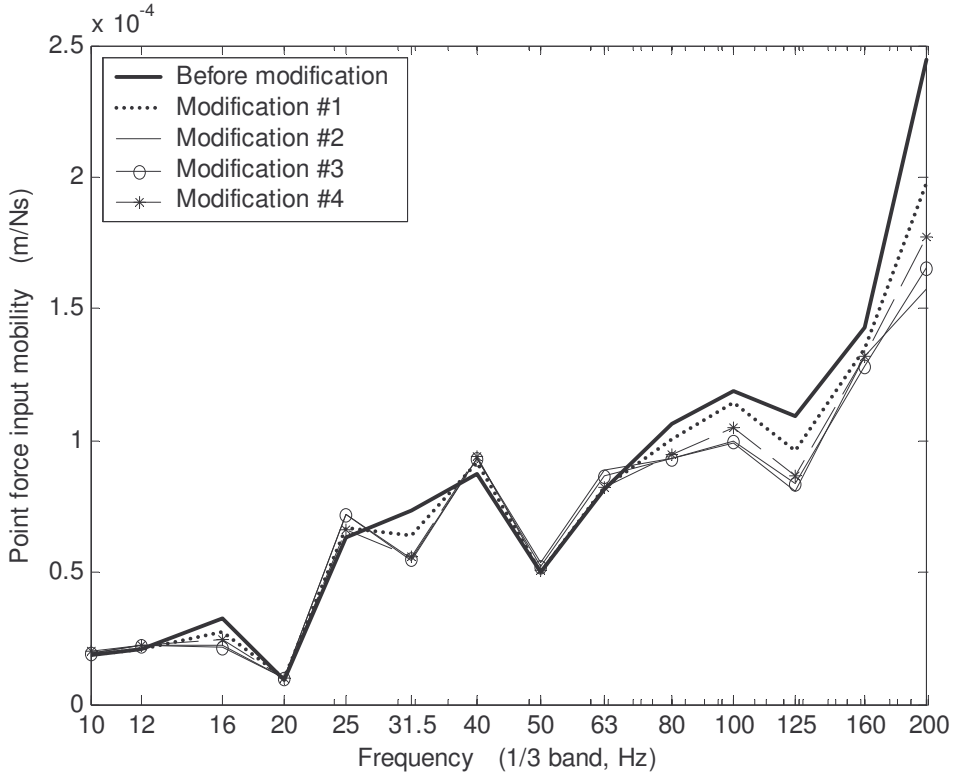

Figure 9.20. Comparison between the point force input mobilities of the engine room before and after structure modifications.

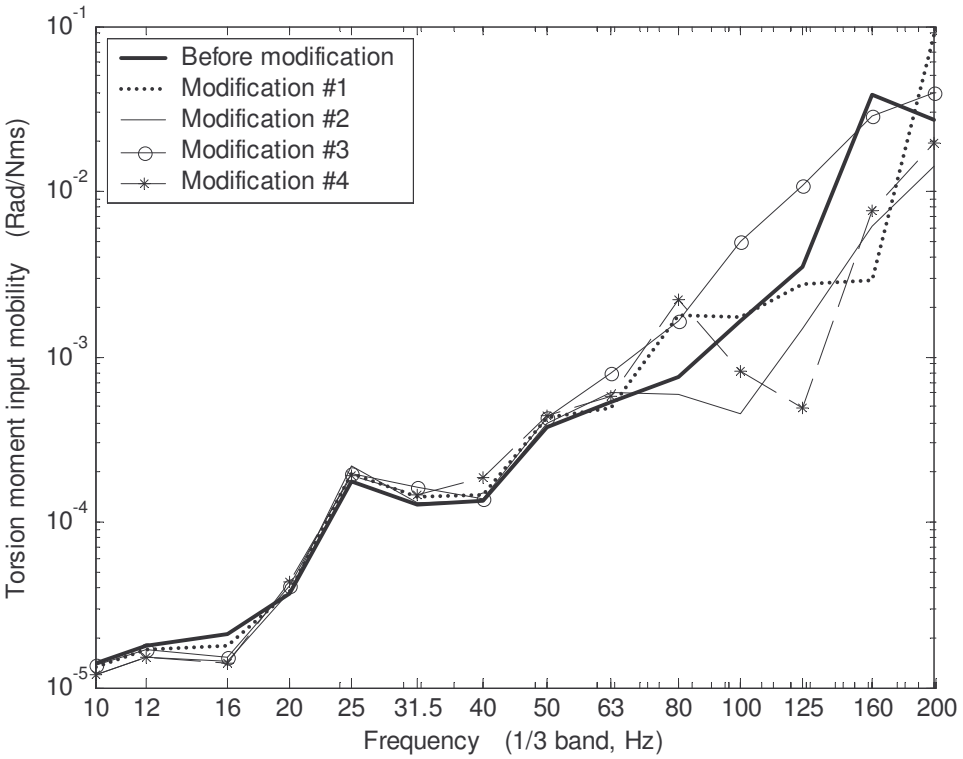

Figure 9.21. Comparison between the torsional moment input mobilities of the engine room before and after structure modifications.

Nevertheless, the control performance of the two modifications (Plans 1 and 3) could be improved if the modifications are extended to the whole span of the engine bed. For example, Figure 9.22 shows that the control performance of modification plan 1 on the point force input mobility of the engine room improves considerably when the girder width of the whole engine bed is increased to 24mm, particularly at frequencies greater than 63Hz frequency band.

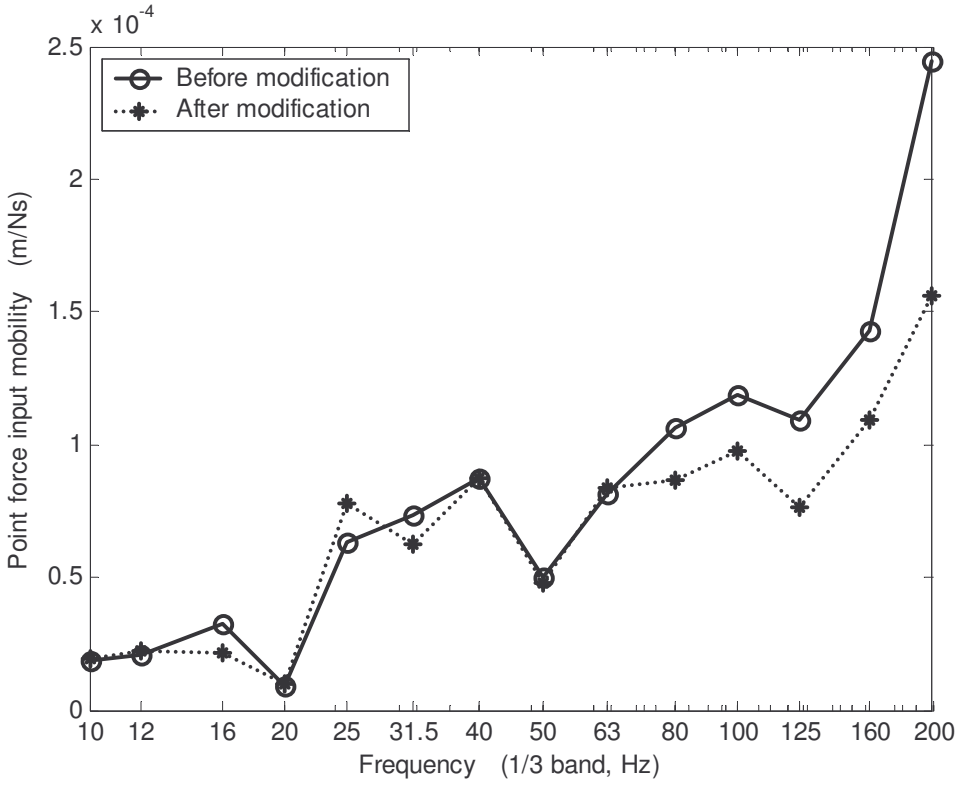

Figure 9.22. Comparison between the point force input mobilities of the engine room before and after structure modification on the engine bed.

b) Control of wave propagations in ship structures

Because wave propagations in ship structures are dominated by the long waves in the major stiffened beams (i.e. keel, girders, etc), the vibration control in ship structures away from the source section could be simplified by controlling the wave motions in beams. Furthermore, because the major stiffness beams are regularly supported by

the ship frames at equal intervals, wave propagation in these beams would possess certain periodic characteristics similar to that of periodic supported beams or periodic ribbed plates (see discussions in Chapters 4 and 6). As a result, wave propagation in ship structures away from the source section could be confined by introducing irregularities on locations of the ship frames.

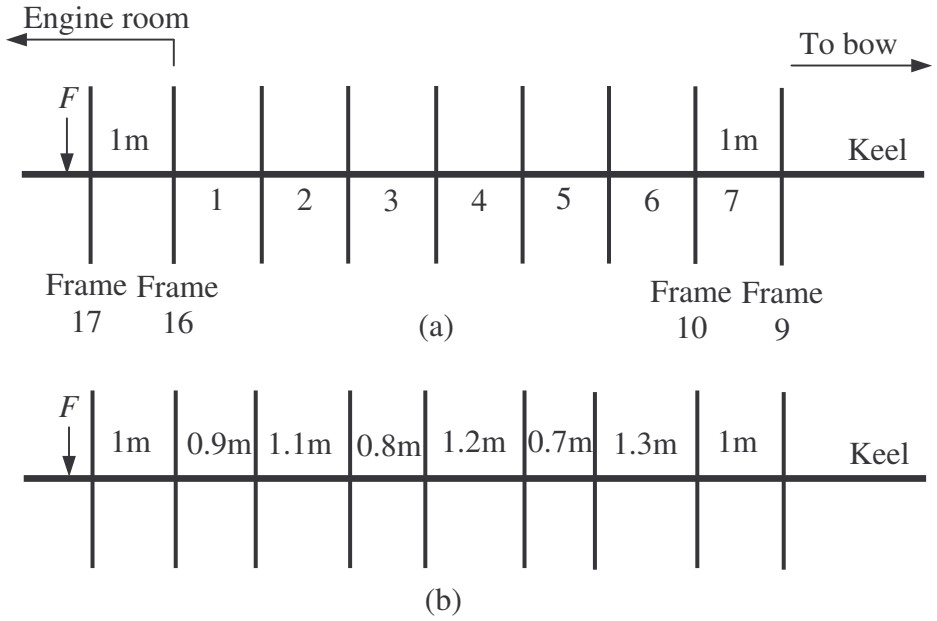

Figure 9.23. Schematic illustrations of the ship hull section used in the study. (a) Regularly supported keel; (b) Irregularly supported keel.

The schematic illustrations of the two FEA models used in this study are shown in Figure 9.23. In the first FEA model, besides the stiffness components of the engine room section as described in Figure 9.14(a), the frames between Frame 9 and Frame 16 are also included in the simulation. All frames are 1m apart from each other in this FEA model. The seven keel sections divided by these frames are manifested by the serial numbers as shown in Figure 9.23 (a). In the second FEA model (Figure 9.23(b)), Frame 15, Frame13 and Frame 11 are moved to the left by 0.1m, 0.2m and 0.3m respectively away from the corresponding periodic locations.

Similar to those in Chapters 4 and 6, the periodic characteristics and vibration confinement of ship structures are studied here by the kinetic energy distributions of the corresponding keel sections. The kinetic energy distribution of each keel section in the FEA model with respect to one of the three translational directions of the keel (one in-plane and two flexural vibrations) is calculated by:

$$\left\langle \overline{T} \right\rangle_x = \frac{1}{2} \sum_{i=1}^{N} L_{ei} A_{ei} \rho \left| \frac{v_{x(i-1)} + v_{xi}}{2} \right|^2, \tag{9.1}$$

where L_{ei} and A_{ei} are respectively the length and the cross sectional area of the i^{th} element, N is the total number of elements enclosed in the keel section. v_{xi} is the velocity response in the x coordinate direction at the i^{th} node of the keel section. The vibration energy of the keel section with respect to the other two coordinate directions (flexural vibration energies) can be evaluated similarly where the subscript x in Equation (9.1) is simply replaced by y or z.

The kinetic energy distributions of the odd numbered sections of the keel in Figure 9.23(a) due to flexural vibration in the direction of the force excitation (z) are shown in Figure 9.24. It is found that at low frequencies, the vibration energy is not attenuated as the waves propagate away from the engine room (source section). This is attributed to the relatively long flexural wavelength of the keel in this frequency range when compared to the span between two consecutive frames. In contrast, vibration in most of the frequency bands at higher frequencies (at frequencies above 100Hz) is attenuated significantly as waves propagate away from the source section. The attenuation is the result of vibration localization attributed to the existing irregularities in the system (i.e. non-uniform cross section area of the keel and non-uniform shapes of the frames). Similar results are also found for wave propagations in the other two translational directions of the keel.

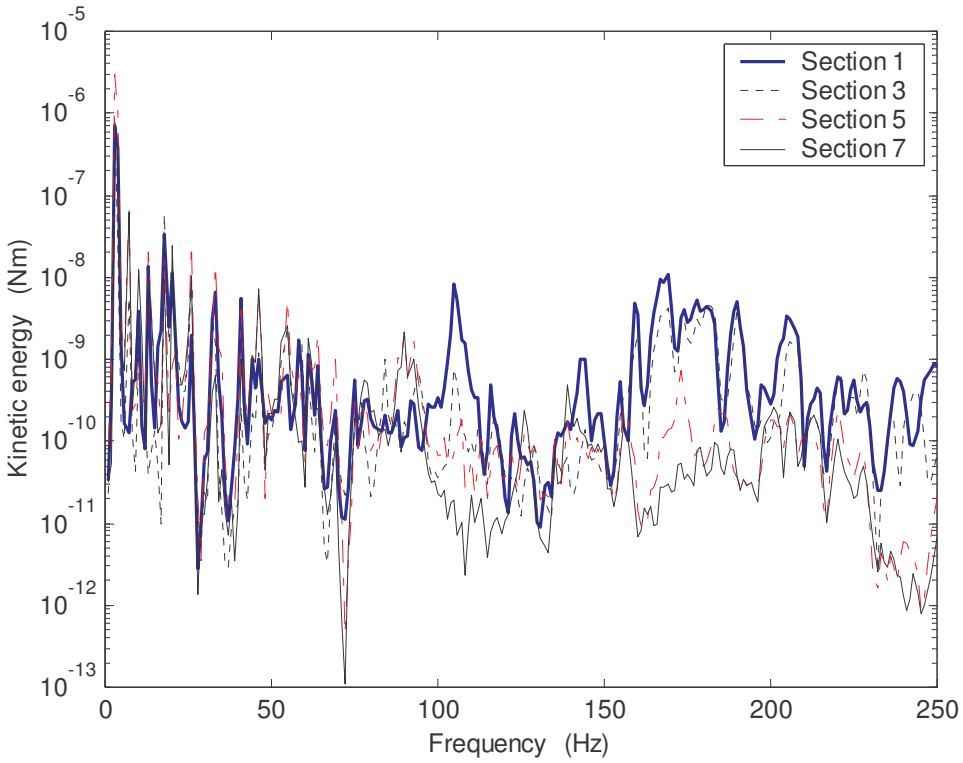

Figure 9.24. Kinetic energy distributions of the odd number keel sections due to flexural vibration in the principle direction of the beam.

The results shown in Figures 9.20 – 9.22 and Figure 9.24 indicate that the low frequency components of ship vibration are difficult to control by applying the traditional passive control methods. A common approach for the low frequency vibration control is active vibration controls. However, active vibration controls on ship structure vibration could be very expensive let alone the uncertainty of control outcomes due to the complexity of ship structures. Alternatively, by utilizing the same philosophy as that used in the investigation of vibration confinement in disordered periodic ribbed plates (see Sections 4.6.2 and 6.4.3), a simple passive vibration control method is proposed here as illustrated in Figure 9.23(b) where some of the frames are moved away from the corresponding periodic locations. The flexural vibration energies for Section 7 of the keel prior and after the irregularity are shown in Figure 9.25.

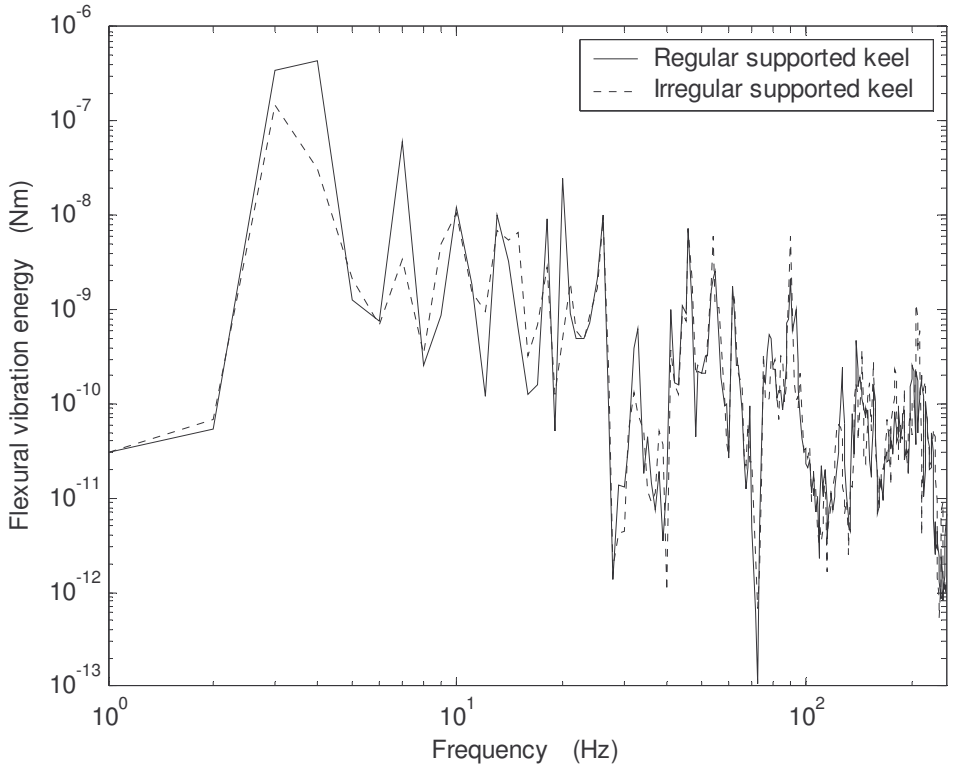

Figure 9.25. The kinetic energy distributions of the keel section 7 in the regular and irregular support cases.

It is found that amplitudes for most of the low frequency peak responses decrease significantly from those in the periodic case after the irregularity. The mechanism for the vibration confinement is the same as discussed in Chapters 4 and 6 where modal vibration amplitude is attenuated by the frame in-plane stiffness when the frames are moved to or close to the anti-nodal position of the mode. However, it is also observed that the response amplitudes for some other modes in the same frequency range are not attenuated by the irregularity. This is mainly attributed to two reasons. Firstly, only three frames are moved away from the periodic locations in the simulation. Secondly, the peaks governed by the moment couplings at the interfaces between the frames and the keel are not localized by the frame location irregularity. It has been exposed in Chapter 4 that to localize this group of modes, one needs to impose property irregularity to the frames, such as irregular frame thickness.

9.5 Conclusion

In this chapter, vibration responses of the engine room section of a 30m crew vessel due to point force, moment excitations applied on one of the engine beds are investigated by FEA analysis. Results obtained from FEA analysis are compared to the analytical results of the corresponding simple structural components. It is found that the input mobilities of the engine room due to point force and moment excitations on the engine bed are dominated by the stiffness of the engine bed (beam) where the force (moment) is applied. The frequency averaged vibration responses of the engine room due to such excitations can be estimated approximately by those of the corresponding beams or beam stiffened plates of finite or infinite extents.

It is shown that vibration responses of ship structures at higher frequencies could be controlled by structural modifications of the mounting structure under direct point force or moment excitations. Wave propagation in ship structures at low frequencies could be confined by imposing structural irregularities on the frames.

Chapter 10
Conclusions and Recommendations

10.1 Conclusions

Vibration responses of finite coupled structures typical for ship constructions were investigated analytical, numerically and experimentally in this study. Interesting vibration and wave propagation characteristics of coupled structures were discussed and summarized in this thesis. Additionally, a simple experimental method was developed in the study to evaluate the frequency dependent stiffness and damping coefficient of rubber mounts. Both analytical and numerical methods were also applied for the prediction and vibration controls of ship hull structures.

It was found in Chapter 2 that effects of off-neutral axis loading on the vibration response of a finite ribbed plate are most significant at low frequencies. Besides changing the amplitude of some peak responses at low frequencies, the off-neutral axis loading also affects the kinetic energy distribution in the component plates of the ribbed plate. It was shown that negative input power is possible at low frequencies if only one component of the input power (either point force or moment) is considered in the off-neutral axis loading case. It was also found that beam torsional vibration could be ignored in the ribbed plate formulation if the point force is applied on the neutral axis of the beam.

It was illustrated in Chapter 3 that input mobilities of a finite ribbed plate due to point force or bending moment excitations are bounded by those of the corresponding uncoupled plate and beam forming the ribbed plate. Beam flexural stiffness dominates the stiffness term of point force or bending moment input

mobilities of the ribbed plate when the point force or bending moment is applied on the beam or very close to the beam. The input mobility is controlled by the plate bending stiffness when the excitation location is more than a quarter of plate bending wavelength away from the beam. In contrast, the torsional moment input mobility of the ribbed plate is dominated by the plate bending stiffness, which does not vary much from that of the corresponding uncoupled plate.

For point force or bending moment excitations, a large reduction in plate vibration can be found at low frequencies after insertion of the stiffened beam on the plate. Negative reduction can be observed in frequency bands associated with some of the shifted peak frequencies after the beam insertion. The vibration reduction tends to zero at high frequencies when the beam is more than a quarter wavelength away from the source. On the other hand, for torsional moment excitation, the insertion of the beam on the plate only changes the peak response frequencies but not the overall frequency averaged plate vibration energy.

The ‘pass band’ and ‘stop band’ properties of finite periodic ribbed plates as well as vibration confinement of finite irregularly ribbed plates were explored in Chapter 4. It was found that the ‘pass band’ of a finite periodic ribbed plate could be classified into two groups according to the coupling mechanisms at the beam/plate interfaces. One group is governed by the shear force couplings at the beam/plate interfaces (i.e. ***F/F*** wave propagation zones), another is governed by the moment couplings at the interfaces (i.e. ***T/F*** wave propagation zones). Physical interpretations were given to the boundary frequencies and the peak responses in each pass band of the finite periodic ribbed plate. It was illustrated that each ***F/F*** wave propagation zone is dominated by one beam flexural wave number (k_n). Modes in the first (***F/F***) pass band ($n=1$) can be approximated by those of the corresponding orthotropic plate

while modes in the second (***F/F***) pass band ($n = 2$) all have similar mode shape distribution corresponding to the modal wave number $(m', n) = (9,2)$. The resonance frequencies for modes in the ***T/F*** bands are closed to the resonances frequencies of the corresponding un-ribbed plate although mode shape distributions for this group of modes are often difficult to describe by numerical modal indices.

Furthermore, the study also shown that irregular beam spacing for a multiple ribbed plate could only localize the group of modes associated with the flexural couplings at beam/plate interfaces but not the group of modes associated with the torsional couplings at the interfaces. To localize the modes in the latter group, one needs to apply torsional stiffness irregularity to the stiffened beams.

Validities of SEA in the prediction of vibration response of plate/plate coupled structures due to deterministic force and moment excitations were examined in Chapter 5. It was found that SEA could be employed to predict the frequency averaged vibration response of L-shaped plates in point force excitation cases providing that the source location is more than a quarter of plate bending wavelength away from the source plate edges. Such restriction could be relaxed further in moment excitation cases where only the distance between the source location and a pair of the source plate edges (the pair of plate edges perpendicular the moment axis) could have large effects on the vibration response of the L-shaped plate.

Analytical solutions were obtained in Chapter 6 to predict the vibration response of a coupled system consisting of two finite periodic or irregular ribbed plates coupled at right angles to point force excitation applied on the plate or on the beams. It was shown that the input mobility of the coupled system is mainly dominated by the flexural stiffness of the source ribbed plate where the lower bounding frequencies of

the ***F/F*** propagation zones of the coupled system remain unchanged from those of the corresponding single (source) periodic ribbed plate. It was found that the number of peaks in each ***F/F*** wave propagation zone of the coupled system is the superposition of the peaks in the corresponding propagation zones of the two periodic ribbed plates when detached from each other. As a result, the upper bounding frequencies and the bandwidthes of wave propagation zones increase slightly from those of the corresponding periodic ribbed plate. Furthermore, the receiving plate would have less modal energy than that of the source plate for peaks in the ***F/F*** zones and corresponding to the resonant responses of the source ribbed plate. It would have higher modal energy than that of the source plate for peaks in the ***F/F*** zones but corresponding to the resonant responses of the receiving plate. It was found that the mode shape distributions for modes in ***F/F*** zones are more complex than those of the corresponding orthogonal plate due to modal interactions between the source and the receiving ribbed plates.

Imposing beam spacing irregularity on the source ribbed plate can only localize modes in ***F/F*** wave propagation zones and corresponding to the resonant responses of the source plate. Modes in ***F/F*** propagation zones but corresponding to the resonant responses of the receiving plate are not localized by the irregularity. On the contrary, most modes of the coupled system are localized when the cross section areas of the beams on the source ribbed plate become irregular. Increased modal amplitude at frequencies corresponding to the new ‘trace-matching’ conditions between the plate bending waves and the flexural/torsional waves of the non-uniform cross section beams after the irregularity were also observed.

Accuracies of analytical solutions of coupled structures obtained in the first six chapters of this thesis were assessed by results obtained from FEA analysis.

Additionally, experiment investigations on the vibration response a completely clamped-clamped ribbed plate were presented in Chapter 7 where the accuracy of the analytical solution was evaluated. General good agreement was found between experimental results and the analytical predictions. Some discrepancies were also observed and were explained in the analysis. The dependency of input mobilities of ribbed plates on the distance between the source location and the beam was also verified experimentally in this chapter. It is beam stiffness control when the excitation location is applied at or very closed to the beam and is plate stiffness control when the beam is more than a quarter of plate bending wavelength away from the source.

A simple experimental method based on an impact test technique was developed in Chapter 8 to evaluate the frequency dependent stiffness and damping characteristics of rubber mounts. The test result quantified the transition of the rubber mount stiffness from the static to the dynamic values and the static stiffness of the rubber element. The dependency of rubber mount stiffness and damping coefficient on static pre-load and on vibration amplitude can be handled well by simply adjusting the mass and impact force amplitude during the test. The results indicate that the rubber mount damping coefficient is a linear function of frequency for frequencies below, at and above the resonance frequency. It also demonstrates that the non-linear dependence of the rubber mount stiffness on frequency in the low frequency range as well as in the resonance frequency band.

Finally, by utilizing the analytical solutions of simple and coupled structures as well as finite element analysis, vibration and vibration control of ship hull structures were studied in Chapter 9. It was found that the input mobility of ship hull structures due to point force or moment excitations (typical for engine excitations) on the engine

bed is dominated by the stiffness of the engine bed where the force (moment) is applied. The frequency averaged vibration responses of the ship structure due to such excitations can be estimated approximately by those of the corresponding beams or beam stiffened plates of finite or infinite extents. It was found that vibration responses of ship structures at higher frequencies could be controlled by structural modifications of the mounting structures where the excitation force or moment applied. Wave propagation in ship structures at low frequencies could be confined by imposing structural irregularities on the ship frames.

10.2 Recommendations and future work

This study provided only analytical solutions for vibration responses of finite coupled structures *in vacuo*. Many questions remain un-answered or were not considered because of the limitation of the time span allocated for this PhD research. These constitute the areas of interest for future research.

10.2.1 Vibration response of finite orthogonal stiffened ribbed plates

The analysis presented in this study considered finite plates reinforced by beams in one direction only, while in practical applications such as ship hull structures, plates are often reinforced by beams in two orthogonal directions. The extension of the analytical approaches to orthogonal ribbed plates requires further effort and contribution from researchers working in this area.

10.2.2 Vibration of periodic structures when coupled with ambient fluid mediums and the sound radiation from the structure

Only *in vacuo* finite coupled structures were considered in this analysis where the fluid loading effect of ambient fluid medium to the structure response was ignored. Sound radiation from the vibrating structure was also not considered in this analysis. These constitute another area of research interest for future study.

10.2.3 Transition from beam/plate coupling to plate/plate coupling

In a periodic or irregular ribbed plate, the structural couplings are usually considered as beam/plate couplings. However, when the spans between the ribs become smaller than the depth of the ribs, the ribs would behave more like narrow plates than beams. Because a beam/plate coupling structure would have different vibration and sound radiation characteristics than a plate/plate coupling structure, choosing the right type of structural couplings to depict a physical system has profound significance in the engineering design and applications. The condition for transitions from beam/plate couplings to plate/plate couplings was not quantified before, which constitutes to another area of research interest for the future.

10.2.4 Limitations of this thesis work

In this thesis, conclusions are drawn based on simulation results of limit examples. The author awares that claims made based on the results of only one or a few particular cases may hinder the generality of the conclusions. Nevertheless, he hopes that those examples may shed some lights to the general understanding of the vibro-acoustics of marine vessels, and stimulate more exciting future work in this area of research.

Appendix A

A.1 Flexural vibration of finite beams

Using Euler-Bernoulli beam formulation, the governing equation of beam flexural displacement (U) to a general force excitation (Q_b) is:

$$\frac{\partial^4 U}{\partial y^4} - k_b^4 U = \frac{Q_b}{B_b}, \tag{A.1}$$

where B_b and k_b are the beam flexural stiffness and wave number respectively.

Equation (A.1) can be solved by modal expansion of the beam displacement as:

$$U = \sum_n u_n \phi_n(y), \tag{A.2}$$

where $\phi_n(y)$ is the mode shape function of the beam, which is given for the three classical boundary conditions, namely, simply supported, clamped-clamped and free-free boundary conditions.

a) Simply supported boundary condition

The mode shape function for a beam with both ends simply supported is given by:

$$\phi_n(y) = \sin(k_n y), \tag{A.3}$$

where $k_n = \frac{n\pi}{L_y}$ is the modal wave number of the simply supported beam.

b) Clamped-clamped boundary condition

The mode shape function for a beam with both ends clamped is given by:

$$\phi_n(y) = \sinh(k_n y) - \sin(k_n y) - \beta_n[\cosh(k_n y) - \cos(k_n y)], \tag{A.4}$$

where $\beta_n = \frac{\sinh(k_n L_y) - \sin(k_n L_y)}{\cosh(k_n L_y) - \cos(k_n L_y)}$ is the modal constant while the modal wave number k_n is given by:

$$k_n = \frac{\pi}{2L_y}[3.011, 5, 7, ..., (2n+1)], \qquad n = 1, ..., \infty . \tag{A.5}$$

c) Free-free boundary condition

The mode shape function for a beam with free-free boundary conditions is given by:

$$\phi_n(y) = \sinh(k_n y) + \sin(k_n y) - \beta_n[\cosh(k_n y) + \cos(k_n y)], \tag{A.6}$$

where β_n and k_n are the same as in the clamped-clamped case.

Substituting Equation (A.2) into Equation (A.1), one has:

$$U = \sum_n \frac{\int_0^{Ly} Q_b \phi_n(y) dy}{G_n} \phi_n(y), \tag{A.7}$$

where $G_n = B_b \Lambda_n (k_n^4 - k_b^4)$ is the modal stiffness term of the beam flexural vibration, Λ_n is given by:

$$\Lambda_n = \int_0^{Ly} \phi_n^2(y) dy = \frac{L_y}{2}, \tag{A.8}$$

for simply supported boundary conditions, and

$$\Lambda_n = \beta_n^2 L_y + \frac{1}{2k_n}\{(1+\beta_n^2)\cosh(k_n L_y)[\sinh(k_n L_y) - 2(-1)^n] + 2\beta_n[2(-1)^n \sinh(k_n L_y) - \cosh^2(k_n L_y)]\}, \tag{A.9}$$

for clamped-clamped boundary conditions, and

$$\Lambda_n = \beta_n^2 L_y + \frac{1}{2k_n}\{(1+\beta_n^2)\cosh(k_n L_y)[\sinh(k_n L_y) + 2(-1)^n] - 2\beta_n[2(-1)^n \sinh(k_n L_y) + \cosh^2(k_n L_y)]\} , \tag{A.10}$$

for free-free boundary conditions.

A.1.1 Point force excitation

For this excitation case, $Q_b = F_b\delta(y - y_b)$, where $\delta(y - y_b)$ is the Dirac Delta function. The modal force term in Equation (A.7) is given by:

$$\int_0^{Ly} Q_b\phi_n(y)dy = F_b\phi_n(y_b). \tag{A.11}$$

The beam flexural response to point force excitation can be obtained by substituting Equation (A.11) into Equation (A.7) and the point force input mobility of the beam is given by:

$$Y^F(y_b) = \frac{j\omega U(y_b)}{F_b} = j\omega\sum_n \frac{\phi_n^2(y_b)}{G_n}. \tag{A.12}$$

The time averaged beam flexural vibration energy is:

$$\left\langle \overline{T} \right\rangle_b = \frac{\rho_L}{2}\int_0^{Ly} \dot{U}\dot{U}^* dy = \frac{\rho_L\Lambda_n\omega^2\left|F_b\right|^2}{2}\sum_n \frac{\phi_n^2(y_b)}{\left|G_n\right|^2}. \tag{A.13}$$

A.1.2 Bending moment excitation

Letting $Q_b = M_b\delta'(y - y_b)$, the modal force term in Equation (A.7) becomes:

$$\int_0^{Ly} Q_b\phi_n(y)dy = M_b\phi_n'(y_b). \tag{A.14}$$

The input mobility of the bending moment is now given by:

$$Y^{M_b}(y_b) = \frac{j\omega U'(y_b)}{M_b} = j\omega\sum_n \frac{\phi_n'^2(y_b)}{G_n}. \tag{A.15}$$

While the beam flexural vibration energy is calculated by:

$$\left\langle \overline{T} \right\rangle_b = \frac{\rho_L\Lambda_n\omega^2\left|M_b\right|^2}{2}\sum_n \frac{\phi_n'^2(y_b)}{\left|G_n\right|^2}. \tag{A.16}$$

A.2 Torsional vibration of finite beams

The governing equation of beam torsional displacement (θ) to torsional moment excitation M_t is:

$$\frac{\partial^2\theta}{\partial y^2} + k_t^2\theta - R\frac{\partial^4\theta}{\partial y^4} = \frac{M_t\delta(y-y_b)}{T}, \tag{A.17}$$

where T and k_t are respectively the torsional stiffness and torsional wave number of the beam, R is the warping to torsional stiffness ratio of the beam. The torsional and warping constants for some typical beam cross sections can be found in reference [4].

Equation (A.17) is solved by modal expansion of the beam torsional displacement (θ) as:

$$\theta = \sum_n \theta_n\phi_n(y). \tag{A.18}$$

Substituting Equation (A.18) into Equation (A.17) to have:

$$\theta = -\sum_n \frac{M_t\phi_n(y_b)}{G_{Tn}}\phi_n(y), \tag{A.19}$$

where $G_{Tn} = T\Lambda_n(Rk_n^4 - \alpha_n k_n^2 - k_t^2)$ is the modal stiffness term for the beam torsional response. For simply supported boundary conditions, $\alpha_n = -1$ while for clamped-clamped or free-free boundary conditions, $\alpha_n = \frac{\Lambda_n^*}{\Lambda_n}$ where

$$\Lambda_n^* = -L_y + \frac{1}{2k_n}[(1+\beta_n^2)\sinh(k_nL_y)\cosh(k_nL_y) + 2\beta_n(1-\sinh^2(k_nL_y))]. \tag{A.20}$$

From Equation (A.19), the torsional moment input mobility is now given by:

$$Y^{M_t} = \frac{j\omega\theta(y_b)}{M_t} = j\omega\sum_n \frac{\phi_n^2(y_b)}{G_{Tn}}. \tag{A.21}$$

The beam torsional vibration energy is then:

$$\left\langle \overline{T} \right\rangle_t = \frac{\rho_b I_p \Lambda_n \omega^2 \left| M_t \right|^2}{2} \sum_n \frac{\phi_n^2(y_b)}{\left| G_{Tn} \right|^2}. \tag{A.22}$$

A.3 Vibration response of infinite beams

The point force input mobility of an infinite beam is given by [1, 7]:

$$Y_{\inf}^{F} = \frac{(1+j)k_b}{4\rho_L \omega}. \tag{A.23}$$

The input mobility of an infinite beam to bending moment excitation is given by:

$$Y_{\inf}^{M_b} = \frac{(1-j)\omega}{4Bk_b}. \tag{A.24}$$

While the input mobility of an infinite beam to torsional moment excitation is:

$$Y_{\inf}^{M_t} = \frac{1}{2\sqrt{T\rho_b I_p}}. \tag{A.25}$$

A.4 Flexural vibration of finite rectangular plates

Using thin plate formulation, the governing equation of plate bending displacement (W) to general force excitations (Q) can be written as:

$$\nabla^4 W - k_p^4 W = \frac{Q_p}{D}, \tag{A.26}$$

where k_p and D are respectively the plate bending wave number and rigidity.

Using two orthogonal beam deflection functions corresponding to the two plate edge directions [6], Equation (A.26) is solved by:

$$W = \sum_m \sum_n w_{m,n} \phi_m(x) \phi_n(y), \tag{A.27}$$

where $w_{m,n}$ is the modal coefficient of the plate vibration modes, $\phi_m(x)$ and $\phi_n(y)$ is the beam mode shape functions with respect to the two plate edge directions. It should be noted that Equation (A.27) in current form is only valid for plates with at least one pair of plate edges simply supported.

A.4.1 Point force excitation

Letting $Q_p = F_p\delta(x-x_0)\delta(y-y_0)$ in Equation (A.26), the plate response can be solved by substituting Equation (A.27) into Equation (A.26) and integrating over the plate surface area as [1, 2]:

$$W = \sum_m \sum_n \frac{F_p \phi_m(x_0)\phi_n(y_0)}{G_{m,n}} \phi_m(x)\phi_n(y), \tag{A.28}$$

where $G_{m,n} = D\Lambda_{m,n}(k_{m,n}^4 - k_p^4)$ is the modal stiffness term of the plate response, $\Lambda_{m,n} = \Lambda_m \Lambda_n$ is the modal constant and $k_{m,n}$ is modal wave number of the plate bending modes, which is given by:

$$k_{m,n} = \left(k_m^4 + 2\alpha_m \alpha_n k_m^2 k_n^2 + k_n^4\right)^{1/4}, \tag{A.29}$$

where $\phi_m(x)$, k_m, α_m, Λ_m and Λ_m^* are similarly defined as in Section A.1 by simply interchanging the modal index m by n and L_y by L_x.

From Equation (A.28), the point force input mobility of the plate is obtained:

$$Y^{F_0} = j\omega \sum_m \sum_n \frac{\phi_m^2(x_0)\phi_n^2(y_0)}{G_{m,n}}. \tag{A.30}$$

While the averaged plate kinetic energy is:

$$\left\langle \overline{T} \right\rangle_P = \frac{\rho_s \Lambda_{m,n} \omega^2 \left|F_p\right|^2}{2} \sum_m \sum_n \left| \frac{\phi_m(x_0)\phi_n(y_0)}{G_{m,n}} \right|^2. \tag{A.31}$$

A.4.2 Moment excitation

Assuming the distance of the force pair that forms the dipole moment is greater than the plate thickness [114], the plate response to a moment excitation $Q_p = -M_0 \cos\varphi\, \delta(x-x_0)\, \delta'(y-y_0) + M_0 \sin\varphi\, \delta'(x-x_0)\, \delta(y-y_0)$ is given by:

$$W = -M_0 \sum_m \sum_n \frac{\cos\varphi\, \phi_m(x_0)\phi_n'(y_0) - \sin\varphi\, \phi_m'(x_0)\phi_n(y_0)}{G_{m,n}} \phi_m(x)\phi_n(y), \tag{A.32}$$

where φ is the angle of the moment axis with respect to the x-coordinate of the coordinate system.

The moment input mobility functions corresponding to the two angular velocity components at the source location of the plate are:

$$Y_x^M = -j\omega \sum_m \sum_n \frac{\cos\varphi\, \phi_m^2(x_0)\phi_n'^2(y_0) - \sin\varphi\, \phi_m(x_0)\phi_m'(x_0)\phi_n(y_0)\phi_n'(y_0)}{G_{m,n}}, \tag{A.33}$$

and

$$Y_y^M = -j\omega \sum_m \sum_n \frac{\cos\varphi\, \phi_m(x_0)\phi_m'(x_0)\phi_n(y_0)\phi_n'(y_0) - \sin\varphi\, \phi_m'^2(x_0)\phi_n^2(y_0)}{G_{m,n}}. \tag{A.34}$$

While the averaged vibration kinetic energy distribution is:

$$\left\langle \overline{T} \right\rangle_P = \frac{\rho_s \Lambda_{m,n} \omega^2 \left|M_0\right|^2}{2} \sum_m \sum_n \left| \frac{\cos\varphi\, \phi_m(x_0)\phi_n'(y_0) - \sin\varphi\, \phi_m'(x_0)\phi_n(y_0)}{G_{m,n}} \right|^2. \tag{A.35}$$

A.5 Flexural vibration of infinite plates

The point force input mobility of an infinite plate is [1, 7]:

$$Y_{\inf}^F = \frac{1}{8\sqrt{D\rho_s}}. \tag{A.36}$$

The moment input mobility of an infinite plate is [1]:

$$Y_{\inf}^{M} = \frac{\omega}{16D}[1 - j\frac{4}{\pi}\ln(0.9k_p a)], \tag{A.37}$$

where a is the dipole distance that measures the distance between the forces forming the dipole moment. Similar expression can also be found in reference [7].

A.6 Vibration response of infinite ribbed plates

A.6.1 Point force input mobility of infinite ribbed plates

The input mobility of infinite ribbed plate to point force excitation on the beam is [7]:

$$Y_{\inf}^{F} = \frac{k_b}{4\rho_L \omega}[1 + j - j\frac{4D}{\pi B_b k_b}(1 + \frac{3 - s^2}{2s^2\sqrt{1 - s^2}}\cos s + \frac{3 + s^2}{2s^3\sqrt{1 + s^2}}\sinh s)], \tag{A.38}$$

where $s = \frac{k_b}{k_p}$ is the beam and plate flexural wave number ratio. It is noted that the real part of input mobility given by Equation (A.38) is the same as that of infinite beam. The difference in the imaginary part is only significant at low frequencies [11].

A.6.2 Bending moment input mobility of infinite ribbed plates

The input mobility of infinite ribbed plates to bending moment excitation on the beam is given [7] as:

$$Y_{\inf}^{M_B} = \frac{\omega}{4B_b k_b}[1 - j - \frac{D(2s^4 + s^2 + 1)}{B_b k_b s^3\sqrt{1 + s^2}}], \tag{A.39}$$

The input mobility given by Equation (A.39) only varies from that of the corresponding infinite beam by an additional real part, which is only important at low frequencies.

A.6.3 Torsional moment input mobility of infinite ribbed plates

The input mobility of infinite ribbed plates to torsional moment excitations on the beam at frequencies above the coincidence frequency ($k_p = k_t$) is [7]:

$$Y_{\text{inf}}^{M_T} = \frac{\omega}{T}\{\frac{1}{2k_t} - \frac{r^2}{k_t^3} + \frac{rk_p^2}{2k_t^4} - j\frac{2r}{\pi k_t^2}[1 + \frac{k_p^2}{k_t^2}\ln(1+\sqrt{2}) + \frac{k_p^2}{4k_t^2}\ln\frac{j(\sqrt{2}-1)+\frac{k_p}{k_t}}{j(\sqrt{2}+1)+\frac{k_p}{k_t}} - \frac{2r^2}{3k_t^2}]\}, \quad \text{(A.40)}$$

where $r = \frac{D}{T}$ is the plate bending to beam torsional stiffness ratio. The first term in the brace is the input mobility of the corresponding uncoupled beam to the same excitation while the other terms are the contributions from the coupled plate, which diminished at high frequencies. At frequencies below the coincidence frequency, the torsional moment input mobility of the infinite ribbed plate can be approximated by that of infinite plates providing that the beam torsional stiffness and inertia are relatively small [7].

Appendix B

B.1 Matrix $[C]_n$ for point force excitation on the beam

$$[C]_n = \begin{bmatrix}
c_1 & 1 & c_2 & 1 & 0 & 0 & 0 & 0 & 0 & 0 & 0 & 0 \\
c_1 & 1 & c_2 H^2 & H^2 & 0 & 0 & 0 & 0 & 0 & 0 & 0 & 0 \\
1 & c_1 & 1 & c_2 & -c_3 & -1 & -c_4 & -1 & 0 & 0 & 0 & 0 \\
1 & -c_1 & H & -c_2 H & -c_3 & 1 & c_4 H & -H & 0 & 0 & 0 & 0 \\
r_1 & c_1 r_1 & r_2 & c_2 r_2 & 0 & 0 & 0 & 0 & -\frac{1}{D\Lambda_n} & 0 & 0 & 0 \\
-r_2 & c_1 r_2 & -r_1 H & c_2 r_1 H & 0 & 0 & 0 & 0 & 0 & -\frac{1}{D\Lambda_n k_{n1}} & 0 & 0 \\
0 & 0 & 0 & 0 & c_3 r_1 & r_1 & c_4 r_2 & r_2 & 0 & 0 & -\frac{1}{D\Lambda_n} & 0 \\
0 & 0 & 0 & 0 & -c_3 r_2 & r_2 & -c_4 r_1 H & r_1 H & 0 & 0 & 0 & -\frac{1}{D\Lambda_n k_{n1}} \\
0 & 0 & 0 & 0 & 1 & c_3 & 1 & c_4 & 0 & 0 & 0 & 0 \\
0 & 0 & 0 & 0 & 1 & c_3 & H^2 & c_4 H^2 & 0 & 0 & 0 & 0 \\
0 & 0 & 0 & 0 & c_3 & 1 & c_4 & 1 & 0 & -\frac{1}{G_n} & 0 & \frac{1}{G_n} \\
.0 & 0 & 0 & 0 & c_3 & -1 & c_4 H & -H & \frac{1}{G_{Tn} k_{n1}} & \frac{-t}{2G_{Tn} k_{n1}} & \frac{-1}{G_{Tn} k_{n1}} & \frac{-t}{2G_{Tn} k_{n1}}
\end{bmatrix} \tag{B.1}$$

where $H = \frac{k_{n2}}{k_{n1}}$, $r_1 = k_{n1}^2 - \nu k_n^2$ and $r_2 = k_{n2}^2 - \nu k_n^2$.

B.2 Matrix $[C]_n$ for point force excitation on the plate

$$
[C]_n = \begin{bmatrix}
c_1 & 1 & c_2 & 1 & 0 & 0 & 0 & 0 & 0 & 0 & 0 & 0 & 0 & 0 & 0 & 0 \\
c_1 & 1 & c_2H^2 & H^2 & 0 & 0 & 0 & 0 & 0 & 0 & 0 & 0 & 0 & 0 & 0 & 0 \\
c_5 & \frac{c_1}{c_5} & c_7 & \frac{c_2}{c_7} & -c_5 & -\frac{c_1}{c_5} & -c_7 & -\frac{c_2}{c_7} & 0 & 0 & 0 & 0 & 0 & 0 & 0 & 0 \\
c_5 & -\frac{c_1}{c_5} & c_7H & -\frac{c_2}{c_7}H & -c_5 & \frac{c_1}{c_5} & -c_7H & \frac{c_2}{c_7}H & 0 & 0 & 0 & 0 & 0 & 0 & 0 & 0 \\
c_5 & \frac{c_1}{c_5} & c_7H^2 & \frac{c_2}{c_7}H^2 & -c_5 & -\frac{c_1}{c_5} & -c_7H^2 & -\frac{c_2}{c_7}H^2 & 0 & 0 & 0 & 0 & 0 & 0 & 0 & 0 \\
c_5 & -\frac{c_1}{c_5} & c_7H^3 & -\frac{c_2}{c_7}H^3 & -c_5 & \frac{c_1}{c_5} & -c_7H^3 & \frac{c_2}{c_7}H^3 & 0 & 0 & 0 & 0 & 0 & 0 & 0 & 0 \\
0 & 0 & 0 & 0 & 1 & c_1 & 1 & c_2 & -c_3 & -1 & -c_4 & -1 & 0 & 0 & 0 & 0 \\
0 & 0 & 0 & 0 & 1 & -c_1 & H & -c_2H & -c_3 & 1 & -c_4H & H & 0 & 0 & 0 & 0 \\
0 & 0 & 0 & 0 & r_1 & r_1c_1 & r_2 & r_2c_2 & 0 & 0 & 0 & 0 & -\frac{1}{D\Lambda_n} & 0 & 0 & 0 \\
0 & 0 & 0 & 0 & -r_2 & r_2c_1 & -r_1H & r_1c_2H & 0 & 0 & 0 & 0 & 0 & -\frac{1}{D\Lambda_n k_{n1}} & 0 & 0 \\
0 & 0 & 0 & 0 & 0 & 0 & 0 & 0 & r_1c_3 & r_1 & r_2c_4 & r_2 & 0 & 0 & -\frac{1}{D\Lambda_n} & 0 \\
0 & 0 & 0 & 0 & 0 & 0 & 0 & 0 & -r_2c_3 & r_2 & -r_1c_4H & r_1H & 0 & 0 & 0 & -\frac{1}{D\Lambda_n k_{n1}} \\
0 & 0 & 0 & 0 & 0 & 0 & 0 & 0 & 1 & c_3 & 1 & c_4 & 0 & 0 & 0 & 0 \\
0 & 0 & 0 & 0 & 0 & 0 & 0 & 0 & 1 & c_3 & H^2 & c_4H^2 & 0 & 0 & 0 & 0 \\
0 & 0 & 0 & 0 & 0 & 0 & 0 & 0 & c_3 & 1 & c_4 & 1 & 0 & -\frac{1}{G_n} & 0 & \frac{1}{G_n} \\
0 & 0 & 0 & 0 & 0 & 0 & 0 & 0 & c_3 & -1 & c_4H & -H & \frac{1}{G_{Tn}k_{n1}} & \frac{-t}{2G_{Tn}k_{n1}} & \frac{-1}{G_{Tn}k_{n1}} & \frac{-t}{2G_{Tn}k_{n1}}
\end{bmatrix}
\tag{B.2}
$$

Appendix C

C.1 Inter-relationships of wave coefficients in point force excitation case

Equation (5.9) together with the boundary condition $W_{1(x_1=0)} = 0$ at the plate/plate junction provide:

$$A_{1n} = -\Theta_1 A_{3n} - \Theta_2 A_{4n}, \tag{C.1}$$

and

$$A_{2n} = -\Theta_3 A_{3n} - \Theta_4 A_{4n}. \tag{C.2}$$

The continuity and compatibility conditions at the virtual interface of the first and the second calculation sub-domains yield:

$$A_{5n} = \frac{A_{1n}}{c_3}, \tag{C.3}$$

$$A_{6n} = A_{2n} c_1, \tag{C.4}$$

$$A_{7n} = \frac{A_{3n}}{c_4}, \tag{C.5}$$

and

$$A_{8n} = A_{4n} c_2. \tag{C.6}$$

While the compatibility and continuity conditions at the source location give:

$$A_{9n} = A_{5n} + \frac{F_n}{c_5}, \tag{C.7}$$

$$A_{10n} = A_{6n} - \frac{F_n}{c_6}, \tag{C.8}$$

$$A_{11n} = A_{7n} - \frac{F_n}{c_7 H_1}, \tag{C.9}$$

and

$$A_{12} = A_8 + \frac{F_n}{c_8 H_1}. \tag{C.10}$$

The compatibility and continuity conditions at the virtual interface of the second and the third calculation sub-domains together with the simply supported boundary conditions of the source plate edge at $x = L_x$ provide:

$$A_{14n} = A_{10n} c_3, \tag{C.11}$$

$$A_{13n} = -A_{14n} c_9, \tag{C.12}$$

$$A_{15n} = \frac{A_{11n}}{c_{10}}, \tag{C.13}$$

and

$$A_{16n} = A_{12n} c_4. \tag{C.14}$$

By using one of the two coupling boundary conditions at the plate/plate junction in conjunction with Equation (5.9) to give:

$$A_{20n} = \frac{A_{1n} c_1 - A_{2n} + A_{3n} H_1 c_2 - A_{4n} H_1}{\Delta_1}. \tag{C.15}$$

C.2 Inter-relationships of wave coefficients in moment excitation case

For this excitation case, the compatibility and continuity conditions at the source location yield:

$$A_{9n} = A_{5n} - \frac{M_n^x - M_n^y}{c_5}, \tag{C.16}$$

$$A_{10n} = A_{6n} - \frac{M_n^x + M_n^y}{c_6}, \tag{C.17}$$

$$A_{11n} = A_{7n} + \frac{M_n^x - M_n^y / H_1}{c_7}, \tag{C.18}$$

and

$$A_{12n} = A_{8n} + \frac{M_n^x + M_n^y / H_1}{c_8}. \tag{C.19}$$

While the inter-relationships between the other wave coefficients are the same as in the point force excitation case.

C.3 Energy coefficients

The four energy coefficients (T_1 - T_4) in Equation (5.28) are given as:

$$\begin{aligned} T_1 = \int_0^{Lx1} \sum_n |w_{1n}|^2 dx = \sum_n \{ & \frac{|A_{1n}|^2 + |A_{2n}|^2}{2\,\mathrm{Re}(k_{n1})}(1-|c_1|^2) + \frac{|A_{3n}|^2 + |A_{4n}|^2}{2\,\mathrm{Re}(k_{n2})}(1-|c_2|^2) - \\ & \frac{2\,\mathrm{Re}(A_{1n}^* A_{2n})\,\mathrm{Im}(c_1)}{\mathrm{Im}(k_{n1})} - \frac{2\,\mathrm{Re}(A_{3n}^* A_{4n})\,\mathrm{Im}(c_2)}{\mathrm{Im}(k_{n2})} + \\ & 2\,\mathrm{Re}[\frac{A_{1n}^* A_{4n} + A_{2n}^* A_{3n}}{k_{n1}^* - k_{n2}}(c_2 - c_1^*) + \frac{A_{1n}^* A_{3n} + A_{2n}^* A_{4n}}{k_{n1}^* + k_{n2}}(1 - c_1^* c_2)]\} \end{aligned}, \tag{C.20}$$

$$\begin{aligned} T_2 = \int_0^{x_0} \sum_n |w_{2na}|^2 dx = \sum_n \{ & \frac{|A_{5n}|^2(|c_5|^2 - |c_3|^2) + |A_{6n}|^2(1-|c_6|^2)}{2\,\mathrm{Re}(k_{n1})} + \\ & \frac{|A_{7n}|^2(|c_7|^2 - |c_4|^2) + |A_{8n}|^2(1-|c_8|^2)}{2\,\mathrm{Re}(k_{n2})} - \frac{\mathrm{Im}[A_{5n}^* A_{6n}(c_3 e^{-2j\arg(c_5)} - c_3^*)]}{\mathrm{Im}(k_{n1})} - \\ & \frac{\mathrm{Im}[A_{7n}^* A_{8n}(c_4 e^{-2j\arg(c_7)} - c_4^*)]}{\mathrm{Im}(k_{n2})} + 2\,\mathrm{Re}[\frac{A_{5n}^* A_{8n}(c_5^* c_8 - c_3^*) + A_{6n}^* A_{7n}(c_4 - c_6^* c_7)}{k_{n1}^* - k_{n2}} + \\ & \frac{A_{5n}^* A_{7n}(c_5^* c_7 - c_3^* c_4) + A_{6n}^* A_{8n}(1 - c_6^* c_8)}{k_{n1}^* + k_{n2}}]\} \end{aligned}, \tag{C.21}$$

$$\begin{aligned} T_3 = \int_{x_0}^{Lx2} \sum_n |w_{2nb}|^2 dx = \sum_n \{ & \frac{|A_{9n}|^2(1-|c_5|^2) + |A_{10n}|^2(|c_6|^2 - |c_3|^2)}{2\,\mathrm{Re}(k_{n1})} + \\ & \frac{|A_{11n}|^2(1-|c_7|^2) + |A_{12n}|^2(|c_8|^2 - |c_4|^2)}{2\,\mathrm{Re}(k_{n2})} - \frac{\mathrm{Im}[A_{9n}^* A_{10n} c_3(1 - e^{-2j\arg(c_5)})]}{\mathrm{Im}(k_{n1})} - \\ & \frac{\mathrm{Im}[A_{11n}^* A_{12n} c_4(1 - e^{-2j\arg(c_7)})]}{\mathrm{Im}(k_{n2})} + 2\,\mathrm{Re}[\frac{A_{9n}^* A_{12n}(c_4 - c_5^* c_8) + A_{10n}^* A_{11n}(c_6^* c_7 - c_3^*)}{k_{n1}^* - k_{n2}} + \\ & \frac{A_{9n}^* A_{11n}(1 - c_5^* c_7) + A_{10n}^* A_{12n}(c_6^* c_8 - c_3^* c_4)}{k_{n1}^* + k_{n2}}]\} \end{aligned}, \tag{C.22}$$

and

$$T_4 = \int_0^{Lx3} \sum_n |w_{3n}|^2 dx = \sum_n \{ \frac{|A_{13n}|^2 + |A_{14n}|^2}{2\,\mathrm{Re}(k_{n1})}(1-|c_9|^2) + \frac{|A_{15n}|^2 + |A_{16n}|^2}{2\,\mathrm{Re}(k_{n2})}(1-|c_{10}|^2) - \frac{2\,\mathrm{Re}(A_{13n}^* A_{14n})\,\mathrm{Im}(c_9)}{\mathrm{Im}(k_{n1})} - \frac{2\,\mathrm{Re}(A_{15n}^* A_{16n})\,\mathrm{Im}(c_{10})}{\mathrm{Im}(k_{n2})} + 2\,\mathrm{Re}[\frac{A_{13n}^* A_{16n} + A_{14n}^* A_{15n}}{k_{n1}^* - k_{n2}}(c_{10} - c_9^*) + \frac{A_{13n}^* A_{15n} + A_{14n}^* A_{16n}}{k_{n1}^* + k_{n2}}(1 - c_9^* c_{10})]\} \quad . \qquad \text{(C.23)}$$

Appendix D

Matrix $[C]_n$ for a completely clamped-clamped ribbed plate:

$$[C]_n = \begin{bmatrix}
c_1 & 1 & c_2 & 1 & 0 & 0 & 0 & 0 & 0 & 0 & 0 & 0 & 0 & 0 & 0 & 0 \\
c_1 & 1 & jc_2H & -jH & 0 & 0 & 0 & 0 & 0 & 0 & 0 & 0 & 0 & 0 & 0 & 0 \\
c_5 & \frac{c_1}{c_5} & c_7 & \frac{c_2}{c_7} & -c_5 & -\frac{c_1}{c_5} & -c_7 & -\frac{c_2}{c_7} & 0 & 0 & 0 & 0 & 0 & 0 & 0 & 0 \\
c_5 & -\frac{c_1}{c_5} & jc_7H & -j\frac{c_2}{c_7}H & -c_5 & \frac{c_1}{c_5} & -jc_7H & j\frac{c_2}{c_7}H & 0 & 0 & 0 & 0 & 0 & 0 & 0 & 0 \\
c_5 & \frac{c_1}{c_5} & -c_7H^2 & -\frac{c_2}{c_7}H^2 & -c_5 & -\frac{c_1}{c_5} & c_7H^2 & \frac{c_2}{c_7}H^2 & 0 & 0 & 0 & 0 & 0 & 0 & 0 & 0 \\
c_5 & -\frac{c_1}{c_5} & -jc_7H^3 & j\frac{c_2}{c_7}H^3 & -c_5 & \frac{c_1}{c_5} & jc_7H^3 & -j\frac{c_2}{c_7}H^3 & 0 & 0 & 0 & 0 & 0 & 0 & 0 & 0 \\
0 & 0 & 0 & 0 & 1 & c_1 & 1 & c_2 & -c_3 & -1 & -c_4 & -1 & 0 & 0 & 0 & 0 \\
0 & 0 & 0 & 0 & 1 & -c_1 & jH & -jc_2H & -c_3 & 1 & -jc_4H & jH & 0 & 0 & 0 & 0 \\
0 & 0 & 0 & 0 & r_1 & r_1c_1 & -r_2 & -r_2c_2 & 0 & 0 & 0 & 0 & -\frac{1}{D\Lambda_n^c} & 0 & 0 & 0 \\
0 & 0 & 0 & 0 & r_3 & -r_3c_1 & -jr_4H & jr_4c_2H & 0 & 0 & 0 & 0 & 0 & -\frac{1}{D\Lambda_n^c k_{n1}} & 0 & 0 \\
0 & 0 & 0 & 0 & 0 & 0 & 0 & 0 & r_1c_3 & r_1 & -r_2c_4 & -r_2 & 0 & 0 & -\frac{1}{D\Lambda_n^c} & 0 \\
0 & 0 & 0 & 0 & 0 & 0 & 0 & 0 & r_3c_3 & -r_3 & -jr_4c_4H & jr_4H & 0 & 0 & 0 & -\frac{1}{D\Lambda_n^c k_{n1}} \\
0 & 0 & 0 & 0 & 0 & 0 & 0 & 0 & 1 & c_3 & 1 & c_4 & 0 & 0 & 0 & 0 \\
0 & 0 & 0 & 0 & 0 & 0 & 0 & 0 & 1 & -c_3 & jH & -jc_4H & 0 & 0 & 0 & 0 \\
0 & 0 & 0 & 0 & 0 & 0 & 0 & 0 & c_3 & 1 & c_4 & 1 & 0 & -\frac{1}{G_n} & 0 & \frac{1}{G_n} \\
0 & 0 & 0 & 0 & 0 & 0 & 0 & 0 & c_3 & -1 & jc_4H & -jH & \frac{1}{G_{Tn}^c k_{n1}} & \frac{-t}{2G_{Tn}^c k_{n1}} & \frac{-1}{G_{Tn}^c k_{n1}} & \frac{-t}{2G_{Tn}^c k_{n1}}
\end{bmatrix} \tag{D.1}$$

where $r_1 = k_{n1}^2 - \nu k_n^2$, $r_2 = k_{n2}^2 + \nu k_n^2$, $r_3 = k_{n1}^2 - (2-\nu)k_n^2$ and $r_4 = k_{n2}^2 + (2-\nu)k_n^2$.

References

[1] L. Cremer, M. Heckl and E. E. Ungar, “Structure-Borne Sound”, Springer-Verlag, 1988

[2] M. C. Junger and D. Feit, “Sound, Structures, and their interaction”, The MIT press, Cambridge, Massachusetts, and London, England 1972

[3] A. W. Leissa, “Vibration of plates”, NASA SP-160, 1969

[4] J. T. Oden and E. A. Ripperger , “Mechanics of elastic structures”, McGraw-Hill Book Company Inc. 1981

[5] W. Soedel, “Vibrations of shells and plates”, Marcel Dekker, Inc, New York, 1981

[6] G. W. Warburton, “The vibration of rectangular plates”, Proceedings of the Institute of Mechanical Engineers, Series A **168**, 371-384, 1954

[7] H. G. D. Goyder, “Vibration analysis using experimental data and approximate methods with consideration of power flow from machinery into built-up structures”, PhD thesis, University of Southampton, 1978

[8] R. H. Lyon, “Statistical energy analysis of dynamical systems: Theory and Applications”, The MIT press, Cambridge, Massachusetts, 1975

[9] P. W. Anderson, “Absence of diffusion in certain random lattices”, Physical Review **109**(5), 1492 – 1505, 1958

[10] G. Maidanik, “Response of Ribbed Panels to Reverberant Acoustic Fields”, J. Acoust. Soc. Am. **34**, 809 – 826, 1962

[11] G. L. Lamb, “Input impedance of a beam coupled to a plate”, J. Acoust. Soc. Am. **33**(5), 628 – 633, 1961

[12] E. E. Ungar, “Transmission of plate flexural waves through reinforcing beams; dynamic stress concentration”, J. Acoust. Soc. Am. **33**(5), 633 – 639, 1961

[13] S. I. Kovinskaya and A. S. Nikiforov, “Flexural wave fields in infinite beam-reinforced plates under point excitation”, Soviet Physics-Acoustics **19**(1), 32-35, 1973

[14] M. L Rumerman, “ Vibration and wave propagation in ribbed plates”, J. Acoust. Soc. Am. 57(2), 370-373, 1975

[15] B. R. Mace, “Periodically stiffened fluid loaded plates, II: response to line and point forces”, J. Sound and Vib. **73**(4), 487-504, 1980

[16] N. J. Kessissoglou and J. Pan, “An analytical investigation on active attenuation of the plate flexural wave transmission through a reinforced beam”, J. Acoust. Soc. Am. **102**(6), 3530-3541, 1997

[17] N. J. Kessissoglou and J. Pan, “Active structural acoustic control of an infinite ribbed plate under light fluid loading”, J. Acoust. Soc. Am. **104**(6), 3398-3407, 1998

[18] N. J. Kessissoglou, “An analytical and experimental investigation on active control of flexural wave transmission in a simply supported ribbed plate”, J. Sound and Vib. **240**(1), 73-85, 2001

[19] D. J. Mead, “Plates with regular stiffening in acoustic media: Vibration and radiation”, J. Acoust. Soc. Am. **88**(1), 391-401, 1990

[20] G. Maidanik and J. Dickey, “Singly and regularly ribbed panels”, J. Sound and Vib. **123**(2), 309-314, 1988

[21] L. Ji, B. R. Mace and R. J. Pinnington, “A hybrid mode/Fourier-transform approach for estimating the vibrations of beam-stiffened plate systems”, J. Sound and Vib. **274**(3), 547-565, 2004

[22] V. N. Romanov, “Radiation of sound by an infinite plate with reinforced beams”, Sov. Phys. Acoust. **17**, 92-96, 1971

[23] V. N. Evseen, “Sound radiation from an infinite plate with periodic inhomogeneities”, Sov. Phys.Acoust. **19**, 226-229, 1973

[24] G. F. Lin and S. I. Hayek, “Acoustic radiation from point excited rib-reinforced plate”, J. Acoust. Soc. Am. **62**(1), 72-83, 1977

[25] D. J. Mead and A. K. Mallik, “An approximate theory for the sound radiated from a periodic line-supported plate”, J. Sound and Vib. **61**(3), 315-326, 1978

[26] G. P. Eatwell and D. Bulter, “The response of a fluid-loaded beam-stiffened plate”, J. Sound and Vib. 84(3), 371-388, 1982

[27] C. L. Kirk, “Vibration Characteristics of Stiffened Plates”, J. Mech. Sci. **2**(3), 242-253, 1960

[28] D. J. Mead and S. Parthan, “Free wave propagation in two dimensional periodic plates”, J. Sound and Vib. **64**(3), 325-348, 1979

[29] P. A. A. Laura and R. H. Gutierrez, “A note on transverse vibrations of stiffened rectangular plates with edges elastically restrained against rotation”, J. Sound and Vib. **78**(1), 139-144, 1981

[30] J. R. Wu and W. H. Liu, “Vibration of rectangular plates with edge restraints and intermediate stiffeners”, J. Sound and Vib. **123**(1), 103-113, 1988

[31] T. Wah, “Vibration of Stiffened Plates”, The Aeronautical Quarterly **15**, 185-198, August, 1964

[32] C. A. Mercer and Miss C. Seavey, “Prediction of Natural frequencies and normal modes of skin-stringer panel rows”, J. Sound and Vib. **6**(1), 149-162, 1967

[33] B. R. Long, “A stiffness-type analysis of the vibration of a class of stiffened plates”, J. Sound and Vib. **16**(3), 323-335, 1971

[34] H. Zeng and C. W. Bert, “A differential quadrature analysis of vibration for rectangular stiffened plates”, J. Sound and Vib. **241**(2), 247-252, 2001

[35] S., Mahalingham, “Vibration of stiffened rectangular plates”, J. Roy. Aero. Soc. **67,** 305 – 307, 1963

[36] R. S. Langley, “Application of the dynamic stiffness method to the free and

forced vibrations of aircraft panels", J. Sound and Vib. **135**(2), 319-339, 1989

[37] D. J. Mead and Y. Yaman, "The harmonic response of rectangular sandwich plates with multiple stiffening: A flexural wave analysis", J. Sound and Vib. **145**(3), 409-428, 1991

[38] R. M. Grice and R. J. Pinnington, "A method for the vibration analysis of built-up structures, Part I: Introduction and analytical analysis of the plate stiffened beam", J. Sound and Vib. **230**(4), 825-849, 2000

[39] D. J. Mead, D. C. Zhu and N. S. Bardell, "Free vibration of an orthogonally stiffened flat plate", J. Sound and Vib. **127**(1), 19-48, 1988

[40] G. S. Palani, N. R. Iyer and T. V. S. R. Appa Rao, "An efficient finite element mode for static and vibration analysis of plates with arbitrary located eccentric stiffeners", J. Sound and Vib. **166**(3), 409-427, 1993

[41] U. Orrenius and S. Finnveden, "Calculation of wave propagation in rib-stiffened plate structures", J. Sound and Vib. **198**(2), 203-224, 1996

[42] R. M. Grice and R. J. Pinnington, "A method for the vibration analysis of built-up structures, Part II: Analysis of the plate stiffened beam using a combination of finite element analysis and analytical impedance", J. Sound and Vib. **230**(4), 851-875, 2000

[43] M. H. Coja and A. C. Nilsson, "Energy transmission through engine foundation", Proc. 10th Intl Congr. Sound and Vib. Stockholm, Sweden, 7-10 July 2003

[44] F. J. Fahy and E. Lindqvist, "Wave propagation in damped, stiffened structures characteristic of ship construction", J. Sound and Vib. **45**(1), 115-138, 1976

[45] D. J. Mead, "A new method of analyzing wave propagation in periodic structures; applications to periodic Timoshenko beams and stiffened plates", J. Sound and Vib. **104**(1), 9-27, 1986

[46] G. W. Steward, "Introduction to matrix computation", Academic Press, New

York and London, 1973

[47] W. W. Smith Jr. and S. Erdman, "A note on the inversion of complex matrix", IEEE Trans. Automat. Contr. **19**(1), 64, 1974

[48] A. Graham, "Matrix theory and applications for engineers and mathematician", Ellis Horwood Limited, Chichester, 1979

[49] MSC/NASTRAN V70.5 "Quick Reference Guide" 1998

[50] T. R. Lin and J. Pan, "Some vibration characteristics of finite ribbed plates", Proc. 11th Intl Congr. Sound and Vib. St Petersburg, Russia, 4-8 July 2004

[51] J. Q. Pan, J. Pan, and C. H. Hansen, "Total power flow from a vibrating rigid body to a thin panel through multiple elastic mounts", J. Acoust. Soc. Am. **92**(2), 895-907, 1992

[52] T. R. Lin and J. Pan, "A closed form solution for the dynamic response of finite ribbed plates", J. Acoust. Soc. Am. **119**(2), 917-925, 2006

[53] M. P. Norton, "Fundamentals of noise and vibration analysis for engineers", Cambridge University Press 1989

[54] D. J. Mead, "Wave propagation in continuous periodic structures: Research contributions from Southampton, 1964-1995", J. Sound and Vib. **190**(3), 495-524, 1996

[55] A. J. Keane and W. G. Price, "On the vibrations of mono-coupled periodic and near-periodic structures", J. Sound and Vib. **128**(3), 423-450, 1989

[56] M. Heckl, "Wave propagation on beam-plate systems", J. Acoust. Soc. Am. **33**(5), 640 – 651, 1961

[57] D. J. Mead, "A general theory of harmonic wave propagation in linear periodic system with multiple coupling", J. Sound and Vib. **27**(3), 235-260, 1973

[58] D. J. Mead, "Wave propagation and natural modes in periodic systems: I. Mono-coupled systems", J. Sound and Vib. **40**(1), 1-18, 1975

[59] D. J. Mead, "Wave propagation and natural modes in periodic systems: II.

Multi-coupled systems, with and without damping", J. Sound and Vib. **40**(1), 19-39, 1975

[60] R. C. Engels, "Response of infinite periodic structures", J. Sound and Vib. **69**(2), 181-197, 1980

[61] M. G. Faulkner and D. P. Hong, "Free vibrations of a mono-coupled periodic system", J. Sound and Vib. **99**(1), 29-42, 1985

[62] A. K. Roy and R. Plunkett, "Wave attenuation in periodic structures", J. Sound and Vib. **104**(3), 395-410, 1986

[63] Y. Yong and Y. K. Lin, "Propagation of decaying waves in periodic and piecewise periodic structures of finite length", J. Sound and Vib. **129**(2), 99-118, 1989

[64] L. Brillouin, "Wave propagation in periodic structures", New York: Dover 1953

[65] L. Meirovitch and R. C. Engels, "Response of periodic structures by the Z-transform method", AIAA Journal **15**, 167 – 174, 1977

[66] R. S. Langley, "A variation principle for periodic structures", J. Sound and Vib. **135**(1), 135-142, 1989

[67] D. J. Mead and A. S. Bansal, "Mono-coupled periodic systems with a single disorder: Free wave propagation", J. Sound and Vib. **61**(4), 481-496, 1978.

[68] D. J. Mead and A. S. Bansal, "Mono-coupled periodic systems with a single disorder: Response to convected loading", J. Sound and Vib. **61**(4), 497-515, 1978.

[69] C. H. Hodges, "Confinement of vibration by structural irregularity", J. Sound and Vib. **82**(3), 411-424, 1982

[70] C. H. Hodges and J. Woodhouse, "Vibration isolation from irregularity in a nearly periodic structure: theory and measurements", J. Acoust. Soc. Am. **74**(3), 894 – 905, 1983

[71] D. M. Photiadis, “Anderson localization of one-dimensional wave propagation on a fluid-loaded plate”, J. Acoust. Soc. Am. **91**(2), 771-780, 1992

[72] M. B. Sobnack and D. G. Crighton, “Anderson localization effects in the transmission of energy down an iregularly ribbed fluid-loaded structure”, Proc. R. Soc. Lond. A **444**, 185-200, 1994

[73] J. L. Guyader, C. Boisson and C. Lesueur, “Energy transmission in finite coupled plates, Part I: Theory”, J. Sound and Vib. **81**(1), 81-92, 1982

[74] C. Boisson, J. L. Guyader, P. Millot and C. Lesueur, “Energy transmission in finite coupled plates, Part II: Application to an L shaped structure”, J. Sound and Vib. **81**(1), 93-105, 1982

[75] J. M. Cuschieri, “Structural power-flow analysis using a mobility approach of an L-shape structure”, J. Acoust. Soc. Am. **87**(3), 1159-1165, 1990

[76] J. M. Cuschieri and M.D. McCollum, “’In-plane and out-of-plane waves’ power transmission through an L-plate junction using the mobility power flow approach”, J. Acoust. Soc. Am. **100**(2), 857-870, 1996

[77] N. J. Kessissoglou, “Power transmission in L-shape plates including flexural and in-plane vibration”, J. Acoust. Soc. Am. **115**(3), 1157-1169, 2004

[78] E. C. N. Wester and B. R. Mace, “Statistical Energy Analysis of two edge-coupled rectangular plates: Ensemble averages”, J. Sound and Vib. **193**(4), 793-822, 1996

[79] E. K. Dimitriadis and A. D. Pierce, “Analytical solution for the power exchange between strongly coupled plates under random excitation: A test of Statistical Energy Analysis concepts”, J. Sound and Vib. **123**(3), 397-412, 1988

[80] E. Rebillard and J. L. Guyader, “Vibrational behaviour of a population of coupled plates: Hypersensitivity to the connexion angle”, J. Sound and Vib. **188**(3), 435-445, 1995

[81] N. F. Farag and J. Pan, "On the free and forced vibration of single and coupled rectangular plates", J. Acoust. Soc. Am. **104**(1), 204-216, 1998

[82] N. F. Farag, "Dynamic response and power flow characteristics of coupled structures – A modal receptance approach", PhD dissertation, The University of Western Australia, 1998

[83] Z. H. Wang, J. T. Xing and W. G. Price, "An investigation of power flow characteristics of L-shaped plates adopting a substructure approach", J. Sound and Vib. **250**(4), 627-648, 2002

[84] A. C. Nilsson, "Attenuation of structure-borne sound in superstructures on ships", J. Sound and Vib. **55**(1), 71-91, 1977

[85] A. N. Bercin, "An assessment of the effects of in-plane vibrations on the energy flow between coupled plates", J. Sound and Vib. **191**(5), 661-680, 1996

[86] Y. K. Tso and C. H. Hansen, "The transmission of vibration through a coupled periodic structures", J. Sound and Vib. **215**(1), 63-79, 1998

[87] A. C. Nilsson, "A method for the prediction of noise and velocity levels in ship constructions", J. Sound and Vib. **94**(3), 411-429, 1984

[88] M. D. Olson and C. R. Hazell, "Vibration studies on some integral rib-stiffened plates", J. Sound and Vib. **50**(1), 43-61, 1977

[89] Ed. by L. L. Beranek, "Noise and Vibration Control", McGraw-Hill Book Company, New York, 1971

[90] A. D. Nashif, D. Jones, J. P. Henderson, "Vibration damping", John Wiley & Sons Inc., 1985

[91] L. Lapcik Jr., P. Augustin, A. Pistek, L. Bujnoch, "Measurement of the dynamic stiffness of recycled rubber based railway track mats according to the DB-TL 918.071 standard", Appl. Acoust. **62**, 1123-1128, 2001

[92] M. Sjoberg, L. Kari, "Testing of nonlinear interaction effects of sinusoidal and noise excitation on rubber isolator stiffness", Polymer Testing, **22**(3), 343-351,

2003

[93] S. Nadeau and Y. Champoux, “Application of the direct complex stiffness method to engine mounts”, Expt. Tech. **24**(3), 21-25, 2000

[94] J. W. Verheij, “Multi-path sound transfer from resiliently mounted shipboard machinery”, Institute of applied physics, TNO-TH, 1986

[95] Å. Fenander, “Frequency dependent stiffness and damping of rail pads”, Proc. Inst. Mech. Eng. **211**(Part F), 51-62, 1997

[96] D. J. Thomson, W. J. Van Vliet and J.W. Verheij, “Developments of the indirect method for measuring the high frequency dynamic stiffness of resilient elements”, J. Sound and Vib. **213**(1), 169-188, 1998

[97] C. J. Norwood, J. D. Dickens, “The effect of vibration isolator properties and structural stiffness on isolator performance”, J. Vib. Contl. **4**, 253-275, 1998

[98] J. D. Dickens, C. J. Norwood, “Universal method to measure dynamic performance of vibration isolators under static load”, J. Sound and Vib. **244**(4), 685-696, 2001

[99] D. J. Ewins, “Modal Testing: Theory and Practice”, Research Study Press Ltd., 1984

[100] C. M. Harris, “Shock and Vibration Handbook”, Fourth edition, McGraw-Hill, New York, 1996

[101] F. H. Todd, “Ship hull vibration”, London: Edward Arnold Ltd. 1961

[102] F. Ward, C. Norris, D. Catley and A. Crexis, “Local vibrations in ship's structures”, Trans. of North East Coast Inst. Engrs. Shipbuilders **98**, 49 – 64, 1982

[103] F. F. Van Gunsteren, “Some further calculations of wave-induced ship hull ibrations”, Dynamics of Marine Vehicles and Structures in Waves, 278 – 290, 1974

[104] O. F. Hughes, “Ship structural design”, Soc. Naval Archs. Marine Engrs,

Jersey city, New Jersey 1988

[105] M. K. Hakala, "Application of the finite element method to fluid-structure interaction in ship vibration", Research Report, Tech. Res. Centre of Finland, 1986

[106] L. J., Xia, W. G. Wu, C. J. Weng and X. D. Jin, "Analysis of fluid-structure-coupled vertical vibration for high speed ships", J. Ship Mech. **4**(3), 43 – 50, 2000

[107] A. C. Nilsson, "Wave propagation in simple hull-frame structures of ships", J. Sound and Vib. **44**(3), 393-405, 1976

[108] A. C. Nilsson, "Reduction of structure-borne sound in simple ship structures: Results of modal tests", J. Sound and Vib. **61**(1), 45-60, 1978

[109] A. C. Nilsson, "Propeller induced hull plate vibrations", J. Sound and Vib. **69**(4), 539-557, 1980

[110] E. V. Lewis, "Stuctural dynamics of Ships", Dynamics of Marine Vehicles and Structures in Waves, 278 – 290, 1974

[111] Z. Y. Ye and K. C. Fang, "The vibration of propeller of high speed ships", Trans. of ASME PVP **122**, 75 – 79, 1987

[112] J. P. Den Hartog, "Mechanical Vibrations", Third Edition, McGraw-Hill Book Company, Inc., New York and London, 1947

[113] R. J. Pinnington and R. G. White, "Power flow through machine isolators to resonant and non-resonant beams", J. Sound and Vib. **75**(2), 179-197, 1981

[114] I. Dyer, "Moment impedance of plates", J. Acoust. Soc. Am. **32**(10), 1290-1297, 1960

Publications originating from this thesis work

T. R. Lin and J. Pan, “A closed form solution for the vibration response of finite ribbed plates”, J. Acoust. Soc. Am. **119**(2), 917-925, 2006

T. R. Lin, N. Farag and J. Pan, “Evaluation of frequency dependent rubber mount stiffness and damping by impact test”, Appl. Acoust. **66**(7), 829-844, 2005

T. R. Lin and J. Pan, “Some vibration characteristics of finite ribbed plates”, Proceedings of the 11th International Congress of Sound and Vibration, St Petersburg, Russia, 3369-3376, July 2004

J. Pan, X. Li, J. Tian and **T. Lin**, "Short sound decay of ancient Chinese music bells", J. Acoust. Soc. Am. **112**(6), 3042-3045, 2002

J. Q. Pan, J. Pan, R. Ming and **T. Lin**, "Three-dimensional response and intensity of torsional vibration in a step shaft", J. Sound Vib. **236**(1), 115-128, 2000

"The thesis extends the state of art in several aspects and is in many aspects quite impressive."

Examiner1's comments

"The body of the work submitted by the candidate more than satisfies the requirements for Ph.D., particularly the candidate's demonstration of expertise in various numerical approaches as well as experiments."

Examiner1's comments

"The initial application to ship structures is a significant achievement."

Examiner1's comments

"The thesis is a substantial contribution demonstrating the ability of the candidate to make vibration predictions of ribbed plate structures using variety of numerical tools."

Examiner1's comments

"Mr Lin has produced a substantial body of work, drawing together a number of topics involved in the prediction of vibration response in complex structures commonly applied to marine vessels."

Examiner2's comments

"Overall, this is an excellent thesis with a substantial contribution to the knowledge of ship noise and vibration."

Examiner3's comments